The Estimation and Statistical Inferences of the Position and Orientation of a Scanning Laser Doppler Vibrometer

by

Xiandi Zeng

Dissertation submitted to the Faculty of the

Virginia Polytechnic Institute and State University

in partial fulfillment of the requirements for the degree of

DOCTOR OF PHILOSOPHY

in

Mechanical Engineering

APPROVED:

Alfred L. Wicks, Chairman

A. Lynn Abbott

Larry D. Mitchell

Harry H. Robertshaw

Robert L. West

November, 1994

Blacksburg, Virginia

c.2

The Estimation and Statistical Inferences of the Position and Orientation of a Scanning Laser Doppler Vibrometer

by

Xiandi Zeng

Committee Chairman: Alfred L. Wicks
Mechanical Engineering

(ABSTRACT)

In this dissertation, two nonlinear regressive models, the forward model and the inverse model, have been developed to determine the pose (position and orientation) of the scanning laser Doppler vibrometer (SLDV) with respect to a structural coordinate system. The parameters in the forward model include the pose and the ranges. The parameters in the inverse model include the pose only. The parameters of those models are obtained by using the least squares technique. A geometrical method is developed to get an estimation of the pose and the ranges. This estimation is used as an initial solution in the iterative procedure for determining the parameters in the nonlinear regressive models. The statistical inferences are made about the inverse model by the linear approximation. The nonlinearity of the inverse modal is measured in order to verify the validity of the linear approximation. Included along with the development of the models, are the implementation of the algorithm (geometrical method and inverse model), the assessment of the inverse model, the calibration of the scanner, and the accuracy evaluation of the algorithm.

To My Mother

ACKNOWLEDGEMENTS

I would like to express my sincere appreciation to my advisor, Dr. Alfred L. Wicks, for his advice and friendship through my graduate studies at Virginia Tech. I thank him for providing me the opportunity to pursue a Ph.D. degree with him and being there to help answer those difficult questions whenever called upon. My grateful thanks go to Dr. Larry D. Mitchell for his guidance, advice, and support. His invaluable suggestions and constant encouragement guided me throughout many difficult times. My special thanks go to Dr. Bob West for his frequent advice and suggestions on the research. I would like to thank Dr. A. Lynn Abbott and Dr. Harry H. Robertshaw for their advice and serving on my committee. I would also like to thank the entire Laser Team especially, William X. Li, David Coe, David Montgomery, Jose Dominguez, Jim DeVlaminck, and David Rice for their help and support. I wish to thank Tao Song, J. Barry Fallon, Jonathan D. Blotter, Yu Liu, Minfu Lu, and Dongbing Zhang and all those who helped me through the research. I also wish to thank Ms. Eloise J. Lafon for her help in many ways.

I wish to thank my beloved wife, Zhiqun Xiao, and my parents, Zhaoling Zeng and Yinju Liu, for their love, encouragement, and support. They also always helped me through the difficult times and shared many happy moments. I also wish to thank my sisters, brothers and in-laws for their support for all those years.

Finally, I have special thanks for Mr. Mark Schiefer and the Zonic Corporation, Milford, Ohio. Without their support, this work would not be possible.

TABLE OF CONTENTS

LIST OF FIGURES

LIST OF TABLES

NOMENCLATURE

Roman

$[A]$	First-order derivative matrix defined in Eq. (4.8)
A, B	Two arbitrary Cartesian coordinate systems
$\{a\}, \{b\}, \{c\}$	Defined in Eq. (4.63) for finding axis k
A_X, B_X, A_Y, B_Y	Defined in Eq. (8.2) based on the scanner parameter a_X, a_Y, b_X, b_Y
a_X, b_X, a_Y, b_Y	Scanner parameters in the linear voltage-angle relation
$\{B\}$	An arbitrary vector
$\{B'\}$	A vector obtained by rotating vector $\{B\}$ by an angle $-\theta$ about axis k
$[BB]$	Matrix defined in Eq. (3.43)
(BB, EE)	Root search interval for $f(L_{P_3})=0$
$\{B_x\}, \{B_y\}, \{B_z\}$	Vectors defined in Eq. (3.44)
CC	Curvature criterion
C_1, C_2	Two positions of the camera coordinate system defined in Fig. 3.4
C_x, C_y	Coordinates of the center of the computer coordinate system
$C^{PE}_{\{k\}}, C^{IN}_{\{k\}}$	Parameter-effects and intrinsic curvatures
D	Distance between the primary and secondary positions defined in Fig. 4.2
D_1, D_2, D_3	Distances between different calibration points defined in Fig. 3.6
$D_{ij,S}, D_{ij,L}$	Distance between registration point P_i and P_j measured in the structural coordinate system and laser coordinate system, respectively
D_x, D_y	Errors in the image coordinates due to lens distortion
dl	Scanner parameter: the separation distance of the reflection centers of the two scanning mirrors
$\{d_i\}$	A vector from average point P_a to the ith registration point P_i
$\{d_i'\}$	A vector obtained by rotating vector $\{d_i\}$ by an angle $-\theta$ about axis k
$\{d_{i,P}\}, \{d'_{i,P}\}$	Projections of vectors $\{d_i\}$ and $\{d_i'\}$ onto the plane normal to axis k
$E[\,]$	Expectation of
E_{ij}	Error defined in Eq. (4.30)

E_{ik}	Error defined in Eq. (4.32)
ER_i	Error defined in Eq. (4.31)
ERR_i	Error defined in Eq. (4.33)
e_1, e_2, e_3, e_4	Four Euler parameters defined in Eq. (3.8)
e_{len}	Error defined in Eq. (3.55)
$\{e_P\}$	Error vector defined in Eq. (3.54)
$\{e_{TOL}\}$	Error defined in Eq. (3.56)
$e_{\varphi_{P_j X}}$, $e_{\varphi_{P_j Y}}$	Prediction error in the scanning angles defined in Eq. (7.21)
$\{F\}$	Values of f_i (i=1, 2, ..., 6) defined in Eq. (4.8), or the left-hand side vector of Eq. (5.26)
f	Effective focus length
f_0	Distance between O_C and the projection of point P onto Z_C axis
f_i (i=1, 2, ..., 6)	Distance difference defined in Eq. (4.4)
$f(L_{P_3})$	A function of $f(L_{P_3})$ defined in Eq. (4.18)
G_1, G_2	Two positions of the gripper coordinate system defined in Fig. 3.4
H	Distance between the laser center and the OP line defined in Fig. 7.1
${}^B_A[H]$	Transformation matrix from coordinate system A to coordinate system B
H_0	Null hypothesis
H_a	Alternative hypothesis
$\{h\}$	Direction vector in the parameter space in the measures of nonlinearity
h_1, h_2, zz	Defined in Eq. (4.68) and Eq. (4.69) for finding axis k
h_3, h_4, yy	Defined in Eq. (4.73) for finding axis k
h_5, h_6, xx	Defined in Eq. (4.75) for finding axis k
$[I]$	Unit (identity) matrix
$[J]$	First-order derivative matrix of inverse model defined in Eq. (5.27) and Eq. (5.24)
$[\hat{J}]$	Matrix $[J]$ evaluated at $\{\gamma\}=\{\hat{\gamma}\}$
k	Equivalent axis for expressing the orientation of a coordinate system
$\{L\}_0$	Initial value for the ranges ($=\{L_{P_1,0}, L_{P_2,0}, L_{P_3,0}, L_{P_4,0}\}^T$)
L_1, L_2, L_3	Length of a ray from O_C to three calibration points defined in Fig. 3.6

L_P	Third component of scanning coordinates of spatial point P
l_i	Distances of the laser beam away from home position defined in Fig. 7.1
$\{l, m, n\}$	Direction cosines of a vector, an axis, or a point in 3D space
M	Number of parameters in regressive model
$MS\varepsilon_{\varphi_X}$, $MS\varepsilon_{\varphi_X}$	Estimations of the standard deviation of residuals of the scanning angles defined in Eq. (7.18)
N	Number of registration points, or number of observations (data points) in regression
O'	Moving laser center
$\{{}_SO'\}$	The origin coordinates of ${}_SO'X'Y'Z'$ with respect to ${}_PO'X'Y'Z'$
${}_PO'X'Y'Z'$	A temporary coordinate system defined for primary position
${}_SO'X'Y'Z'$	A temporary coordinate system defined for secondary position
$O_CX_CY_CZ_C$	Camera coordinate system
$O_GX_GY_GZ_G$	Gripper coordinate system
$O_IX_IY_IZ_I$	Intermediate coordinate system
$O_LX_LY_LZ_L$	Laser coordinate system
$O_OX_OY_OZ_O$	Object coordinate system
$O_RX_RY_RZ_R$	Robot world coordinate system
$O_SX_SY_SZ_S$	Structural coordinate system
P	An arbitrary registration or spatial point
P_a	Average point of all registration points defined in Eq. (4.55)
P_i	The ith registration or spatial point
$[PP]$	Matrix defined in Eq. (3.49)
Q	Sum of (weighted) squared residuals, or the point obtained by rotating point P
$[QQ]$	Matrix defined in Eq. (3.49)
Q_i	The point obtained by rotating point P_i
${}^B_A[R]$	Rotation matrix from coordinate system A to coordinate system B
r	Length of vector $\{B\}$, or $=\sqrt{X_d^2+Y_d^2}$
S	Uncertainty of the horizontal scale factor, δu
$\{S_1\}$, $\{S_2\}$	Two vectors defined in Fig. 4.2

SLDV	Scanning Laser Doppler Vibrometer
s	Estimated standard deviation of the residuals in regression model
s^2	Estimated variance of the residuals in regression model
$s(\,)$	Estimated standard deviation of
s_{pq}	Inner product of two arbitrary vectors $\{p\}$ and $\{q\}$
s_{Pre}	Prediction standard deviation defined in Eq. (7.22)
s_{φ}	Estimated standard deviation of the residuals of the scanning angles ($=s_{\theta}$)
s_{θ}	Estimated standard deviation of the residual of the first two components of the scanning coordinates
${}^{B}_{A}\{T\}$	Origin coordinates of coordinate system A with respect to coordinate system B
${}^{B}_{A}\{T_X,\ T_Y,\ T_Z\}^T$	Three components of ${}^{B}_{A}\{T\}$
t^*	Statistic for hypothesis test with t-distribution
$[U]$, $[\Sigma]$, $[V]$	Matrices obtained from a singular value decomposition of a matrix
$[V]$	First-order derivative matrix in nonlinear regressive model
$\lfloor \dot{V} \rfloor$	Second-order derivative matrix array in the nonlinear regressive model
$Var[\,]$	Variance of
V_{PX}, V_{PY}	Input voltages to scanner controller for X and Y mirror for spatial point P
$\{v_{P_0,X_L}\}$	Derivative vector of μ_{P_0,X_L} as defined in Eq. (5.68)
$\{v_{P_0,Y_L}\}$	Derivative vector of μ_{P_0,Y_L} as defined in Eq. (5.68)
$[X]$	Derivative matrix in the linear regression
$\{x\}$	Regressor variable vector in regression model
X_d, Y_d	Actual image coordinates of a calibration point
X_f, Y_f	Computer image coordinates for a calibration point
X_u, Y_u	Ideal image coordinates of a calibration point
x_u, y_u	Scaled image coordinates as defined in Eq. (3.22)
x_C, y_C, z_C	Camera coordinates of a calibration point
x_L, y_L, z_L	Laser coordinates of a registration point
x_M, y_M, z_M	Translational movement of laser head from primary position to secondary position

x_O, y_O, z_O	Object coordinates of a calibration point
x_S, y_S, z_S	Structural coordinates of a registration point
$x_{P,L}, y_{P,L}, z_{P,L}$	Laser coordinates of point P
$x_{P,S}, y_{P,S}, z_{P,S}$	Structural coordinates of point P
$\bar{x}_A, \bar{y}_A, \bar{z}_A$	Weighted average coordinates defined in Eq. (3.40)
$\bar{x}_B, \bar{y}_B, \bar{z}_B$	Weighted average coordinates defined in Eq. (3.40)
$\{Y\}$	Response vector in regression model

Greek

$\alpha_1, \alpha_2, \alpha_3$	Three angles defined in Figure 4.2
α, β, γ	Three *Z-Y-X* Euler angles
$\{\beta\}$	Parameters in the linear regressive model
$\{\hat{\beta}\}$	Least squares estimator of the parameters $\{\beta\}$
$\{\delta L\}$	Increment of the ranges defined in Eq. (4.9)
$\delta u, \delta v$	Known image scale factor
$\{\delta\gamma\}$	Increment of the six pose parameters defined in Eq. (5.26)
$\{\varepsilon\}$	Residual vector in regressive model
$\{\varepsilon\}_\theta$	Column vector formed by all the residuals in the scanning coordinates defined in Eq. (5.7)
$\{\varepsilon_{P_i}\}_S$	$=\{\varepsilon_{x_{P_i S}}, \varepsilon_{y_{P_i S}}, \varepsilon_{z_{P_i S}}\}^T$: residuals in the structural coordinates for point P_i in Eq. (4.44)
$\{\varepsilon_{P_i}\}_\theta$	$=\{\varepsilon_{\theta_{P_i X_L}}, \varepsilon_{\theta_{P_i Y_L}}\}^T$: residuals in the scanning coordinates for point P_i in Eq. (5.14)
$\varepsilon_{V_{P_i X}}, \varepsilon_{V_{P_i Y}}$	Residuals in the input voltages defined in Eq. (8.5)
$\varepsilon_{\varphi_{P_i X}}, \varepsilon_{\varphi_{P_i Y}}$	Residuals in the scanning angles defined in Eq. (7.16)
ϕ_1, ϕ_2, ϕ_3	Separation angles between different calibration points defined in Fig. 3.6
ϕ_i	Angle between vector $\{d_i\}$ and axis k

φ_i	Scanning angle defined in Fig. 7.1
$\varphi_{P,X}$, $\varphi_{P,Y}$	X scanning angle and Y scanning angle for spatial point P
$\{\gamma\}$	Parameters in the inverse model or in the general nonlinear regression
$\{\hat{\gamma}\}$	Least squares estimator of parameters $\{\gamma\}$
$\eta_{\{h\}}^{PE}$, $\eta_{\{h\}}^{IN}$	Relative parameter-effects and relative intrinsic curvature
η_{max}^{PE}, η_{max}^{IN}	Maximum relative parameter-effects and maximum relative intrinsic curvature
κ, κ_1, κ_2	lens distortion coefficients used in Eqs. (3.17) and (3.19)
λ	Scale factor
$\{\mu\}$	Expectation function in regression model
$\hat{\mu}_\varphi$	Average of the residuals of the scanning coordinates
$\{\dot{\mu}_{\{h\}}\}$, $\{\ddot{\mu}_{\{h\}}\}$	Velocity and acceleration of curve $\{\mu(\{\hat{\gamma}\}+\lambda\{h\})\}$ on the expectation surface through $\{\mu(\{\hat{\gamma}\})\}$
$\{\ddot{\mu}_{\{h\}}\}^{PE}$, $\{\ddot{\mu}_{\{h\}}\}^{IN}$	The acceleration in and normal to the tangent plane
μ_{P_i,X_L}, μ_{P_i,Y_L}	Expectation function of the scanning coordinates defined in Eq. (5.20)
θ	Equivalent angle for expressing the orientation of a coordinate system
θ_i'	Angle between vector $\{d_i\}$ and vector $\{d_i'\}$
θ_{P,X_L}, θ_{P,Y_L}	First two components of scanning coordinates of spatial point P
ρ	Standard radius defined in Eq. (5.93)
$\hat{\rho}$	Correlation coefficient

Symbols

{ }, [ ]	Vector and matrix
$\{\ \}^T$, $[\ ]^T$	Transpose of vector and matrix
$\|\ \|$	Length of a vector
$\|\ \|$	Absolute value of

CHAPTER ONE

INTRODUCTION

In this chapter, a scanning laser Doppler vibrometer (SLDV) will be briefly described. Then, two measurement systems and their problems using the SLDV will be discussed. Finally, the objective of this dissertation and the problem definition will be stated.

1.1 Scanning laser Doppler vibrometer and its application

With the development of laser technology, a variety of new instruments have appeared for scientific and industrial measurements. The SLDV is one of those instruments. The SLDV consists of two parts: a Michelson interferometer and a scanner [1.1-1.4]. The Michelson interferometer performs the measurement of the velocity. The scanner aims the laser beam at desired measurement points on a testing structure. It can scan a rectangular area within its viewable angles.

The SLDV offers many advantages over the conventional accelerometer in dynamic measurements. It offers non-contacting measurements, high measurement speed, high sensitivity, high accuracy, and high spatial resolution. Its non-contact feature is particularly useful for testing light-weight structures and for measuring the velocity in severe conditions such as high temperatures. Its high spatial resolution makes it possible to get the angular velocity by numerically operating on the measured translational velocity field [1.5-1.8]. Therefore, it has found many applications in the research laboratory and industry for dynamic testing, modal analysis, noise predication and control, and damage identification [1.9-1.15].

1.2 Laser-based mobility measurement systems and concerned problems

When used for dynamic measurements, the SLDV scans a structure which may be a simple beam, a compressor, a tire, or the fuselage of an airplane. The velocity fields over the structure are measured. Figure 1.1 shows a typical SLDV setup. The structure being tested is a plate. A Cartesian coordinate system called structural coordinate system $O_S X_S Y_S Z_S$ is established. The points on the plate are well defined with respect to this coordinate system, which means the structural coordinates (x_S, y_S, z_S) of these points are known. Although the structural coordinate system in this example is on the plate in Fig. 1.1, it can be placed anywhere in space. Another Cartesian coordinate system called laser coordinate system $O_L X_L Y_L Z_L$ is also established. It is placed at the laser head of the SLDV. A more detailed description of these coordinate systems will be given in chapter 2. The laser coordinates (x_L, y_L, z_L) of those points on the plate are not known yet.

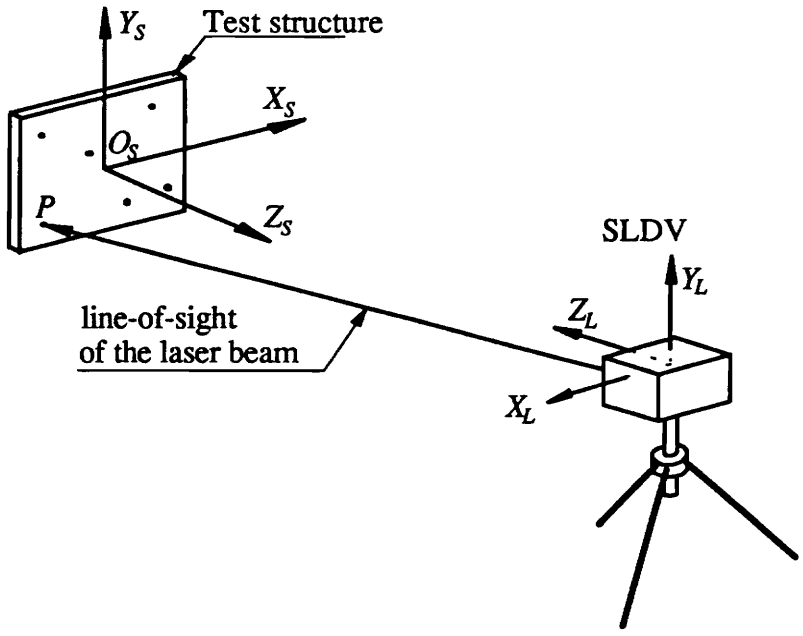

Figure 1.1 A scanning laser Doppler vibrometer at work

In the laser-based mobility measurement system described in [1.16-1.17], the structural response is dominated by the vibration in one direction. The velocities of a vibrating structure at some specific known locations are desired. One problem with this system is how to automatically aim the laser beam at those specific locations.

In another system, the velocities of six degree-of-freedom (three translational and three rotational degrees) for a vibrating structure are desired. However, the SLDV can only measure the velocity along the line-of-sight of the laser beam, i.e., the translational velocity in the line-of-sight direction (see Fig. 1.1). Thus, some strategies are required to obtain the six degree-of-freedom velocities. A complete description of the velocity in Cartesian coordinate system can be given by its three components along the three axes or by its magnitude and three direction cosines. The SLDV measures the component of the velocity along the direction of line-of-sight, or the projection of the velocity along the direction of line-of-sight. Mathematically, if one knows three independent projections of the velocity along three known directions, the three components of the velocity along the reference axes may be found. Experimentally, the SLDV can be placed at three different positions to obtain three projections of the velocity. If the directions of the line-of-sight of the laser beam for those positions are known in the structural coordinate system, the velocity along the three axes may be reconstructed. In this way, the three translational velocities are found or reconstructed [1.18-1.19]. The three angular velocities can not be directly measured by the SLDV. But they can be obtained by numerical operations on the measured (reconstructed) velocity field [1.9-1.15]. Therefore, it is necessary to obtain the direction of the line-of-sight of the laser beam with respect to the structural coordinate system.

The two problems previously discussed are actually the two stages of one problem. In other words, if one can aim the laser beam at the desired location (first stage), one will be able to obtain the direction of the line-of-sight of the laser beam (second stage). Further study shows that the problem can be solved once the pose (position and orientation) of the SLDV is determined with respect to the structural coordinate system. The pose of the SLDV is defined as the pose of the laser coordinate system with respect to the structual coordinate system. Therefore, the problem of concern in this dissertation is how to determine the pose of the laser coordinate system.

1.3 Objective of this dissertation

The objective of this dissertation is to develop a method that will give the best estimation of the pose of the laser coordinate system with respect to the structural coordinate system using experimentally obtained data. The method will give the inferences about the estimated pose and will be able to predict the positioning error of the laser beam.

1.4 Problem difinition

In the experimental data acquisition, some points defined as registraiton points on the test strucure are used to determine the SLDV pose. The known information for each registration point is the structural coordinates (x_S, y_S, z_S) and the input voltages (V_X, V_Y) to the scanner controller. The input voltages can be linearly converted to the scanning angles (φ_X, φ_Y). Thus, the problem in this dissertaiton is defined as the fillowing. Given N (N>=4) noncollinear registration points whose structural coordinates (x_S, y_S, z_S) are

known and whose scanning angles (φ_X , φ_Y) are measured, estimate the pose of the SLDV as well as its statistical properties. The more detailed descripions about the defined problem will be given in chapter 2.

CHAPTER TWO

MATHEMATICAL MODEL FOR THE POSE DETERMINATION OF THE SLDV

In this chapter, the definition of the pose of the SLDV will be given. The relationship between the input voltages and the structural coordinates for a spatial point P will be derived. Then, the pose determination problem will be mathematically defined. Next, it will be shown that once the pose of the SLDV is obtained, the input voltages and the direction of the line-of-sight of the laser beam for a known point P can be determined. Finally, the procedure to solve the defined problem will be discussed.

2.1 Coordinate transformation and the pose of the SLDV

A spatial point P can be fully determined by its structural coordinates $(x_{P,S}, y_{P,S}, z_{P,S})$. It can also be fully determined by its laser coordinates $(x_{P,L}, y_{P,L}, z_{P,L})$. Figure 2.1 shows the two coordinate systems and the spatial point P.

The relationship between the structural coordinate $(x_{P,S}, y_{P,S}, z_{P,S})$ and the laser coordinate $(x_{P,L}, y_{P,L}, z_{P,L})$ is the coordinate transformation. Following equation is the transformation from the laser coordinates to the structural coordinates.

$$\begin{Bmatrix} x_P \\ y_P \\ z_P \end{Bmatrix}_S = {}^S_L\{T\} + {}^S_L[R] \begin{Bmatrix} x_P \\ y_P \\ x_P \end{Bmatrix}_L = {}^S_L \begin{Bmatrix} T_X \\ T_Y \\ T_Z \end{Bmatrix} + {}^S_L[R] \begin{Bmatrix} x_P \\ y_P \\ x_P \end{Bmatrix}_L \tag{2.1}$$

where ${}^S_L\{T\}$ is the translation vector. It is the coordinates of the origin O_L measured from the structural coordinate system, i.e., the position vector of the laser coordinate system

measured from the structural coordinate system. ${}^{S}_{L}[R]$ is the rotation matrix which rotates a vector from the laser coordinate system into the structural coordinate system. The columns of ${}^{S}_{L}[R]$ are the direction cosines of the three axes (X_L, Y_L, and Z_L) measured in the structural coordinate system. Thus, ${}^{S}_{L}[R]$ is the orientation of the laser coordinate system.

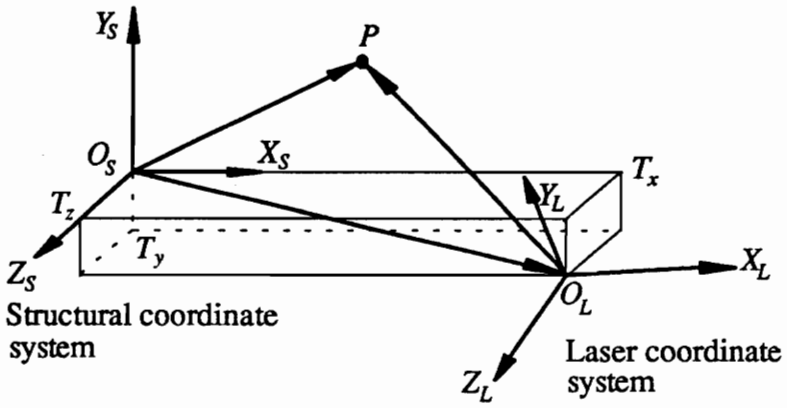

Figure 2.1 Relationship between the structural and laser coordinate system

As pointed out in chapter 1, the term "pose" is defined as the position and orientation. The pose of the SLDV is defined as the position and orientation of the laser coordinate system, i.e., ${}^{S}_{L}\{T\}$ and ${}^{S}_{L}[R]$ with respect to the structural coordinate system.

From Eq. (2.1), the transformation from the structural coordinates to the laser coordinates can be obtained. Using the orthogonality of the rotation matrix, one gets

$$\begin{Bmatrix} x_P \\ y_P \\ z_P \end{Bmatrix}_L = -{}^{S}_{L}[R]^T \left({}^{S}_{L}\{T\} \right) + {}^{S}_{L}[R]^T \begin{Bmatrix} x_P \\ y_P \\ z_P \end{Bmatrix}_S = {}^{L}_{S}\{T\} + {}^{L}_{S}[R] \begin{Bmatrix} x_P \\ y_P \\ z_P \end{Bmatrix}_S . \tag{2.2}$$

It can be seen that the pose of the structural coordinate system with respect to the laser coordinate system is the following:

$$ {}^{L}_{S}\{T\} = -{}^{S}_{L}[RT]^{T}\left({}^{S}_{L}\{T\}\right), \text{ and } {}^{L}_{S}[R] = {}^{S}_{L}[R]^{T} \ . \tag{2.3} $$

Therefore, if the pose of the laser coordinate system is obtained relative to the structural coordinate system, the pose of the structural coordinate system can be easily found with respect to the laser coordinate system, or vise versa.

Using homogeneous transformation, Eq. (2.1) can be written as

$$ \{x_P, y_P, z_P, 1\}^{T}_{S} = {}^{S}_{L}[H]\{x_P, y_P, z_P, 1\}^{T}_{L} \tag{2.4} $$

where

$$ {}^{S}_{L}[H] = \begin{bmatrix} {}^{S}_{L}[R] & {}^{S}_{L}\{T\} \\ 0\ 0\ 0 & 1 \end{bmatrix}. \tag{2.5} $$

It can be seen that if the structural coordinates and the laser coordinates are known, the pose of the SLDV can be determined from Either Eq. (2.1) or Eq. (2.2). In the real situation, only the structural coordinates are known for point *P*. Information contained in the laser coordinates is the mirror drive voltages or input voltages. These input voltages are the required voltages that will aim the laser beam at the spatial point *P*. Thus, to determine the pose, the relationship between the input voltages and the laser coordinates for point *P* is required. The pose can be determined by using the structural coordinates and the input voltages from a number of points.

2.2 Relationship between the input voltages and the laser coordinates

The relationship between the input voltages and the laser coordinates for point *P* will be developed in this section.

2.2.1 The operation of the scanner: input voltages and scanning angles

The scanner used by the SLDV is a two-dimensional one. It uses two independently controlled scanning mirrors to direct the laser beam to different spatial positions. The mirror directing the laser beam horizontally is called *X* mirror. The other directing the laser beam vertically is called *Y* mirror. The mirrors are rotated to change the deflection angle of the laser beam. The rotation of the mirrors is controlled by a scanner controller. Two voltages are input to the controller to control the *X* and *Y* mirror, respectively. The rotated angle of a mirror is proportional to the input voltage. When the input voltages for both mirrors are zero, the laser beam position is defined as home position. If the input voltage for *X* mirror is zero, the laser will move along a vertical line called *VV*. If the input voltage for *Y* mirror is zero, the laser beam will move along a horizontal line called *HH*. These two lines divide the space into four quadrants as shown in Fig. 2.2. The angle of the laser beam away from its home position is called the scanning angle. This scanning angle has a known relationship with the input voltage. In quadrant I, the laser beam has positive *X* scanning angle and positive *Y* scanning angle; in quadrant II, negative *X* and positive *Y*; in quadrant III, negative *X* and negative *Y*; in quadrant IV, positive *X* and negative *Y*.

A linear relationship is assumed between the scanning angle of the laser beam and the input voltage to the scanner controller for both *X* and *Y* mirrors [2.1]

$$\left.\begin{aligned}\varphi_X &= a_X + b_X V_X \\ \varphi_Y &= a_Y + b_Y V_Y\end{aligned}\right\} \tag{2.6}$$

where V_X and V_Y are the input voltages in volts. φ_X and φ_Y are scanning angles in degrees, a_X, b_X, a_Y, and b_Y are scanner parameters and can be obtained by calibration. Equation 2.6 is called the linear voltage-angle relation which is from the manufacturer and will be verified in chapter 7. If the scanning angles are known, the input voltages can be found as

$$\left.\begin{aligned}V_X &= (\varphi_X - a_X)/b_X \\ V_Y &= (\varphi_Y - a_Y)/b_Y\end{aligned}\right\}. \tag{2.7}$$

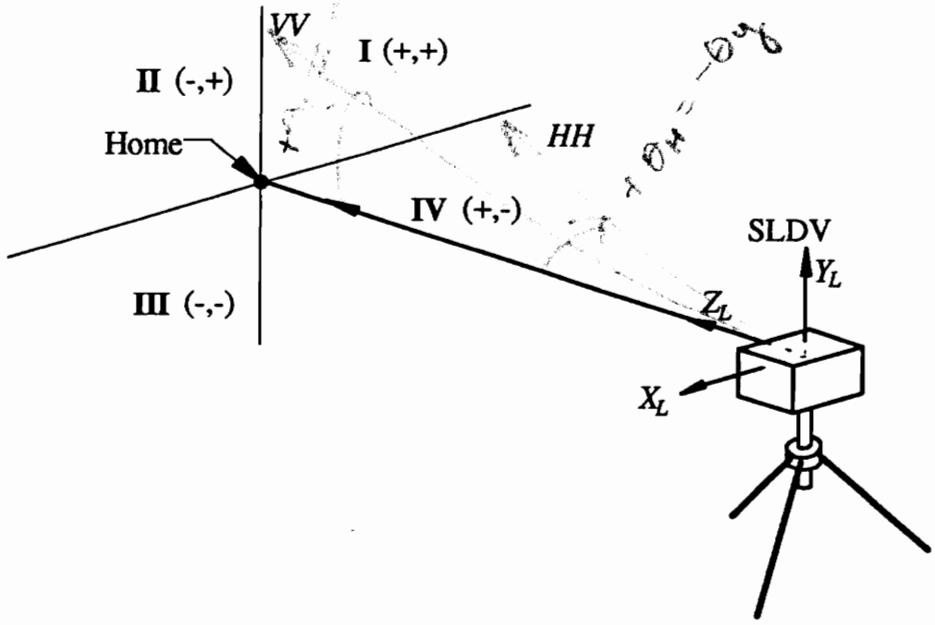

Figure 2.2 Laser head and relative scanning quadrants

2.2.2 Scanner model: scanning coordinates and laser coordinates

Figure 2.3 shows that the two mirrors are installed such that their rotation axes are perpendicular to each other, which is specific to the type of scanner in the SLDV laser

head in our laboratory. The two mirrors are inclined 45 degrees relative to the vertical while in their home position. The distance between the mirror surface along the laser beam at the home position is called separation distance *dl* of the reflection centers of the two mirrors. This distance is another scanner parameter and needs to be defined. The surfaces of the *X* and *Y* mirrors are assumed to be on the center of their rotation axes. The laser beam to the scanner is assumed to be parallel to the rotation axis of the *Y* mirror and to be incident on the center of the rotation axis of the *X* mirror. The laser beam reflected from the *X* mirror is assumed to be incident on the center of the rotation axis of the *Y* mirror. These assumptions are going to be verified in chapter 7 by analyzing the scanning angle residuals obtained from a nonlinear regression. Chapter 7 will also tell why the error caused by assuming the mirror surfaces to be on the center of their rotation axes is negligible.

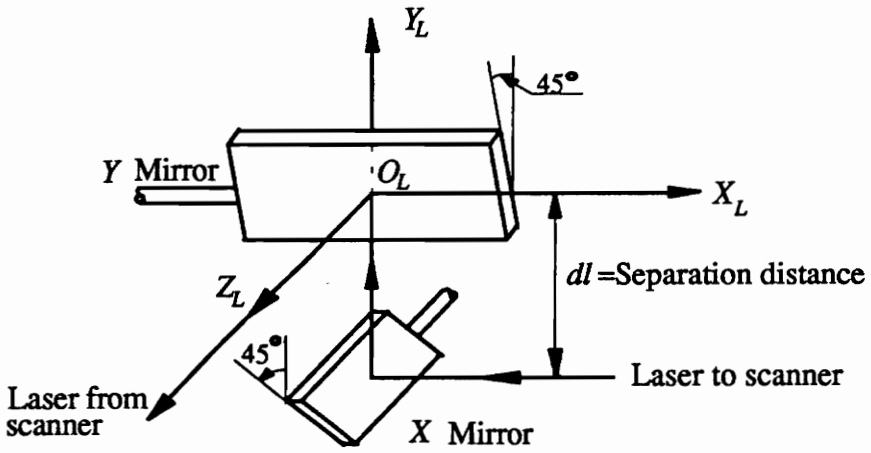

Figure 2.3 The laser home position and laser coordinate system

Figure 2.3 shows that the origin of the laser coordinate system is on the surface of the *Y* mirror at the reflection point while in the home position. The X_L axis is on center of the rotation axis of the *Y* mirror due to the assumptions mentioned previously. The Z_L axis is

along the laser beam at home position. X_L, Y_L, and Z_L form a right-hand coordinate system. The laser coordinate system is fixed at this position.

A spatial point P seen by the laser beam can be fully determined relative to the laser coordinates system in two ways.

The first is through the use of laser coordinates $(x_{P,L}, y_{P,L}, z_{P,L})$. The second is through the use of scanning coordinates $(\theta_{P,X_L}, \theta_{P,Y_L}, L_P)$ defined later. The scanner model is defined as the relationship between the laser coordinates $(x_{P,L}, y_{P,L}, z_{P,L})$ and the scanning coordinates $(\theta_{P,X_L}, \theta_{P,Y_L}, L_P)$. Due to the fact that two mirrors are separated, the scanner model can not be derived without further considerations.

When the X mirror rotates, the laser beam will move horizontally. It is equivalent to say that the laser beam comes from an imaginary point O' behind the Y mirror in Fig. 2.4 (a) (note that subscript P is omitted for angles in Figs. 2.4 and 2.5 for simplicity). The different horizontal positions are achieved by rotating the laser beam an angle θ_{P,Y_L} about an axis which passes O' and is parallel to the Y_L while the Y mirror is at home position. Angle θ_{P,Y_L} does not change with the rotation of the Y mirror.

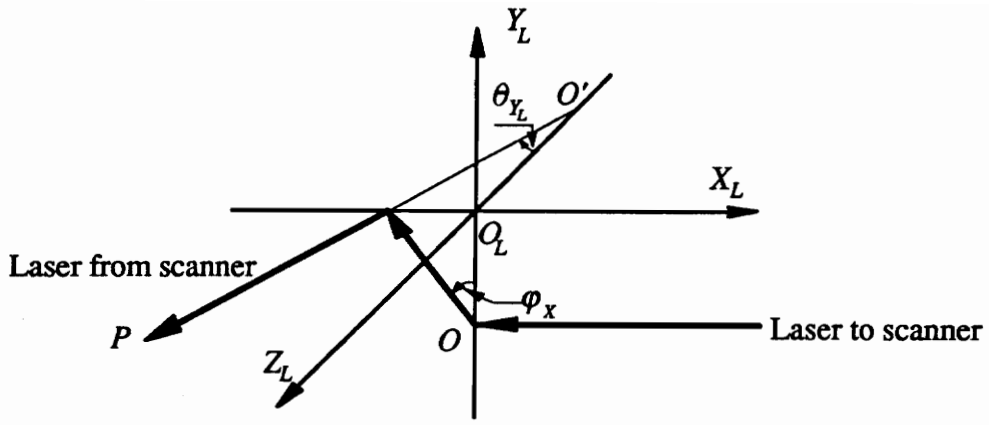

(a) $\theta_{X_L} = \varphi_Y = 0$ and $\theta_{Y_L} = -\varphi_X \neq 0$

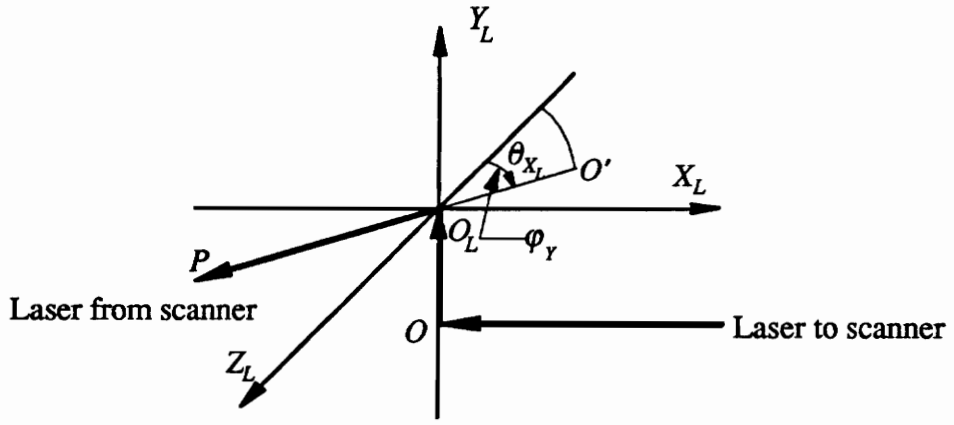

(b) $\theta_{X_L} = \varphi_Y \neq 0$ and $\theta_{Y_L} = -\varphi_X = 0$

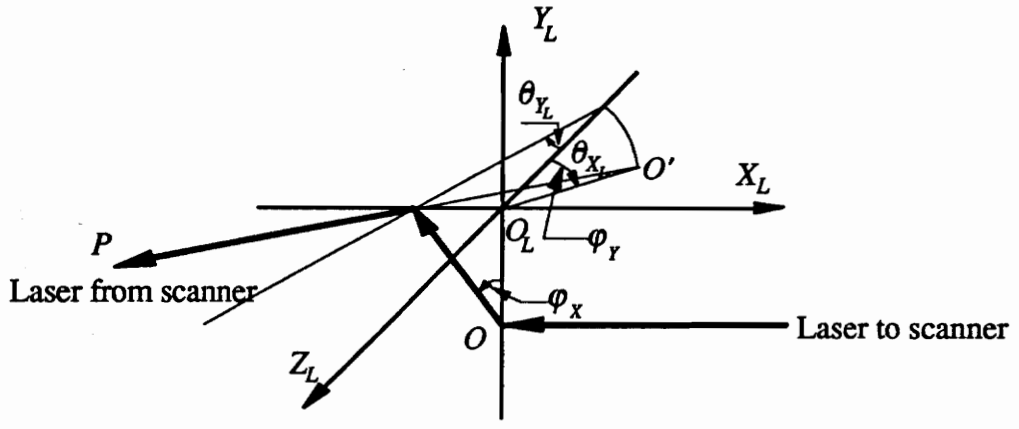

(c) $\theta_{X_L} = \varphi_Y \neq 0$ and $\theta_{Y_L} = -\varphi_X \neq 0$

Figure 2.4 Relationship between the scanning angles and the scanning coordinates

When the Y mirror rotates, the laser beam moves vertically. This rotation makes the imaginary point O', called moving laser center, move along a circle arc whose radius is equal to the separation distance centered at O_L and swinging in $Y_L - Z_L$ plane (see Fig 2.4 (b) and (c)). Different vertical laser positions are obtained by rotating the laser beam an angle θ_{P,X_L} about X_L axis. The range L_P is defined as the distance between the spatial point P and the moving laser center O'. It is clear that the point P is fully determined by its scanning coordinate $(\theta_{P,X_L}, \theta_{P,Y_L}, L_P)$. To make the sign agree between the laser coordinate and the scanning coordinate, we define that θ_{P,X_L} as positive if it moves the laser beam to a positive $y_{P,L}$, and visa versa. The same is true for θ_{P,Y_L}, which is referenced to the positive and negative $x_{P,L}$. Equation (2.8) can be easily obtained from Fig. 2.4. The negative sign in Eq. (2.8) is caused by the sign definition of the scanning angles and the scanning coordinates.

$$\left.\begin{aligned} \theta_{P,X_L} &= \varphi_{P,Y} \\ \theta_{P,Y_L} &= -\varphi_{P,X} \end{aligned}\right\} \tag{2.8}$$

From Eq. (2.8), the scanning angles can be found as

$$\left.\begin{aligned} \varphi_{P,X} &= -\theta_{P,Y_L} \\ \varphi_{P,Y} &= \theta_{P,X_L} \end{aligned}\right\} \tag{2.9}$$

Figure 2.5 which is obtained from Fig. 2.4, provides the geometry to develop the equations. The following equations are for the transformations of the scanning coordinates to the laser coordinates for point P.

$$\left.\begin{aligned} x_{P,L} &= L_P \sin\theta_{P,Y_L} \\ y_{P,L} &= (L_P \cos\theta_{P,Y_L} - dl)\sin\theta_{P,X_L} \\ z_{P,L} &= (L_P \cos\theta_{P,Y_L} - dl)\cos\theta_{P,X_L} \end{aligned}\right\} \tag{2.10}$$

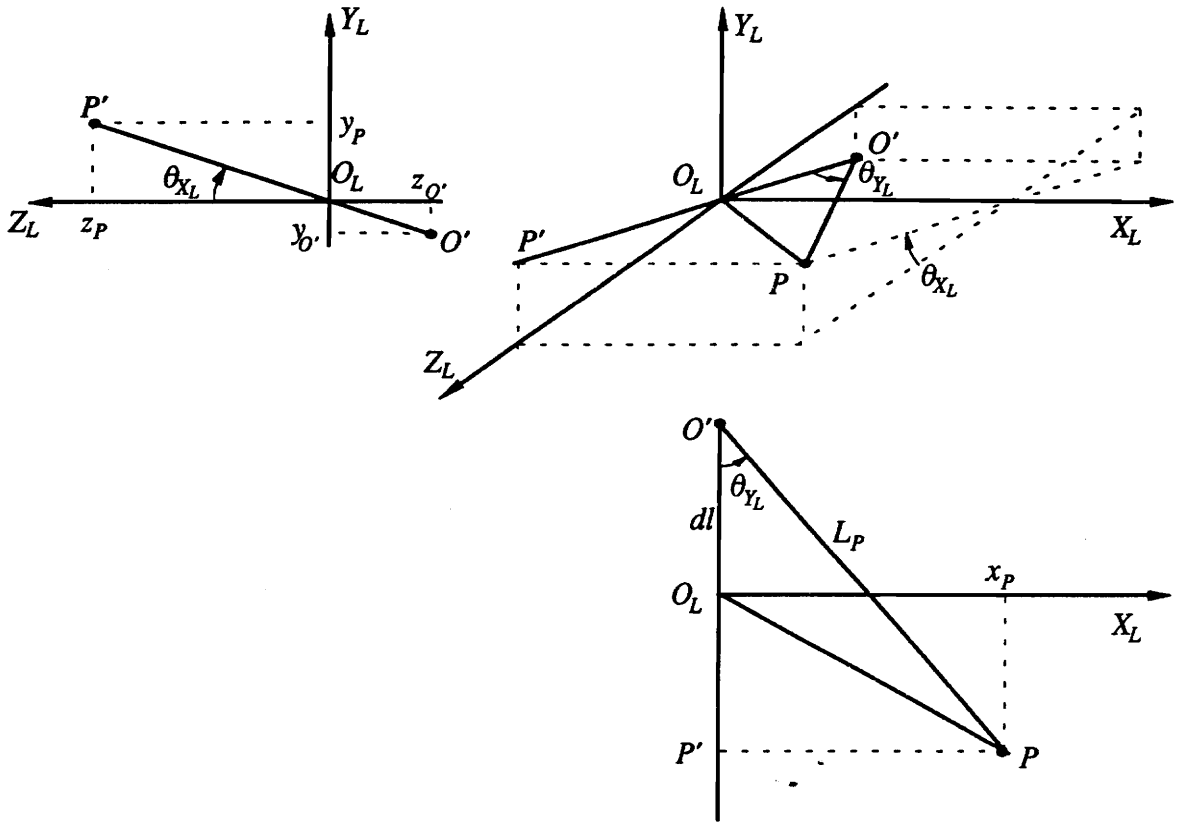

Figure 2.5 Geometry for deriving the scanner model

And following equations transfer the laser coordinates to the scanning coordinates.

$$\left.\begin{aligned} \theta_{PX_L} &= tan^{-1}\left(y_{PL} / z_{PL}\right) \\ \theta_{PY_L} &= tan^{-1}\left(x_{PL} / (\sqrt{y_{PL}^2 + z_{PL}^2} + dl)\right) \\ L_P &= \left(x_{PL}^2 + (\sqrt{y_{PL}^2 + z_{PL}^2} + dl)^2\right)^{1/2} \end{aligned}\right\} \tag{2.11}$$

Equations (2.10-2.11) refer to the scanner model. From this model, it can be seen that scanning angles are not sufficient to determine a spatial point. Any point on the line-of-sight of the laser beam will have the same scanning angles. But L_P defines the point.

2.2.3 Summary of various coordinate systems

Various coordinate systems have been introduced when deriving the relationship between the input voltages and the structural coordinates for a spatial point P. The transformations between them are Eqs. (2.1-2.2, 2.6-2.11). Table 2.1 is a summary of them.

Table 2.1 Various coordinate systems

Coordinate System	Variables
Input voltages	V_X and V_Y
Scanning angles	φ_X, and φ_Y
Scanning coordinate system	θ_{X_L}, θ_{Y_L}, and L
Laser coordinate system	x_L, y_L, and z_L
Structural coordinate system	x_S, y_S, and z_S

2.3 Discussions on the relationship between the input voltages and structural coordinates

In the previous two sections, the transformation has been derived from the input voltages to the structural coordinates, or vise versa, for a spatial point P. There are several

intermediate variables involved for that processing. Figure 2.6 shows the details about the transformation.

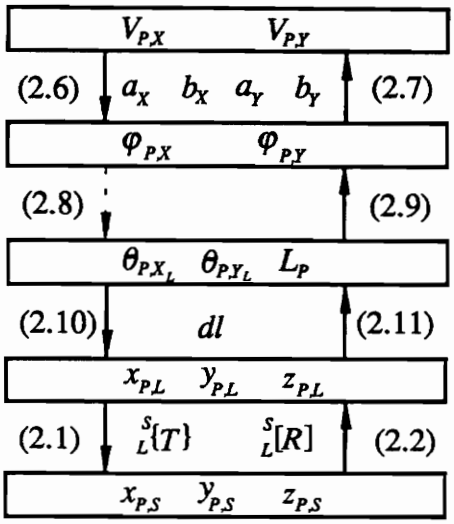

(Numbers in parentheses are reference equation number)

Figure 2.6 From the input voltages to structural coordinates or vise versa

In Fig. 2.6, the rectangular box contains the variables. The top box is the measured input voltages. The bottom box is the known structural coordinates. The down arrow ↓ presents the transformation from the upper box to the lower box. The number on the left side of the down arrow is the equation's number that can complete that transformation. The upper arrow ↑ and the number on the right side of it do the same thing, but they present the transformation from the lower box to the upper box. The parameters listed between the boxes are the required parameters for completing the transformation between that two boxes.

There are two group parameters in Fig. 2.6:

I). The five scanner parameters: a_X, b_X, a_Y, b_Y, and dl;

II). The pose parameters of the SLDV: ${}^{S}_{L}\{T\}$ and ${}^{S}_{L}[R]$.

The five scanner parameters are independent of the pose of the SLDV. Once calibrated, they can use as known parameters. However, they may change with time. Thus, occasional calibrations of them are needed. The pose of the SLDV contains six parameters (three translations and three rotations). It varies with the relative positions of the laser head to the structural coordinate system.

The range L_P in the scanning coordinate is something special. Currently, it can not be measured with the SLDV. If the input voltages are transformed to the structural coordinates, L_P remains unknown and must be figured out. The broken line in Fig. 2.6 shows this. However, if the structural coordinates are transformed to the input voltages, it can be directly calculated. The reason for these characteristics of the range L_P is that the scanning angles alone can not uniquely determine a spatial point. Any point on the path of the laser beam, or on the line passing O' and P, will have the same scanning angles.

Theoretically, using the known structural coordinates and the measured input voltages from enough points, all the unknowns can be solved which include the scanner parameters, the pose of the SLDV, and the ranges. In practice, it is not necessary to do that each time. The scanner parameters are independent of the pose of the SLDV. Once attained, they can be used as known quantities. By using the known scanning parameters, the scanning angles can be obtained from the measured input voltages. Thus, the remaining unknowns are the ranges and the pose of the SLDV. The ranges may or may not need to be determined. If the structural coordinates are expressed as functions of the scanning angles, the ranges are in the expression and need to be determined. The reason is that both the

scanning angles and the ranges are needed to uniquely determine a spatial point. If the scanning angles are expressed as a function of the structural coordinates, the ranges are not in the expression as unknowns.

In addition, the minimum number of points required to determine the pose uniquely must be defined. The pose contains six unknowns. If the scanning angles are expressed as functions of structural coordinates, two scanning angle equations are available for each point. Thus, three points (3×2=6) are needed to obtain a solution from a determined equation set (six equations for six unknowns) if the three points are not on a straight line in space. Due to the nonlinearity, multiple solutions exist with three points (see section **3.3.3** and section **4.1**). There is no way to find a uniquely solution. Another shortcoming with three points is that the measurement errors are forced to go into the determined pose. Therefore, at least four noncollinear points are needed. The least squares method can be applied to the overdetermined equation set to obtain a uniquely solution. If the structural coordinates are expressed as functions of the scanning coordinates, three equations are available for each point. However, one more unknown (the range L_p) is introduced for each point. Thus, three points will again yield a determined equation set (nine equations for nine unknowns). Four noncollinear points are still needed for a unique solution. In summary, four is the minimum number of points required for a unique solution of the pose of the SLDV.

On the basis of previous discussions, the problem in this dissertation can be defined. It was given in section **1.4**. For convenience, it is repeated here as the following. Given N (N>=4) noncollinear registration points whose structural coordinates (x_s, y_s, z_s) are known and

whose scanning angles (φ_X, φ_Y) are measured, estimate the pose of the SLDV as well as its statistical properties.

Of course, it is assumed that the laser head doesn't move when the laser beam is aimed at those N points.

2.4 Required input voltages and direction of line-of-sight for a known point P

2.4.1 The required input voltages to aim the laser beam at point P

Since P is known in structural coordinate system, its structural coordinate (x_{PS}, y_{PS}, z_{PS}) is known. Figure 2.6 has already shown the steps to obtain the input voltages. Using Eq. (2.2), the laser coordinates (x_{PL}, y_{PL}, z_{PL}) can be found. Then, using Eq. (2.11), the scanning coordinates can be obtained. Next, using Eq. (2.9), the scanning angles can be obtained. Finally, Eq. (2.7) is used to get the required input voltages.

2.4.2 The direction of the line-of-sight of the laser beam

From Figs. 2.4-2.5 it can be seen that the line-of-sight of the laser beam is the line PO'. The direction of line-of-sight is the direction cosines of line PO' measured in structural coordinate system. Referring to Fig. 2.5, the laser Cartesian coordinates of O' can be found as

$$\begin{Bmatrix} x_{O'} \\ y_{O'} \\ z_{O'} \end{Bmatrix}_L = \begin{Bmatrix} 0 \\ -dl \sin\theta_{P,X_L} \\ -dl \cos\theta_{P,X_L} \end{Bmatrix} \tag{2.12}$$

where (θ_{P,X_L}) is the scanning coordinate obtained in section **2.4.1.** The structural coordinates of O' can be obtained from Eq. (2.1),

$$\begin{Bmatrix} x_{O'} \\ y_{O'} \\ z_{O'} \end{Bmatrix}_S = {}^S\begin{Bmatrix} T_X \\ T_Y \\ T_Z \end{Bmatrix}_L + {}^S_L[R]\begin{Bmatrix} x_{O'} \\ y_{O'} \\ x_{O'} \end{Bmatrix}_L \tag{2.13}$$

Now vector PO' is

$$\{PO'\} = \{x_{O',S} - x_{P,S} \quad y_{O',S} - y_{P,S} \quad z_{O',S} - z_{P,S}\}^T \tag{2.14}$$

Therefore, the direction cosines for vector PO' can be easily found as

$$(l_{PO'}\ m_{PO'}\ n_{PO'})^T = \{PO'\} / \|\{PO'\}\| \tag{2.15}$$

where (l, m, n) is the direction cosines of a vector and $\|\bullet\|$ is the length of a vector.

2.4.3 A numerical example of the aforementioned

Problem: Given the origin coordinates and rotation matrix:

$${}^S_L\{T\} = \begin{Bmatrix} 0 \\ 0 \\ 60 \end{Bmatrix} \text{ inches } \left(\begin{Bmatrix} 0 \\ 0 \\ 1524 \end{Bmatrix} \text{ mm}\right), \quad {}^S_L[R] = \begin{bmatrix} -1 & 0 & 0 \\ 0 & 1 & 0 \\ 0 & 0 & -1 \end{bmatrix} \tag{2.16}$$

What is the required input voltages and the direction of line-of-sight of the laser beam for a known point $P=\{-3, -3, 0\}^T$ inches ($\{-76.2, -76.2, 0\}^T$ mm) in the structural coordinate system. Using following scanner parameters: a_X=0.0115 degrees, b_X=2.3988

degrees/volts, a_Y=0.0212 degrees, b_Y=2.4998 degrees/volts, and dl=1.8110 inches (46 mm).

Solution:

I). The required input voltages

Equation (2.2) is used to the laser coordinates for point P.

$$\begin{Bmatrix} x_P \\ y_P \\ z_P \end{Bmatrix}_L = \begin{bmatrix} -1 & 0 & 0 \\ 0 & 1 & 0 \\ 0 & 0 & -1 \end{bmatrix} \left(\begin{Bmatrix} -3 \\ -3 \\ 0 \end{Bmatrix} - \begin{Bmatrix} 0 \\ 0 \\ -60 \end{Bmatrix} \right) = \begin{Bmatrix} 3 \\ -3 \\ 60 \end{Bmatrix} \text{ inches } \left(\begin{Bmatrix} 76.2 \\ -76.2 \\ 1524 \end{Bmatrix} \text{ mm} \right) \quad (2.17)$$

Putting the laser coordinate into Eq. (2.11), one has

$$\left.\begin{aligned} \theta_{P,X_L} &= -2.8624 \text{ degrees} \\ \theta_{P,Y_L} &= 2.7753 \text{ degrees} \\ L_P &= 61.5986 \text{ inches } (1564.6044 \text{ mm}) \end{aligned}\right\} \quad (2.18)$$

Equation (2.9) gives

$$\left.\begin{aligned} \varphi_{P,X} &= -\theta_{P,Y_L} = -2.7753 \text{ degrees} \\ \varphi_{P,Y} &= \theta_{P,X_L} = -2.8624 \text{ degrees} \end{aligned}\right\} \quad (2.19)$$

The required input voltages is obtained from Eq. (2.7).

$$\left.\begin{aligned} V_{P,X} &= -1.1617 \text{ volts} \\ V_{P,Y} &= -1.1535 \text{ volts} \end{aligned}\right\} \quad (2.20)$$

II). Direction of the line-of-sight

Equation (2.12) gives the laser coordinate of O' as

$$\begin{Bmatrix} x_{O'} \\ y_{O'} \\ z_{O'} \end{Bmatrix}_L = \begin{Bmatrix} 0 \\ 0.0904 \\ -1.8087 \end{Bmatrix} \text{ inches } \left(\begin{Bmatrix} 0 \\ 2.2962 \\ -45.9410 \end{Bmatrix} \text{ mm} \right) \tag{2.21}$$

Using Eq. (2.13), one can find the structural coordinate for O' as

$$\begin{Bmatrix} x_{O'} \\ y_{O'} \\ z_{O'} \end{Bmatrix}_S = \begin{Bmatrix} 0 \\ 0 \\ 60 \end{Bmatrix} + \begin{bmatrix} -1 & 0 & 0 \\ 0 & 1 & 0 \\ 0 & 0 & -1 \end{bmatrix} \begin{Bmatrix} 0 \\ 0.0904 \\ -1.8087 \end{Bmatrix} = \begin{Bmatrix} 0 \\ 0.0904 \\ 61.8087 \end{Bmatrix} \text{ inches } \left(\begin{Bmatrix} 0 \\ 2.2962 \\ 1569.9410 \end{Bmatrix} \text{mm} \right) \tag{2.22}$$

Equation (2.14) is used to find the vector PO'.

$$\{PO'\} = \begin{Bmatrix} 0+3 \\ 0.0904+3 \\ 61.8087-0 \end{Bmatrix} = \begin{Bmatrix} 3 \\ 3.0904 \\ 61.8087 \end{Bmatrix} \text{ inches } \left(\begin{Bmatrix} 76.2000 \\ 78.4962 \\ 1569.9410 \end{Bmatrix} \text{mm} \right) \tag{2.23}$$

Finally the direction cosine of vector PO' is found to be

$$\begin{Bmatrix} l \\ m \\ n \end{Bmatrix}_{PO'} = \begin{Bmatrix} 0.0484 \\ 0.0499 \\ 0.9976 \end{Bmatrix}. \tag{2.24}$$

This example shows a case at which the laser is aligned with the testing structure. This is a good position for measuring the velocity of structures dominated by vibration in the Z_S direction.

2.5 Experimental setup and procedure to determine the pose of the SLDV

There may be two experimental setups for determining the pose of the SLDV. One is defined as the fixed setup. The other is defined as the index setup.

In the fixed setup, the laser head is placed at one position. The pose determination and velocity measurement will be completed at that position. That setup is being currently used. The advantage for this setup is that no additional equipment is needed to determine the pose of the SLDV. The disadvantage is the complexity involved in finding the range L_p.

In the index setup, the laser head is placed at two positions. One is called primary position and the velocity measurement will be completed at that position. The other is called secondary position. That position is mainly used to find the pose. The advantage of this setup is the simplicity in finding the ranges. The disadvantage of the setup is the need of additional equipment for recording the movement of the laser head from the primary position to the secondary position.

The procedure to determine the pose of the SLDV using the fixed setup follows.

1). Choose four or more known points on the test structure as registration points. They should be clearly and accurately marked on the structure.

2). Place the laser head at a position from which the velocity is to be measured and from which all registration points can be viewed by the laser.

3). Manually aim the laser beam at all the reference points one at a time. Record the corresponding scanner input voltages. These voltages will be converted to scanning coordinates through Eqs. (2.6) and (2.8).

4). Determine the pose of the SLDV using the information from step 1 and 3. In other word, the following information for each of the registration points will be used: the structural coordinates (x_S, y_S, z_S) and the scanning coordinates $(\theta_{X_L}, \theta_{Y_L})$.

There is an alternative procedure to determine the pose for the fixed set up.

1). Place the laser head at a position from which the velocity is to be measured.

2). Choose four or more pairs of scanner input voltages. They should be on the DAC steps of the D/A converter and should cover the desired area on the testing structure. These voltages will be converted to scanning coordinates through Eqs. (2.6) and (2.8).

3). Send the input voltages to the D/A converter one pair at a time, measure and record the corresponding locations of the laser beam spot on the structure with respect to the structural coordinate system. The measured locations are the structural coordinates for a registration point.

4). Determine the pose of the SLDV using the information from step 1 and 3. In other word, the following information for each of the registration points will be used: the structural coordinates (x_S, y_S, z_S) and the scanning coordinates $(\theta_{X_L}, \theta_{Y_L})$.

The procedure for determining the pose of the SLDV using the index setup follows.

1). Same as step 1 for fixed setup.

2). Place the laser head at the primary position from which the velocity is to be measured.

3). Same as step three for fixed setup.

4). Translationally move the laser head to the secondary position, record the movement in each coordinate axis direction. Repeat step 3.

5). Determine the pose of the SLDV for the primary position using the information from step 1, 3, and 4.

The pose determination procedure is also called SLDV registration because this procedure registers the pose of the SLDV in the structural coordinate system. The most difficulty

step is the last step in the three procedures. This dissertation will concentrate on the pose determination and develop methods that will give the best estimation of the pose of the SLDV using the data obtained from either the fixed setup or the index setup.

2.6 Summary

This chapter presented the basis for the determination of the pose of the SLDV. The mathematical model has been derived which is the relationship between the input voltages and the structural coordinates. The parameters used to relate to the input voltages to the structural coordinates are the scanner parameters, the pose of the SLDV, and the ranges. The scanner parameter can be obtained by calibration. The problem to be solved in this dissertation is to estimate the pose of the SLDV using experimentally obtained data. The minimum number of registration points required to uniquely determine the pose is 4. This chapter has also shown how to automatically aim the laser beam at a desired location and how to obtain the direction of the line-of-sight of the laser beam by using the known (or estimated) pose. In addition, the experimental setups and procedures for determining the pose of the SLDV are also given.

CHAPTER THREE

LITERATURE REVIEW

As stated in chapter 2, the goal of this dissertation is to estimate the pose of the laser coordinate system with respect to the structural coordinate system (or vice versa). In this chapter, some of the techniques will be reviewed that can estimate the pose of a coordinate system with respect to another coordinate system.

There are engineering applications involving the estimation of the position and orientation of a coordinate system [3.1-3.2]. Figure 3.1 shows a robot system [3.1]. In order to control the movement of the robot hand, the position and the orientation of the object coordinate system has to be found with respect to the robot world coordinate system. To do this, the relationships among the four coordinate systems must be found. That task can be completed by three calibrations. In each calibration, the position and orientation of a frame with respect another frame are found.

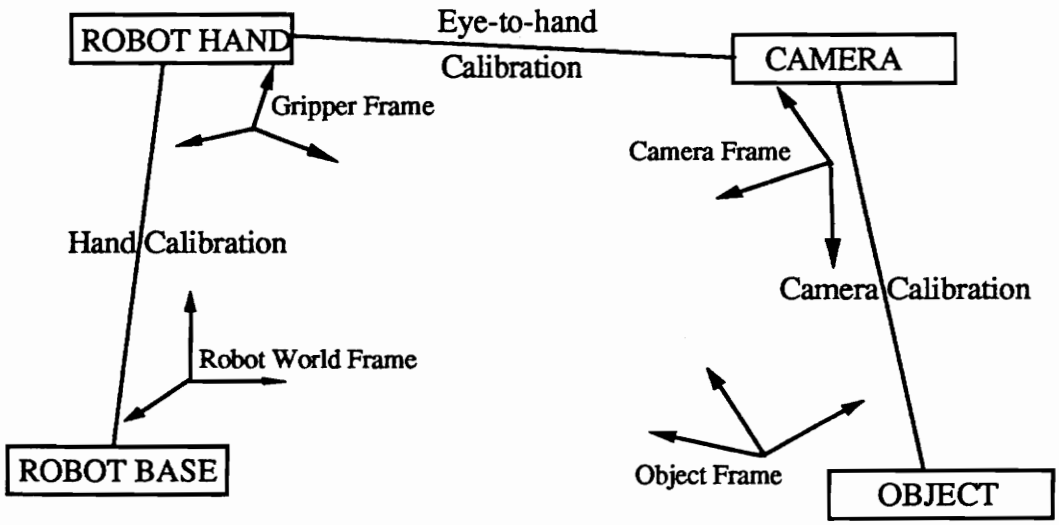

Figure 3.1 A robot system with four coordinate systems (adapted from [3.1])

In some applications, the different coordinate systems have same position (common origin) but different orientation. The rotation matrix is to be estimated. The satellite attitude estimation [3.4] is such an example. Other applications involve the estimation of a rotation matrix which rotates a set of vectors into another set of vectors. The two sets of vectors are measured in the same coordinate system. Vector correlation [3.4] is such an example.

In following sections, the different representations of the orientation of a coordinate system will first be reviewed. Then, the techniques for estimating the position and/or orientation of a coordinate system with respect to another coordinate system will be reviewed.

3.1 Various representations of the rotation matrix

The rotation matrix presents the orientation of a coordinate system with respect to another. Without loss of generality, two Cartesian coordinate systems, A and B, are taken as examples. The rotation matrix specified here is the orientation of coordinate system B with respect to coordinate system A. In following discussions, the two coordinate systems are assumed to have a common origin.

The several representations of the orientation discussed here are from Craig [3.5]. In the angle set conventions for expressing orientation, only the Z-Y-X Euler angles are reviewed.

3.1.1 The unit vector expression

In the unit vector expression, the orientation of the $O_B X_B Y_B Z_B$ is expressed by a 3 by 3 rotation matrix ${}^{A}_{B}[R]$. Each column of that matrix is one of the three axes of coordinate system B expressed as a unit vector. More specifically speaking, the first column is the direction cosines of the X_B axis, the second column the Y_B axis, and the third column the Z_B axis. They can be written as follows

$$ {}^{A}_{B}[R] = \begin{bmatrix} l_{X_B} & l_{Y_B} & l_{Z_B} \\ m_{X_B} & m_{Y_B} & m_{Z_B} \\ n_{X_B} & n_{Y_B} & n_{Z_B} \end{bmatrix}. \tag{3.1} $$

Since the three axes of X_B, Y_B, and Z_B are mutually orthogonal and each column of the ${}^{A}_{B}[R]$ is the direction cosines of one axis, the rotation matrix is an orthogonal matrix or

$$ ({}^{A}_{B}[R]^{T})({}^{A}_{B}[R]) = [I] \tag{3.2} $$

Note that the determinant of the rotation matrix is positive one since both coordinate systems agree with right hand rule. This orthogonality presents six constraints among the nine elements.

$$ \begin{aligned} l_{X_B} l_{X_B} + m_{X_B} m_{X_B} + n_{X_B} n_{X_B} &= 1 \\ l_{Y_B} l_{Y_B} + m_{Y_B} m_{Y_B} + n_{Y_B} n_{Y_B} &= 1 \\ l_{Z_B} l_{Z_B} + m_{Z_B} m_{Z_B} + n_{Z_B} n_{Z_B} &= 1 \\ l_{X_B} l_{Y_B} + m_{X_B} m_{Y_B} + n_{X_B} n_{Y_B} &= 0 \\ l_{Y_B} l_{Z_B} + m_{Y_B} m_{Z_B} + n_{Y_B} n_{Z_B} &= 0 \\ l_{Z_B} l_{X_B} + m_{Z_B} m_{X_B} + n_{Z_B} n_{X_B} &= 0 \end{aligned} \tag{3.3} $$

From above equation, it can be seen that there are only three independent variables in the rotation matrix. This can be demonstrated geometrically. Assume that the orientation of

the laser coordinate system that is going to be specified. For the X_B axis, two of its three direction cosines can be arbitrarily chosen, the third one can not be chosen because of following constraint

$$l_{X_B}^2 + m_{X_B}^2 + n_{X_B}^2 = 1 \tag{3.4}$$

For the Y_B axis, only one of its three direction cosines can be arbitrarily chosen since it must be perpendicular to the X_B axis and since there is a constraint similar to Eq. (3.4). For the Z_B axis, none of its three direction cosines can be arbitrarily chosen since it must be perpendicular to the X_B and the Y_B axes and since there is also a constraint similar to Eq. (3.4). This procedure clearly shows that only three direction cosines for the three axes can be arbitrarily chosen, which means there are only three independent variables in the rotation matrix ${}^{A}_{B}[R]$.

3.1.2 The three $Z_B - Y_B - X_B$ Euler angle expression

Figure 3.2 shows the Euler rotation procedure [3.5]. Using Euler angles, the final relative position of the two frames is achieved. Initially, the two frames coincide. Then frame $O_B X_B Y_B Z_B$ is rotated about the Z_B axis by an angle α. Frame $O_B X_B Y_B Z_B$ reaches a new position called position one. At position one, the frame $O_B X_B Y_B Z_B$ is rotated through angle β about the Y_B axis to reach position two. At position two, frame $O_B X_B Y_B Z_B$ rotates an angle γ about the X_B axis to reach the third new position called position three (not shown in Fig. 3.2). That is the final relative position. Those three angles are called $Z_B - Y_B - X_B$ Euler angles.

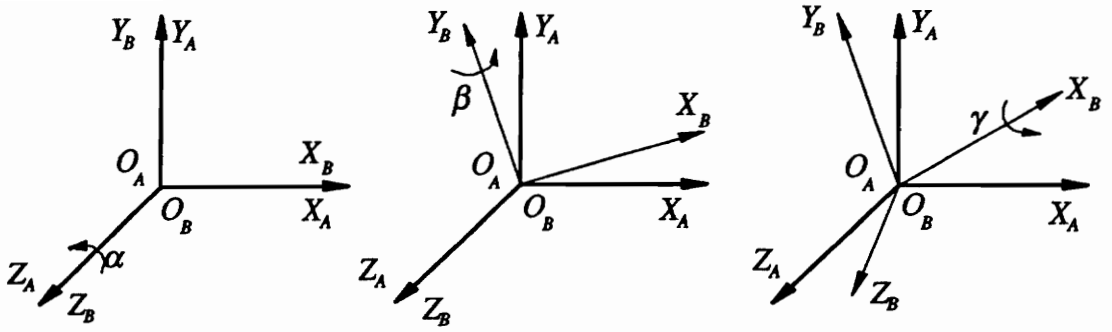

Initial position Position 1 Position 2

Figure 3.2 The three $Z_B - Y_B - X_B$ Euler angles

The rotation matrix obtained by this way is

$$ {}^{A}_{B}[R] = \begin{bmatrix} \cos\alpha\cos\beta & \cos\alpha\sin\beta\sin\gamma - \sin\alpha\cos\gamma & \cos\alpha\sin\beta\cos\gamma + \sin\alpha\sin\gamma \\ \sin\alpha\cos\beta & \sin\alpha\sin\beta\sin\gamma + \cos\alpha\cos\gamma & \sin\alpha\sin\beta\cos\gamma - \cos\alpha\cos\gamma \\ -\sin\beta & \cos\beta\sin\gamma & \cos\beta\cos\gamma \end{bmatrix} \quad (3.5) $$

The three independent variables in the rotation matrix are the three Euler angles. The rotation matrix obtained in this way will automatically satisfy the orthogonal condition. The determinant of the rotation matrix will be positive one.

3.1.3 Equivalent angle-axis expression

Figure 3.3 shows the equivalent angle-axis rotation procedure [3.5]. Using the equivalent angle-axis expression, the final relative position of the two frames can be achieved. Initially, the two frames coincide. Then frame $O_B X_B Y_B Z_B$ rotates an angle θ about an axis k according to the right-hand rule. The axis k is measured in the coordinate system $O_A X_A Y_A Z_A$ and its direction cosines are (l_k, m_k, n_k).

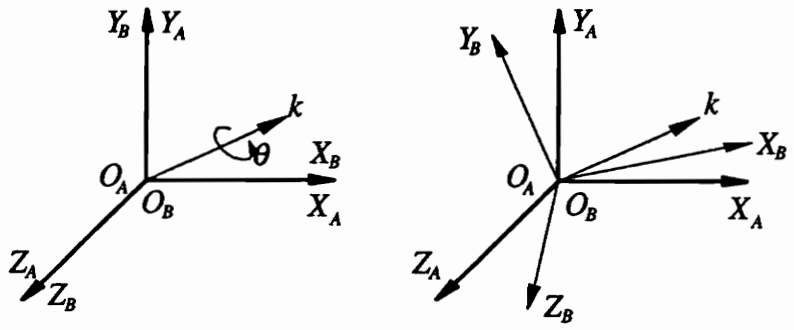

Figure 3.3 Equivalent axis-angle rotation procedure

The rotation matrix for this case is

$$ {}^{A}_{B}[R] = \begin{bmatrix} l_k l_k v\theta + \cos\theta & l_k m_k v\theta - n_k \sin\theta & l_k n_k v\theta + m_k \sin\theta \\ l_k m_k v\theta + n_k \sin\theta & m_k m_k v\theta + \cos\theta & m_k n_k v\theta - l_k \sin\theta \\ l_k n_k v\theta - m_k \sin\theta & m_k n_k v\theta + l_k \sin\theta & n_k n_k v\theta + \cos\theta \end{bmatrix} \tag{3.6} $$

where $v\theta = 1 - \cos\theta$. It appears that there are four variables in ${}^{A}_{B}[R]$. However there is an additional constraint for the direction cosines of the axis k.

$$ l_k^2 + m_k^2 + n_k^2 = 1 \tag{3.7} $$

Therefore, there are only three independent variables. The rotation matrix obtained in this way will automatically satisfy the orthogonal condition. The determinant of the rotation matrix will be positive one.

3.1.4 Euler parameter expression

The rotation matrix can be expressed as functions of four Euler parameters [3.5]. In terms of the equivalent axis k and the equivalent rotation angle θ, the Euler parameters are defined as

$$\left.\begin{aligned} e_1 &= l_k \sin(\theta/2) \\ e_2 &= m_k \sin(\theta/2) \\ e_3 &= n_k \sin(\theta/2) \\ e_4 &= \cos(\theta/2) \end{aligned}\right\} \tag{3.8}$$

Using above four parameter, the rotation matrix ${}^{A}_{B}[R]$ is

$${}^{A}_{B}[R] = \begin{bmatrix} 1-2e_2^2-2e_3^2 & 2(e_1e_2-e_3e_4) & 2(e_1e_3+e_2e_4) \\ 2(e_1e_2+e_3e_4) & 1-2e_3^2-2e_1^2 & 2(e_2e_3-e_1e_4) \\ 2(e_1e_3-e_2e_4) & 2(e_2e_3+e_1e_4) & 1-2e_1^2-2e_2^2 \end{bmatrix} \tag{3.9}$$

It once again appears that there are four variables in the rotation matrix. However, there is a constraint on the four parameters. Equation (3.8) gives the constraint

$$e_1^2+e_2^2+e_3^2+e_4^2=1. \tag{3.10}$$

Thus, the independent variables are three. The ${}^{A}_{B}[R]$ obtained in this way will automatically satisfy the orthogonal condition. The determinant of the rotation matrix will be positive one.

A quaternion is defined as a vector consisting of four elements [3.6-3.8]. It is called a unit or normalized quaternion if the length of the quaternion is one. It can be seen that the Euler parameters defined in Eq. (3.8) is a unit or normalized quaternion.

3.2 The three calibrations of the robot system

In this section, the techniques used to do the three calibrations in the robot system shown in Fig. 3.1 will be reviewed. The camera calibration will also be addressed since it is close to the problem of this dissertation.

3.2.1 Hand calibration

In the hand calibration (see Fig. 3.1), the position and orientation of the gripper coordinate system with respect to the robot world coordinate system will be found. The calibration can be furnished by built-in sensors or joint measurements. The calibration methods are also dependent on the structure of the robot, i.e., the number of the degree-of -freedom of the robot hand.

Lenz and Tsai [3.1] developed a technique to calibrate a Cartesian robot with six degree-of-freedom. The technique is one part of a trio for real-time 3D robotics eye [3.9-3.10], eye-to-hand [3.11], and hand calibration [3.1]. The key idea of their method is that only one single rotary joint is allowed to move for each movement while the robot motion can still be controlled such that calibration object remains within the field of view. That idea allows the calibration parameters to be fully decoupled. Thus, a multiple dimension problem is converted into a series of one dimensional problem.

3.2.2 Eye-to-hand calibration

In the eye-to-hand calibration, the position and orientation of the camera coordinate system with respect to the gripper coordinate system is found. There are several techniques to do this. In general, the calibration can be done after the hand calibration and camera calibration have been completed.

Shiu and Ahmad [3.12-3.13] developed a technique to do the eye-to-hand calibration by solving a homogenous transformation equation

$$\left({}^{G_2}_{G_1}[H]\right)\left({}^{G}_{C}[H]\right)=\left({}^{G}_{C}[H]\right)\left({}^{C_2}_{C_1}[H]\right) \tag{3.11}$$

where ${}^{G}_{C}[H]$ is the homogeneous transformation matrix from the camera coordinate system to the gripper coordinate system. Figure 3.4 shows how Eq. (3.11) can be derived. The homogenous transformation matrix for route $R-G_1-C_1-O$ and for route $R-G_2-C_2-O$ should be the same. Thus,

$$\left({}^{R}_{G_1}[H]\right)\left({}^{G}_{C}[H]\right)\left({}^{C_1}_{O}[H]\right)=\left({}^{R}_{G_2}[H]\right)\left({}^{G}_{C}[H]\right)\left({}^{C_2}_{O}[H]\right) \tag{3.12}$$

Comparing Eq. (3.12) and Eq. (3.11), one has

$$\left.\begin{aligned}{}^{G_2}_{G_1}[H]&=\left({}^{R}_{G_2}[H]\right)^{-1}\left({}^{R}_{G_1}[H]\right)\\ {}^{C_2}_{C_1}[H]&=\left({}^{C_2}_{O}[H]\right)\left({}^{C_1}_{O}[H]\right)^{-1}\end{aligned}\right\} \tag{3.13}$$

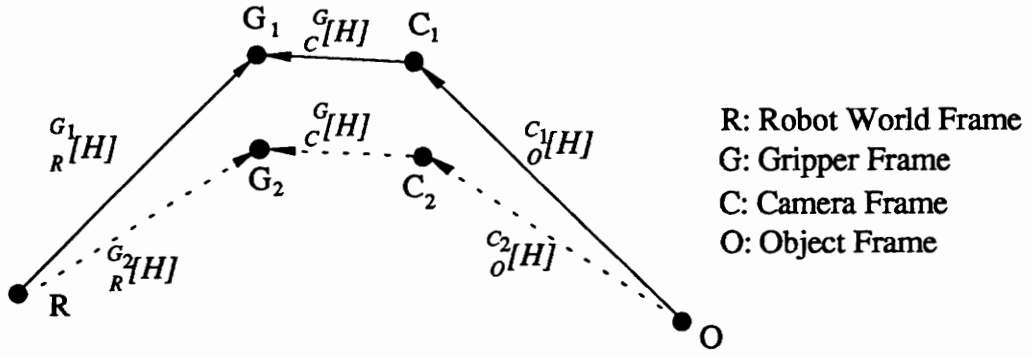

Figure 3.4 The coordinate transformation relationship

In the experiment, the robot hand is moved to position one. At that position, hand calibration and camera calibration are done to yield ${}^{G_1}_{R}[H]$ and ${}^{C_1}_{O}[H]$. Next the hand is moved to position two, the hand calibration and the camera calibration are done again to

yield ${}^{C_2}_{R}[H]$ and ${}^{C_2}_{O}[H]$. By treating cosine and sine functions as independent variables, Shiu and Ahmad obtained a linear equation to solve for ${}^{G}_{C}[H]$

Chou and Kamel [3.6] developed another method to solve for the ${}^{G}_{C}[H]$ from Eq. (3.11). They used quaternion to express the rotation matrix. Thus, a simple and well-structured linear system can be derived. A singular value decomposition technique is used to obtain the rotation matrix.

Tsai and Lenz [3.11] developed a technique to do the eye-to-hand calibration. That is another part of the trio for real-time robotics eye [3.9-3.10], eye-to-hand [3.11], and hand calibration [3.1]. Although independently developed, they used experimental schemes similar to those of Shiu and Ahmad. However, they solve that problem very differently. Tsai and Kamel's method can easily handle more stations (Figure 3.4 shows two stations) while keeping the number of the unknowns unchanged.

The techniques in [3.6, 3.11-3.13] require that the robot arm have at least two rotational degrees of freedom and that there are at least three camera calibrations. Chang et al [3.14] developed an eye-to-hand calibration method for a robot with one rotational degree of freedom. Chen and Zheng [3.15] developed a method which requires only one camera calibration.

3.2.3 Camera calibration

In camera calibration, two sets of parameters will be determined. One set is the camera intrinsic parameters which include effective focal length, horizontal scale factor (or the

uncertainty of the horizontal scale factor), image center, and lens distortion coefficient. The other set is the camera's extrinsic parameters which are the position and orientation of the camera coordinate system with respect to the object coordinate system. The intrinsic parameter will not vary with different camera positions while the extrinsic parameters will. Once the intrinsic parameters are determined, one just needs to calibrate the extrinsic parameters, which is called camera pose determination. In next section, the techniques for calibrating the extrinsic parameters will be reviewed.

Many techniques have been developed for camera calibration [3.9-3.10, 3.16-3.22]. They can be broadly classified according to different criterion: nonlinear versus linear systems, algorithms which consider the lens distortion and those which don't consider the lens distortion, and iterative solution procedures versus non-iterative solution procedures. Generally speaking, the consideration of the lens distortion will lead to a nonlinear equation set which requires an iterative solution procedure. Different techniques use different camera models and different experimental setups. The calibration techniques for a pinhole camera model with lens distortion considered will be reviewed.

3.2.3.1 Mathematical model for camera calibration

The information used for camera calibration is a set of points whose object coordinates $(x_o, y_o, z_o)^T$ are known and whose computer image coordinates (X_f, Y_f) are measured. The mathematical model is the relation between the object coordinates and the computer image coordinates for each point. The relation derived will be based on a pinhole camera with lens distortion considered. Four steps are involved to derive the relationship [3.10-

3.15]. Figure 3.5 shows the coordinate systems and perspective projection for a pinhole camera.

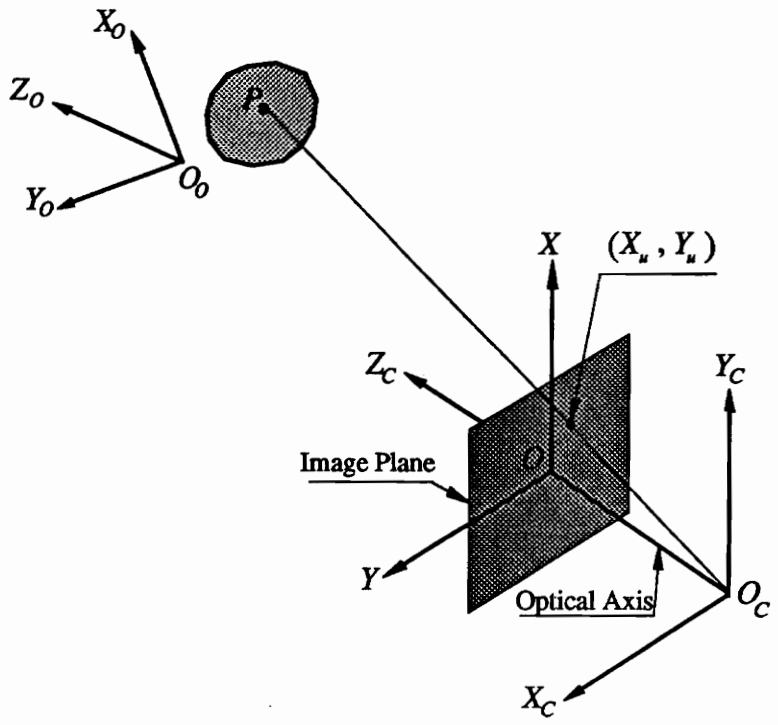

Figure 3.5 Pinhole camera and coordinate systems

I). From object coordinates to camera coordinates

This is simply a coordinate transformation. Expressed in translation and rotation, one has

$$\begin{Bmatrix} x \\ y \\ z \end{Bmatrix}_C = {}^C_O\{T\} + {}^C_O[R] \begin{Bmatrix} x \\ y \\ z \end{Bmatrix}_O \tag{3.14}$$

The parameters to be calibrated are the camera's extrinsic parameters, i.e., the position and orientation.

II). From camera coordinates to ideal image coordinates

With the assumption of a pinhole camera, one can obtain the ideal image coordinates (X_u, Y_u) by using perspective projection.

$$\left.\begin{aligned} X_u &= f\frac{x_C}{z_C} \\ Y_u &= f\frac{y_C}{z_C} \end{aligned}\right\} \tag{3.15}$$

where f is the effective focal length which is to be calibrated in this step. It is one of the intrinsic parameters of the camera.

III). From ideal image coordinates to actual image coordinates

Due to the lens distortion, the actual image coordinates will not be the same as the ideal image coordinates. The following equation is the relationship between the actual image coordinates and the ideal image coordinates.

$$\left.\begin{aligned} X_d + D_x &= X_u \\ Y_d + D_y &= Y_u \end{aligned}\right\} \tag{3.16}$$

where (X_d, Y_d) are the actual image coordinates on the image plane and

$$\left.\begin{aligned} D_x &= X_d(\kappa r^2) \\ D_y &= Y_d(\kappa r^2) \\ r^2 &= X_d^2 + Y_d^2 \end{aligned}\right\} \tag{3.17}$$

The calibration in this step is the radial lens distortion coefficient κ. There are two kinds of lens distortion: radial and tangential. An infinite series is required for each distortion. However, Tsai [3.10-3.11] found that for industrial machine vision applications, only the radial distortion needs to be considered and only the first term of the infinite series is needed. This results in Eq. (3.17).

IV). From actual image coordinates to computer image coordinates

The computer image coordinates are expressed in pixels. Thus the transformation of actual image coordinates to computer coordinates can be found as

$$\left.\begin{aligned} X_f &= S\delta u X_d + C_x \\ Y_f &= \delta v Y_d + C_y \end{aligned}\right\} \tag{3.18}$$

where (X_f, Y_f) are the computer image coordinates. δu and δv are the known image scale factors. S is the uncertainty of the horizontal image scale factor. There is no such uncertainty in the vertical direction for a solid state camera [3.9-3.10, 3.16-3.19]. C_x and C_y are the coordinates in pixels (row and column number) of the center of the computer image coordinate system (computer frame memory). In this step, the parameters to be calibrated are S, C_x, and C_y.

It can be seen that there are 11 parameters (6 extrinsic variables (3 translation plus three rotation) and 5 intrinsic variables (f, κ, S, C_x, and C_y)) to be calibrated. For each point, two equations are available that relate the measured (X_f, Y_f) to the known object coordinates $(x_O, y_O, z_O)^T$. Thus, at least 6 points are required to find a unique solution. More points will yield a more accurate estimation for the 11 parameters. It is clear that the equation set from which the calibration factors are solved are nonlinear.

3.2.3.2 Techniques for camera calibration

Tsai [3.9-3.10] obtained the calibration parameters in two steps. When noncoplanar calibration points were used, parameters ${}^{C}_{O}[R]$, ${}^{C}_{O}T_X$,${}^{C}_{O}T_Y$ and S are solved without iteration in the first step. Other parameters, f, ${}^{C}_{O}T_Z$ and k are solved iteratively in the second step. This is the third part of a trio for real-time robotics eye [3.9-3.10], eye-to-hand [3.11], and hand calibration [3.1]. Chang and Liang [3.16] solved the calibration problem by a recursive technique. Shih et al [3.17] developed an efficient and accurate technique for the camera calibration. The radial lens distortion coefficient is obtained by solving an 8 by 8 matrix eigenvalue problem. They claimed that their method is faster and more accurate than Tsai's method. Ito and Ishii [3.18] developed a non-iterative procedure for camera calibration. Lai [3.19] considered two terms in the lens distortion equation

$$\left.\begin{aligned} D_x &= \kappa X_d r^2 + \kappa_1\left(r^2 + 2X_d^2\right) + \kappa_2\left(2X_d Y_d\right) \\ D_y &= \kappa Y_d r^2 + \kappa_1\left(2X_d Y_d\right) + \kappa_2\left(r^2 + 2Y_d^2\right) \end{aligned}\right\} \qquad (3.19)$$

Newton method was used to solve for the 13 calibration parameters. He also made some sensitivity analysis. Other techniques [3.20-3.22] also developed for camera calibration. However, those techniques do not use the same camera model as outlined above.

3.3 Camera pose estimation and 3D information extraction

Using the calibrated camera intrinsic parameters, one can find the ideal image coordinates from the computer image coordinates through Eqs. (3.16-3.17). Equations (3.14-3.15) relate the object coordinates to the ideal image coordinates. Thus the position and

orientation of camera with respect to the object coordinate system can be determined. However, if one knows the ideal image coordinates of a 3D point, one can not find the camera coordinates of that point. The reason is that any point along a ray can result in the same ideal image coordinates. To infer the 3D camera coordinates from the ideal image coordinates, some additional conditions are required.

In this section, the techniques of finding the camera pose by using the ideal image coordinates and the object coordinates will be reviewed. The techniques of extracting the 3D information from the 2D image will also be reviewed.

3.3.1 Camera pose determination from plane curves

The camera pose can be determined by using plane curves whose ideal image is measured and whose object description is known. The key theory for this processing is that the perspective projection in the image plane of any plane conic curve is still conic. The most used plane curve for camera calibration is a circle and many techniques have been developed for that purpose [3.23-3.27].

3.3.2 Camera pose determination from points

The camera pose can be estimated by using a set of points whose ideal image coordinates are measured and whose object coordinates are known. The techniques reviewed here do not involve the estimation of the range (section **3.3.3**). Combining Eq. (3.14) with Eq. (3.15), one has

$$\left.\begin{aligned} X_u &= f\frac{({}^{C}_{O}R_{11}\ {}^{C}_{O}R_{12}\ {}^{C}_{O}R_{13})(x_O\ y_O\ z_O)^T+{}^{C}_{O}T_x}{({}^{C}_{O}R_{31}\ {}^{C}_{O}R_{32}\ {}^{C}_{O}R_{33})(x_O\ y_O\ z_O)^T+{}^{C}_{O}T_z} \\ Y_u &= f\frac{({}^{C}_{O}R_{21}\ {}^{C}_{O}R_{22}\ {}^{C}_{O}R_{23})(x_O\ y_O\ z_O)^T+{}^{C}_{O}T_y}{({}^{C}_{O}R_{31}\ {}^{C}_{O}R_{32}\ {}^{C}_{O}R_{33})(x_O\ y_O\ z_O)^T+{}^{C}_{O}T_z} \end{aligned}\right\} \tag{3.20}$$

The perspective projection of point P on the image plane has the following coordinates in the camera coordinate system

$$\{P_p\}=\begin{Bmatrix} X_u \\ Y_u \\ f \end{Bmatrix}=f\begin{Bmatrix} x_u \\ y_u \\ 1 \end{Bmatrix} \tag{3.21}$$

In Eq. (3.21), (x_u, y_u) can be found. It is clear that every point along the ray O_CP in Fig. 3.5 can be expressed as

$$\begin{Bmatrix} x_{ray} \\ y_{ray} \\ z_{ray} \end{Bmatrix}_C = f_o\begin{Bmatrix} x_u \\ y_u \\ 1 \end{Bmatrix} \tag{3.22}$$

When $f_0 = 0$, Eq. (3.22) is the origin of the camera coordinate system. When $f_0 = f$, it is the perspective projection of point P on the image plane. When f_0 equals a certain value, it will be the point P. Haralick et al [3.28-3.30] developed two techniques to estimate the camera pose. The first technique is an iterative method. The following is the procedure.

I). Give an initial guess $f_{P_i,0}$ for all the points

II). Estimate the pose by minimizing the following

$$Q = \sum_{i=1}^{N} w_i \left\| {}^{C}_{O}\{T\} + {}^{C}_{O}[R] \begin{Bmatrix} x_{P_i} \\ y_{P_i} \\ z_{P_i} \end{Bmatrix}_O - f_{P_i,0} \begin{Bmatrix} x_{P_i,\mu} \\ y_{P_i,\mu} \\ 1 \end{Bmatrix} \right\|^2 \tag{3.23}$$

where P_i is the ith point. w_i is the corresponding weight.

III). Modify $f_{P_i,0}$ for all the point. Two schemes are developed in [3.24-3.26] for the modification.

IV). Repeat step (II) and (III) until convergence is achieved

The second technique is a linearization method. Expressing the rotation matrix as a function of the three Euler angles, it is linearized as in Eq. (3.20). The least squares method is applied to the linearized equation. To improve the results, robust estimation methods are suggested.

Ho and McClamroch [3.31] developed a technique using four points to determine the position and orientation of a camera. The four points actually are the four corners of a rhombus mark. Thus the pose of the camera is relative to that rhombus mark.

3.3.3 3D information extraction from 2D image

Given an image point, a corresponding unique spatial point can not be obtained. That is because any point along a ray will produce the same image point. In order to extract the 3D coordinate of a spatial point from its 2D image coordinate, some additional conditions must be given. Haralick [3.32] studied some conditions under which 3D information can be recovered from their 2D images. The most interesting case is the so-called three point

problem. Figure 3.6 shows this problem. A, B, and C are three spatial points. The distances between them are known, D_1, D_2, D_3. Their ideal image coordinates are measured. From their image coordinates, one can find the direction cosines for each of the three rays. Thus, the angle between the three rays can also be found. Let L_i (for i=1, 2, and 3) to be the ranges between the spatial points (A, B, and C) and the origin O_C of the camera coordinate system. Then following three equation can be obtained after applying the cosine law to the three triangles: ABO_C, BCO_C, and CAO_C.

$$\left.\begin{aligned} D_1^2 &= L_1^2 + L_2^2 - 2L_1L_2\cos\phi_1 \\ D_2^2 &= L_2^2 + L_3^2 - 2L_2L_3\cos\phi_2 \\ D_3^2 &= L_3^2 + L_1^2 - 2L_3L_1\cos\phi_3 \end{aligned}\right\} \tag{3.24}$$

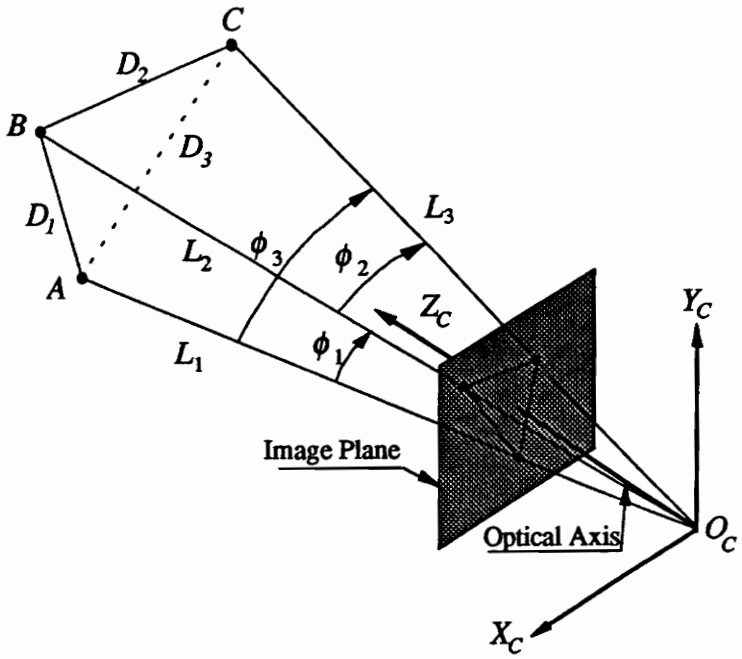

Figure 3.6 Perspective projection of three points

Haralick [3.32] and Wolf et al [3.33-3.34] has shown that Eq. (3.24) can have as many as 8 solutions. Linnainmaa et al [3.35] have derived an analytical solution for Eq. (3.24). The problem with three points is the difficulty in obtaining a physically true solution of the three ranges. To get a unique solution for the range, at least four points should be used. Haralick [3.36] studied a special case in which four points are coplanar and form a rectangle. Hung et al [3.37] developed a techniques for finding the range for four coplanar points whose coordinate in the object coordinate system are given.

Once the range L is obtained for one point, its camera coordinate (x_c, y_c, z_c) can be found. Thus, the 3D information for the corresponding 2D image is extracted. The available information for that point is its object coordinates and its camera coordinates. Using a set of such points, the position and orientation of the camera coordinate system with respect to the object coordinate system should be obtained.

3.4 Pose estimation using a set of corresponding points

In this section, the techniques will be reviewed which estimate the position and orientation of a coordinate system with respect to another from a set of known points whose coordinates in both coordinate systems are known, either given or measured. The three point situation will be discussed. Then, multiple point case will be reviewed. The case that the two coordinate systems have different engineering units will be also reviewed.

3.4.1 Pose estimation from three points

Once three noncollinear points are given, i.e., their coordinates in both coordinate systems are known, the position and orientation of a coordinate system with respect to another coordinate system can be uniquely determined [3.2, 3.38]. To do this, an intermediate coordinate system is defined using the three points. Figure 3.7 shows three points and the intermediate coordinate system. The other two coordinate systems in Fig. 3.7 are coordinate system A and B. The origin O_I is put right on the point P_1. The Z_I axis is along the direction of the vector from P_1 to P_2. The X_I axis is perpendicular to the plane determined by the points P_1, P_2, and P_3. Its direction is determined by the cross-product of the vector from P_1 to P_2 and the vector from P_1 to P_3. Finally the Y_I axis is determined by the requirement that the intermediate coordinate system is a right-hand coordinate system.

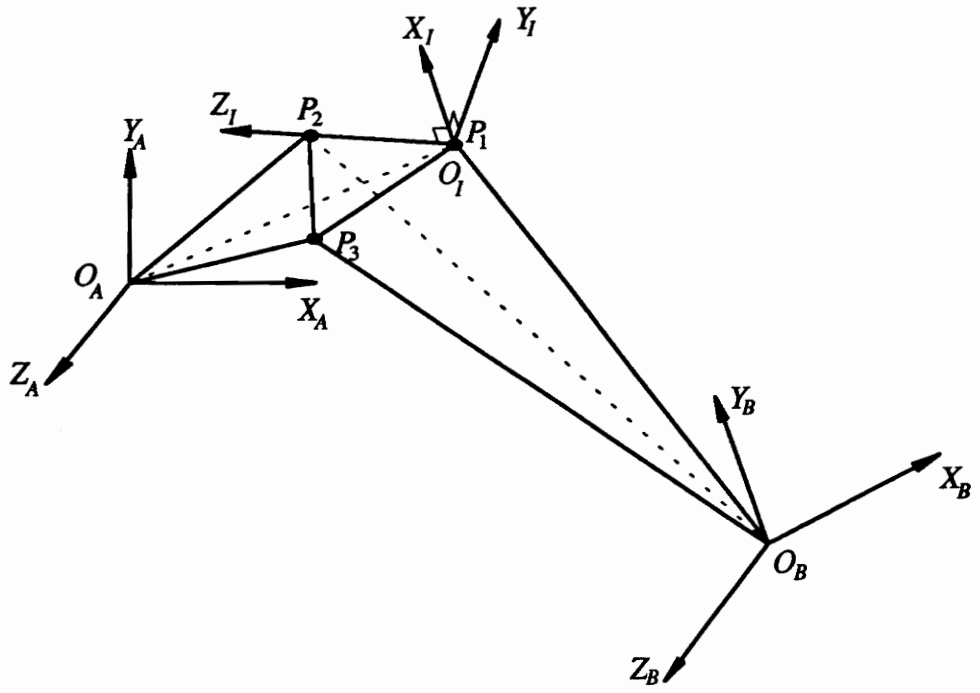

Figure 3.7 The definition of the intermediate coordinate system

The pose of the intermediate coordinate system relative to coordinate system B can be directly determined by the definition of the intermediate coordinate system. For point P, its intermediate coordinates can be transferred to the B coordinates by

$$\begin{Bmatrix} x_P \\ y_P \\ z_P \end{Bmatrix}_B = {}^B_I\{T\} + {}^B_I[R] \begin{Bmatrix} x_P \\ y_P \\ z_P \end{Bmatrix}_I \tag{3.25}$$

where ${}^B_I[R]$ is the rotation matrix from the intermediate coordinate system to coordinate system B. According to the definition of the intermediate coordinate system, the rotation matrix ${}^B_I[R]$ can be found without much difficulty. The vector from P_1 to P_2 is

$$\{P_{12}\}_B = \{x_{P_2,B} - x_{P_1,B},\ y_{P_2,B} - y_{P_1,B},\ z_{P_2,B} - z_{P_1,B}\}^T \tag{3.26}$$

where subscript B means the coordinates are measured in coordinate system B. The vector from P_1 to P_3 is

$$\{P_{13}\}_B = \{x_{P_3,B} - x_{P_1,B},\ y_{P_3,B} - y_{P_1,B},\ z_{P_3,B} - z_{P_1,B}\}^T \tag{3.27}$$

The direction cosines of the Z_I axis is found to be

$$\{Z_I\}_B = \{l_{Z_I},\ m_{Z_I},\ n_{Z_I}\}^T = \frac{\{P_{12}\}_B}{\|\{P_{12}\}_B\|} \tag{3.28}$$

The direction cosine of X_I axis is

$$\{X_I\}_B = \{l_{X_I},\ m_{X_I},\ n_{X_I}\}^T = \frac{\{P_{12}\}_B \times \{P_{13}\}_B}{\|\{P_{12}\}_B \times \{P_{13}\}_B\|} \tag{3.29}$$

Finally the direction cosine of the Y_I axis is

$$\{Y_I\}_B = \{l_{Y_I},\ m_{Y_I},\ n_{Y_I}\}^T = \{Z_I\} \times \{X_I\} \tag{3.30}$$

By combining Eq. (3.28-3.30), the rotation matrix is

$${}^B_I[R] = [\{X_I\}_B\ \{Y_I\}_B\ \{Z_I\}_B]. \tag{3.31}$$

The origin coordinates are simply the coordinates of point P_1

$$ {}^{B}_{I}\{T\} = \left\{ x_{P_1,B}, y_{P_1,B}, z_{P_1,B} \right\}^{T} \tag{3.32} $$

The transformation matrix from the intermediate coordinate system to coordinate system B can be found using Eqs. (3.31-3.32).

$$ {}^{B}_{I}[H] = \begin{bmatrix} {}^{B}_{I}[R] & {}^{B}_{I}\{T\} \\ 0\ 0\ 0 & 1 \end{bmatrix} \tag{3.33} $$

Replacing the coordinates $\left(x_{P_i,B}, y_{P_i,B}, y_{P_i,B}\right)$ (for i=1, 2, 3) in Eqs. (3.26-3.32) with the coordinates $\left(x_{P_i,A}, y_{P_i,A}, y_{P_i,A}\right)$, the transformation matrix from the intermediate coordinate system to coordinate system A can be found.

$$ {}^{A}_{I}[H] = \begin{bmatrix} {}^{A}_{I}[R] & {}^{A}_{I}\{T\} \\ 0\ 0\ 0 & 1 \end{bmatrix} \tag{3.34} $$

Finally the transformation matrix from coordinate system B to coordinate system A is

$$ {}^{A}_{B}[H] = \left({}^{A}_{I}[H]\right)\left({}^{B}_{I}[H]\right)^{-1} \tag{3.35} $$

From Eq. (3.35), the position and orientation of coordinate system B relative to coordinate system A is

$$ \left.\begin{aligned} {}^{A}_{B}\{T\} &= {}^{A}_{I}\{T\} - \left({}^{A}_{I}[R]\right)\left({}^{I}_{B}[R]\right){}^{B}_{I}\{T\} \\ {}^{A}_{B}[R] &= \left({}^{A}_{I}[R]\right)\left({}^{I}_{B}[R]\right) \end{aligned}\right\} \tag{3.36} $$

3.4.2 Pose estimation from more that three points

When more than three points are available, an overdetermined equation set will be obtained. The least squares method can be employed to find a unique solution. Haralick et al [3.29-3.30] developed a technique to analytically determine the pose based on the least

squares method. The technique can be applied to any two coordinate system. However, coordinate systems A and B are taken as examples again. For point P_i the coordinate transformation can be written as

$$\begin{Bmatrix} x_{P_i} \\ y_{P_i} \\ z_{P_i} \end{Bmatrix}_A = {}^A_B\{T\} + {}^A_B[R] \begin{Bmatrix} x_{P_i} \\ y_{P_i} \\ z_{P_i} \end{Bmatrix}_B \tag{3.37}$$

The unit vector expression for the rotation matrix (Eq. (3.1)) was used and the pose estimation problem was treated as a constrained least squares problem. The mathematical formulation is the following.

Find ${}^S_L\{T\}$ and ${}^S_L[R]$ that satisfy $({}^S_L[R]^T)({}^S_L[R]) = [I]$ and simultaneously minimize Q as

$$Q = \sum_{i=1}^{N} w_i \left\| \begin{Bmatrix} x_{P_i} \\ y_{P_i} \\ z_{P_i} \end{Bmatrix}_A - {}^A_B\{T\} - {}^A_B[R] \begin{Bmatrix} x_{P_i} \\ y_{P_i} \\ z_{P_i} \end{Bmatrix}_B \right\|^2 \tag{3.38}$$

Using the Lagrangian multipliers method and setting the partial derivative of Q with respect to the variables in the pose and the Lagrangian multiplier to be zero, the position and orientation (rotation matrix) were estimated. The position is found to be

$${}^A_B\{T\} = \begin{Bmatrix} \bar{x} \\ \bar{y} \\ \bar{z} \end{Bmatrix}_A - {}^A_B[R] \begin{Bmatrix} \bar{x} \\ \bar{y} \\ \bar{z} \end{Bmatrix}_B \tag{3.39}$$

where

$$\begin{Bmatrix} \bar{x} \\ \bar{y} \\ \bar{z} \end{Bmatrix}_A = \frac{1}{\sum_{i=1}^{N} w_i} \sum_{i=1}^{N} w_i \begin{Bmatrix} x_{P_i} \\ y_{P_i} \\ z_{P_i} \end{Bmatrix}_A, \quad \begin{Bmatrix} \bar{x} \\ \bar{y} \\ \bar{z} \end{Bmatrix}_B = \frac{1}{\sum_{i=1}^{N} w_i} \sum_{i=1}^{N} w_i \begin{Bmatrix} x_{P_i} \\ y_{P_i} \\ z_{P_i} \end{Bmatrix}_B \tag{3.40}$$

The rotation matrix is found to be

$$ {}^{S}_{L}[R] = [V][U]^T \tag{3.41} $$

where $[U]$ and $[V]$ is the singular value decomposition of matrix $[BB]$

$$ [BB] = [U][\Sigma][V]^T \tag{3.42} $$

Matrix $[BB]$ is defined as

$$ [BB] = \left[\{B_x\}\ \{B_y\}\ \{B_z\}\right] \tag{3.43} $$

where

$$ \{B_x\} = \sum_{i=1}^{N} w_i \left(x_{P_i,A} - \bar{x}_{P_i,A}\right) \begin{Bmatrix} x_{P_i,B} - \bar{x}_{P_i,B} \\ y_{P_i,B} - \bar{y}_{P_i,B} \\ z_{P_i,B} - \bar{z}_{P_i,B} \end{Bmatrix} \tag{3.44} $$

The expression for $\{B_y\}$ and $\{B_z\}$ is similar to Eq. (3.34). Replacing $\left(x_{P_i,A} - \bar{x}_{P_i,A}\right)$ with $\left(y_{P_i,A} - \bar{y}_{P_i,A}\right)$ and $\left(z_{P_i,A} - \bar{z}_{P_i,A}\right)$, $\{B_y\}$ and $\{B_z\}$ are obtained.

Sanso [3.7] developed a technique to estimate the pose plus a scale factor using corresponding points. Mathematically, the relationship between the corresponding data points can be written as

$$ \begin{Bmatrix} x_{P_i} \\ y_{P_i} \\ z_{P_i} \end{Bmatrix}_A = {}^{A}_{B}\{T\} + \lambda \left({}^{A}_{B}[R]\right) \begin{Bmatrix} x_{P_i} \\ y_{P_i} \\ z_{P_i} \end{Bmatrix}_B \tag{3.45} $$

where λ is a scale factor. The scale factor is necessary if the two coordinate systems have different engineering units. Sanso used quaternion (Euler parameters) to express the rotation matrix. The problem is then converted to an eigenvalue problem for finding the rotation matrix. An analytical solution for the position, the orientation, and the scale factor is found.

Maikhail [3.39] tried to solve the problem in Eq. (3.45). He used three Euler angles to express the rotation matrix. Then he linearized Eq. (3.45) and found the least squares solution for the linearized equation set. An iteration is required in order to obtain a converged solution of the pose and the scale factor.

3.5 Rotation matrix estimation

There are two cases in which a rotation matrix needs to be estimated. The first case is that there are two set of points measured with respect to one coordinate system. This is the so-called vector rotation. The first set of points are rotated to become the second set of points. If point P becomes point Q after an rotation, the relationship between that two points can be written as:

$$\begin{Bmatrix} x_Q \\ y_Q \\ z_Q \end{Bmatrix} = [R] \begin{Bmatrix} x_P \\ y_P \\ z_P \end{Bmatrix} \tag{3.46}$$

Since P and Q are measured in the same coordinate system, no subscript is needed to identify the coordinate system in which the vectors are measured. The object is to estimate the rotation matrix $[R]$ which will rotate the first set of points P_i into second set of points Q_i. (i=1, 2, ..., N)

The second case is that there are only one set of points. Those points are measured in two coordinate systems which have common origin but different orientation. This is the so-called frame rotation. For this situation, Eq. (3.37) can be written as

$$\begin{Bmatrix} x_{P_i} \\ y_{P_i} \\ z_{P_i} \end{Bmatrix}_A = {}^A_B[R] \begin{Bmatrix} x_{P_i} \\ y_{P_i} \\ z_{P_i} \end{Bmatrix}_B \tag{3.47}$$

The object is to estimate the rotation matrix which brings the measurements of points in one coordinate system into another coordinates system.

From Eq. (3.46) and Eq. (3.47), we can see that mathematically there is no difference between the two cases. The techniques for estimating the orientation will also be the same. There are more discussions about this in chapter 4.

Using the first case as example, following mathematical model can be derived.

Find $[R]$ that satisfy $[R]^T[R] = [I]$ and minimize

$$Q = \sum_{i=1}^{N} w_i \left\| \begin{Bmatrix} x_{Q_i} \\ y_{Q_i} \\ z_{Q_i} \end{Bmatrix} - [R] \begin{Bmatrix} x_{P_i} \\ y_{P_i} \\ z_{P_i} \end{Bmatrix} \right\|^2 \tag{3.48}$$

The solution was found [3.3-3.4, 3.40] by a singular value decomposition for the case that all weights w_i=1. Define

$$[PP] = \left[\begin{Bmatrix} x_{P_1} \\ y_{P_1} \\ z_{P_1} \end{Bmatrix} \begin{Bmatrix} x_{P_2} \\ y_{P_2} \\ z_{P_2} \end{Bmatrix} \cdots \begin{Bmatrix} x_{P_N} \\ y_{P_N} \\ z_{P_N} \end{Bmatrix} \right], \quad [QQ] = \left[\begin{Bmatrix} x_{Q_1} \\ y_{Q_1} \\ z_{Q_1} \end{Bmatrix} \begin{Bmatrix} x_{Q_2} \\ y_{Q_2} \\ z_{Q_2} \end{Bmatrix} \cdots \begin{Bmatrix} x_{Q_N} \\ y_{Q_N} \\ z_{Q_N} \end{Bmatrix} \right] \tag{3.49}$$

The singular value decomposition of matrix $[PP][QQ]^T$ leads to

$$[PP][QQ]^T = [U][\Sigma][V]^T \tag{3.50}$$

The rotation matrix is found to be

$$[R]=[V][U]^T \tag{3.51}$$

It can be seen that if the rank of matrix $[PP]$ is 3, then the estimated rotation matrix will be unique.

Moran [3.8] expressed the rotation matrix by a quaternion. The problem is converted into an eigenvalue problem and an analytical solution was obtained.

The statistics of the estimated $[R]$ was studied by Chang [3.41-3.44], by Waston [3.45], and by Mardian and Jupp [3.46]. However, they assumed that the vectors P_i and Q_i are unit vectors and the results are valid only for $N \rightarrow \infty$.

3.6 Pose estimation of a scanning laser Doppler vibrometer

In the literature, no attempts were made to determine the pose of a scanning laser Doppler vibrometer except for papers from Structural Imaging and Modal Analysis Laboratory at Virginia Tech. The reasons for this is perhaps that the scanning laser Doppler vibrometer is a newly developed instrument and no one has ever tried to develop a six degree-of-freedom mobility measurement system based up on it.

3.6.1 A geometrical method using four registration points

Zeng et al [3.47-3.48] developed a method to determine the pose of the scanning laser vibrometer using four registration points. In this geometrical method, three steps are involved. The first step is the estimation of the ranges. The second step is the estimation of

the rotation matrix expressed as equivalent angle and equivalent axis. The third step is the estimation of the origin coordinates of the laser coordinate system. Only three points are used to find the pose. Thus, four three-point combinations are obtained and four poses will be found. Based on an error function, the best pose is chosen from the four obtained poses. The problem with this method is that the four registration points were not used simultaneously. This method is further developed in chapter 4 to use four or more registration points simultaneously.

3.6.2 An iterative method using multiple registration points

Montgomery et al [3.38] developed an iterative method to determine the pose of the scanning laser vibrometer using multiple registration points. They took the three ranges of three chosen registration points as independent variables and expressed all the other related variables as functions of them. An error function was defined which had three equations. When the minimum of the error function was achieved, the three ranges and the pose were obtained.

In order to understand the differences between the method in [3.38] and the method in this dissertation, the Montgomery method will be reviewed based on the definition of the laser coordinate system in this dissertation. The only difference between their definition and the definition in this dissertation is that they placed the laser coordinate system at the design center of the laser head. There will be a constant offset between the two origins of the two defined laser coordinate systems. However, this offset does not make any difference in reviewing their iterative method.

I). The pose of the structural coordinate system expressed as functions of three ranges

For each of the registration points, its structural coordinates (x_S, y_S, z_S) and the corresponding scanning coordinates $(\theta_{X_L}, \theta_{Y_L})$ are known. If the ranges are obtained, one can find the laser coordinates (x_L, y_L, z_L) by using Eq.(2.10). For the time being, the ranges for the first three registration point L_{P_1}, L_{P_2}, and L_{P_3} are assumed to be known. Thus, the laser coordinates of the first three registration points can be used as known.

The pose of the structural coordinate system with respect to the laser coordinate system can be determined by the method described in section **3.4.1** from the laser coordinates and structural coordinates of the three registration points. Once the pose of the structural coordinate is obtained, the laser coordinates of the registration points other than the first three can be found by using Eq. (2.2). Their ranges can be found by using the last equation of Eq. (2.10). Taking the fourth registration points as an example, one will have

$$\begin{Bmatrix} x_{P_4} \\ y_{P_4} \\ z_{P_4} \end{Bmatrix}_L = {}^L_S\{T\} + {}^L_S[R] \begin{Bmatrix} x_{P_4} \\ y_{P_4} \\ z_{P_4} \end{Bmatrix}_S \tag{3.52}$$

and

$$L_{P_4} = \left(x^2_{P_4 L} + \left(\sqrt{y^2_{P_4 L} + z^2_{P_4 L}} + dl \right)^2 \right)^{1/2} \tag{3.53}$$

The above derivation shows that the pose of the structural coordinates system, the laser coordinates and the ranges of the other registration points are functions of the first three ranges. They will vary with the first three ranges. Note that it is not necessary to take the first three ranges as unknowns. Any three registration points can be used.

II). The error function

There are two things to be considered to define an error function. First, the laser coordinates for the same registration points should be the same whether it is transformed from the structural coordinates or it is converted from the scanning coordinates (θ_{X_L}, θ_{Y_L}, L). Secondly, the distance between the registration points will not change whether it is measured in the structural coordinate system or measured in the laser coordinate system. The difference in the former is called the position error and the difference in the later is called the length error. The position error for point P is

$$\{e_P\} = \begin{Bmatrix} e_{P,x} \\ e_{P,y} \\ e_{P,z} \end{Bmatrix} = \begin{Bmatrix} x_{PL} \\ y_{PL} \\ z_{PL} \end{Bmatrix}_T - \begin{Bmatrix} x_{PL} \\ y_{PL} \\ z_{PL} \end{Bmatrix}_C \tag{3.54}$$

where subscript T means that the laser coordinates are transformed coordinates obtained by Eq.(3. 52) and subscript C means that the laser coordinates are converted coordinates obtained by using Eq. (2.10) with θ_{PX_L} and θ_{PY_L} being the measured value and range L_P being the calculated value from Eq. (3.53). The length error is

$$e_{len} = \left(D_{23L} - D_{23S}\right)^2 + \sum_{i=2}^{N} \left(D_{1iL} - D_{1iS}\right)^2 \tag{3.55}$$

where D_{ijS} is the distance between point P_i and P_j measured in the structural coordinate system and D_{ijL} the distance measured in the laser coordinate system. The laser coordinates of all the registration points used in the calculation of D_{ijL} are the converted coordinates. Adding those errors together, the total error is gotten.

$$\{e_{TOL}\} = \sqrt{e_{len} + \sum_{i=4}^{N} \{e_{P_i}^2\}} = \sqrt{e_{len} + \sum_{i=4}^{N} \left(e_{P_i,x}^2,\ e_{P_i,y}^2,\ e_{P_i,z}^2\right)^T} \tag{3.56}$$

Equation (3.56) have three equations. They are functions of the first three ranges. The three unknown ranges can be solved for from this equation.

III). The iterative procedure

The errors in Eq. (3.56) is minimized by adjusting the first three ranges. In the implementation, a nonlinear quasi-Newton equation solver based on Broyden's method [3.49] is used iteratively to minimize the error in Eq. (3.56) from an initial guess of the ranges. Once the error reaches its minimum, the pose of the structural coordinate system is obtained.

From the above review of the method in [3.38], the main difference between the Montgomery method and the method (inverse model) in this dissertation is the formulation. First, the parameters to be determined are different. In the Montgomery method, there are three unknown ranges to be determined. This puts more emphasis on the three chosen points since error $\{e_p\}$ defined in Eq. (3.54) is always zero for those three chosen points. The inverse model in this dissertation takes the pose directly as unknown parameters. Every registration point is equally considered. Second, the error functions are different. In the Montgomery method, the error is defined as a function of the difference in the laser coordinates and the difference in the distances between registration points. In this dissertation, the error function is defined as the difference in the scanning angles which are directly connected to the measured input voltages. In addition, the method in this dissertation can make statistical inferences about the estimated pose parameters since the inverse model solution results from a nonlinear regressive model.

3.7 Summary

In this chapter, some techniques have been reviewed that can determine the pose of one coordinate system with respect to another coordinate system. Most of the techniques are developed in the areas of robotics and computer vision.

In chapter 2, the mathematical model has been developed for the pose determination of the SLDV. It can be seen that the hand calibration and eye-to-hand calibration (reviewed in section **3.2.1-3.2.2**) are different problems from the pose determination problem. The differences are the known conditions. The camera calibration problem is similar to the pose determination problem. Figure 3.8 shows both the camera calibration and pose determination of the SLDV.

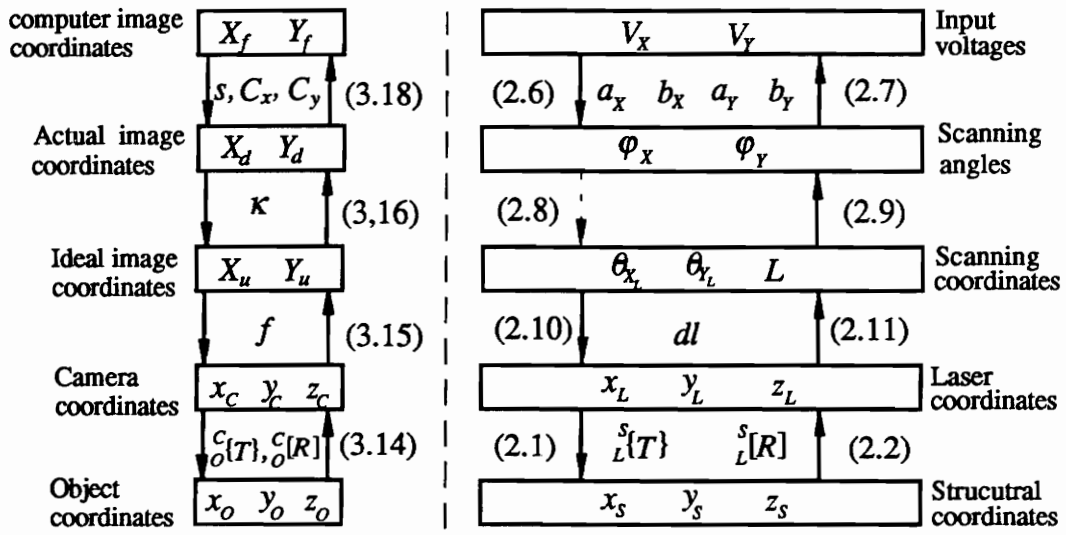

(a) Camera Calibration (b) Pose Determination of the SLDV

(Numbers in parentheses are reference equation number)

Figure 3.8 Camera calibration and pose determination of the SLDV

The left side of Fig. 3.8 shows the camera calibration model. The box contains the variables. The up arrow and down arrow presents the coordinates transformation between the adjacent box. The top box contains the measured computer image coordinates for a spatial (calibration) point while the bottom box contains the object coordinates. The right side of Fig. 3.8 shows the pose determination model. The numbers in the figure are the equation's number for completing the coordinates transformation between the adjacent box. These two problems look similar, they are different problems. First, the measured quantities are different. In the camera calibration, the measured variables are the computer image coordinates. In the pose determination, the measured variables are the input voltages. Second the transformation equations (from camera coordinates to computer image coordinates for camera calibration and from laser coordinates to the input voltages for pose determination) are not the same because of the different intrinsic parameters. Third, the pose determination has a moving laser center problem while the camera calibration does not have such a problem. Fourth, the camera calibration has a lens distortion problem while the pose determination does not have such a problem. Because of these differences, the techniques developed for camera calibration (reviewed in section **3.2.3**) can not be directly applied to pose determination problem.

Once the camera intrinsic parameters are calibrated, one can get the ideal image coordinates from the measured computer image coordinates. Only the pose of the camera needs to be determined from the known object coordinates and the derived ideal image coordinates. This problem is similar to the following problem: determining the pose of the SLDV from the known structural coordinates and measured scanning angles, however, they are different. The differences are the transformation equation as mentioned in last paragraph. The techniques reviewed in section **3.3.2** can not directly applied to the pose

determination problem again. The idea to directly solve a nonlinear equation set is appreciated. The techniques reviewed in **3.3.1** used plane curve to determine the pose. These techniques are not applicable to the pose determination problem for which there are 3D points instead of plane curves.

The ideal image coordinates can not directly map into the camera coordinates. This is because that the image coordinates are two dimensional while the camera coordinates are three dimensional. Thus to get the camera coordinates from the ideal image coordinates, some additional conditions are needed. The same is true for the pose determination. One can not get the laser coordinates directly from the first two scanning coordinates. As shown in Fig. 3.8 (b), the range L is introduced which is the third scanning coordinate. Due to the moving laser center problem in the pose determination of the SLDV, the techniques reviewed in section **3.3.3** can not be directly used. In addition, the developed techniques are only use either three points or four coplanar points to find out the ranges. In the pose determination, those limitations are not tolerable.

If the camera coordinates and the laser coordinates are obtained, the techniques reviewed in section **3.4** and **3.5** can be directly applied to the camera calibration problem and the pose determination problem. Two things are worth pointing out. First, the techniques developed in that two sections are not developed for camera calibration problem. They are for general inverse problem of the coordinate transformation. Second, the problem solved in section **3.5** is a subproblem in section **3.4**. By eliminating the origin coordinates (translation vector) as unknowns from the problem in section **3.4**, the resulting problem is the one in section **3.5**. However, the techniques reviewed in that two sections have two shortcomings. First, when all the points are in a plane, the techniques can not find a unique

solution. Second, the determinant of the obtained rotation matrix may be negative one. Therefore, even if the laser coordinates can be obtained, new techniques need developing.

A problem with all the developed techniques is that only the solution is found. No statistical properties are available. New techniques are needed which will not only give a best estimation of the pose, but also give the statistical properties of the estimated pose. That is the target of this dissertation.

CHAPTER FOUR

A GEOMETRIC METHOD FOR THE POSE DETERMINATION OF THE SLDV

In this chapter, a geometrical method is developed to find the pose of the SLDV. The measured scanning angles (φ_X, φ_Y) and the known structural coordinates (x_S, y_S, z_S) of all registration points will be simultaneously used. In this method, the pose is found in three steps. The first step is to find the ranges. The second step is to obtain the rotation matrix. The third step is to obtain the origin coordinates of the laser coordinate system. The nonlinear equation set is only presented in the first step. The number of unknowns in this nonlinear equation set is equal to the number of the registration points. A closed-form solution is available for the rotation matrix and origin coordinates.

The geometrical method presented in this chapter is developed from the previous work [3.47-3.48] for an automated mechanical mobility measurement system [1.16-1.17]. However, only four registration points were used in the previous work.

4.1 Determination of the ranges

In section **2.5**, two methods were developed to solve the pose determination problem. Actually the index setup is designed exclusively for finding the ranges. The method for finding the rotation matrix and origin coordinates are exactly the same for both methods. Since the ranges will be used to find the rotation matrix and origin coordinates, it is essential to develop methods that will give the most accurate estimation of the ranges.

4.1.1 Method for fixed setup

4.1.1.1 Nonlinear equation set for range determination

The ranges can be determined without the knowledge of the pose of the SLDV. This is based on the fact that the distance between any two registration points remains the same whether it is measured in the structural coordinate system or it is measured in the laser coordinate system.

For any two points P_i and P_j, the distance between them measured in the structural coordinate system is found to be

$$D_{ij,S} = \left(\left(x_{P_j,S} - x_{P_i,S} \right)^2 + \left(y_{P_j,S} - y_{P_i,S} \right)^2 + \left(z_{P_j,S} - z_{P_i,S} \right)^2 \right)^{1/2} \tag{4.1}$$

The same value is obtained when measured in the laser coordinate system.

$$\begin{aligned} D_{ij,L} = [& \left(L_{P_j} \sin\theta_{P_j Y_L} - L_{P_i} \sin\theta_{P_i Y_L} \right)^2 + \\ & \left(\left(L_{P_j} \cos\theta_{P_j Y_L} - dl \right) \sin\theta_{P_j X_L} - \left(L_{P_i} \cos\theta_{P_i Y_L} - dl \right) \sin\theta_{P_i X_L} \right)^2 + \\ & \left(\left(L_{P_j} \cos\theta_{P_j Y_L} - dl \right) \cos\theta_{P_j X_L} - \left(L_{P_i} \cos\theta_{P_i Y_L} - dl \right) \cos\theta_{P_i X_L} \right)^2 \ ]^{1/2} \end{aligned} \tag{4.2}$$

Equation (4.2) is obtained by replacing the structural coordinates in Eq. (4.1) with the laser coordinates. The two angles $(\theta_{X_L}, \theta_{Y_L})$ in the scanning coordinates are obtained from the scanning angles (φ_X, φ_Y) by Eq. (2.8). The distance remains the same, thus

$$D_{ij,S} = D_{ij,L} \tag{4.3}$$

The left-hand side of Eq. (4.3) is known since the structural coordinates are known. The right-hand side contains two unknown ranges L_{P_i} and L_{P_j}. For N registration points, there

will be $N(N\text{-}1)/2$ distances. Therefore, there will be $N(N\text{-}1)/2$ equations similar to Eq.(4.3). However, the number of unknowns is N. An overdetermined nonlinear equation set will be obtained if N is equal to or larger than four. Taking four registrations as an example, following six equations are obtained if the four points are called P_1, P_2, P_3, and P_4.

$$\left.\begin{aligned} f_1 &= D_{12,S} - D_{12,L} = 0 \\ f_2 &= D_{13,S} - D_{13,L} = 0 \\ f_3 &= D_{14,S} - D_{14,L} = 0 \\ f_4 &= D_{23,S} - D_{23,L} = 0 \\ f_5 &= D_{24,S} - D_{24,L} = 0 \\ f_6 &= D_{34,S} - D_{34,L} = 0 \end{aligned}\right\} \tag{4.4}$$

where the D's are similar to Eqs. (4.1) and (4.2). In Eq. (4.4), there are only four unknown ranges L_{P_1}, L_{P_2}, L_{P_3}, and L_{P_4}.

The least squares method can be applied to Eq. (4.4) to yield a unique solution. There are two methods to do that. The first one is to develop an optimization model. Applying the least squares method to Eq. (4.4), an optimization model can be derived.

$$\begin{aligned} &\text{Find } L_{P_1}, L_{P_2}, L_{P_3}, \text{ and } L_{P_4} \text{ that satisfy} \\ &L_{P_i} > 0 \ (i = 1,2,3,4) \text{ and minimize} \\ &Q = \sum_{j=1}^{6} f_j^2 \end{aligned} \tag{4.5}$$

There is no closed-form solution for this model. The ranges can be found from the above model by using optimization techniques. This is not difficult since the degree of nonlinearity here is relatively low. An additional requirement is a good initial solution that is essential for an optimization algorithm to reach the global minimum.

The second method to solve Eq. (4.4) is to linearize the equation. The least squares method is applied to the linearized equation set to obtain a solution. The procedure is iterative, repeating until a converged solution is obtained. Assuming that an initial solution is known $\{L\}_0$. A series expansion of f_j is developed and keeping only the first two terms, one gets

$$f_j(\{L\}_0 + \delta L) = f_j(\{L\}_0) + \sum_{i=1}^{4} \frac{\partial f_j}{\partial L_{P_i}} \delta L_{P_i} = 0 \qquad (\text{for } j=1, 2, .., 6) \tag{4.6}$$

where $\{L\}_0 = \left(L_{P_1,0}, L_{P_2,0}, L_{P_3,0}, L_{P_4,0}\right)^T$. The results can be written in matrix form as

$$[A]\{\delta L\} = -\{F\} \tag{4.7}$$

where

$$A_{ji} = \frac{\partial f_j}{\partial L_{P_i}} \Big|_{\{L\}=\{L\}_0} \text{ for } j = 1,\ 2,\ \ldots,\ 6 \text{ and } i = 1,\ 2,\ 3,\ 4$$

$$\{\delta L\} = \left\{\delta L_{P_1} \quad \delta L_{P_2} \quad \delta L_{P_3} \quad \delta L_{P_4}\right\}^T \tag{4.8}$$

$$\{F\} = \left\{f_1 \quad f_2 \quad f_3 \quad f_4 \quad f_5 \quad f_6\right\}^T \Big|_{\{L\}=\{L\}_0}$$

The least squares solution for the increment of the ranges from Eq. (4.7) is

$$\{\delta L\} = -\left([A]^T[A]\right)^{-1}[A]^T\{F\} \tag{4.9}$$

An improved solution called $\{L_1\}$ is obtained from the initial solution.

$$L_{P_i,1} = L_{P_i,0} + \delta L_{P_i} \quad (\text{for } i=1, 2, 3, 4) \tag{4.10}$$

This procedure is usually called the Gauss-Newton method. The Gauss-Newton method usually converges to the solution. However, if the initial solution is not close enough to the true solution, the solution may diverge.

For both methods, a good initial solution for the ranges is required. For the optimization model, different initial solutions may lead to different local minima. The global minimum is desired. For the Gauss-Newton method, the solution may diverge if the initial solution is not close enough to the true solution. Therefore, it is very important to find a good initial solution for the ranges. The next section will concentrate on finding a good initial solution without any guessing.

4.1.1.2 Determination of an initial solution for the ranges

The separation distance *dl* of the two scanning mirrors is very small compared to the ranges. If it is set to be zero, the laser beam will come from the origin of the laser coordinate system for all the registration points (see Fig. 2.3-2.4). This condition will present certain advantages for finding the ranges. This section will show how to use this to get an estimation of the ranges.

Three points P_1, P_2, and P_3 are considered first. As shown in Fig. 4.1, point P_1, point P_2 and origin O_L form a triangle. Applying the cosine law to that triangle, an equation which relates the known distance to the unknown ranges can be obtained. For three points , there will be three triangles available. Figure 4.1 shows that the three triangles are formed by $P_1P_2O_L$, $P_2P_3O_L$ and $P_3P_1O_L$. The following three equations can be obtained by applying the cosine law to that three triangles.

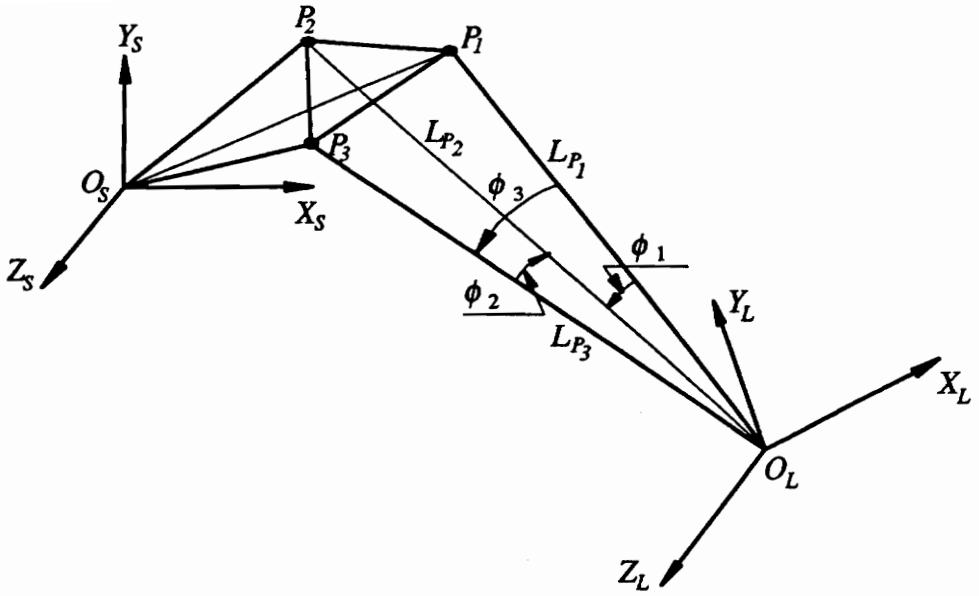

Figure 4.1 Schematic diagram for finding the three ranges

$$\left.\begin{aligned} D_{12,S}^2 &= L_{P_1}^2 + L_{P_2}^2 - 2L_{P_1}L_{P_2}\cos\phi_1 \\ D_{23,S}^2 &= L_{P_2}^2 + L_{P_3}^2 - 2L_{P_2}L_{P_3}\cos\phi_2 \\ D_{31,S}^2 &= L_{P_3}^2 + L_{P_1}^2 - 2L_{P_3}L_{P_1}\cos\phi_3 \end{aligned}\right\} \tag{4.11}$$

The left-hand side of Eq. (4.11) is known. It is the distance between two registration points in the structural coordinate system. The right-hand side of Eq. (4.11) contains three unknown ranges L_{P_1}, L_{P_2} and L_{P_3}. The cosines of the three angles ϕ_1,ϕ_2, and ϕ_3 can be obtained from the scanning coordinates (θ_{X_L},θ_{Y_L}). There are three issues associated with Eq. (4.11): (I) the calculation of $\cos\phi_i$ (i=1, 2, 3), (II) the solution of L_{P_i} (i=1, 2, 3) and (III) the selection of the physically true solution. They are to be addressed one by one in followings.

I). The calculation of $\cos\phi_i$

For any point P, its laser coordinates can be found from Eq. (2.10) (note that dl=0) as

$$\left.\begin{aligned} x_{P,L} &= L_P \sin\theta_{PY_L} \\ y_{P,L} &= L_P \cos\theta_{PY_L} \sin\theta_{P,X_L} \\ z_{P,L} &= L_P \cos\theta_{PY_L} \sin\theta_{P,X_L} \end{aligned}\right\} \tag{4.12}$$

Using the above equations, the direction cosines for point P are

$$\left.\begin{aligned} l_P &= \sin\theta_{PY_L} \\ m_P &= \cos\theta_{PY_L} \sin\theta_{P,X_L} \\ n_P &= \cos\theta_{PY_L} \sin\theta_{P,X_L} \end{aligned}\right\} \tag{4.13}$$

The direction cosines of points P_1, P_2, and P_3 are the direction cosines of vector $O_L \rightarrow P_1$, $O_L \rightarrow P_2$ and $O_L \rightarrow P_3$. They can be obtained by using Eq. (4.13)

$$\left.\begin{aligned} (l, m, n)^T_{P_1} &= \left(\sin\theta_{P_1Y_L},\ \cos\theta_{P_1Y_L}\sin\theta_{P_1X_L},\ \cos\theta_{P_1Y_L}\cos\theta_{P_1X_L}\right)^T \\ (l, m, n)^T_{P_2} &= \left(\sin\theta_{P_2Y_L},\ \cos\theta_{P_2Y_L}\sin\theta_{P_2X_L},\ \cos\theta_{P_2Y_L}\cos\theta_{P_2X_L}\right)^T \\ (l, m, n)^T_{P_3} &= \left(\sin\theta_{P_3Y_L},\ \cos\theta_{P_3Y_L}\sin\theta_{P_3X_L},\ \cos\theta_{P_3Y_L}\cos\theta_{P_3X_L}\right)^T \end{aligned}\right\} \tag{4.14}$$

The cosines of the three angles ϕ_1,ϕ_2, and ϕ_3 can be easily obtained by using the direction cosines of the three points P_1, P_2, and P_3 as

$$\left.\begin{aligned} \cos\phi_1 &= l_{P_1}l_{P_2} + m_{P_1}m_{P_2} + n_{P_1}n_{P_2} \\ \cos\phi_2 &= l_{P_2}l_{P_3} + m_{P_2}m_{P_3} + n_{P_2}n_{P_3} \\ \cos\phi_3 &= l_{P_3}l_{P_1} + m_{P_3}m_{P_1} + n_{P_3}n_{P_1} \end{aligned}\right\} \tag{4.15}$$

II). The solution of L_{P_i}

It can be seen that Eq. (4.11) has exactly the same form as Eq. (3.24). The number of possible solutions for this equation is eight. However, some of the solutions may be negative or complex. Only the real and positive solutions are acceptable since physically

the range is larger than zero. An algorithm is developed [3.48] to find all the real and positive solutions of Eq. (4.11). The algorithm is presented here.

From the third equation of Eq. (4.11), L_{P_1} can be found as a function of L_{P_3}

$$L_{P_1} = L_{P_3}\cos\phi_3 \pm \sqrt{\left(L_{P_3}\cos\phi_3\right)^2 - \left(L_{P_3}^2 - D_{31,S}^2\right)} \tag{4.16}$$

From the second equation of Eq. (4.11), L_{P_2} can be found as a function of L_{P_3}

$$L_{P_2} = L_{P_3}\cos\phi_2 \pm \sqrt{\left(L_{P_3}\cos\phi_2\right)^2 - \left(L_{P_3}^2 - D_{23,S}^2\right)} \tag{4.17}$$

Putting Eqs. (4.16) and (4.17) into the first equation of Eq. (4.11), an equation will be obtained that contains only one unknown, L_{P_3}. This resulting equation can be written as

$$f\left(L_{P_3}\right) = L_{P_1}^2 + L_{P_2}^2 - 2L_{P_1}L_{P_2}\cos\phi_1 - D_{12,S}^2 = 0 \tag{4.18}$$

The roots of Eq. (4.18) are the solutions of the range L_{P_3}. Putting them back to Eqs. (4.16) and (4.17), the solutions for range L_{P_1} and range L_{P_2} are obtained.

To insure L_{P_1} to be positive and real, it is required that

$$\left.\begin{aligned} &\left(L_{P_3}\cos\phi_3\right)^2 - \left(L_{P_3}^2 - D_{31,S}^2\right) \geq 0 \\ &L_{P_3}\cos\phi_3 - \sqrt{\left(L_{P_3}\cos\phi_3\right)^2 - \left(L_{P_3}^2 - D_{31,S}^2\right)} \geq 0 \end{aligned}\right\} \tag{4.19}$$

which leads to

$$\left.\begin{aligned} &L_{P_3} \leq D_{31,S} / \sin\phi_3 \\ &L_{P_3} \geq D_{31,S} \end{aligned}\right\} \tag{4.20}$$

To insure L_{P_2} to be real and positive, it is required that

$$\left.\begin{aligned} &\left(L_{P_2}\cos\phi_2\right)^2 - \left(L_{P_2}^2 - D_{23,S}^2\right) \geq 0 \\ &L_{P_2}\cos\phi_2 - \sqrt{\left(L_{P_2}\cos\phi_2\right)^2 - \left(L_{P_2}^2 - D_{23,S}^2\right)} \geq 0 \end{aligned}\right\} \tag{4.21}$$

which leads to

$$\left.\begin{aligned} L_{P_2} &\le D_{21,S} / \sin\phi_2 \\ L_{P_2} &\ge D_{21,S} \end{aligned}\right\} \tag{4.22}$$

To insure both L_{P_1} and L_{P_2} to be real and positive, L_{P_3} must satisfy

$$max\left(D_{23,S}, D_{31,S}\right) \le P_{L_3} \le min\left(D_{23,S} / \cos\phi_2, D_{31,S} / \cos\phi_3\right) \tag{4.23}$$

Equation (4.23) produces the root search interval for solving Eq. (4.18). Equation (4.23) can be written as

$$BB \le P_{L_3} \le EE \tag{4.24}$$

where

$$\left.\begin{aligned} BB &= max\left(D_{23,S}, D_{31,S}\right) \\ EE &= min\left(D_{23,S} / \cos\phi_2, D_{31,S} / \cos\phi_3\right) \end{aligned}\right\} \tag{4.25}$$

Observe Eqs. (4.16) and (4.17). The following four cases are available for $f\left(L_{P_3}\right)$=0.

1). Plus-plus case:

$$\begin{aligned} L_{P_1} &= L_{P_3}\cos\phi_3 + \sqrt{\left(L_{P_3}\cos\phi_3\right)^2 - \left(L_{P_3}^2 - D_{31,S}^2\right)} \\ L_{P_2} &= L_{P_3}\cos\phi_2 + \sqrt{\left(L_{P_3}\cos\phi_2\right)^2 - \left(L_{P_3}^2 - D_{23,S}^2\right)} \\ f\left(L_{P_3}\right) &= L_{P_1}^2 + L_{P_2}^2 - 2L_{P_1}L_{P_2}\cos\phi_1 - D_{12,S}^2 = 0 \end{aligned} \tag{4.26}$$

2). Plus-minus case

$$\begin{aligned} L_{P_1} &= L_{P_3}\cos\phi_3 + \sqrt{\left(L_{P_3}\cos\phi_3\right)^2 - \left(L_{P_3}^2 - D_{31,S}^2\right)} \\ L_{P_2} &= L_{P_3}\cos\phi_2 - \sqrt{\left(L_{P_3}\cos\phi_2\right)^2 - \left(L_{P_3}^2 - D_{23,S}^2\right)} \\ f\left(L_{P_3}\right) &= L_{P_1}^2 + L_{P_2}^2 - 2L_{P_1}L_{P_2}\cos\phi_1 - D_{12,S}^2 = 0 \end{aligned} \tag{4.27}$$

3). Minus-plus case

$$
\begin{aligned}
L_{P_1} &= L_{P_3}\cos\phi_3 - \sqrt{\left(L_{P_3}\cos\phi_3\right)^2 - \left(L_{P_3}^2 - D_{31,S}^2\right)} \\
L_{P_2} &= L_{P_3}\cos\phi_2 + \sqrt{\left(L_{P_3}\cos\phi_2\right)^2 - \left(L_{P_3}^2 - D_{23,S}^2\right)} \\
f\left(L_{P_3}\right) &= L_{P_1}^2 + L_{P_2}^2 - 2L_{P_1}L_{P_2}\cos\phi_1 - D_{12,S}^2 = 0
\end{aligned}
\tag{4.28}
$$

4). Minus-minus case

$$
\begin{aligned}
L_{P_1} &= L_{P_3}\cos\phi_3 - \sqrt{\left(L_{P_3}\cos\phi_3\right)^2 - \left(L_{P_3}^2 - D_{31,S}^2\right)} \\
L_{P_2} &= L_{P_3}\cos\phi_2 - \sqrt{\left(L_{P_3}\cos\phi_2\right)^2 - \left(L_{P_3}^2 - D_{23,S}^2\right)} \\
f\left(L_{P_3}\right) &= L_{P_1}^2 + L_{P_2}^2 - 2L_{P_1}L_{P_2}\cos\phi_1 - D_{12,S}^2 = 0
\end{aligned}
\tag{4.29}
$$

Since $f\left(L_{P_3}\right)$ is also a quadratic function, it at most has two real and positive solutions. Thus, the total number of solution is eight. The search interval for $f\left(L_{P_3}\right)$=0 is same for all the four case. The numerical procedure of finding L_{P_3} from Eq. (4.18) is a search procedure. All the possible solutions in the given interval are found. The following is the actual procedure. First, the given search interval of (*BB*, *EE*) is evenly divided into small sub-intervals. Next, the value of $f\left(L_{P_3}\right)$ at the sub-interval boundaries is calculated. Finally, each subsequent value is compared to find a sign change. Meanwhile, the minimum absolute value ($|F|_{min}$) of $f\left(L_{P_3}\right)$ at the sub-interval boundaries is found and kept during the search process. If there are sign changes, the bisection method is used to determine the root. If there is no sign change, there may be a multiple root. $|F|_{min}$ is compared with $\left|f\left(L_{P_3}\right)\right|$ at boundary *BB* and *EE*. If $|F|_{min}$ is less than the absolute value of both $f(BB)$ and $f(EE)$, there will be an extreme value for $f\left(L_{P_3}\right)$ in the search interval. A one-dimensional optimization method is used to find a point at which $\left|f\left(L_{P_3}\right)\right|$ is minimum. The found point may or may not be a multiple root. Mathematically, the minimum absolute

value of $f(L_{P_3})$ is zero for a multiple root. However, for experimental data, zero is hard to reach. An accuracy condition is put forth on the detection of the multiple root. If the condition is satisfied, that point is accepted as a root.

III). The selection of the physically true solution

Equation (4.11) may have more than one real and positive solution. However, only one of them is the physically true solution. The problem is to pick the physically true solution. From only three points, it is not possible to do this since all the solutions are real and positive. Fortunately, more than three registration points are available. Four points can form four three-point combinations. If the four points are P_1, P_2, P_3, and P_4, the four three-point combinations are: (I) $P_1P_2P_3$, (II) $P_1P_2P_4$, (III) $P_1P_3P_4$, and (IV) $P_2P_3P_4$. A set of real and positive solutions can be found for each combination. The physically true solution is one of the solutions found in each combination. Second, the range for one point is same from all the combinations used to find it. Based on these two observations, a physically true solution can be picked up for each of the four combinations.

Combinations (I) and (II) will be considered first. For each solution in combination (I), an "identical" solution can be found in combination (II) by selecting the minimum difference along the index j defined in following equation

$$E_{ij} = \left|{}_iL_{P_1} - {}_jL_{P_1}\right| + \left|{}_iL_{P_2} - {}_jL_{P_2}\right| \tag{4.30}$$

where the left subscript i means the ith solution in combination (I), left subscript j means the jth solution in combination (II). Now a new one-dimensional error can be defined as

$$ER_i = \min_j\left[E_{ij}\right] \tag{4.31}$$

If ER_p is the minimum in ER, the pth solution in combination (I) is the physically true solution. Its "identical" solution in combination (II) is the physically true solution for combination (II). The geometrical meaning for this is that the triangle $P_1P_2O_L$ is shared by combination (I) and combination (II), thus the solution from the two combinations should give the same triangle. In other words, the summation of L_{P_1} and L_{P_2} from combination (I) should be the same as that from combination (II).

The information in combination (III) can be used to improve the selection of the physically true solution in combination (I) and (II). For each solution combination (I), an "identical" solution in combination (III) can be found by selecting the minimum difference along the index k defined in following equation

$$E_{ik} = \left|{}_iL_{P_1} - {}_kL_{P_1}\right| + \left|{}_iL_{P_3} - {}_kL_{P_3}\right| \tag{4.32}$$

where left subscript i again means the ith solution in combination (I), left subscript k means the kth solution in combination (III). Define another error vector as

$$ERR_i = ER_i + \min_k[E_{ik}] \tag{4.33}$$

If ERR_q is the minimum in ERR, the qth solution in combination (I) is the physically true solution. Its "identical" solution in combination (II) is the physically true solution for combination (II). Note that q may or may not equal to p. The geometrical explanation of Eq. (4.33) is that the leg P_1O_L is shared by triangle $P_1P_2O_L$ and $P_1P_3O_L$ which are determined from solutions of combination (I), combination (II) and combination (III). Therefore L_{P_1} from triangle $P_1P_2O_L$ should be the same as that from triangle $P_1P_3O_L$.

In the same way the physically true solution can be determined for combination (III) and combination (IV) by considering the triangle $P_3P_4O_L$ and leg P_4O_L

Once the physically true solution is picked up for each combination, an initial range can be obtained for each of the four registration points. For example, the initial range for point P_1 is

$$L_{P_1,0} = \left(L_{P_1}(\mathrm{I}) + L_{P_1}(\mathrm{II}) + L_{P_1}(\mathrm{III})\right)/3 \tag{4.34}$$

where $L_{P_1}(\mathrm{I})$ is the physically true solution for point P_1 from combination (I). The other terms in Eq. (4.34) have the similar meaning. Equation (4.34) is derived from the fact that the first three combinations contain point P_1. The same thing can be done for points P_2, P_3, and P_4. If there are only four registration points, every thing is done for finding the initial solution. If there are more than four points, the initial range can be found for four points at a time. If the number of registration point is not an even number of multiple of four, some registration points may be used twice. The initial solution for those twice-used points can be the average from the two groups. Taking 6 points as an example, two four-point groups can be formed as $P_1P_2P_3P_4$ and $P_3P_4P_5P_6$. Thus, points P_3 and P_4 have been used twice. Group $P_1P_2P_3P_4$ gives an initial range for P_3 and P_4. Group $P_3P_4P_5P_6$ also gives an initial range for P_3 and P_4. The average of initial solution from both group can be used as the final initial solution for L_{P_3} and L_{P_4}.

Since the separation distance *dl* is very small compared with the range, the found initial solution here will be close enough to the true solution.

4.1.2 Method for index setup

Using this setup, the range can be found point by point instead of solving a nonlinear equation set. In the primary position, the laser beam is manually aimed at P_1, the

corresponding scanning coordinate $({}_P\theta_{P_1X_L}, {}_P\theta_{P_1Y_L})$ is obtained. After translationally moving the laser head to a new position called secondary position, the laser beam is manually aimed at point P_1 again. So another set of scanning coordinate $({}_S\theta_{P_1X_L}, {}_S\theta_{P_1Y_L})$ is obtained. Note that the left subscripts P and S are used to indicate the primary position and secondary position. The movement of the laser head is along the directions of three axes (X_L, Y_L, Z_L) and is measured as (x_M, y_M, z_M). These three pieces of information can be used to find out the range for both positions. Figure 4.2 shows a triangle for this case.

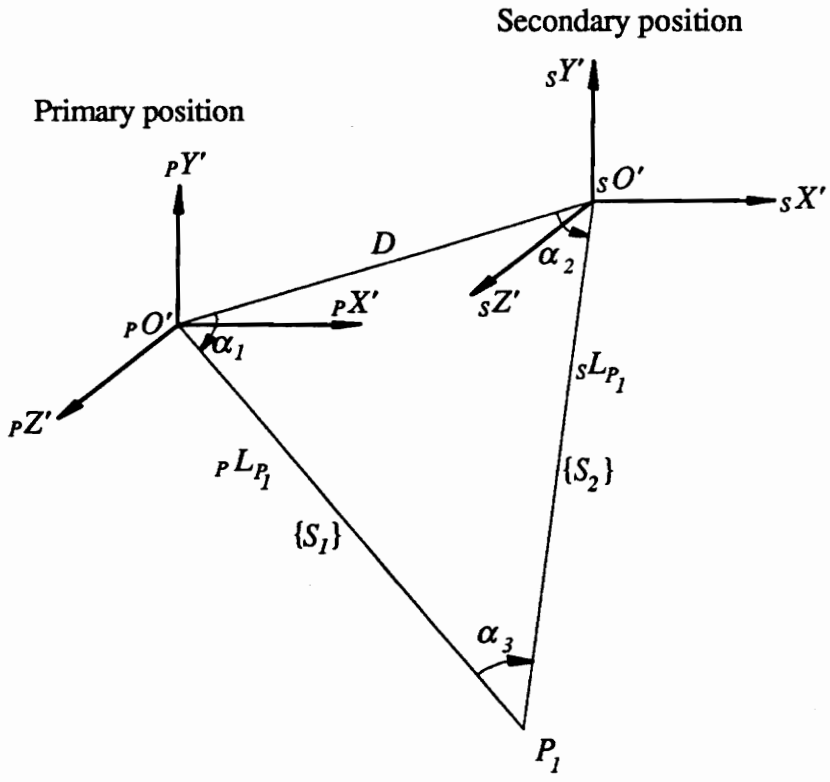

Figure 4.2 Schematic diagram for finding range in index setups

The ranges shown in figure 4.2 can be found for the primary and secondary positions.

$$\left.\begin{aligned} \alpha_3 &= \pi - \alpha_1 - \alpha_2 \\ {}_P L_{P_1} &= D \sin\alpha_2 / \sin\alpha_3 \\ {}_S L_{P_1} &= D \sin\alpha_1 / \sin\alpha_3 \end{aligned}\right\}. \tag{4.35}$$

where D, α_1 and α_2 can be found by using the known three pieces of information. A temporary Cartesian coordinate system is placed at the moving laser center for both the primary position and secondary position. This coordinate system has the same orientation with the laser coordinate system (see Fig. 4.2). In the primary position, it is called ${}_P O' X' Y' Z'$. In the secondary position it is called ${}_S O' X' Y' Z'$. Those two coordinate systems will have the same orientation since the laser head makes only a translational movement. Taking the primary position as reference, the coordinates of ${}_S O'$ with respect to the coordinate system of ${}_P O' X' Y' Z'$ is

$$\{{}_S O'\} = \begin{Bmatrix} 0 \\ dl \sin({}_P\theta_{P_1,X_L}) \\ dl \cos({}_P\theta_{P_1,X_L}) \end{Bmatrix} + \begin{Bmatrix} x_M \\ y_M \\ z_M \end{Bmatrix} + \begin{Bmatrix} 0 \\ -dl \sin({}_S\theta_{P_1,X_L}) \\ -dl \cos({}_S\theta_{P_1,X_L}) \end{Bmatrix} \tag{4.36}$$

The above equation can be derived from following relationship

$$\{{}_P O' \to {}_S O'\} = \{{}_P O' \to {}_P O_L\} + \{{}_P O_L \to {}_S O_L\} + \{{}_S O_L \to {}_S O'\} \tag{4.37}$$

where ${}_P O_L$ and ${}_S O_L$ are the origin of the laser coordinate system at the primary and secondary positions, respectively. The first and third term in Eq. (4.36) are found by using the relationship in Fig. 2.4. Now distance D between ${}_P O'$ and ${}_S O'$ is the length of the vector from ${}_P O'$ to ${}_S O'$

$$D = \left\| \{{}_S O'\} \right\| \tag{4.38}$$

The direction cosines of the vector from ${}_P O'$ to ${}_S O'$ are

$$\{l, m, n\}^T_{\{{}_S O'\}} = \{{}_S O'\} / D \tag{4.39}$$

The direction cosine of the vector $\{S_1\}$ from ${}_P O'$ to P_1 is

$$\begin{Bmatrix} l \\ m \\ n \end{Bmatrix}_{\{S_1\}} = \begin{Bmatrix} \sin\left({}_P\theta_{P_1Y_L}\right) \\ \cos\left({}_P\theta_{P_1Y_L}\right)\sin\left({}_P\theta_{P_1X_L}\right) \\ \cos\left({}_P\theta_{P_1Y_L}\right)\cos\left({}_P\theta_{P_1X_L}\right) \end{Bmatrix} \tag{4.40}$$

Using the direction cosines of vector from ${}_PO'$ to ${}_SO'$ and vector $\{S_1\}$, the angle α_1 can be found as

$$\alpha_1 = \cos^{-1}\left(l_{\{{}_SO'\}}l_{\{S_1\}} + m_{\{{}_SO'\}}m_{\{S_1\}} + n_{\{{}_SO'\}}n_{\{S_1\}}\right) \tag{4.41}$$

The direction cosine of the vector $\{S_2\}$ from ${}_SO'$ to P_1 is

$$\begin{Bmatrix} l \\ m \\ n \end{Bmatrix}_{\{S_2\}} = \begin{Bmatrix} \sin\left({}_S\theta_{P_1Y_L}\right) \\ \cos\left({}_S\theta_{P_1Y_L}\right)\sin\left({}_S\theta_{P_1X_L}\right) \\ \cos\left({}_S\theta_{P_1Y_L}\right)\cos\left({}_S\theta_{P_1X_L}\right) \end{Bmatrix} \tag{4.42}$$

Using those direction cosines of vector from ${}_SO'$ to ${}_PO'$ and vector $\{S_2\}$, the desired angles α_2 can be found as

$$\alpha_2 = \cos^{-1}\left(-l_{\{{}_SO'\}}l_{\{S_2\}} - m_{\{{}_SO'\}}m_{\{S_2\}} - n_{\{{}_SO'\}}n_{\{S_2\}}\right) \tag{4.43}$$

Putting D, α_1 and α_2 into Eq. (4.35), one can find out the two desired ranges. In the same way, the ranges for all the registration points can be found.

In the index setup, one answer is obtained for each unknown range. There is no nonlinear equation set to solve. However, there is no statistical degree of freedom, either. Therefore, it forces the estimated ranges to fit the measurement errors. To get more accurate estimation, two or more secondary positions may be used. In this way, two or more estimations for each range can be obtained., the average of them will be more accurate than the estimation just from one secondary position.

4.2 Determination of the rotation matrix

After the range L is found for a registration point, it is easy to get its laser coordinate by using Eq. (2.10). Thus, the structural coordinate (x_S, y_S, z_S) and the laser coordinate (x_L, y_L, z_L) are available for each of the registration points. The relationship between them is Eq. (2.1). The goal is to use these two pieces of information from the registration points to find the rotation matrix and origin coordinates. This section will concentrate on finding the rotation matrix.

Considering the measurement error, one can obtain the following equation for point P_i.

$$\begin{Bmatrix} x_{P_i} \\ y_{P_i} \\ z_{P_i} \end{Bmatrix}_S = {}^S_L\{T\} + {}^S_L[R] \begin{Bmatrix} x_{P_i} \\ y_{P_i} \\ z_{P_i} \end{Bmatrix}_L + \begin{Bmatrix} \varepsilon_{x_{P_i}} \\ \varepsilon_{y_{P_i}} \\ \varepsilon_{z_{P_i}} \end{Bmatrix}_S \tag{4.44}$$

Haralick et al [3.29-3.30] determined the origin coordinate and rotation matrix from Eq. (4.44) by using a weight least squares method. However, their method has two problems. First, when all the points are on the same plane, their method can not find a unique solution. Second, this method can not insure that the determinant of the found rotation matrix will be one. If the determinant of the rotation matrix is negative one, one of the coordinate systems is a left-hand coordinate system, which is not correct for the real situation. The method developed in this chapter will not have those problems. A unique solution can always be found and the determinant of the found rotation matrix is always one.

4.2.1 Elimination of the origin coordinate as unknowns

One method to eliminate the origin coordinates as unknowns is to translationally move the two coordinate systems to a common point. The common point can be any registration point, or the average point (to be defined soon). The utility of the average point is developed by Haralick et al [3.29-3.30].

The average point P_a of the N registration points is defined as the center of those points.

$$\begin{Bmatrix} x_{P_a} \\ y_{P_a} \\ z_{P_a} \end{Bmatrix}_S = \frac{1}{N}\sum_{i=1}^{N}\begin{Bmatrix} x_{P_i} \\ y_{P_i} \\ z_{P_i} \end{Bmatrix}_S, \quad \begin{Bmatrix} x_{P_a} \\ y_{P_a} \\ z_{P_a} \end{Bmatrix}_L = \frac{1}{N}\sum_{i=1}^{N}\begin{Bmatrix} x_{P_i} \\ y_{P_i} \\ z_{P_i} \end{Bmatrix}_L \tag{4.45}$$

The coordinate transformation between the two coordinate systems should hold for the average point. Thus,

$$\begin{Bmatrix} x_{P_a} \\ y_{P_a} \\ z_{P_a} \end{Bmatrix}_S = {}^S_L\{T\} + {}^S_L[R]\begin{Bmatrix} x_{P_a} \\ y_{P_a} \\ z_{P_a} \end{Bmatrix}_L \tag{4.46}$$

Equation (4.46) can be obtained in another way. Adding all the registration points together from Eq. (4.44) and dividing by N,

$$\frac{1}{N}\sum_{i=1}^{N}\begin{Bmatrix} x_{P_i} \\ y_{P_i} \\ z_{P_i} \end{Bmatrix}_S = {}^S_L\{T\} + {}^S_L[R]\left(\frac{1}{N}\sum_{i=1}^{N}\begin{Bmatrix} x_{P_i} \\ y_{P_i} \\ z_{P_i} \end{Bmatrix}_L\right) + \frac{1}{N}\sum_{i=1}^{N}\begin{Bmatrix} \varepsilon_{x_{P_i}} \\ \varepsilon_{y_{P_i}} \\ \varepsilon_{z_{P_i}} \end{Bmatrix}_S \tag{4.47}$$

Notice that the last term in Eq. (4.47) is zero since the measurement errors are assumed to be normal distribution with zero mean. Using the definition in Eq. (4.45), Eq. (4.47) becomes Eq. (4.46).

Subtracting both sides of Eq. (4.46) from Eq. (4.44), the following equation can be obtained.

$$\begin{Bmatrix} x_{P_i} - x_{P_a} \\ y_{P_i} - y_{P_a} \\ z_{P_i} - z_{P_a} \end{Bmatrix}_S = {}^S_L[R] \begin{Bmatrix} x_{P_i} - x_{P_a} \\ y_{P_i} - y_{P_a} \\ z_{P_i} - z_{P_a} \end{Bmatrix}_L + \begin{Bmatrix} \varepsilon_{x_{P_i}} \\ \varepsilon_{y_{P_i}} \\ \varepsilon_{z_{P_i}} \end{Bmatrix}_S \tag{4.48}$$

Defining a new vector $\{d_i\}$ which is from average point P_a to registration point P_i, Eq. (4.48) can be written as

$$\{d_i\}_S = {}^S_L[R]\{d_i\}_L + \left(\varepsilon_{x_{P_i}} \; \varepsilon_{y_{P_i}} \; \varepsilon_{z_{P_i}}\right)^T_S \tag{4.49}$$

In fact, $\{d_i\}_S$ and $\{d_i\}_L$ present the same vector $\{d_i\}$ but they are measured in different coordinate systems. $\{d_i\}_S$ is the measurement of vector $\{d_i\}$ in structural coordinate system while $\{d_i\}_L$ is the measurement of vector $\{d_i\}$ in the laser coordinate system. The geometrical meaning of Eq. (4.49) is that the two frames now have the same origin at P_a and their relative orientation of the two frames remains unchanged. In this way, the two coordinate systems are translationally moved to the average point and the origin coordinates are eliminated as unknowns. Thus, the only unknown is the rotation matrix. In Eq. (4.49), the rotation matrix expresses the orientation of the laser coordinate system with respect to the structural coordinate system. It relates a vector's measurement in one coordinate system to its measurement in another coordinate system.

N registration points will present N pairs of information ($\{d_i\}_S$ and $\{d_i\}_L$ for i=1,2,..., N). Each pair satisfies Eq. (4.49). The rotation matrix can be found by directly applying the least squares method to minimize the sum of the squared residuals. Wahba [3.3], Stephens [3.4], and Mackenzie [3.40] obtained the rotation matrix in that way. However, their

method has the same problem as Haralick et al [3.29-3.30]. A geometrical method is sought here to avoid these two problems. The equivalent angle and equivalent axis are found first. Equation (3.6) is then used to obtain the rotation matrix.

4.2.2 Equivalence of frame rotation and vector rotation: principle and application

Figure 4.3 graphically shows the principle of the equivalence between the vector rotation and the frame rotation for two-dimensional case.

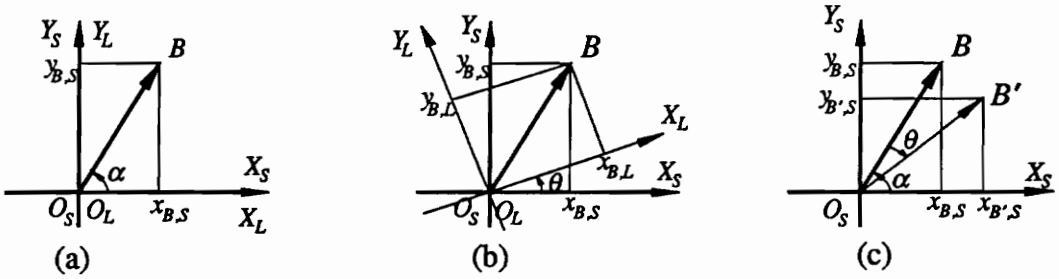

Figure 4.3 The equivalence of frame rotation and vector rotation

Figure 4.3 (a) shows a vector $\{B\}$ and two frames $O_S X_S Y_S$ and $O_L X_L Y_L$. The coordinates of vector $\{B\}$ in $O_S X_S Y_S$ is

$$\{B\}_S = \begin{Bmatrix} x_B \\ y_B \end{Bmatrix}_S = \begin{Bmatrix} r\cos\alpha \\ r\sin\alpha \end{Bmatrix} \tag{4.50}$$

where r is the length of vector $\{B\}$, α is the angle between $\{B\}$ and X_L. In Fig 4.3 (b), frame $O_L X_L Y_L$ rotates an angle θ about axis Z_S to reach a new position. The coordinates of $\{B\}$ in $O_L X_L Y_L$ can be found by using a geometrical relation

$$\{B\}_L = \begin{Bmatrix} x_B \\ y_B \end{Bmatrix}_L = \begin{Bmatrix} x_{B,S}\cos\theta + y_{B,S}\sin\theta \\ -x_{B,S}\sin\theta + y_{B,S}\cos\theta \end{Bmatrix} = \begin{bmatrix} \cos\theta & \sin\theta \\ -\sin\theta & \cos\theta \end{bmatrix} \begin{Bmatrix} x_B \\ y_B \end{Bmatrix}_S \tag{4.51}$$

In Fig. 4.3 (c), vector $\{B\}$ rotates an angle $-\theta$ to become a new vector $\{B'\}$. The coordinates of $\{B'\}$ in $O_S X_S Y_S$ can be found as

$$\{B'\}_S = \begin{Bmatrix} x_{B'} \\ y_{B'} \end{Bmatrix}_S = \begin{Bmatrix} r\cos(\alpha-\theta) \\ r\sin(\alpha-\theta) \end{Bmatrix} = \begin{bmatrix} \cos\theta & \sin\theta \\ -\sin\theta & \cos\theta \end{bmatrix} \begin{Bmatrix} x_B \\ y_B \end{Bmatrix}_S \tag{4.52}$$

The above equation is obtained by expanding sine and cosine functions and using Eq. (4.50). Equation (4.51) and Eq. (4.52) show that $\{B'\}_S$ is equal to $\{B\}_L$. That is, the so-called equivalence between the vector rotation and the frame rotation. Note that the rotation is about the same axis but the rotated angle has opposite sign according to the right-hand rule, i.e., the direction of rotation is opposite.

The equivalence relationship can be used to find the rotation matrix. The rotation matrix for the case that $O_L X_L Y_L$ rotates about Z_S axis by angle θ (according to the right-hand rule) is given by Eq. (4.53).

$${}^S_L[R] = \begin{bmatrix} \cos\theta & -\sin\theta \\ \sin\theta & \cos\theta \end{bmatrix} \tag{4.53}$$

Assume that the coordinates of vector $\{B\}$ is $\{B\}_S$ in $O_S X_S Y_S$ and is $\{B\}_L$ in $O_L X_L Y_L$. By the equivalent relationship, the coordinate of $\{B'\}$ in the $O_S X_S Y_S$ is equal to $\{B\}_L$. From Fig. 4.3 (c), the angle θ rotated by vector $\{B\}$ from $\{B\}$ to $\{B'\}$ can be found as

$$\theta = tan^{-1}(y_{B'S} / x_{B'S}) - tan^{-1}(y_{BS} / x_{BS}), \tag{4.54}$$

also, the above equation can be written as by using the equivalence relation

$$\theta = tan^{-1}(y_{BL} / x_{BL}) - tan^{-1}(y_{BS} / x_{BS}) \tag{4.55}$$

Put $-\theta$ into Eq. (4.53), the rotation matrix ${}^S_L[R]$ will be obtained. This procedure has shown how to use $\{B\}_S$ and $\{B\}_L$ to find the rotation matrix.

The example for the two-dimensional space case is also true for the three-dimensional case. Assume a vector $\{B\}$ and two frames coinciding. The coordinates of $\{B\}$ in frame $O_S X_S Y_S Z_S$ are

$$\{B\}_S = (x_B \quad y_B \quad z_B)_S^T \tag{4.56}$$

Now, frame $O_L X_L Y_L Z_L$ rotates about axis k by an angle θ according to the right-hand rule. The coordinates of $\{B\}$ in frame $O_L X_L Y_L Z_L$ become

$$\{B\}_L = (x_B \quad y_B \quad z_B)_L^T \tag{4.57}$$

If vector $\{B\}$ rotates about axis k by angle $-\theta$ (according to the right-hand rule) to become $\{B'\}$, the coordinates of $\{B'\}$ in $O_S X_S Y_S Z_S$ are

$$\{B'\}_S = (x_{B'} \quad y_{B'} \quad z_{B'})_S^T \tag{4.58}$$

Parallel to the equivalence of the vector rotation and the frame rotation in the two-dimensional case, it can be shown that $\{B'\}_S$ will be equal to $\{B\}_L$. Since $\{B'\}$ and $\{B\}$ are described in $O_S X_S Y_S Z_S$, they will be used to find the axis k and rotated angle θ. In the two-dimensional case, one vector is enough to determine θ because the axis k is Z_S by default. In the three-dimensional case, k and θ are to be determined. Thus, at least two vectors are required. Once k and θ are found, one can put k and $-\theta$ into Eq. (3.6) to calculate the rotation matrix. Since the rotation is made according to the right-hand rule, putting -k and θ into Eq. (3.6) will also give the same answer. The next section shows the details for the determination of the rotation matrix by determining the equivalent axis and angle.

4.2.3 The rotation matrix from equivalent angle and equivalent axis

The vector in the real problem is $\{d_i\}$ instead of $\{B\}$. The coordinates of vector $\{d_i\}$ are $\{d_i\}_S$ in $O_S X_S Y_S Z_S$ and $\{d_i\}_L$ in $O_L X_L Y_L Z_L$. By the equivalence relationship, the

coordinate of vector $\{d_i'\}$ in $O_S X_S Y_S Z_S$ is equal to $\{d_i\}_L$. It is known that $\{d_i\}$ rotates about axis k by an angle θ to became $\{d_i'\}$. Using $\{d_i\}$ and $\{d_i'\}$ (for i=1, 2,..., N), the k and θ can be found.

During the rotation, the angle between the vector $\{d_i\}$ and axis k remain fixed. Therefore, the angle between k and $\{d_i\}$ and the angle between k and $\{d_i'\}$ remain the same, which leads to

$$l_k l_{d_i} + m_k m_{d_i} + n_k n_{d_i} = l_k l_{d_i'} + m_k m_{d_i'} + n_k n_{d_i'} \tag{4.59}$$

where $(l_{d_i}, m_{d_i}, n_{d_i})$ is the direction cosine of vector $\{d_i\}$ and $(l_{d_i'}, m_{d_i'}, n_{d_i'})$ is the direction cosine of vector $\{d_i'\}$. Equation (4.59) can be written as

$$a_i l_k + b_i m_k + c_i n_k = 0 \text{ (for } i=1, 2, ..., N) \tag{4.60}$$

where $a_i = l_{d_i} - l_{d_i'}$, $b_i = m_{d_i} - m_{d_i'}$, and $c_i = n_{d_i} - n_{d_i'}$. There is a constraint for the direction cosine of axis k

$$l_k^2 + m_k^2 + n_k^2 = 1 \tag{4.61}$$

Equation (4.60) can be written in matrix form as

$$[\{a\}\ \{b\}\ \{c\}]\{k\} = \{0\} \tag{4.62}$$

where

$$\left.\begin{aligned} \{a\} &= (a_1, a_2, ..., a_N)^T \\ \{b\} &= (b_1, b_2, ..., b_N)^T \\ \{c\} &= (c_1, c_2, ..., c_N)^T \\ \{k\} &= (l_k, m_k, n_k)^T \end{aligned}\right\} \tag{4.63}$$

Equations (4.61-4.62) are the desired equations to determine axis k. If N is 3, a determined equation set is obtained. If N is equal to or larger than 4, an overdetermined equation set is obtained. For the overdetermined case, the least squares method can be

used to find out a closed-form solution. Following is the detailed procedure for finding the equivalent axis k.

From Eq. (4.62), (l_k, m_k) can be found as a function n_k. Moving the third column to right-hand side

$$[\{a\}\ \{b\}]\begin{Bmatrix} l_k \\ m_k \end{Bmatrix} = -\{c\}n_k \tag{4.64}$$

and applying the least squares method to Eq. (4.64), one obtain

$$\begin{Bmatrix} l_k \\ m_k \end{Bmatrix} = -\left([\{a\}\ \{b\}]^T[\{a\}\ \{b\}]\right)^{-1}[\{a\}\ \{b\}]^T\{c\}n_k \tag{4.65}$$

Let s_{pq} be the inner product of vector $\{p\}$ and $\{q\}$

$$s_{pq} = \{p\} \bullet \{q\} \tag{4.66}$$

where $\{p\}, \{q\} = \{a\}, \{b\}, \{c\}$. Using the above equation, Eq. (4.65) can be written as

$$\begin{aligned} \ell_k &= h_1 n_k \\ m_k &= h_2 n_k \end{aligned} \tag{4.67}$$

where

$$\left.\begin{aligned} h_1 &= (-s_{bb}s_{ca} + s_{ab}s_{bc}) / zz \\ h_2 &= (s_{ab}s_{ca} - s_{aa}s_{bc}) / zz \end{aligned}\right\} \tag{4.68}$$

and

$$zz = s_{aa}s_{bb} - s_{ab}s_{ab} \tag{4.69}$$

Substituting Eq.(4.67) into Eq. (4.61), one has

$$(h_1^2 + h_2^2 + 1)n_k^2 = 1 \tag{4.70}$$

Taking the positive square root of n_k, the solution for n_k is obtained as

$$n_k = 1 / \sqrt{h_1^2 + h_2^2 + 1} \tag{4.71}$$

Putting n_k back into Eq. (4.67), all the direction cosines of axis k are obtained. Since the positive square root of n_k is taken and since n_k may be negative in the real situation, the solution for k has directional uncertainty.

If l_k and n_k are expressed as a function of m_k, the following can be obtained after a similar derivation.

$$\left.\begin{aligned} l_k &= h_3 m_k \\ n_k &= h_4 n_k \\ m_k &= 1/\sqrt{h_3^2+1+h_4^2} \end{aligned}\right\} \tag{4.72}$$

where

$$\left.\begin{aligned} h_3 &= \left(-s_{cc}s_{ab}+s_{ca}s_{bc}\right)/\ yy \\ h_4 &= \left(s_{ca}s_{ab}-s_{aa}s_{bc}\right)/\ yy \\ yy &= s_{aa}s_{cc}-s_{ca}s_{ca} \end{aligned}\right\} \tag{4.73}$$

In the same way, one can obtain the following equation if m_k and n_k are expressed as a function of l_k.

$$\left.\begin{aligned} m_k &= h_5 l_k \\ n_k &= h_6 l_k \\ l_k &= 1/\sqrt{1+h_5^2+h_6^2} \end{aligned}\right\} \tag{4.74}$$

where

$$\left.\begin{aligned} h_5 &= \left(-s_{cc}s_{ab}+s_{bc}s_{ca}\right)/\ xx \\ h_6 &= \left(s_{bc}s_{ab}-s_{bb}s_{ca}\right)/\ xx \\ xx &= s_{bb}s_{cc}-s_{bc}s_{bc} \end{aligned}\right\} \tag{4.75}$$

Three schemes have been developed to find axis k. From numerical point of view, a relatively large denominator will result in less error amplification. Based on this, the method for choosing a solution scheme is obvious. Finding which is the largest among the three numbers xx, yy, and zz, the scheme corresponding to the largest should be used. For example, if xx is the largest absolute value, Eq. (4.74-4.75) should be used.

Once the axis k is obtained, θ can be found. Since θ is measured in a plane perpendicular to axis k, the angle between $\{d_i\}$ and $\{d_i'\}$ is not required information. The method is to project $\{d_i\}$ and $\{d_i'\}$ onto a plane perpendicular to k and then find the angle between the projections of $\{d_i\}$ and $\{d_i'\}$.

Figure 4.4 shows the geometry used to determine the rotated angle. Angle θ_i', between $\{d_i\}$ and $\{d_i'\}$, is found to be

$$\cos\theta_i' = l_{d_i} l_{d_i'} + m_{d_i} m_{d_i'} + n_{d_i} n_{d_i'} \tag{4.76}$$

angle ϕ_i between $\{d_i\}$ and k is

$$\cos\phi_i = l_{d_i} l_k + m_{d_i} m_k + n_{d_i} n_k \tag{4.77}$$

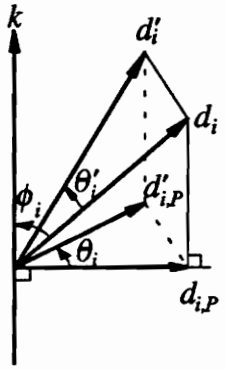

Figure 4.4 The determination of rotation angle

The distance D between the tips of vector $\{d_i\}$ and $\{d_i'\}$ is found by the cosine law.

$$D^2 = \|\{d_i\}\|^2 + \|\{d_i\}\|^2 - 2\|\{d_i\}\|\|\{d_i\}\| cos\,\theta_i' \tag{4.78}$$

The distance D_p between the tips of vector $d_{i,P}$ and $d_{i,P}'$ is

$$D_p^2 = \|\{d_i\}\|^2 sin^2\,\phi_i + \|\{d_i\}\|^2 sin^2\,\phi_i - 2\|\{d_i\}\|^2 sin^2\,\phi_i\, cos\,\theta_i \tag{4.79}$$

where $sin^2\,\phi_i = 1 - cos^2\,\phi_i$. The projection does not change the distance. Thus, Eqs. (4.78-4.79) give

$$2\|\{d_i\}\|^2(1 - cos\,\theta_i') = 2\|\{d_i\}\|^2 sin^2\,\phi_i(1 - cos\,\theta_i) \tag{4.80}$$

From above equation, one finds the angle θ_i as

$$cos\,\theta_i = 1 - \frac{1 - cos\,\theta_i'}{sin^2\,\phi_i} \tag{4.81}$$

With N vectors, N rotated angles can be found. The best estimation of angle θ is to average all the obtained angles

$$\theta = \frac{1}{N}\sum_{i=1}^{N}\theta_i \tag{4.82}$$

where θ_i is given by Eq. (4.81). The sign of θ_i may be wrong because of the uncertainty of the axis k's direction. However, the correct rotation matrix ${}_L^S[R]$ can be constructed with the found k and θ. Note that the rotation is made according to the right-hand rule. If the found axis has correct direction, putting k and $-\theta$ to Eq. (3.6) will result in the correct answer. If the found k has wrong direction, putting k and θ into Eq. (3.6) will yield a correct rotation matrix. Accordingly, two rotation matrices are formed. One called ${}_L^S[R]^+$ is obtained by using the found k and positive θ. The other called ${}_L^S[R]^-$ is obtained by using the found k and $-\theta$. One of them must be the correct rotation matrix. To pick up the correct one, Eq. (4.49) can be used. The correct rotation matrix will make Eq. (4.49) hold.

4.3 Determination of the origin coordinate

Once the rotation matrix is obtained, the origin coordinate can be found by using Eq. (4.46).

$$ {}^{S}_{L}\{T\} = \begin{Bmatrix} x_{P_a} \\ y_{P_a} \\ z_{P_a} \end{Bmatrix}_S - {}^{S}_{L}[R] \begin{Bmatrix} x_{P_a} \\ y_{P_a} \\ z_{P_a} \end{Bmatrix}_L \tag{4.83} $$

As shown by Haralick et al [3.29-3.30], this is the least squares solution of Eq. (4.44) if all weights are equal to 1.

4.4 Summary

The geometrical method for pose determination has been developed in this chapter. It finds the pose in three steps: ranges, rotation matrix, and origin coordinates. In the first step, the total error is the sum of the squared difference in the distance between any two registration points. Minimization of this total error gives an accurate estimation of the ranges.

In the second step, the total error to be minimized is (see Eq. (4.44))

$$ Q = \sum_{i=1}^{N} \left\| \begin{Bmatrix} \varepsilon_{x_n} \\ \varepsilon_{y_n} \\ \varepsilon_{z_n} \end{Bmatrix}_S \right\|^2 \tag{4.84} $$

This total error is minimized in two steps by finding the equivalent angle and then equivalent axis. Thus the resulting estimation of the rotation matrix may minimize this total error. However, it is possible that the estimation just make the total error in Eq. (4.84) close enough to the global minimum. However, each single error in Eq. (4.84) is the squared distance between the actual registration point and the fitted registration point in the structural coordinate system. Thus, a global minimum in Eq. (4.84) does not necessarily imply a global minimum in the sum of the squared difference between the measured scanning angles and the fitted scanning angles. The fitted scanning angles are computed from the structural coordinates by using the obtained pose. Figure 4.5 shows two situations. The spatial error in situation one is smaller than that in situation two while the angle error in situation one is larger than that in situation two. Therefore, if one wants to aim the laser beam at a registration point more accurately, he needs less error between the measured scanning angles and the fitted scanning angles.

The origin coordinate is obtained after the rotation matrix is found. The estimation minimizes the total error defined in Eq. (4.84).

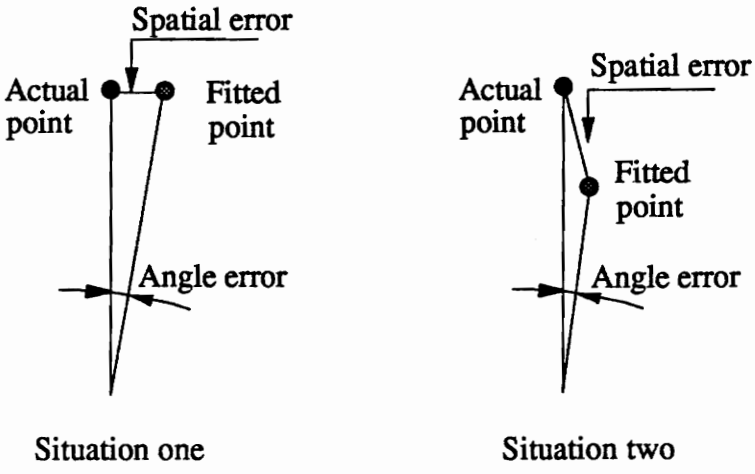

Figure 4.5 Spatial error and angle error

CHAPTER FIVE

NONLINEAR REGRESSIVE MODELS FOR THE POSE DETERMINATION OF THE SLDV

In this chapter, two nonlinear regressive models will be developed for the pose determination of the SLDV. The least squares method will be used to estimate the parameters in the models. The statistical inferences are derived based on the linear approximation. To verify the validity of the linear approximation, the nonlinearity of the models will be measured.

5.1 Two nonlinear regressive models

As discussed in section **2.3**, there are two pieces of information available for each registration point. One is the structural coordinates (x_S, y_S, z_S). The other is the scanning coordinates $(\theta_{X_L}, \theta_{Y_L})$. The structural coordinates can be expressed as a function of the scanning coordinates. The scanning coordinates can also be expressed as a function of the structural coordinates. From those two expressions, two nonlinear regressive models can be developed.

5.1.1 Forward model

When the structural coordinates are expressed in terms of the scanning coordinates, a forward model is obtained. Putting Eq. (2.10) into Eq. (2.1), one has the following equation

$$\begin{Bmatrix} x_P \\ y_P \\ z_P \end{Bmatrix}_S = {}^S_L\{T\} + {}^S_L[R] \begin{Bmatrix} L_P \sin\theta_{PY_L} \\ (L_P \cos\theta_{PY_L} - dl)\sin\theta_{PX_L} \\ (L_P \cos\theta_{PY_L} - dl)\cos\theta_{PX_L} \end{Bmatrix}_L \tag{5.1}$$

Taking the measurement errors into account, one can obtain the following equation from Eq. (5.1) for point P_i

$$\begin{Bmatrix} x_{P_i} \\ y_{P_i} \\ z_{P_i} \end{Bmatrix}_S = {}^S_L\{T\} + {}^S_L[R] \begin{Bmatrix} L_{P_i} \sin\theta_{P_iY_L} \\ (L_{P_i} \cos\theta_{P_iY_L} - dl)\sin\theta_{P_iX_L} \\ (L_{P_i} \cos\theta_{P_iY_L} - dl)\cos\theta_{P_iX_L} \end{Bmatrix} + \begin{Bmatrix} \varepsilon_{x_{P_i}} \\ \varepsilon_{y_{P_i}} \\ \varepsilon_{z_{P_i}} \end{Bmatrix}_S \tag{5.2}$$

The above equation is the forward model. The scanning coordinates ($\theta_{P_iX_L}$, $\theta_{P_iY_L}$) in the forward model are the regressor variables while the structural coordinates ($x_{P_i,S}$, $y_{P_i,S}$, $z_{P_i,S}$) are the response variables. The last term in Eq. (5.2) is the error (disturbance or residual) which accounts for the uncertainty in the measurements of the structural coordinates. The parameters in the forward model are the SLDV pose and the ranges L_{P_i} (i=1, 2, ..., N). Thus, the number of parameters in the forward model is 6+N. The structural coordinates in Eq. (5.2) are linear functions of the origin coordinates. However, they are nonlinear functions of the rotation matrix and ranges. There are two reasons for this statement. First, the range and rotation matrix are multiplied together. Second, the rotation matrix has nonlinear constraints or is a nonlinear function of the other independent variables or both. Therefore, the forward model is a nonlinear regressive model.

5.1.2 Inverse model

When the scanning coordinates are expressed in terms of the structural coordinates, an inverse model is obtained. For convenience, recall Eq. (2.2)

$$\begin{Bmatrix} x_P \\ y_P \\ z_P \end{Bmatrix}_L = {}^L_S\{T\} + {}^L_S[R] \begin{Bmatrix} x_P \\ y_P \\ z_P \end{Bmatrix}_S \tag{5.3}$$

Using the first two equations of Eq. (2.11), the scanning coordinates are found to be

$$\begin{aligned} \theta_{P,X_L} &= tan^{-1}\left(\frac{y_{P,L}}{z_{P,L}}\right) \\ \theta_{PY_L} &= tan^{-1}\left(\frac{x_{P,L}}{\sqrt{y_{P,L}^2 + z_{P,L}^2} + dl}\right) \end{aligned} \tag{5.4}$$

Equations (5.3-5.4) show that the scanning coordinates are expressed in terms of the structural coordinates. Considering the measurement errors, one can obtain the following equation from Eq. (5.4) for point P_i

$$\begin{aligned} \theta_{P_i,X_L} &= tan^{-1}\left(\frac{y_{P_i,L}}{z_{P_i,L}}\right) + \varepsilon_{\theta_{P_i X_L}} \\ \theta_{P_i Y_L} &= tan^{-1}\left(\frac{x_{P_i,L}}{\sqrt{y_{P_i,L}^2 + z_{P_i,L}^2} + dl}\right) + \varepsilon_{\theta_{P_i Y_L}} \end{aligned} \tag{5.5}$$

where the laser coordinates $(x_{P_i,L}, y_{P_i,L}, z_{P_i,L})$ are obtained from the structural coordinates $(x_{P_i,S}, y_{P_i,S}, z_{P_i,S})$ by Eq. (5.3). Equations (5.3) and (5.5) form the inverse model. The structural coordinates $(x_{P_i,S}, y_{P_i,S}, z_{P_i,S})$ in the inverse model are the regressor variables while the scanning coordinates $(\theta_{P_i,X_L}, \theta_{P_i Y_L})$ are the response variables. The last term in

Eq. (5.5) is the errors which account for the uncertainty in the measurements of the scanning coordinates. The parameters in the inverse model are the pose of the structural coordinate system. The range is not an unknown parameter any more. Thus, the number of parameters in the inverse model is 6. Form Eqs. (5.3) and (5.5), it can be seen that the scanning coordinates are nonlinear functions of ${}^{L}_{S}\{T\}$ and ${}^{L}_{S}[R]$. Therefore, the inverse model is also a nonlinear regressive model. Note that ${}^{L}_{S}\{T\}$ and ${}^{L}_{S}[R]$ in Eq. (5.3) are the position and the orientation of the structural coordinate system with respect to the laser coordinate system. Once the ${}^{L}_{S}\{T\}$ and ${}^{L}_{S}[R]$ are found, the pose of the SLDV can be obtained from them by using Eq. (2.3).

5.1.3 Some properties of the two nonlinear models

Both the forward and inverse models are multiresponse models. That is, for a given value of the regressor variables, there is more than one response variables. For the forward model, the response variables are $x_{P_i,S}$, $y_{P_i,S}$, and $z_{P_i,S}$. For the inverse model, the response variables are θ_{P_i,X_L} and θ_{P_i,Y_L}. Additional consideration should be made for the multiresponse situation in estimating the parameters and evaluating the nonlinearity.

In the forward model, the measurement errors are associated with the structural coordinate $(x_{P_i,S}, y_{P_i,S}, z_{P_i,S})$. The scanning coordinates $(\theta_{P_i,X_L}, \theta_{P_i,Y_L})$ are assumed to be error free. In the inverse model, the measurement errors are associated with the scanning coordinate. The structural coordinates are assumed to be error free. However, in the real situation, both measurements have errors. Thus, the parameters estimated from either model are biased.

The errors in the forward model are assumed to be identically and independently distributed normal random variables with zero mean and finite variance. So are the errors in the inverse model. This independence means two things for multiresponse model. (i): Errors in different cases (different registration points) are independently distributed even for the same response. (ii). The errors in different responses for the same case (same registration point) are independently distributed. For the forward model, the structural coordinates of a registration point are measured by the coordinate measurement instrument. Thus, measurement accuracy is same for different registration points and for the x, y and z coordinates of the same registration points. The measurements of the coordinates are conducted independently for different registration points and for the x, y, and z coordinates of the same registration points. Thus, the errors in the forward model can be assumed to be independent and have equal variance. For the inverse model, the two mirrors are independently controlled by two galvanometers. The two galvanometers have the same structure and their control boards have the same gains. These imply that the errors in the scanning angles will have the same properties as those of the errors in the input voltages. The input voltages are from two channels of a D/A converter. The accuracy in the input voltages is same for the two channels and for different voltages (corresponding to different registration points). The accuracy is independent of the channels and of different voltages. These mean that the errors in the input voltages can be assumed to be independent and have equal variance. Therefore, the errors in the inverse model can be assumed to be independent and have equal variance. With the above discussed assumption, the statistical properties of the errors can be mathematical expressed. Taking the inverse model as an example, one has

$$\left.\begin{aligned} E\left[\{\varepsilon\}_\theta\right] &= \{0\} \\ Var\left[\{\varepsilon\}_\theta\right] &= E\left[\{\varepsilon\}_\theta \{\varepsilon\}_\theta^T\right] = \sigma^2 [I] \end{aligned}\right\} \tag{5.6}$$

where $[I]$ is a $2N$ by $2N$ identity matrix and

$$\{\varepsilon\}_\theta = \left\{\varepsilon_{\theta_{R_1 X_L}}, \varepsilon_{\theta_{R_1 Y_L}}, \ldots, \varepsilon_{\theta_{R_N X_L}}, \varepsilon_{\theta_{R_N Y_L}}\right\}^T \tag{5.7}$$

5.1.4 Comparison of the two nonlinear regressive models

The forward and inverse models have common and different properties. The common properties are the followings.

I). They are nonlinear regressive models with multiple responses.

II). The regressor variables have measurement errors

III). The errors in the forward model are assumed to be identically and independently distributed normal random variables with zero mean and finite variance. So are the errors in the inverse model. Note that the variance of the errors in the forward model is not equal to the variance of the errors in the inverse model.

The differences between the two models are the followings.

I). The number of the parameters for the forward model is $6+N$ while the number of parameters for the inverse model is 6.

II). There is a constraint for the range, i.e., $L_{P_i} > 0$, for the forward while the ranges are not parameters in the inverse model. Note that there is no effective way to make inferences about a constrained parameter.

III). After the forward model is fitted, it can not predict the response variables (structural coordinates) from the given regressor variables ($\theta_{P_i X_L}$, $\theta_{P_i Y_L}$) for a spatial point. However, after the inverse model is fitted, it can predict the response variables ($\theta_{P_i X_L}$, $\theta_{P_i Y_L}$) from the given regressor variables (structural coordinates) for a spatial point. The direction of the line-of-sight of the laser beam for that point can also be obtained.

IV). The errors in the forward model are in the structural coordinates while the errors in the inverse model are in the scanning coordinates ($\theta_{P_i X_L}$, $\theta_{P_i Y_L}$) which are directly connected to the scanning angles (Eqs (2.8-2.9)). As pointed out in section **4.4**, the global minimum of the sum of the squared errors in the structural coordinates does not necessarily imply a global minimum of the sum of the squared errors in the scanning angles. To aim the laser beam at a spatial point more accurately, the errors in the scanning angles should be less. After the inverse model is fitted, the sum of the squared errors (residuals) in the scanning angles is minimized. Thus, the laser beam will be aimed at those registration points more accurately.

It can be seen from those differences that the inverse model is better. Therefore, most of the efforts will be made on the inverse model in the remainder of this dissertation.

5.2 The estimation of the parameters in the nonlinear models

There are several methods to estimate the parameters in a nonlinear regressive model [5.1-5.5]. The least squares method is the most commonly used. This method minimizes the sum of the squared errors by adjusting the parameters. When the assumptions about the errors in section **5.1.3** are correct, the least squares method is appropriate for multiresponse model [5.3, 5.5-5.7]. If the errors have statistical properties other than Eq. (5.6), other criterion may be used for the parameter estimation [5.3, 5.5]. The least squares method will be used here to obtain the parameters in the forward and inverse models.

There may be two ways to apply the least squares method to a nonlinear regressive model. One way is to directly transfer the nonlinear regressive model into an optimization model. In general, a constraint optimization model will be obtained from the original nonlinear regressive model. The other way is to linearize the nonlinear model and then to apply the least squares method to the linearized equation. One solution can be obtained for each linearized equation without iteration. The procedure has to be repeated until a converged solution is obtained.

5.2.1 Optimization models for the nonlinear regressive models

In chapter 3, four representations of the rotation matrix were introduced. For each representation, an optimization model can be obtained for each of the two nonlinear regressive models.

5.2.1.1 Optimization model for the forward model

The followings are the four optimization models for the forward model for the pose determination of the SLDV.

I). Rotation matrix represented by unit vectors

$$\text{Find } {}^{S}_{L}\{T\},\ {}^{S}_{L}[R] \text{ and } L_{P_i}\ (i=1, 2, ..., N) \text{ that}$$
$$\text{satisfy } ({}^{S}_{L}[R]^{T})({}^{S}_{L}[R]) = [I]\ ,\ \det({}^{S}_{L}[R]) = 1, \text{ and } L_{P_i} > 0, \tag{5.8}$$
$$\text{and minimize } Q = \sum_{i=1}^{N} \left\| \{\varepsilon_{P_i}\}_S \right\|^2$$

where

$$\{\varepsilon_{P_i}\}_S = \{\varepsilon_{x_{P_i S}},\ \varepsilon_{y_{P_i S}},\ \varepsilon_{z_{P_i S}}\}^T \tag{5.9}$$

which are the residuals for point P_i in the structural coordinate system.

II). Rotation matrix represented by three Euler angles

$$\text{Find } {}^{S}_{L}\{T\},\ \alpha,\ \beta,\ \gamma, \text{ and } L_{P_i}\ (i=1, 2, ..., N) \text{ that}$$
$$\text{satisfy } L_{P_i} > 0, \tag{5.10}$$
$$\text{and minimize } Q = \sum_{i=1}^{N} \left\| \{\varepsilon_{P_i}\}_S \right\|^2$$

III). Rotation matrix represented by equivalent angle and equivalent axis

$$\text{Find } {}^{S}_{L}\{T\},\ \theta,\ l_k,\ m_k,\ n_k, \text{ and } L_{P_i}\ (i=1, 2, ..., N) \text{ that}$$
$$\text{satisfy } l_k^2 + m_k^2 + n_k^2 = 1, \text{ and } L_{P_i} > 0, \tag{5.11}$$
$$\text{and minimize } Q = \sum_{i=1}^{N} \left\| \{\varepsilon_{P_i}\}_S \right\|^2$$

IV). Rotation matrix represented by Euler parameters

$$\text{Find } {}^{S}_{L}\{T\},\ e_1,\ e_2,\ e_3,\ e_4, \text{ and } L_{P_i}\ (i=1, 2, ..., N) \text{ that}$$

$$\text{satisfy } e_1^2 + e_2^2 + e_3^2 + e_4^2 = 1, \text{ and } L_{P_i} > 0, \tag{5.12}$$

$$\text{and minimize } Q = \sum_{i=1}^{N} \left\| \{\varepsilon_{P_i}\}_S \right\|^2$$

5.2.1.2 Optimization models for the inverse model

The followings are the four optimization models for the inverse model for the pose determination of the SLDV.

I). Rotation matrix represented by unit vectors

$$\text{Find } {}^{S}_{L}\{T\},\ {}^{S}_{L}[R] \text{ that}$$

$$\text{satisfy } ({}^{S}_{L}[R]^T)({}^{S}_{L}[R]) = [I]\ ,\ \det({}^{S}_{L}[R]) = 1, \tag{5.13}$$

$$\text{and minimize } Q = \sum_{i=1}^{N} \left\| \{\varepsilon_{P_i}\}_\theta \right\|^2$$

where

$$\{\varepsilon_{P_i}\}_\theta = \left\{ \varepsilon_{\theta_{P_i X_L}},\ \varepsilon_{\theta_{P_i Y_L}} \right\}^T \tag{5.14}$$

which are the residuals for point P_i in the scanning coordinate.

II). Rotation matrix represented by three Euler angles

$$\text{Find } {}^{S}_{L}\{T\},\ \alpha,\ \beta,\ \gamma \text{ that}$$

$$\text{minimize } Q = \sum_{i=1}^{N} \left\| \{\varepsilon_{P_i}\}_\theta \right\|^2 \tag{5.15}$$

III). Rotation matrix represented by equivalent angle and equivalent axis

$$\text{Find } {}_L^S\{T\},\ \theta,\ l_k,\ m_k,\ n_k \text{ that}$$

$$\text{satisfy } l_k^2 + m_k^2 + n_k^2 = 1, \tag{5.16}$$

$$\text{and minimize } Q = \sum_{i=1}^{N} \left\| \{\varepsilon_{P_i}\}_\theta \right\|^2$$

IV). Rotation matrix represented by Euler parameters

$$\text{Find } {}_L^S\{T\},\ e_1,\ e_2,\ e_3, \text{ and } e_4 \text{ that}$$

$$\text{satisfy } e_1^2 + e_2^2 + e_3^2 + e_4^2 = 1, \tag{5.17}$$

$$\text{and minimize } Q = \sum_{i=1}^{N} \left\| \{\varepsilon_{P_i}\}_\theta \right\|^2$$

5.2.2 Gauss-Newton method for the inverse model

Linearization technique used for parameter estimation in nonlinear regression is called Gauss-Newton method [5.2-5.5]. It has been widely used in uniresponse model. It can also be used for multiresponse model [5.5]. When Gauss-Newton method is applied to a nonlinear regressive model, both the model and the associated constraint equation need to be linearized. The resulting linear equation with linear constraint can be solved by linear programming techniques. However, there is no effective way to make inferences about a model with constrained parameters. Thus, a nonlinear regressive model without constraints among its parameters is desired.

In the forward model, the range is a parameter. There is always a constraint, $L_{P_i} > 0$. Thus, the forward model is not desired. In the inverse model, the range is no longer a parameter. There is no constraint among the three position parameters. If the rotation matrix is represented by three Euler angles, there will be no constraints among the three Euler angles, either. It follows that the inverse model with the rotation matrix being represented by three Euler angles will not present any constraints among the six pose parameters. It is clear that this model is more desirable. Only this model will be considered here for linearization.

For easy of notion, an parameter vector $\{\gamma\}$ for the six pose parameters is defined as

$$\left.\begin{array}{l} \gamma_1 = {}^{L}_{S}T_X, \quad \gamma_2 = {}^{L}_{S}T_Y, \quad \gamma_3 = {}^{L}_{S}T_Z \\ \gamma_4 = \alpha, \quad \gamma_5 = \beta, \quad \gamma_6 = \gamma \end{array}\right\} \tag{5.18}$$

Equation (5.5) can be written as

$$\begin{aligned} \theta_{P_i X_L} &= \mu_{P_i X_L} + \varepsilon_{\theta_{P_i X_L}} \\ \theta_{P_i Y_L} &= \mu_{P_i Y_L} + \varepsilon_{\theta_{P_i Y_L}} \end{aligned} \tag{5.19}$$

where $\mu_{P_i X_L}$ and $\mu_{P_i Y_L}$ are the expectation functions [5.5] of the scanning coordinates. Compared with Eq. (5.5), the expectation functions are as followings.

$$\mu_{P_i X_L} = tan^{-1}\left(\frac{y_{P_i L}}{z_{P_i L}}\right), \quad \mu_{P_i Y_L} = tan^{-1}\left(\frac{x_{P_i L}}{\sqrt{y_{P_i L}^2 + z_{P_i L}^2} + dl}\right) \tag{5.20}$$

An initial value for the parameter vector is assumed to be $\{\gamma^*\}$ which is not far from the true value. Taking the Taylor series expansion of Eq. (5.20) about $\{\gamma\}$ and putting it into Eq. (5.19), one will have the following if only the linear term is kept.

$$\theta_{P_i X_L} = \mu_{P_i X_L}(\{\gamma^*\}) + \sum_{i=1}^{6} \frac{\partial \mu_{P_i X_L}(\{\gamma^*\})}{\partial \gamma_i} \delta\gamma_i + \varepsilon_{\theta_{P_i X_L}}$$
$$\theta_{P_i Y_L} = \mu_{P_i Y_L}(\{\gamma^*\}) + \sum_{i=1}^{6} \frac{\partial \mu_{P_i Y_L}(\{\gamma^*\})}{\partial \gamma_i} \delta\gamma_i + \varepsilon_{\theta_{P_i Y_L}} \quad (5.21)$$

The above equation can be written as a matrix form

$$\{F_{P_i}\} = [J_{P_i}]\{\delta\gamma\} + \{\varepsilon_{P_i}\}_\theta \quad (5.22)$$

where $\{\varepsilon_{P_i}\}_\theta$ is defined in Eq. (5.14) and

$$\{F_{P_i}\} = \begin{Bmatrix} \theta_{P_i X_L} - \mu_{P_i X_L}(\{\gamma^*\}) \\ \theta_{P_i Y_L} - \mu_{P_i Y_L}(\{\gamma^*\}) \end{Bmatrix} \quad (5.23)$$

$$[J_{P_i}] = \begin{bmatrix} \frac{\partial \mu_{P_i X_L}}{\partial \gamma_1} & \frac{\partial \mu_{P_i X_L}}{\partial \gamma_2} & \frac{\partial \mu_{P_i X_L}}{\partial \gamma_3} & \frac{\partial \mu_{P_i X_L}}{\partial \gamma_4} & \frac{\partial \mu_{P_i X_L}}{\partial \gamma_5} & \frac{\partial \mu_{P_i X_L}}{\partial \gamma_6} \\ \frac{\partial \mu_{P_i Y_L}}{\partial \gamma_1} & \frac{\partial \mu_{P_i Y_L}}{\partial \gamma_2} & \frac{\partial \mu_{P_i Y_L}}{\partial \gamma_3} & \frac{\partial \mu_{P_i Y_L}}{\partial \gamma_4} & \frac{\partial \mu_{P_i Y_L}}{\partial \gamma_5} & \frac{\partial \mu_{P_i Y_L}}{\partial \gamma_6} \end{bmatrix} \quad (5.24)$$

$$\{\delta\gamma\} = \{\delta\gamma_1,\ \delta\gamma_2,\ \delta\gamma_3,\ \delta\gamma_4,\ \delta\gamma_5,\ \delta\gamma_6\}^T \quad (5.25)$$

Matrix $[J_{P_i}]$ is evaluated at $\{\gamma\} = \{\gamma^*\}$. The actual expressions of the elements in matrix $[J_{P_i}]$ are given in appendix A. Linearizing Eq. (5.19) for all N registration points and writing the results in matrix, one will have the following equation.

$$\{F\} = [J]\{\delta\gamma\} + \{\varepsilon\}_\theta \quad (5.26)$$

where

$$\{F\}=\begin{Bmatrix}\{F_{P_1}\}\\ \vdots \\ \{F_{P_N}\}\end{Bmatrix},\ [J]=\begin{bmatrix}[J_{P_1}]\\ \vdots \\ [J_{P_N}]\end{bmatrix},\ \{\varepsilon\}_\theta=\begin{Bmatrix}\{\varepsilon_{P_1}\}_\theta\\ \vdots \\ \{\varepsilon_{P_N}\}_\theta\end{Bmatrix} \tag{5.27}$$

The least squares solution of the increment $\{\delta\gamma\}$ in Eq. (5.26) is

$$\{\delta\gamma\}=\left([J]^T[J]\right)^{-1}[J]^T\{F\} \tag{5.28}$$

The improved solution for the parameters are as followings

$$\{\gamma**\}=\{\gamma*\}+\{\delta\gamma\} \tag{5.29}$$

This procedure may be repeated until a converged solution is obtained.

5.3 Inferences about the nonlinear regressive models

The inferences about the nonlinear regressive models will be made exclusively about the inverse model with the rotation matrix being represented by three Euler angles. The reason is that there is no constraint among the pose parameters. The results of the inferences about a general linear regressive model will be applied to the inverse model through the linear approximation technique. Therefore, the linear regressive model will be reviewed before the inferences about the nonlinear models are made.

5.3.1 Review of general linear regression

5.3.1.1 The model and the assumptions of a general linear regression

A general linear regressive model can be written as [5.6, 5.8-5.9]

$$Y_i=x_{i1}\beta_1+x_{i2}\beta_2+...+x_{iM}\beta_M+\varepsilon_i \tag{5.30}$$

where:

Y is the response variable and Y_i is the observation or measurement for the ith case;

$x_1, x_2, ..., x_M$ are the regressor variables and $x_{i1}, x_{i2}, ..., x_{iM}$ are the known values for the ith case (in some applications, $x_{i1} \equiv 1$);

$\beta_1, \beta_2, ..., \beta_M$ are the M parameters to be determined;

ε is the error in the measurements and ε_i is the error for the ith case.

Model (5.30) can be written in matrix form for all N cases

$$\{Y\} = [X]\{\beta\} + \{\varepsilon\} \tag{5.31}$$

where

$$\{Y\} = \{Y_1 \ Y_2 \ ... \ Y_N\}^T \tag{5.32}$$

$$\{\beta\} = \{\beta_1 \ \beta_2 \ ... \ \beta_M\}^T \tag{5.33}$$

$$\{\varepsilon\} = \{\varepsilon_1 \ \varepsilon_2 \ ... \ \varepsilon_N\}^T \tag{5.34}$$

$$[X]_{ij} = x_{ij} \quad \text{for } (i=1, 2, .., N \text{ and } j=1, 2, ..., M) \tag{5.35}$$

There are basically two assumptions for model (5.31). The relationship between the response variable and the regressor variables is assumed to be correctly expressed in the form of Eq. (5.30). The errors are assumed to be identically and independently distributed normal random variables with zero means and finite variance σ^2, i.e.,

$$E[\{\varepsilon\}] = \{0\}, \quad Var[\{\varepsilon\}] = \sigma^2[I] \tag{5.36}$$

With Eq. (5.36), the random response vector $\{Y\}$ is also independent normal random variable with

$$E[\{Y\}] = [X]\{\beta\}, \quad Var[\{Y\}] = \sigma^2[I] \tag{5.37}$$

Because $[X]\{\beta\}$ is the expectation of $\{Y\}$, it is sometimes called the expectation function. It may be written as

$$\{\mu\} = [X]\{\beta\} \tag{5.38}$$

Matrix [X] is also called the derivative matrix since element $[X]_{ij}$ is the derivative of expectation function μ_i with respect to parameter β_j.

5.3.1.2 The Least squares estimator

A hat is used to denote the estimated parameters. The least squares estimator for the parameters in Eq. (5.31) is

$$\left\{\hat{\beta}\right\} = \left([X]^T[X]\right)^{-1}[X]^T\{Y\} \tag{5.39}$$

If the assumptions about the errors are held, the least squares estimator is the same as the maximum likelihood estimator. The least squares estimator is unbiased, consistent, sufficient, and has minimum variance among the unbiased linear estimators [5.9]. Thus, it is the best available estimator in practice [5.4].

5.3.1.3 Inferences about the general linear regressive model

There are several inference results for the linear regression [5.5, 5.9]. The most widely used are the sampling theory results which are presented here. They result from the least squares estimator.

The least squares estimator is normal distributed random variables with

$$E\left[\left\{\hat{\beta}\right\}\right] = \{\beta\},\ Var[\{\beta\}] = \sigma^2\left([X]^T[X]\right)^{-1} \tag{5.40}$$

In general, the variance σ^2 of the errors is not known. Its estimate

$$s^2 = \frac{\left\| \{Y\} - [X]\{\hat{\beta}\} \right\|^2}{N - M} \tag{5.41}$$

can be used to estimate σ^2.

The inferences about the general linear model include the inferences about the individual parameters, the inferences about all the parameters, the inferences about the expected response, and the inferences about the prediction of a response. The following are the details.

I). The inferences about the individual parameters

The inferences about the individual parameters include confidence interval estimation and hypothesis testing. The $100(1-\alpha)\%$ confidence interval for parameter β_k is

$$\hat{\beta}_k \pm s(\hat{\beta}_k) t(N - M;\ \alpha / 2) \tag{5.42}$$

where $t(N - M;\ \alpha / 2)$ is the upper $100(\alpha / 2)$ percentile of the Student t distribution with N-M degrees-of-freedom, and

$$s(\hat{\beta}_k) = s\sqrt{\left([X]^T[X]\right)^{-1}_{kk}} \tag{5.43}$$

In the above equation, s is defined in Eq. (5.41) and subscript kk means the kth diagonal element of matrix $\left([X]^T[X]\right)^{-1}$.

The hypothesis test are conducted to check if parameter β_k is statistically equal to, or larger than, or less than, a specific value β_{k0}. If the equality is to be checked, the two alternatives are

$$\left.\begin{array}{l} H_0:\ \beta_k = \beta_{k0} \\ H_a:\ \beta_k \neq \beta_{k0} \end{array}\right\} \tag{5.44}$$

The statistic

$$t^* = \frac{\hat{\beta}_k - \beta_{k0}}{s(\hat{\beta}_k)} \tag{5.45}$$

can be used to perform the test. The decision rule with this statistic for significance level α is

$$\text{if } |t^*| > t(N-M;\ \alpha/2), \text{ reject } H_0$$

II). The inferences about all the parameters

The inferences about all the parameters include confidence region and simultaneous confidence interval. The $100(1-\alpha)\%$ confidence region for $\{\beta\}$ is given by

$$\left(\{\beta\}-\{\hat{\beta}\}\right)^T [X]^T [X] \left(\{\beta\}-\{\hat{\beta}\}\right) \le Ms^2 F(M, N-M;\ \alpha) \tag{5.46}$$

where $F(M, N-M;\ \alpha)$ is the upper 100α percentile of the F distribution with M and N-M degrees-of-freedom.

The simultaneously $100(1-\alpha)\%$ confidence interval for β_k are given by

$$\hat{\beta}_k \pm s(\hat{\beta}_k)\sqrt{MF(M, N-M;\ \alpha)} \tag{5.47}$$

III). The inference about the expected response

The $100(1-\alpha)\%$ confidence interval for the expected response at a given value of $\{x\}_0 = \{x_{01}\ x_{02}\ \ldots\ x_{0M}\}^T$ is

$$\{x\}_0^T \{\hat{\beta}\} \pm s(\hat{Y}_0) t(N-M;\ \alpha/2) \tag{5.48}$$

where

$$s(\hat{Y}_0) = s\sqrt{\{x\}_0^T \left([X]^T [X]\right)^{-1} \{x\}_0} \tag{5.49}$$

IV). The inferences about the prediction of a response

The $100(1-\alpha)\%$ confidence interval for the prediction of a response at a given value of $\{x\}_0 = \{x_{01}\ x_{02}\ \ldots\ x_{0M}\}^T$ is

$$\{x\}_0^T\left\{\hat{\beta}\right\} \pm s\left(\hat{Y}_0'\right)t(N-M;\ \alpha/2) \tag{5.50}$$

where

$$s\left(\hat{Y}_0'\right) = s\sqrt{1+\{x\}_0^T\left([X]^T[X]\right)^{-1}\{x\}_0} \tag{5.51}$$

Sometimes the confidence interval for the prediction of a response is called prediction interval. This dissertation will use the term prediction interval.

5.3.2 The inferences about the inverse model

5.3.2.1 The least squares estimator of a nonlinear regression

A nonlinear regressive model can be written as

$$Y_i = f\left(\{x\}_i,\ \{\gamma\}\right) + \varepsilon_i \tag{5.52}$$

where:

Y is the response variable and Y_i is the observation or measurements for ith case;

$\{x\}$ is the regressor variables and $\{x\}_i$ is the known values for the ith case;

$\{\gamma\}$ is the parameter vector to be determined;

$f\left(\{x\}_i,\ \{\gamma\}\right)$ is the expectation function which is a nonlinear function of parameters $\{\gamma\}$;

ε is the error in the measurements and ε_i is error for the ith case.

The parameters $\{\gamma\}$ can be obtained by the least squares method which minimizes

$$Q = \sum_{i=1}^{N} \varepsilon_i^2 \tag{5.53}$$

If the errors are identically and independently distributed normal random variables, i.e.,

$$E[\{\varepsilon\}] = \{0\}, \quad Var[\{\varepsilon\}] = \sigma^2[I] \tag{5.54}$$

the response variables $\{Y\}$ are also independently distributed normal random variables with

$$E[\{Y\}] = \{\mu\} = \{f(\{x\}, \{\beta\})\}, \quad Var[\{Y\}] = \sigma^2[I] \tag{5.55}$$

The least squares estimator $\{\hat{\gamma}\}$ is not a linear combination of the response vector$\{Y\}$ for the nonlinear regression. Thus, it does not have the properties of $\{\hat{\beta}\}$ in linear regression [5.4]. In general, $\{\hat{\gamma}\}$ is not normally distributed. It is biased for $\{\gamma\}$. And it does not have the minimum variance, either.

However, it has been shown that the least squares estimator $\{\hat{\gamma}\}$ has asymptotic normality [5.3]. Given the assumption of Eq. (5.54) and proper regularity conditions, for large N (sampling cases), it can be shown that [5.3]

$$\{\hat{\gamma}\} \sim N\left(\{\gamma\}, \sigma^2\left(\left[\hat{V}\right]^T\left[\hat{V}\right]\right)^{-1}\right) \tag{5.56}$$

where $\left[\hat{V}\right]$ is the derivative matrix evaluated at $\{\hat{\gamma}\}$ and

$$\left[\hat{V}\right]_{ij} = \frac{\partial \mu_i}{\partial \gamma_j} = \left.\frac{\partial f(\{x_i\}, \{\gamma\})}{\partial \gamma_j}\right|_{\{\gamma\}=\{\hat{\gamma}\}} \tag{5.57}$$

From another point of view, Eq. (5.56) is a linear approximation to the nonlinear model. By replacing matrix [X] with $\left[\hat{V}\right]$, one can obtain Eq. (5.56) from the results of the linear

regression. Thus, the inferences about a nonlinear regressive model can be made by analog to the linear regression.

In practice, it is difficult to say how large the sample size N should be for Eq. (5.56) to be held [5.4]. It depends on the nonlinear model itself.

5.3.2.2 The inferences about the inverse model by linear approximation

The linear approximation technique is used to derive the inference about the inverse model with rotation matrix represented by three Euler angles. Currently it is assumed that the linear approximation is valid. In the next section, its validity will be evaluated by analyzing the nonlinearity of the inverse model.

Once the least squares estimator $\{\hat{\gamma}\}$ is available, the estimation of error variance and the derivative matrix can be obtained. For the inverse model, the error variance estimate is

$$s_\theta^2 = \frac{\{\varepsilon\}_\theta^T \{\varepsilon\}}{2N-6} \tag{5.58}$$

Note that $\{\varepsilon\}_\theta$ is evaluated at $\{\gamma\} = \{\hat{\gamma}\}$. The derivative matrix [J] is defined in Eq. (5.27). It is denoted as $\left[\hat{J}\right]$ since it is evaluated at $\{\gamma\} = \{\hat{\gamma}\}$. The least squares estimator for the 6 pose parameters will have the asymptotic normal distribution

$$\{\hat{\gamma}\} \sim N\left(\{\gamma\}, \sigma^2\left(\left[\hat{J}\right]^T\left[\hat{J}\right]\right)^{-1}\right) \tag{5.59}$$

Analog to the linear regression, following inferences about the inverse model are made.

I). The inferences about individual parameters

The inferences about individual parameter include confidence interval estimation and hypothesis test. The $100(1-\alpha)\%$ confidence interval for parameter γ_k are

$$\hat{\gamma}_k \pm s(\hat{\gamma}_k) t(2N-6;\ \alpha/2) \tag{5.60}$$

where $t(2N-6;\ \alpha/2)$ is the upper $100(\alpha/2)$ percentile of the Student t distribution with $2N$-6 degrees-of-freedom, and

$$s(\hat{\gamma}_k) = s_\theta \sqrt{\left(\left[\hat{J}\right]^T\left[\hat{J}\right]\right)^{-1}_{kk}} \tag{5.61}$$

In the above equation, s_θ is defined in Eq. (5.58) and subscript kk means the kth diagonal element of matrix $\left(\left[\hat{J}\right]^T\left[\hat{J}\right]\right)^{-1}$.

The hypothesis tests are conducted to check if parameter γ_k is statistically equal to, or larger than, or less than, a specific value γ_{k0}. If the equality is to be checked, the two alternatives are

$$\left.\begin{array}{l} H_0:\ \gamma_k = \gamma_{k0} \\ H_a:\ \gamma_k \neq \gamma_{k0} \end{array}\right\} \tag{5.62}$$

The statistic

$$t^* = \frac{\hat{\gamma}_k - \gamma_{k0}}{s(\hat{\gamma}_k)} \tag{5.63}$$

can be used to perform the test. The decision rule with this statistic for significance level α is

$$\text{if } |t^*| > t(2N-6;\ \alpha/2), \text{ reject } H_0$$

II). The inferences about all parameters

The inferences about all the parameters include confidence region and simultaneous confidence interval. The $100(1-\alpha)\%$ confidence region for $\{\gamma\}$ is given by

$$\left(\{\gamma\}-\{\hat{\gamma}\}\right)^T\left[\hat{J}\right]^T\left[\hat{J}\right]\left(\{\gamma\}-\{\hat{\gamma}\}\right)\le 6s_\theta^2F(6,2N-6;\ \alpha) \tag{5.64}$$

where $F(6,2N-6;\ \alpha)$ is the upper 100α percentile of the F distribution with 6 and $2N$-6 degrees-of-freedom.

The simultaneously $100(1-\alpha)\%$ confidence interval for γ_k are given by

$$\hat{\gamma}_k \pm s(\hat{\gamma}_k)\sqrt{6F(6,2N-6;\ \alpha)} \tag{5.65}$$

III). The inference about the expected scanning coordinates

The $100(1-\alpha)\%$ confidence interval for the expected scanning coordinates at a given spatial point of $\{P_0\}=\left\{x_{P_0,S}\ \ y_{P_0,S}\ \ z_{P_0,S}\right\}^T$ are

$$\begin{aligned}&\hat{\mu}_{P_0,X_L} \pm s\left(\hat{\mu}_{P_0,X_L}\right)t(2N-6;\ \alpha/2)\\ &\hat{\mu}_{P_0,Y_L} \pm s\left(\hat{\mu}_{P_0,Y_L}\right)t(2N-6;\ \alpha/2)\end{aligned} \tag{5.66}$$

where $\hat{\mu}_{P_0,X_L}$ and $\hat{\mu}_{P_0,Y_L}$ are calculated from Eq. (5.20) by using the structural coordinates of $\{P_0\}$ and the estimated parameters $\{\hat{\gamma}\}$, and

$$\begin{aligned}s\left(\hat{\mu}_{P_0,X_L}\right)&=s_\theta\sqrt{\left\{v_{P_0,X_L}\right\}^T\left(\left[\hat{J}\right]^T\left[\hat{J}\right]\right)^{-1}\left\{v_{P_0,X_L}\right\}}\\ s\left(\hat{\mu}_{P_0,Y_L}\right)&=s_\theta\sqrt{\left\{v_{P_0,Y_L}\right\}^T\left(\left[\hat{J}\right]^T\left[\hat{J}\right]\right)^{-1}\left\{v_{P_0,Y_L}\right\}}\end{aligned} \tag{5.67}$$

The $\left\{v_{P_0,X_L}\right\}$ and $\left\{v_{P_0,Y_L}\right\}$ in Eq. (5.67) are the derivatives of the expectation function ($\hat{\mu}_{P_0,X_L}$ and $\hat{\mu}_{P_0,Y_L}$) with respect to the six pose parameters and evaluated at $\{\hat{\gamma}\}$, i.e.

$$\left\{v_{P_0,X_L}\right\}=\left.\frac{\partial \mu_{P_0,X_L}}{\partial\{\gamma\}}\right|_{\{\gamma\}=\{\hat{\gamma}\}}$$
$$\left\{v_{P_0,Y_L}\right\}=\left.\frac{\partial \mu_{P_0,Y_L}}{\partial\{\gamma\}}\right|_{\{\gamma\}=\{\hat{\gamma}\}} \tag{5.68}$$

IV). The inferences about the prediction of the scanning coordinates

The $100(1-\alpha)\%$ prediction interval for the prediction of the scanning coordinates at a given spatial point of $\{P_0\}=\left\{x_{P_0,S}\ \ y_{P_0,S}\ \ z_{P_0,S}\right\}^T$ is

$$\hat{\mu}_{P_0,X_L} \pm s\left(\hat{\mu}'_{P_0,X_L}\right)t(2N-6;\ \alpha/2)$$
$$\hat{\mu}_{P_0,Y_L} \pm s\left(\hat{\mu}'_{P_0,Y_L}\right)t(2N-6;\ \alpha/2) \tag{5.69}$$

where $\hat{\mu}_{P_a,X_L}$ and $\hat{\mu}_{P_a,Y_L}$ are calculated from Eq. (5.20) by using the structural coordinates of $\{P_a\}$ and the estimated parameters $\{\hat{\gamma}\}$, and

$$s\left(\hat{\mu}'_{P_0,X_L}\right)=s_\theta\sqrt{1+\left\{v_{P_0,X_L}\right\}^T\left(\left[\hat{J}\right]^T\left[\hat{J}\right]\right)^{-1}\left\{v_{P_0,X_L}\right\}}$$
$$s\left(\hat{\mu}'_{P_0,Y_L}\right)=s_\theta\sqrt{1+\left\{v_{P_0,Y_L}\right\}^T\left(\left[\hat{J}\right]^T\left[\hat{J}\right]\right)^{-1}\left\{v_{P_0,Y_L}\right\}} \tag{5.70}$$

The inferences made about a nonlinear regression model by the linear approximation are sometimes extremely misleading [5.5]. To verify the validity of those inferences, one definitely needs to evaluate the nonlinearity of that model.

5.4 The nonlinearity evaluation of the nonlinear models

In the last section, inferences about the inverse model were derived based on the linear approximation. If the number of registration points is large enough, those inferences will be valid. However, in the real measurements, the number of the registration point is not very large. In the minimum case, there may be only four points. In another case, nine points may be used. When the N is small, the validity of those inferences will depend on the level of nonlinearity of the inverse model.

The measures of the nonlinearity of a nonlinear regressive model are based on the work of Bates and Watts [5.10]. Their work is referred by several books on the nonlinear regression [5.2-5.5]. By using some concepts in the differential geometry, they extended Beale's pioneering work [5.11] and developed useful measures of nonlinearity based on the notion of curvature. In this section, their work will be derived and applied to the inverse model. To better understand the concept of the curvature, the geometry of the least squares method is presented first.

5.4.1 The geometry of the least squares

The geometry of the least squares method is reviewed for both linear and nonlinear regression. After the review, the two assumptions in the linear approximation are discussed.

5.4.1.1 The geometry of the linear regression

For a linear regressive model

$$\{Y\}=[X]\{\beta\}+\{\varepsilon\} \tag{5.71}$$

its parameters can be estimated by the least squares method which minimizes the sum of the squared errors

$$Q=\sum_{i=1}^{N}\varepsilon_i^2=\left\|\{Y\}-[X]\{\beta\}\right\|^2=\left\|\{Y\}-\{\mu\}\right\|^2 \tag{5.72}$$

Equation (5.72) implies that the sum of the squared errors is the squared distance between the response vector $\{Y\}$ and the expected response vector $[X]\{\beta\}$. This relates the subject of linear regression to the Euclidean geometry. In the N-dimensional response space, the response vector $\{Y\}$ is a fixed point. For a given value of the parameters $\{\beta\}$, the expected response vector is also a point in that space. However, this point moves as the parameters vary. The possible expected response vectors $\{\mu(\{\beta\})\}$ form a M-dimensional expectation plane. This expectation plane is also called solution locus [5.11] because it corresponds to the possible values of parameters $\{\beta\}$ which are the solution of the linear regression model. Geometrically the minimum Q is the squared shortest distance between the response vector and the expectation plane. By drawing a line from the response vector and making it perpendicular to the expectation plane, one can obtain the least squares estimator $\{\hat{\beta}\}$ for the model parameters. Actually, the parameters corresponding to the intersection point of the line with the expectation plane are the desired solution. The followings are two examples to illustrate those geometrical properties.

I). One parameter model

The one parameter model may have this form

$$Y_i = x_{i1}\beta_1 + \varepsilon_i \tag{5.73}$$

Two responses are obtained which form a two-dimensional response space. The regressors and the corresponding responses are: (i) $x_{11} = 1$, $y_1 = 0.9$, (ii) $x_{21} = 2$, $y_2 = 2.2$. These data are simulated data. Figure 5.1 (a) shows the parameter space which is one-dimensional space. The equally-spaced five marks are for β_1 =0, 0.5, 1, 1,5 and 2. In Fig 5.1 (b), the two-dimensional response space are shown. The respect vector $\{Y\}$ is shown along with the expectation line. The 'o' in this plot is vector $\{Y\}$. The expectation line has the form ($\mu_1 = \beta_1$, $\mu_2 = 2\beta_1$). When the parameter varies from 0 to 2, the expectation line is obtained. The five stars on that line are corresponding to β_1 =0, 0.5, 1, 1.5 and 2. It can be seen that the five stars are equally spaced.

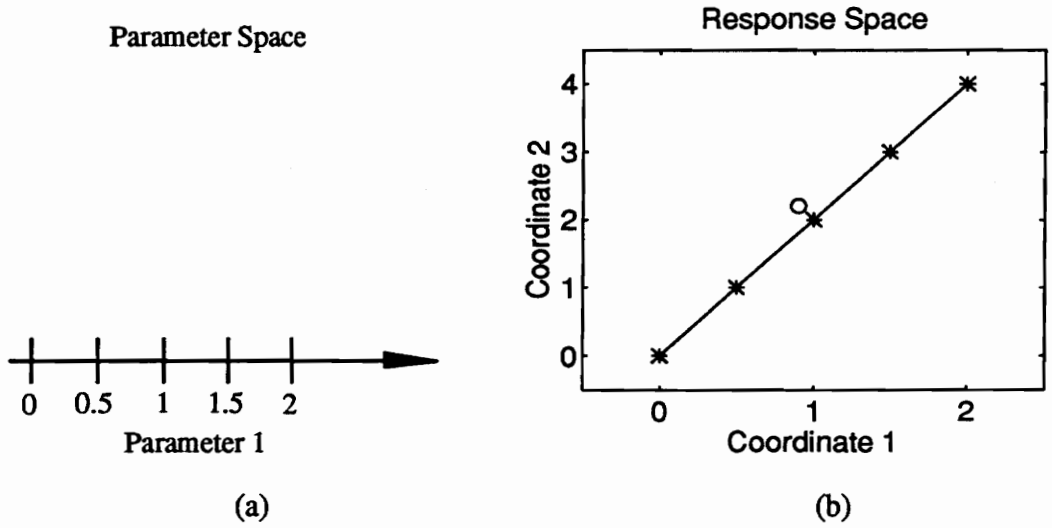

Figure 5.1 Geometry of linear regression with one parameter and two responses

II). Two parameters model

The sine wave fitter [5.12] is a two parameter linear model

$$Y_i = \beta_1 \cos \omega t_i + \beta_2 \sin \omega t_i + \varepsilon_i \tag{5.74}$$

Comparing to the general model, one can seen that

$$x_{i1} = \cos \omega t_i, \quad x_{i2} = \sin \omega t_i \tag{5.75}$$

where ω is the circle frequency of the signal. Three responses are obtained for this example. The regressors and the corresponding responses are: (i) $x_{11} = 1.0000$, $x_{12} = 0.0000$, $y_1 = 0.7000$; (ii) $x_{21} = -0.8090$, $x_{22} = 0.5878$, $y_2 = -0.1500$; (iii) $x_{31} = 0.3090$, $x_{32} = -0.9511$, $y_3 = -0.4500$. These data are simulated data for which $\omega = 2\pi$ and t={0, 0.4, 0.8) are used. In figure 5.2 (a), the two-dimensional parameter space is shown. The grid lines are called parameter lines which are obtained by changing one parameter while the other is kept constant. The vertical (solid) lines are called β_1 line while the horizontal (dotted) lines are called β_2 lines. The β_1 lines are parallel and equally spaced. So are the β_2 lines. Figure 5.2 (b) is the three-dimensional response space. The response vector $\{Y\}$ is shown along with the expectation plane. The "o" in this plot is vector $\{Y\}$. The expectation plane is obtained by varying the parameters in the expected vector in Eq. (5.76)

$$\left.\begin{aligned} \mu_1 &= \beta_1 \\ \mu_2 &= -0.8090\,\beta_1 + 0.5878\,\beta_2 \\ \mu_3 &= 0.3090\,\beta_1 - 0.9511\,\beta_2 \end{aligned}\right\} \tag{5.76}$$

The two sets of lines (solid and dotted) on the expectation plane are corresponding to the parameter lines in the parameter space. The lines in each set are straight, parallel, and equally spaced.

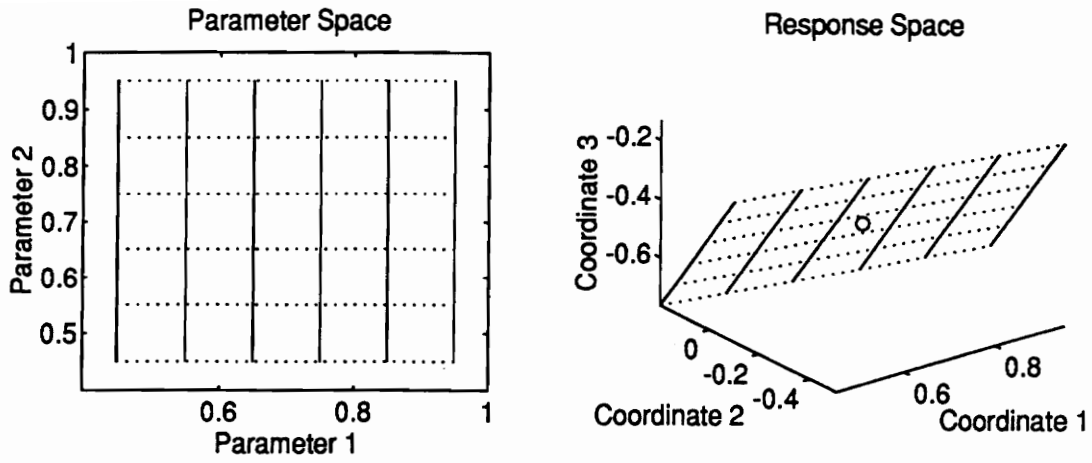

(a) (b)

Figure 5.2 Geometry of linear regression with two parameters and three responses

What has seen from above examples is true for all linear regressive models. That is, for any linear model, parameter lines (straight parallel equispaced lines) in the parameter space map to straight parallel equispaced lines on the expectation plane in the response space. From this, one can see that rectangles in one plane map to parallelepipeds in the other plane, and circles and spheres in one space map to ellipses or ellipsoids in the other space [5.5].

5.4.1.2 The geometry of the nonlinear regression

For a nonlinear regressive model

$$\{Y\} = \left\{f(\{x\},\{\gamma\})\right\} + \{\varepsilon\} = \{\mu\} + \{\varepsilon\} \tag{5.77}$$

the least squares estimator for the parameters are obtained when the summation of the squared error

$$Q = \sum_{i=1}^{N} \varepsilon_i^2 = \left\| \{Y\} - \{\mu\} \right\|^2 \tag{5.78}$$

is minimized. The summation of the squared errors is the squared distance from the response vector to the expected vector. In the N-dimensional response space, the response vector is a fixed point. However, the M-dimensional expectation surface formed by all possible expected vectors $\left\{\mu(\{\gamma\})\right\}$ is not a plane any more. It is a curved surface. The minimum Q is the squared shortest distance from the response vector to the expectation surface. The least squares estimator is the parameters corresponding to the point on the expectation surface which is closest to the response vector. The following two examples are used to illustrate the geometry of the nonlinear regressive model.

I). One parameter model

The one parameter model may have this form

$$y_i = 1 - e^{-t_i \gamma_1} + \varepsilon_i \tag{5.79}$$

Two responses are obtained for this example. The regressors and the corresponding response are: (i) $t_1 = 0.4,\ y_1 = 0.57$; (ii) $t_2 = 1.5,\ y_2 = 0.93$. Figure 5.3 (a) shows the one-dimensional parameter space. The marks are for γ_1=1, 1.5, 2, 2.5, and 3. Figure 5.3 (b) shows the three-dimensional response space. The response vector $\{Y\}$ is shown along with the expectation curve. The "o" in this plot is vector $\{Y\}$. The curve is obtained by varying the parameters γ_1 in

$$\mu_1 = 1 - e^{-0.4\gamma_1},\quad \mu_2 = 1 - e^{-1.5\gamma_1} \tag{5.80}$$

The stars on the curve are corresponding to the parameter values in Fig. 5.3 (a). It can be seen that the stars are not equally spaced. This feature differs from the linear regression.

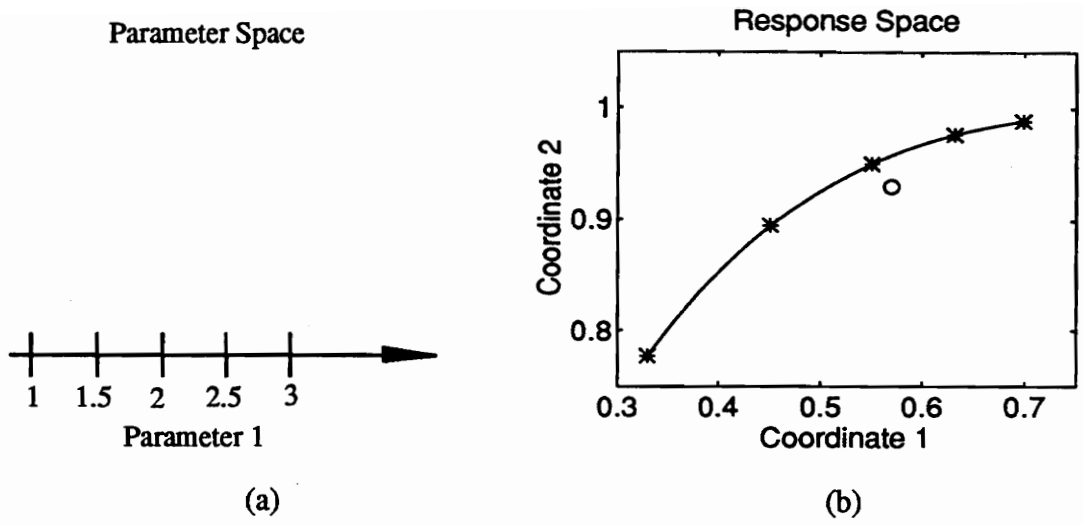

(a) (b)

Figure 5.3 Geometry of nonlinear regression with one parameter and two responses

II). Two parameters model

The sine wave fitter model can be written as

$$y_i = \gamma_1 \sin(\omega t_i + \gamma_2) \tag{5.81}$$

This model can be transferred to the linear version (5.73) through reparameterization. Three responses are obtained. The regressors and the corresponding response are: (i) $t_1 = 0.00,\ y_1 = 0.70$; (ii) $t_2 = 0.40,\ y_2 = -0.15$; (iii) $t_3 = 0.80,\ y_3 = -0.45$. The simulated data is for $\omega = 2\pi$. Figure 5.4 (a) shows the two-dimensional parameter space. The horizontal and vertical lines are the γ_2 and γ_1 parameter lines, respectively. Figure 5.4 (b) is the three-dimensional response space. The response vector is shown along with the expectation surface. This surface is obtained by varying the parameters γ_1 and γ_2 in following

$$\left.\begin{aligned}\eta_1 &= \gamma_1 \sin(\gamma_2)\\ \eta_2 &= \gamma_1 \sin(0.8\pi + \gamma_2)\\ \eta_3 &= \gamma_1 \sin(1.6\pi + \gamma_2)\end{aligned}\right\} \qquad (5.82)$$

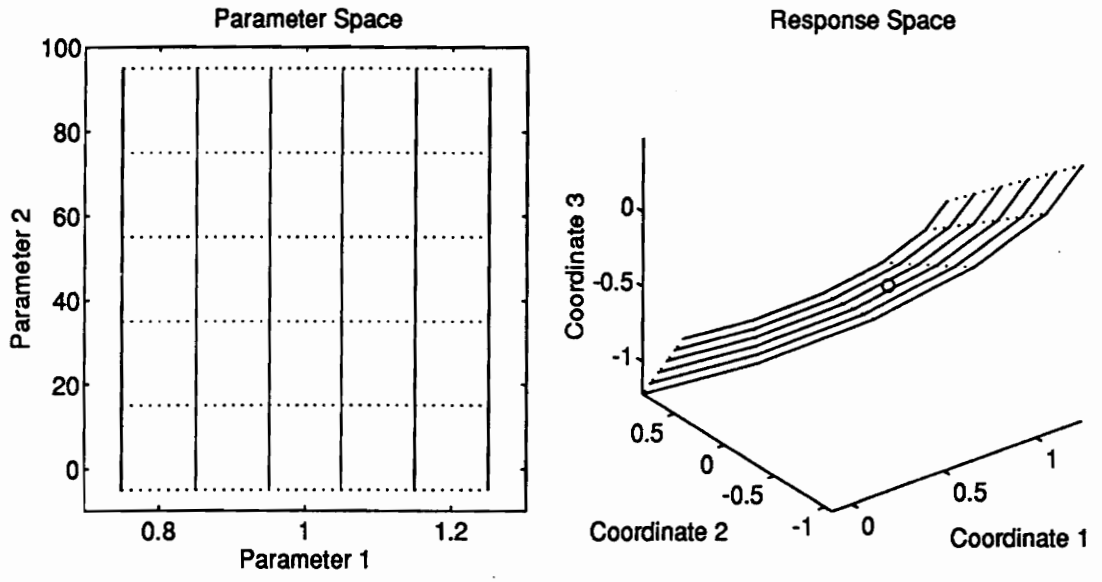

(a) (b)

Figure 5.4 Geometry of nonlinear regression with two parameters and three responses

The two sets of line (solid and dotted) on that surface are corresponding to the parameter lines in the parameter space. Those lines are not parallel. Nor are they equispaced. The solid lines are curves. The dotted lines (corresponding to the γ_2 parameter lines) are straight lines. This is because that the expectation function is a linear function of parameter γ_1. If it were a nonlinear function, those lines would also be curves.

What has shown for those examples is true for a general nonlinear model. That is, for any nonlinear model, the expectation surface is the M-dimensional curved surface in the N-

dimensional response space. Parameter lines in the parameter space map to curves on the expectation surface in the response space. Those curves are, in general, not parallel. Nor are they equally spaced for nonlinear functional relationship between a parameter and the expectation function.

5.4.1.3 Two assumptions of the linear approximation

The linear approximation to the expectation function at the vicinity of $\{\hat{\gamma}\}$ is

$$\{\mu\} = \left\{\mu(\{\hat{\gamma}\})\right\} + \left[\hat{V}\right]\{\delta\gamma\} \tag{5.83}$$

In using this approximation for inferences, two things are assumed about the local behavior of the expectation surface. The first one is the planar assumption: the expectation surface is locally replaced by the tangent plane. The second is the uniform coordinate assumption: straight parallel equispaced lines in the parameter space map into straight parallel equispaced lines in the expectation surface. Those two assumptions are not tenable if the nonlinearity of the model is high at $\left\{\mu(\{\hat{\gamma}\})\right\}$.

5.4.2 Curvature measures of a nonlinear regression model

In order to evaluate the effectiveness of the linear approximation, the nonlinearity of a nonlinear regressive model has to be measured. Bates and Watts [5.10] developed two curvature measurements. The intrinsic curvature can be used to determine how planar the expectation surface is. The parameter-effects curvature can be used to determine how uniform the parameter lines are on the tangent plane. If both curvatures are small, the

linear approximation will be tenable. Most of the materials in this section are based on the work of Bates and Watts [5.10].

5.4.2.1 The velocity and the acceleration vector

In the linear model, the second and high order derivatives of the expectation function with respect to the parameters are zero. It is natural extension to measure the nonlinearity of a nonlinear model by investigating the second-order derivatives of the expectation function with respect to the parameters.

For the nonlinear model shown in Eq. (5.73), the first-order derivatives of the expectation function with respect to parameters is an N by M matrix with elements

$$[V]_{ij} = \frac{\partial f(\{x\}_i, \{\gamma\})}{\partial \gamma_j} \quad \text{for } (i=1, 2, ..., N, \text{ and } j=1, 2, ..., M) \tag{5.84}$$

Matrix $[V]$ can be regarded as consisting of M vectors $\{V\}_j$, j=1, 2, ..., M.

The second-order derivative of the expectation function with respect to the parameters is an N by M by M array with elements

$$\left[\dot{V}\right]_{ijk} = \frac{\partial^2 f(\{x\}_i, \{\gamma\})}{\partial \gamma_j \partial \gamma_k} \quad \text{for } (i=1, 2, ..., N, j, k=1, 2, ..., M) \tag{5.85}$$

Each face (referred by index i) is a complete M by M second-order derivative matrix of the ith element of $\{\mu\}$ with respect to parameters $\{\gamma\}$. The second-order derivative array may be regarded as consisting of M by M vectors $\left\{\dot{V}\right\}_{jk}$, j, k=1, 2, ..., M.

The vectors $\{V\}_j$ can be called velocity vectors because they present the rate of change of $\{\mu\}$ with respect to each parameter. Similarly, the vectors $\left\{\dot{V}\right\}_{jk}$ can be called acceleration vectors because they present the rate of change of velocity with respect to each parameter. Note that the velocity vector $\{V\}_j$ is not the velocity measured by the SLDV for the vibrating structure. The reason for using the term "velocity" is to comply with the terminology used in the field of the nonlinear regression.

5.4.2.2 Derivatives in an arbitrary direction

The velocity matrix $[V]$ and acceleration array $\left\lfloor \dot{V} \right\rfloor$ only provide the information for the expectation surface corresponding to the change along the directions of the parameter axes in the parameter space. The velocity and acceleration near $\{\hat{\gamma}\}$ in an arbitrary direction $\{h\}$ in the parameter space is of interest. They can be measured by introducing a scale λ and letting

$$\{\gamma\} = \{\hat{\gamma}\} + \lambda\{h\} \tag{5.86}$$

where $\{h\}$ is a direction vector. Above equation is a straight line in the parameter space. Its mapping $\left\{\mu\left(\{\hat{\gamma}\} + \lambda\{h\}\right)\right\}$ on the expectation surface is a curve through $\left\{\mu\left(\{\hat{\gamma}\}\right)\right\}$. The velocity and acceleration of that curve at $\{\hat{\gamma}\}$ will be corresponding to the change of the expectation surface along the arbitrary direction $\{h\}$ in the parameter space. This velocity and acceleration may be shown to be [5.10]

$$\begin{aligned} \left\{\dot{\mu}_{\{h\}}\right\} &= [V]\{h\} \\ \left\{\ddot{\mu}_{\{h\}}\right\} &= \{h\}^T\left\lfloor \dot{V} \right\rfloor\{h\} \end{aligned} \tag{5.87}$$

The N by 1 acceleration vector is obtained in this way

$$\ddot{\mu}_{\{h\},i} = \{h\}^T \left\lfloor \dot{V} \right\rfloor_i \{h\} \tag{5.88}$$

where $\left\lfloor \dot{V} \right\rfloor_i$ is a M by M matrix. It is the ith face of the N by M by M array $\left\lfloor \dot{V} \right\rfloor$. It can be seen that the velocity and acceleration of that curve at $\{\hat{y}\}$ are the linear combination of the velocity and acceleration vectors, respectively. It is clear that $\left\{\ddot{\mu}_{\{h\}}\right\}$ is a function of the direction vector $\{h\}$. In one direction, it may be small. It another direction, it may be large.

The acceleration $\left\{\ddot{\mu}_{\{h\}}\right\}$ can be written as two components

$$\left\{\ddot{\mu}_{\{h\}}\right\} = \left\{\ddot{\mu}_{\{h\}}\right\}^{PE} + \left\{\ddot{\mu}_{\{h\}}\right\}^{IN} \tag{5.89}$$

where $\left\{\ddot{\mu}_{\{h\}}\right\}^{PE}$ is the component in the tangent plane. It determines the change in direction and magnitude of the $\left\{\dot{\mu}_{\{h\}}\right\}$ in the tangent plane. $\left\{\ddot{\mu}_{\{h\}}\right\}^{IN}$ is the component normal to the tangent plane. It determines the change in direction of the $\left\{\dot{\mu}_{\{h\}}\right\}$ normal to the tangent plane.

5.4.2.3 Relative curvatures

The accelerations are the indictors of the nonlinearity. However, they are not useful since they depend on the scaling (unit) of the measured data and the parameters. To eliminate this dependence, the accelerations are converted to the curvatures. The curvature in direction $\{h\}$ at a point is defined as the ratio of the length of the acceleration vector to the squared length of the tangent vector, i.e.,

$$c_{\{h\}} = \frac{\left\| \left\{ \ddot{\mu}_{\{h\}} \right\} \right\|}{\left\| \left\{ \dot{\mu}_{\{h\}} \right\} \right\|^2} \tag{5.90}$$

The tangent component $\left\{ \ddot{\mu}_{\{h\}} \right\}^{PE}$ of the acceleration vector, which is caused by model parameterization, can be converted to a parameter-effects curvature

$$c_{\{h\}}^{PE} = \frac{\left\| \left\{ \ddot{\mu}_{\{h\}} \right\}^{PE} \right\|}{\left\| \left\{ \dot{\mu}_{\{h\}} \right\} \right\|^2} \tag{5.91}$$

This curvature depends on the particular parameterization. If it is too large, the parameter lines on the expectation surface are not uniform. Thus, the uniform coordinate assumption will not be acceptable.

The normal component $\left\{ \ddot{\mu}_{\{h\}} \right\}^{IN}$ of the acceleration can be converted to an intrinsic curvature

$$c_{\{h\}}^{IN} = \frac{\left\| \left\{ \ddot{\mu}_{\{h\}} \right\}^{IN} \right\|}{\left\| \left\{ \dot{\mu}_{\{h\}} \right\} \right\|^2} \tag{5.92}$$

Geometrically, this curvature is the inverse of the radius of the circle that best approximate the solution locus in the direction of $\left\{ \dot{\mu}_{\{h\}} \right\}$ at $\{\gamma\}$. This curvature is a property of the solution locus and it is the intrinsic property of the expectation surface. That is the reason why it is called intrinsic curvature. If this curvature is too large, the planar assumption will not be acceptable.

The curvatures $c_{\{h\}}^{PE}$ and $c_{\{h\}}^{IN}$ are measured in unit of 1/response. To eliminate this dependence and to assess the effect of the nonlinearity on inference, those curvatures are converted to standardized relative curvatures $\eta_{\{h\}}^{PE}$ and $\eta_{\{h\}}^{IN}$ by dividing the response and model function by the standard radius

$$\rho = s\sqrt{M} \tag{5.93}$$

since in the linear regression, the $100(1-\alpha)\%$ confidence region (see Eq. (5.46)) has a radius $\rho\sqrt{F(M,N-M;\ \alpha)}$. Equations (5.91) and (5.92) shows that dividing the response and model function by a factor will multiply the curvatures by the same factor, i.e.,

$$\eta_{\{h\}}^{PE} = \rho c_{\{h\}}^{PE}, \quad \eta_{\{h\}}^{IN} = \rho c_{\{h\}}^{IN} \tag{5.94}$$

The relative curvatures will also vary with the direction $\{h\}$. The maximum relative curvatures

$$\eta_{max}^{PE} = \max_{\{h\}} \rho \frac{\left\| \left\{ \ddot{\mu}_{\{h\}} \right\}^{PE} \right\|}{\left\| \left\{ \dot{\mu}_{\{h\}} \right\} \right\|^2} \tag{5.95}$$

$$\eta_{max}^{IN} = \max_{\{h\}} \rho \frac{\left\| \left\{ \ddot{\mu}_{\{h\}} \right\}^{IN} \right\|}{\left\| \left\{ \dot{\mu}_{\{h\}} \right\} \right\|^2} \tag{5.96}$$

can be obtained by changing the direction vector $\{h\}$.

The derived formulas can be used to calculate the parameter-effects and intrinsic curvatures. However, the procedure is not simple since the tangent and normal components of the acceleration need to be determined. Bates and Watts [5.10] developed an efficient procedure for calculating those curvatures. This procedure will be presented in the appendix B of this dissertation.

5.4.2.4 Statistical significance of the relative curvatures

By the linear approximation, the $100(1-\alpha)\%$ confidence region for the parameters $\{\gamma\}$ in a nonlinear regression model is

$$\left(\{\gamma\}-\{\hat{\gamma}\}\right)^T\left[\hat{V}\right]^T\left[\hat{V}\right]\left(\{\gamma\}-\{\hat{\gamma}\}\right) \le Ms^2F(M,N-M;\ \alpha) \tag{5.97}$$

After dividing the response and model function by the standard radius, the above equation becomes

$$\left(\{\gamma\}-\{\hat{\gamma}\}\right)^T\left[\frac{\hat{V}}{\rho}\right]^T\left[\frac{\hat{V}}{\rho}\right]\left(\{\gamma\}-\{\hat{\gamma}\}\right) \le F(M,N-M;\ \alpha). \tag{5.98}$$

From the above equation, it can be seen that the value $1/\sqrt{F(M,N-M;\ \alpha)}$ may be regarded as the curvature of the $100(1-\alpha)\%$ confidence region of parameters $\{\gamma\}$ for the scaled data.

To determine the impact of the nonlinearity on the inferences, the maximum relative curvatures may be compared to $1/\sqrt{F(M,N-M;\ \alpha)}$. It has been pointed out [5.3-5.4, 5.10] that if η_{max}^{PE} is less than $1/\left(2\sqrt{F(M,N-M;\ \alpha)}\right)$, the uniform coordinate assumption is tenable over the region of interest. Similarly, if η_{max}^{IN} is less than $1/\left(2\sqrt{F(M,N-M;\ \alpha)}\right)$, the solution locus is sufficiently flat over the confidence region disc and hence the planar assumption is acceptable. Since both maximum relative curvatures are compared to $1/\left(2\sqrt{F(M,N-M;\ \alpha)}\right)$, this value may be defined as the curvature criterion (*CC*), i.e.

$$CC=1/\left(2\sqrt{F(M,N-M;\ \alpha)}\right) \tag{5.99}$$

5.4.2.5 Examples of the nonlinearity evaluation

The nonlinearity of the two nonlinear regression examples presented in section **5.4.1.2** can be evaluated by using the curvatures.

I). One parameter model

The model of Eq. (5.79) with the given data has the following least squares estimates

$$\hat{\gamma}_1 = 2.0555,\ s = 0.0260 \tag{5.100}$$

Since there is only one parameter, the derivative matrices are reduced to one vector. From Eq. (5.80), the velocity and acceleration vectors are found as

$$\{\hat{V}\}_1 = \begin{Bmatrix} 0.1758 \\ 0.0687 \end{Bmatrix},\quad \{\hat{\dot{V}}\}_{11} = \begin{Bmatrix} -0.0703 \\ -0.1031 \end{Bmatrix} \tag{5.101}$$

In the parameter space, there is only one direction vector, i.e., the direction along the parameter axis. Thus

$$\{\dot{\mu}\} = \begin{Bmatrix} 0.1758 \\ 0.0687 \end{Bmatrix},\quad \{\ddot{\mu}\} = \begin{Bmatrix} -0.0703 \\ -0.1031 \end{Bmatrix} \tag{5.102}$$

The tangent plane is reduced to a tangent line. The direction of the tangent line is the direction of velocity vector. The acceleration can be projected to the direction of the tangent line and normal to the tangent line

$$\{\ddot{\mu}\}^{PE} = \begin{Bmatrix} -0.0959 \\ -0.0375 \end{Bmatrix},\quad \{\ddot{\mu}\}^{IN} = \begin{Bmatrix} 0.0256 \\ -0.0656 \end{Bmatrix} \tag{5.103}$$

Using Eqs. (5.91) and (5.92), the curvatures are obtained

$$c^{PE} = 2.8919,\ \ c^{IN} = 1.9762 \tag{5.104}$$

Multiplying above equation by the standard radius $\rho = 0.0260$, the relative curvatures are obtained,

$$\eta^{PE} = 0.0751, \quad \eta^{IN} = 0.0513 \tag{5.105}$$

The above curvatures are the maximum curvatures since there is only one direction in the parameter space. From a F-distribution table, one finds that $F(1, 1; 0.05) = 161.4$, thus $1/(2\sqrt{F})$=0.0394. It can be seen that both the relative parameter-effects curvature and the relative intrinsic curvature are larger than $1/(2\sqrt{F})$. Therefore, the linear approximation for this model is not acceptable. By looking at Fig. 5.2 (b), one would not say that the linear approximation is good enough.

II). Two parameter model

The two parameter model is the model shown in Eq. (5.81). From Eq. (5.82) the velocity vectors and the acceleration vectors are found as the followings.

$$\{V\}_1 = \begin{Bmatrix} sin(\gamma_2) \\ sin(0.8\pi + \gamma_2) \\ sin(1.6\pi + \gamma_2) \end{Bmatrix}, \quad \{V\}_2 = \begin{Bmatrix} \gamma_1 cos(\gamma_2) \\ \gamma_1 cos(0.8\pi + \gamma_2) \\ \gamma_1 cos(1.6\pi + \gamma_2) \end{Bmatrix} \tag{5.106}$$

and

$$\{\dot{V}\}_{11} = \begin{Bmatrix} 0 \\ 0 \\ 0 \end{Bmatrix}, \quad \{\dot{V}\}_{12} = \{\dot{V}\}_{21} = \begin{Bmatrix} cos(\gamma_2) \\ cos(0.8\pi + \gamma_2) \\ cos(1.6\pi + \gamma_2) \end{Bmatrix}, \quad \{\dot{V}\}_{22} = \begin{Bmatrix} -\gamma_1 sin(\gamma_2) \\ -\gamma_1 sin(0.8\pi + \gamma_2) \\ -\gamma_1 sin(1.6\pi + \gamma_2) \end{Bmatrix} \tag{5.107}$$

From the above equations, it can be seen that all the acceleration vectors are the linear combination of the velocity vectors. This shows that for all the $\{h\}$'s, $\left\{\ddot{\eta}_{\{h\}}\right\}$ will be in the tangent plane. The intrinsic curvature for this model is always zero. Thus, through proper reparameterization, this model can be converted to a linear model. This is true. The linear model of Eq (5.74) can be converted from this nonlinear model.

5.4.3 Curvature measures of the inverse model

The inferences made about the inverse model are based on the linear approximation. To verify the validity, the nonlinearity of the inverse model needs to be evaluated. The curvature measures developed by Bates and Watts [5.10] will be used for this purpose. Although their method was developed for a uniresponse model, it can be applied to the inverse model since the errors are assumed to be identically and independently distributed normal random variables.

The expectation function of the inverse model is a $2N$-dimensional vector.

$$\{\mu\} = \left\{\mu_{P_1,X_L}, \mu_{P_1,Y_L}, \ldots, \mu_{P_N,X_L}, \mu_{P_N,Y_L}\right\}^T \tag{5.108}$$

The first order-derivative matrix of the expectation function with respect to the six pose parameters has been obtained which is denoted as $[J]$ in section **5.2.2**. The second-order derivative array of the expectation function with respect to the six pose parameters is an array with dimensions of $2N \times 6 \times 6$. Its $(2i\text{-}1)$th and $(2i)$th faces are the followings.

$$\left.\begin{aligned} \left[\dot{V}\right]_{2i-1,jk} &= \frac{\partial^2 \mu_{P_i X_L}}{\partial \gamma_j \partial \gamma_k} \\ \left[\dot{V}\right]_{2i,jk} &= \frac{\partial^2 \mu_{P_i Y_L}}{\partial \gamma_j \partial \gamma_k} \end{aligned}\right\} \text{ for } i=1, 2, ..., N \text{ and } j, k=1, 2, ..., 6 \qquad (5.109)$$

The detailed procedure to obtain the analytical expressions for the first-order and second-order derivatives of the inverse model with respect to the six pose parameters is presented in appendix A.

The procedure to evaluate the nonlinearity of the inverse model follows.

I). Obtain the analytical expressions of the first-order and second-order derivatives by using the procedure in appendix A. Those derivatives should be evaluated at $\{\gamma\} = \{\hat{\gamma}\}$.

II). Find the maximum relative parameter-effects curvature and the maximum relative intrinsic curvature by following the steps in section **5.4.2** or by using the efficient algorithm which was developed by Bates and Watts [5.10] and is implemented in appendix B.

III). Compare those maximum relative curvatures with the *CC* which is

$$CC = \frac{1}{2\sqrt{F(6,\ 2N-6;\ \alpha)}} \qquad (5.110)$$

for the inverse model. If the maximum curvatures are less than the *CC*, the inferences by the linear approximation are acceptable. Otherwise, more registration points are required to make the inferences valid.

5.5 Summary

This chapter is on the nonlinear regressive models for the SLDV pose determination. In section **5.1,** two nonlinear models for the pose determination have been developed. It has been pointed out that the inverse model is the better model. In section **5.2,** the ways of using least squares method to estimate the model parameters are given. One is to transfer the problem to an optimization model. The other is to use Gauss-Newton method. Only the inverse model is considered for the Gauss-Newton method. In section **5.3,** the inferences about the inverse model are derived based on the linear approximation technique. However, the validity of those inferences is dependent on the nonlinearity of the inverse model. In section **5.4,** the parameter-effects curvature and the intrinsic curvature developed by Bates and Watts are derived. The way to use these two curvatures to measure the nonlinearity of the inverse model are given.

CHAPTER SIX

IMPLEMENTATION OF THE DEVELOPED ALGORITHM

In this chapter, the implementation of the developed algorithm (the geometrical method and the inverse model) will be presented. Simulated data and experimentally obtained data will be used to test the implementation. The results of the tests will be shown.

6.1 Implementation of developed algorithm

6.1.1 Overview of the implementation

In chapter 5, two nonlinear regressive models were developed for the pose determination of the SLDV. It was pointed out in section **5.1.4** that the inverse model with the rotation matrix being presented by three Euler angles is a desired model. This model has two main advantages. First, it contains only the six pose parameters as unknowns. When the number of registration points increases, the number of unknowns remains unchanged. The second advantage is that there are no constraints among the six pose parameters. This fact makes it possible to derive statistical inferences. After developing methods to obtain the estimate of the six pose parameters, the statistical inferences about the inverse model were derived in chapter 5. The effectiveness of those inferences is dependent on the nonlinearity of the model. The measures of the nonlinearity of the inverse model are based on the curvatures defined by Bates and Watts [5.10]. A problem with a nonlinear regression is the selection of an initial solution for the parameters. If the initial solution is inappropriate, the iterative procedure for finding the parameters may converge to a local minimum or even diverge.

In chapter 4, a geometrical method was developed to determined the pose of the SLDV. The geometrical method is to minimize the sum of the squared errors in structural coordinates, Q, as defined in Eq. (4.84). Since measures were taken to reduce the effects of the measurement errors in each of the three steps involved in the geometrical method, the solution was close enough to the global minimum of Q. Thus, the solution from the geometrical method provides an excellent initial solution for the iteration procedure for determining the parameters in the nonlinear models.

On the basis of the above discussions, the developed algorithm is implemented in two parts. Figure 6.1 shows the overall flow chart of the implementation. The left side of Fig. (6.1) is for obtaining the least squares estimation of the pose of the structural coordinate system with respect to the laser coordinate system. This part is implemented in the C computer language. This implementation has also been incorporated into the software system for data acquisition, signal processing, and system calibration. The right side of Fig. 6.1 is for the statistical inferences of the inverse model and their verification. This part is implemented in Matlab [6.1].

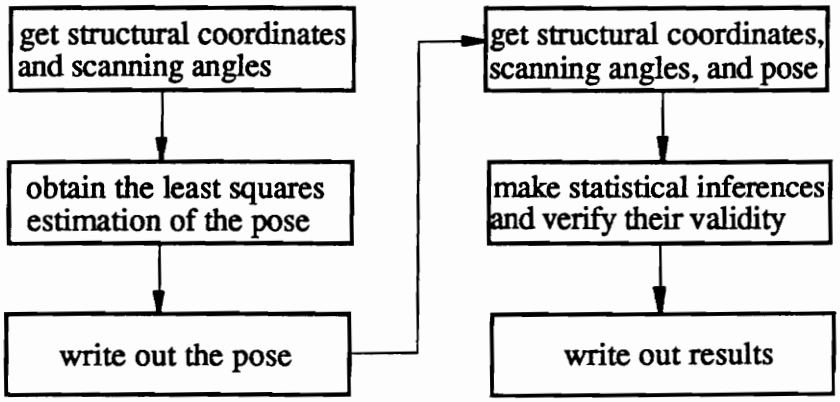

Figure 6.1 The overall flow chart of the implementation

6.1.2 Implementation of the least squares estimation of the pose

The geometrical method developed in chapter 4 is implemented. The result from this method is the pose of the SLDV with respect to the structural coordinate system. From the pose of the SLDV, one can get the pose of the structural coordinate system, i.e.,

$$ {}^{L}_{S}[R] = {}^{S}_{L}[R]^{T}, \quad {}^{L}_{S}\{T\} = -\left({}^{S}_{L}[R]^{T}\right)\left({}^{S}_{L}\{T\}\right). \tag{6.1} $$

The three Euler angles can be derived from the rotation matrix ${}^{L}_{S}[R]$ by using Eq. (3.5).

$$ \alpha = Atan2\left(\frac{{}^{L}_{S}R_{2,1}}{\cos\beta}, \frac{{}^{L}_{S}R_{1,1}}{\cos\beta}\right) \tag{6.2} $$

$$ \beta = Atan2\left(-{}^{L}_{S}R_{3,1}, \sqrt{{}^{L}_{S}R^{2}_{1,1} + {}^{L}_{S}R^{2}_{2,1}}\right) \tag{6.3} $$

$$ \gamma = Atan2\left(\frac{{}^{L}_{S}R_{3,2}}{\cos\beta}, \frac{{}^{L}_{S}R_{3,3}}{\cos\beta}\right) \tag{6.4} $$

where *Atan2* is the four-quadrant arctangent function. The obtained six pose parameters of the structural coordinate system can be used as the initial solution in the search for the least squares estimation of the pose.

The optimization model, Eq. (5.15), is implemented for finding the least squares estimation of the pose parameters for the inverse model. By adjusting the six pose parameters, the sum of the squared errors between the measured scanning angles and the fitted scanning angles is minimized.

Figure 6.2 shows the flow chart of the implementation of finding the least squares estimation of the pose of the structural coordinate system.

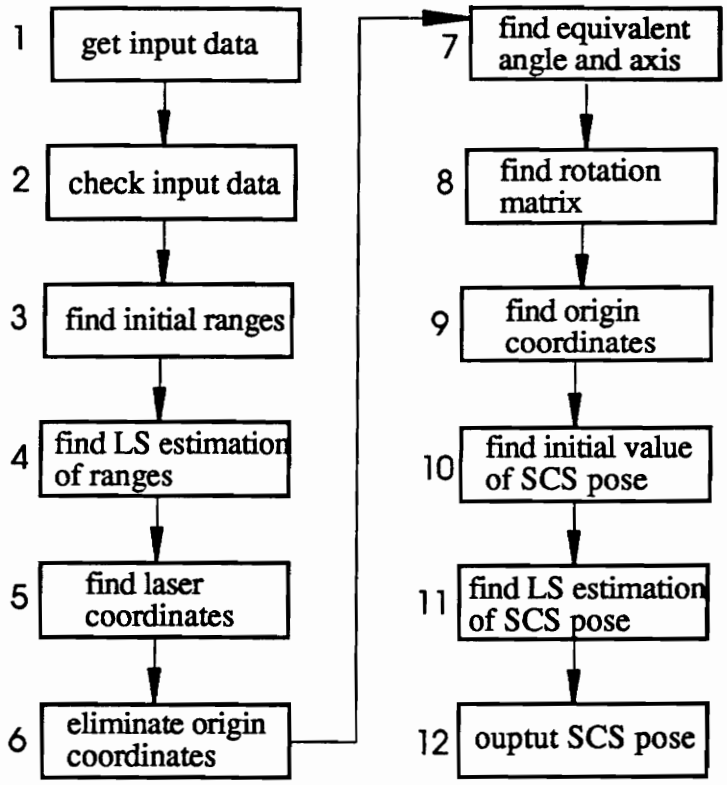

LS: Least Squares, SCS: Structural Coordinate System

Figure 6.2 Flow chart of finding the least squares estimation of the SCS pose

In box 1 of Fig. 6.2, the input data are the structural coordinates and the scanning angles for all the registration points. In box 2, the input data are checked to see if there are less than four registration points and to see if there are common structural coordinates or common scanning angles for any two registration points. This is because the geometrical method requires that each registration point have unique structural coordinates and unique scanning angles. Box 3 requires one to find the initial ranges according to the description in chapter 4. In box 4, two optimizations are performed. In the first optimization,

$Q_1 = \sum_{i=1}^{N-1} \sum_{j=i+1}^{N} \left(D_{ij,S} - D_{ij,L}\right)^2$ is minimized. In the second optimization, $Q_2 = \sum_{i=1}^{N-1} \sum_{j=i+1}^{N} \left(D_{ij,S}^2 - D_{ij,L}^2\right)^2$ is minimized. The initial ranges for the second optimization are the solution from the first optimization. After the second optimization, the solution is more accurate. The reason for this is that in the second optimization, the differences between the ranges are enlarged, which makes the objective function Q_2 less flat than objective function Q_1 in the vicinity of the global minimum. Box 5 and 6 are implemented according the description in chapter 4. In box 7, special considerations are made for the following cases. In finding the equivalent axis $\{k\}$, the program checks:

(i) if the equivalent axis is one of the three axes X_S, Y_S, Z_S, and

(ii) if there is no rotation at all.

In finding the equivalent angle θ_i, the program checks if $\{d_i\}$ is parallel to axis $\{k\}$. Box 8 and 9 are implemented according to the description in chapter 4. The first 9 boxes are the implementation of the geometrical method developed in chapter 4. The result is the pose of the SLDV. In box 10, the six pose parameters of the structural coordinate system are obtained from the pose of the SLDV by using Eqs. (6.1-6.4). They will be used as the initial parameters for the optimization in box 11. The optimization is based on model of Eq. (5.15). Once the minimum is obtained, the least squares estimation of the six pose parameters are found. Box 12 writes the results into a data file.

6.1.3 The implementation of the statistical inference and measures of the nonlinearity

This part is the implementation of the work developed in chapter 5. Figure 6.3 is the flow chart of this implementation.

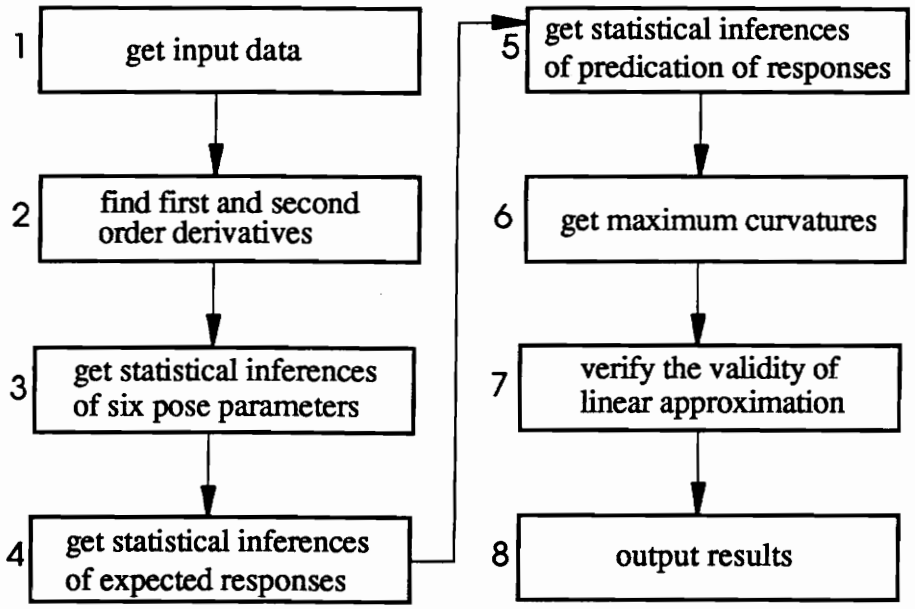

Figure 6.3 The flow chart of statistical inference and measures of nonlinearity

The input data in box 1 includes the structural coordinates, scanning angles, and the pose of the structural coordinate system. In box 2, the first and second derivatives of the inverse model with respect to the six pose parameters are obtained by numerically evaluating the analytical derivative expressions. Those expressions are obtained by Mathematica [6.2]. The details about how to get those derivatives are presented in appendix A. Box 3 to box 5 are implemented based on the descriptions in chapter 5. In box 6, the maximum relative parameter-effects curvature and maximum relative intrinsic

curvature are obtained by using the procedure developed by Bates and Watts [5.10]. The detail about this procedure is presented in appendix B. In box 7, the maximum curvatures are compared to the *CC* (curvature criterion) defined in Eq. (5.110). From the comparison, a conclusion can be drawn about the adequacy of the linear approximation which is used in obtaining the statistical inferences. The obtained results are output to a data file in box 8.

6.2 Two testing cases on the implementation and their results

The implementation has been tested by simulated data and real data. Two testing cases are presented here. One is for simulated data. The other is for experimental data.

6.2.1 Case one: simulated data

The simulated data is formed in following way. The scanning angles for sixteen registration points are assumed. Those scanning angles are transferred to the scanning coordinates $(\theta_{X_L}, \theta_{Y_L})$. By assuming range L to be 2500 mm for every registration point, a completed set of scanning coordinates is available. Letting dl=46 mm and using Eq. (2.10), the laser coordinates can be obtained for all the sixteen points. Now the pose of the SLDV is assumed as

$$ {}^{S}_{L}\{T\} = \begin{Bmatrix} 5000 \\ 8000 \\ 10000 \end{Bmatrix} (\text{mm}),\ {}^{S}_{L}[R] = \begin{bmatrix} 0.17101007 & 0.11185620 & -0.97889925 \\ 0.29619813 & -0.95341225 & -0.05719915 \\ -0.93969262 & -0.28016650 & -0.19617469 \end{bmatrix}. \quad (6.5) $$

From them the pose of the structural coordinate system can be obtained (Eq. (6.1)).

$$ {}^{L}_{S}[R] = \begin{bmatrix} 0.17101007 & 0.29619813 & -0.93969262 \\ 0.11185620 & -0.95341225 & -0.28016650 \\ -0.97889925 & -0.05719915 & -0.19617469 \end{bmatrix} \quad (6.6) $$

$$ {}^{L}_{S}\{T\} = \left(6.17229081\times10^{3},\ 9.86968200\times10^{3},\ 7.31383635\times10^{3}\right)^{T} \text{(mm)} \quad (6.7) $$

Using the assumed pose of the SLDV and Eq. (2.1), the structural coordinates can be obtained for all the registration points. Table 6.1 shows the simulated input data for testing the algorithm, i.e., the structural coordinates (x_S, y_S, z_S) and the scanning angles (φ_X, φ_Y).

Table 6.1 The simulated structural coordinates and scanning angles

Point ID	x_S (mm)	y_S (mm)	z_S (mm)	$-\varphi_Y$ (degrees)	$-\varphi_X$ (degrees)
0	2.86186822e+03	7.53237293e+03	8.88766673e+03	-12.500000	12.500000
1	2.77451944e+03	7.44107394e+03	9.12918372e+03	-12.500000	6.250000
3	2.68143278e+03	7.27984312e+03	9.64069072e+03	-12.500000	-6.250000
4	2.67680145e+03	7.21182788e+03	9.90460027e+03	-12.500000	-12.500000
5	2.79141915e+03	7.77554750e+03	8.95149649e+03	-6.250000	12.500000
6	2.70276418e+03	7.68875721e+03	9.19419695e+03	-6.250000	6.250000
8	2.60967752e+03	7.52752639e+03	9.70570394e+03	-6.250000	-6.250000
9	2.60635238e+03	7.45500245e+03	9.96843003e+03	-6.250000	-12.500000
15	2.73309557e+03	8.27267164e+03	9.09757970e+03	6.250000	12.500000
16	2.64335922e+03	8.19509852e+03	9.34298869e+03	6.250000	6.250000
18	2.55027256e+03	8.03386769e+03	9.85449569e+03	6.250000	-6.250000
19	2.54802880e+03	7.95212659e+03	1.01145132e+04	6.250000	-12.500000
20	2.74591436e+03	8.52071173e+03	9.17809662e+03	12.500000	12.500000
21	2.65641569e+03	8.44773752e+03	9.42499847e+03	12.500000	6.250000
23	2.56332903e+03	8.28650669e+03	9.93650547e+03	12.500000	-6.250000
24	2.56084760e+03	8.20016668e+03	1.01950302e+04	12.500000	-12.500000

Note: e+03=10^3

Using the data in Table 6.1, the pose of the structural coordinate system is found to be

$$ {}^{L}_{S}[R] = \begin{bmatrix} 0.17101006 & 0.29619813 & -0.93969262 \\ 0.11185621 & -0.95341225 & -0.28016650 \\ -0.97889925 & -0.05719916 & -0.19617469 \end{bmatrix}, \tag{6.8} $$

$$ {}^{L}_{S}\{T\} = \left(6.17229083\times10^{3},\ 9.86968198\times10^{3},\ 7.31383645\times10^{3}\right)^{T}\text{(mm)}. \tag{6.9} $$

They are the same as the assumed values (Eqs. (6.6-6.7)).

6.2.2 Case two: experimental data

The experimental data were obtained by aiming the laser beam at sixteen preselected points on a graph paper which was smoothly attached to a flat wood board. The thermal drifting and hysterises errors were virtually eliminated in obtaining those data by turning on the system two hours in advance and approaching all registration points from the same direction (see sections **7.2.3** and **8.1.3**). The following scanner parameters are used.

$$ \left.\begin{aligned} \varphi_X &= 0.0115 + 2.3988V_X \\ \varphi_Y &= 0.0212 + 2.4998V_Y \\ dl &= 1.811\text{(inches)}\ (46\text{mm}) \end{aligned}\right\} \tag{6.10} $$

Using the structural coordinates and scanning angles (columns 2 to 5 in Table 6.2), the implemented algorithm finds the least squares estimation of the pose of the structural coordinate system with respect to the laser coordinate system as

$$
{}^{L}_{S}[R] = \begin{bmatrix} -0.9999 & 0.0043 & -0.0004 \\ -0.0043 & -0.9998 & 0.0203 \\ -0.0005 & -0.0203 & 0.9998 \end{bmatrix} \tag{6.11}
$$

$$
{}^{L}_{S}\{T\} = (14.8718,\ 15.0410,\ 66.0991)^{T}\ (\text{inches}) \quad ((377.7437,\ 382.0414,\ 1678.9171)^{T}\ \text{mm}) \tag{6.12}
$$

From above equation, the six pose parameters can be obtained which are shown in the second column of Table 6.3.

Table 6.2 The measured data and residuals for case two

Point ID	Structural coordinates (z_S=0) (inches)		Scanning angles (degrees)		Residuals in scanning angles (degrees)	
	x_S	y_S	φ_X	φ_Y	ε_{φ_X}	ε_{φ_Y}
1	2.0000	2.0000	-10.5301	11.1653	0.0224	0.0045
2	10.5000	2.0000	-3.6195	11.1409	0.0061	0.0097
3	19.5000	2.0000	3.8182	11.1043	-0.0054	0.0044
4	28.0000	2.0000	10.7639	11.0677	0.0149	-0.0026
5	2.0000	10.5000	-10.7761	3.9516	0.0020	0.0143
6	10.5000	10.5000	-3.7249	3.9149	-0.0003	0.0088
7	19.5000	10.5000	3.8416	3.8905	-0.0234	0.0173
8	28.0000	10.5000	10.9162	3.8539	-0.0006	0.0119
9	2.0000	19.5000	-10.8229	-3.8969	0.0156	-0.0107
10	10.5000	19.5000	-3.7601	-3.9214	0.0070	-0.0034
11	19.5000	19.5000	3.8182	-3.9458	-0.0245	0.0058
12	28.0000	19.5000	10.8928	-3.9824	-0.0197	0.0008
13	2.0000	28.0000	-10.7058	-11.2206	0.0160	-0.0323
14	10.5000	28.0000	-3.7366	-11.2328	0.0085	-0.0133
15	19.5000	28.0000	3.7479	-11.2572	-0.0113	-0.0047
16	28.0000	28.0000	10.7288	-11.2938	-0.0053	-0.0102

Note: 1 inch = 25.4 mm

The residuals shown in the last two columns in Table 6.2 are calculated by Eq. (5.19)

$$\left.\begin{aligned} \varepsilon_{\varphi_{P_i}X} &= -\varepsilon_{\theta_{P_i}Y_L} = -\left(\theta_{P_i Y_L} - \hat{\mu}_{P_i Y_L}\right) \\ \varepsilon_{\varphi_{P_i}Y} &= \varepsilon_{\theta_{P_i}X_L} = \theta_{P_i X_L} - \hat{\mu}_{P_i X_L} \end{aligned}\right\}. \tag{6.13}$$

The estimated standard deviation for the residuals in the scanning angles is

$$s_\varphi = \sqrt{\frac{1}{(2\times 16)-6}\sum_{i=1}^{16}\left(\varepsilon^2_{\varphi_{P_i}X} + \varepsilon^2_{\varphi_{P_i}Y}\right)} = 0.0145 \text{ (degrees)} \tag{6.14}$$

Using Eq. (5.60), the 95% confidence intervals for the six pose parameters are obtained which are shown in the second column of Table 6.3.

Table 6.3 The estimated six pose parameters and their 95% confidence intervals

Parameters	95% confidence intervals
γ_1	14.8718 ± 0.0145 (inches)
γ_2	15.0410 ± 0.0141 (inches)
γ_3	66.0991 ± 0.1130 (inches)
γ_4	-179.7541 ± 0.0344 (degrees)
γ_5	0.0286 ± 0.2865 (degrees)
γ_6	-1.1631 ± 0.2865 (degrees)

Note: 1 inch = 25.4 mm

Table 6.4 shows the 95% confidence intervals for the expected scanning angles for all the sixteen registration points. Those intervals are obtained by using Eq. (5.66). The prediction intervals for the prediction of the scanning angles of the registration points can also be found. But they are not presented here. For any other given point (given its structural coordinates), its confidence intervals for the expected scanning angles and prediction intervals for the prediction of the scanning angles can also be obtained.

Table 6.4 The 95% confidence intervals for the expected scanning angles

Point ID	φ_X (degrees)	φ_Y (degrees)
1	-10.5525 ± 0.0159	11.1608 ± 0.0177
2	-3.6256 ± 0.0116	11.1313 ± 0.0126
3	3.8236 ± 0.0116	11.0999 ± 0.0126
4	10.7490 ± 0.0160	11.0703 ± 0.0176
5	-10.7781 ± 0.0119	3.9373 ± 0.0125
6	-3.7246 ± 0.0094	3.9061 ± 0.0096
7	3.8650 ± 0.0094	3.8732 ± 0.0096
8	10.9168 ± 0.0119	3.8420 ± 0.0125
9	-10.8385 ± 0.0121	-3.8863 ± 0.0123
10	-3.7670 ± 0.0096	-3.9180 ± 0.0098
11	3.8427 ± 0.0097	-3.9515 ± 0.0098
12	10.9125 ± 0.0121	-3.9832 ± 0.0123
13	-10.7218 ± 0.0165	-11.1883 ± 0.0168
14	-3.7452 ± 0.0122	-11.2195 ± 0.0121
15	3.7592 ± 0.0122	-11.2524 ± 0.0121
16	10.7341 ± 0.0165	-11.2836 ± 0.0168

The above statistical inferences are obtained based on the linear approximation. To verify the validity of those approximation, the nonlinearity of the inverse model needs studying. Using the algorithm developed By Bates and Watts [5.10] which is implemented in Matlab in this dissertation (see appendix B), the maximum parameter-effects and maximum intrinsic curvatures are found to be

$$\eta_{max}^{PE} = 0.0862, \text{ and } \eta_{max}^{IN} = 0.0233. \tag{6.15}$$

Note that the *CC* value is

$$CC = 1/\left(2\sqrt{F(6,26;\ 0.05)}\right) = 0.3179. \tag{6.16}$$

It can be seen from above two equations that the maximum curvatures of this model is much smaller than the *CC*. Thus, the linear approximation is acceptable. In other word, the expectation surface at the vicinity of $\{\hat{\gamma}\}$ is sufficiently flat and the parameter lines are sufficiently uniform on the tangent plane. Thus, the statistical inferences about the inverse model are valid. The validity can be verified by comparing the confidence intervals for the expected scanning angles (Table 6.4) with the measured scanning angles (Table 6.2)

The residuals ε_{φ_X} and ε_{φ_Y} shows in Table 6.2 may be used to check the equal variance assumption made about the errors in the scanning angles in section **5.1.3**. The estimation of the variances of the residuals in the scanning angles may be calculated as

$$\left.\begin{aligned} s^2_{\varphi_X} &= \frac{1}{16-1}\sum_{i=1}^{16}\varepsilon^2_{\varphi_X} = 2.0746\times10^{-4} \\ s^2_{\varphi_Y} &= \frac{1}{16-1}\sum_{i=1}^{16}\varepsilon^2_{\varphi_Y} = 1.5785\times10^{-4} \end{aligned}\right\} \text{(degrees}^2\text{)} \qquad (6.17)$$

The alternatives in the hypothesis testing for the equal variance are

$$\left.\begin{aligned} H_0&: \sigma^2_{\varepsilon_{\varphi X}} = \sigma^2_{\varepsilon_{\varphi Y}} \\ H_a&: \sigma^2_{\varepsilon_{\varphi X}} \neq \sigma^2_{\varepsilon_{\varphi Y}} \end{aligned}\right\} \qquad (6.18)$$

The statistic [5.9]

$$F^* = \frac{s^2_{\varphi_X}}{s^2_{\varphi_Y}} = 1.3143 \qquad (6.19)$$

can be used to perform the test. For significance level α =0.05, one can find

$$\left.\begin{aligned} F(15,15;\ 0.025) &= 0.3494 \\ F(15,15;\ 0.975) &= 2.8621 \end{aligned}\right\} \qquad (6.20)$$

It can be seen from the Eqs. (6.19-6.20) that

$$F(15,15;\ 0.025) < F^* < F(15,15;\ 0.975)$$

Therefore, null hypothesis in Eq. (6.18) is accepted. This verifies the equal variance assumptions about the residuals in the scanning angles.

6.3 Summary

The implementation of the geometrical method and the inverse model has been presented in this chapter. The implementation is in C for finding the least squares estimation of the pose parameters. The implementation is in Matlab for finding the statistical inferences about the inverse model and for measuring the nonlinearity of the inverse model. For the simulated data, the estimated pose is the same as the assumed value. For the experimental data, the residuals (Table 6.2) in the scanning angles are small and the statistical inferences are valid. The equal variance assumption is verified by using the residuals in the scanning angles. Those results of the two cases show that the implementation is correct.

CHAPTER SEVEN

ASSESSMENT OF THE INVERSE MODEL

In this chapter, attention will be focused on the assessment of the inverse model. The errors associated with the determination of the SLDV pose will be reviewed. The linear voltage-angle relation of the scanner will be verified. The repeatability of the D/A converter and the scanner will be experimentally evaluated. The inverse model will be assessed by analyzing the residuals, checking the predictive ability, and studying the effects of the number of the registration points and the effects of the separation angles.

7.1 Review of the inverse model and its assumptions

In chapter 2, three relationships were used to derive the equation relating the input voltages to the structural coordinates for a registration point. The first relationship is the scanner's linear voltage-angle relation (Eqs. (2.6-2.7)) which results from the assumption that the scanning angle is a linear function of the input voltage for both the X mirror and the Y mirror. The second relationship is the scanner model, i.e., the transformation between the scanning coordinates and the laser coordinates (Eqs. (2.10-2.11)). The assumptions in deriving this transformation are: (i) the rotation axes of the X and Y mirrors are perpendicular to each other (specific to the type of scanner in the SLDV laser head in our laboratory), (ii) the mirror surfaces are on the rotation center of their axes, (iii) the laser beam entering the scanner is parallel to the rotation axis of the Y mirror and is incident on the center of the rotation axis of the X mirror (partly due to assumption (ii)), and (iv) the laser beam reflected from the X mirror is incident on the center of the rotation axis of the Y mirror (partly due to assumption (ii)). The third relationship is the coordinate

transformation between the laser coordinates and the structural coordinates. There is no assumption for this relationship.

The inverse model is obtained by expressing the scanning coordinates (θ_{X_L}, θ_{Y_L}) as functions of the structural coordinates (x_S, y_S, z_S). For convenience, the model is rewritten here (Eq. (5.19)) as

$$\left.\begin{aligned} \theta_{P_i X_L} &= \mu_{P_i X_L} + \varepsilon_{\theta_{P_i X_L}} \\ \theta_{P_i Y_L} &= \mu_{P_i Y_L} + \varepsilon_{\theta_{P_i Y_L}} \end{aligned}\right\} \tag{7.1}$$

The residuals in the above equation are assumed to be identically and independently distributed normal random variables with zero mean and finite variance.

For linear or nonlinear regression analysis, it is necessary to verify all the assumptions about the model and the assumptions about the residuals. In the following sections, the work for verifying the inverse model will be presented.

7.2 Error sources in the determination of the SLDV pose

There are a number of error sources involved in the pose determination procedure. These errors may be classified as measurement errors, modeling errors, and other errors.

7.2.1 Measurement errors

.

The input voltages and the structural coordinates are the measurable variables in the pose determination. Both of them have measurement errors. For the voltages, the measurement

errors are very small. When a calibrated D/A converter board is used to generate the input voltages to the scanner controller, the measurement errors are the repeatability errors of the D/A converter board since the desired D/A voltages sent to the D/A converter is used as the input voltages. For the structural coordinates, the measurement errors are determined by the resolution used in measuring the structural coordinates of the registration point. Higher measurement resolution will result in lower measurement errors. These measurement errors can be controlled by the person who conducts the experiments.

7.2.2 Modeling errors

Modeling errors arise when the model can not present the actual behavior of a processing or a relationship. There are two possible modeling errors in the inverse model. The first modeling error is from the assumption that the relationship between the input voltages and the scanning angles are linear. If the true relationship is nonlinear, the linear assumption will result in error. This assumption will be evaluated in section **7.3**. The second error is from the scanner model. If the four assumptions can not be satisfied about the scanner and the laser beam (see section **7.1**), the modeling error exists. The misalignment in the installation of the mirrors, the galvanometers, and helium-neon laser in the laser head will make the assumptions (i), (iii) and (iv) invalid and result in error. The error caused by assuming the mirror surface is on the rotation center of its axis was defined as the laser beam parallel shift error in [2.1]. Both Li [2.1] and Dominguez [1.18] showed that this error can be neglected.

7.2.3 Other errors

Generally speaking, the errors involved in a linear or nonlinear regression analysis are the measurement errors and the modeling errors. The other errors here result from the scanner. The scanner consists of two independently controlled plane mirrors. The mirrors are installed separately. The rotation of the mirrors is controlled by galvanometers. It is known that there are three kinds of errors from the galvanometers [2.1]. In addition to the above-mentioned possible nonlinearity error, there are hysteresis and thermal drifting errors. The hysteresis error is the difference in the scanning angles by applying the same input voltages to the scanner controller from the different positions. In other words, if one applies zero voltage to the scanner controller from a previous position represented by positive 5 volts, one gets a scanning angle. Now if one applies the zero volts to the scanner controller again from negative 5 volts, a different scanner angle will be obtained. The difference between that two angles is the hysteresis error. For the scanner used in our SLDV, the hysteresis error is experimentally found to be about 0.05 degree for both X and Y mirror at zero voltage. These errors can be eliminated if one always approaches a position from the same direction (either positive or negative). The thermal drifting error is the differences in scanning angles at the condition that the input voltage is held constant. This error is purely caused by the changes of the temperature of the rotary transducer in the galvanometer system. This error can be largely reduced if a device is installed to keep the temperature of the galvanometer constant. For our SLDV, a number of holes are drilled in the case of the laser head to enhance the convection cooling. If the laser head is turned on sometime before the measurements, the laser head will warm up and approximately approach a thermal balance state. In this way, the temperature of the galvanometer inside the laser head will remain approximately constant and thermal drifting

error is virtually eliminated. Practically, the hysterises and thermal drifting errors can be considered as repeatability errors. The repeatability of the D/A converter and the scanner will be tested in section **7.4**.

When trying to aiming the laser beam at a known point, there are two possible errors. The first one is from the limited resolution of the D/A converter. Thus, it is possible for the laser beam to miss a registration point. The second error is from the fact that the laser beam has finite size. When locating the laser beam spot, one may only be able to "guess" the location of the center of the laser beam spot. However, these two errors can be considered as the measurement errors in the structural coordinates. Hence, it is not necessary to consider them separately.

7.2.4 Residuals in the inverse model

The inverse model implies that the structural coordinates are error-free and all errors are associated with the scanning coordinates. However, the residuals in the inverse model consists of the following three kind errors: (i) the errors converted from the measurement errors in the input voltages, (ii) the possible modeling errors, for example, if the misalignment does exist in installation of the components of the scanner, and (iii) the errors converted from the measurement errors in the structural coordinates. The residuals are assumed to be identically and independently distributed normal random variable with zero mean and finite variances. These residuals will be analyzed in section **7.5**.

7.2.5 Strategies for assessing the inverse model

On the basis of the discussions about the various errors, the assessment of the inverse model will focus on following issues: (i) verifying the linear voltage-angle relation, (ii) checking the repeatability of the D/A converter and the scanner, (iii) analyzing the residuals in the inverse model, (iv) checking the predictive ability, and (v) studying the effects of the number of registration points and the effects of the separation angles. Actually, analyzing the residuals includes the verification of the linear voltage-angle relation and the scanner model since any modeling errors will have their effects on the residuals.

7.3 The linear voltage-angle relation and its verification

7.3.1 Linear voltage-angle relation

The linear voltage-angle relation is defined as the linear relationship between the input voltages and the scanning angles (Eq. (2.6-2.7))

$$\left.\begin{aligned} \varphi_X &= a_X + b_X V_X \\ \varphi_Y &= a_Y + b_Y V_Y \end{aligned}\right\}. \tag{7.2}$$

In an ideal situation, the offsets (a_X, a_Y) should be zero since it is assumed that at zero input voltages, scanning angles are zero. Those two nonzero parameters may be considered as a compensation for those misalignment errors in the installation of the mirrors and galvanometers.

7.3.2 Calibration and verification of the linear voltage-angle relation

From the manufacturer [1.2] of our SLDV, the parameters in Eq. (7.2) are

$$\left.\begin{aligned} a_X &= a_Y = 0 \\ b_X &= b_Y = 2.5 \end{aligned}\right\} \tag{7.3}$$

In the development of an automatic mobility measurement system [1.16-1.17], it was found that the values of the four parameters in Eq. (7.3) would cause significant errors in the determination of the pose of the SLDV. Experiments were completed to calibrate those four parameters. The data obtained in that calibration are used here to verify the validity of the linear voltage-angle relation.

The details about the experiments and calibration were given in [1.16]. Based on the fact that the rotation of the two mirrors are controlled by two separately installed galvanometers, the two equations in Eq. (7.2) are calibrated separately. Figure 7.1 shows the principle. X mirror may be taken as an example. When a voltage V_X is applied to the scanner controller (V_Y=0), the X mirror will deflect the laser beam from home O to a point P. By measuring the distance H and l_i, the scanning angle is

$$\varphi_i = tan^{-1}\left(\frac{l_i}{H}\right). \tag{7.4}$$

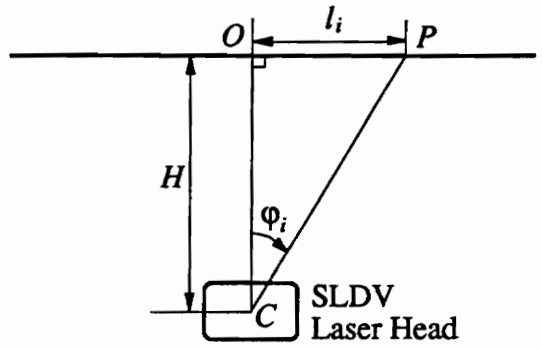

Figure 7.1 The principle for calibrating one scanning mirror at a time.

By applying a set of voltages covering the full range from negative 5 volts to positive 5 volts, a set of scanning angles can be obtained. From the calculated scanning angles and the applied voltages, the parameters in Eq. (7.2) for the X mirror can be obtained through the use of the least squares technique. The parameters for Y mirror can be obtained in the same way. The only difference is that one needs to apply different voltage V_Y and hold V_X to zero. This method is called one-dimensional calibration method since the laser beam is moved along only one direction and one mirror is calibrated at a time. Note that the moving laser center will not cause any problem for one-dimensional calibration. For the calibration of the Y mirror, the center (C in Fig. 7.1) is at the origin of the laser coordinate system, O_L. For the calibration of the X mirror, the center is at the imaginary point, O'. Therefore, the value of H for calibrating X mirror is not the same as that for calibrating the Y mirror.

The accuracy of the calculated angle depends on the measurement errors in H and l_i. From the Eq. (7.4), the error in the scanning angle can be estimated as

$$\delta\varphi_i = \frac{\partial\varphi_i}{\partial H}\delta H + \frac{\partial\varphi_i}{\partial l_i}\delta l_i = \frac{1}{H^2 + l_i^2}\left(H\delta l_i - l_i\delta H\right) \tag{7.5}$$

where δH and δl_i are the measurement errors. The worst case is that two errors, δl_i and δH, have opposite sign.

Table 7.1 shows a set of data obtained for calibrating the X mirror. The maximum measurement error in l_i was 1/32 inches (0.7838 mm). The error in measuring H was no worse than 0.25 inches (6.35 mm). For that set of data, H was measured as 398.6732

inches (10126.2993 mm). Using Eq. (7.5), the maximum measurement error in the scanning angles is

$$\delta\varphi_i = \frac{398.6732 \times 0.03125 + 85.3750 \times 0.25}{398.6732^2 + 85.3750^2} = 0.0117 \text{ (degrees)} \qquad (7.6)$$

For most of the scanning angles, the error will be less than this value.

Table 7.1 A set of calibration data for X mirror (H=398.6732 inches)

Points	$V_{i,X}$ (volts)	l_i (inches)	$\varphi_{i,X}$ (degrees)
1	-4.9726	-85.3750	-12.0872
2	-4.4761	-76.7500	-10.8969
3	-3.9787	-68.0625	-9.6883
4	-3.4813	-59.3750	-8.4709
5	-2.9836	-50.7500	-7.2546
6	-2.4860	-42.1250	-6.0317
7	-1.9886	-33.6875	-4.8300
8	-1.4908	-25.2500	-3.6240
9	-0.9922	-16.6250	-2.3879
10	-0.4957	-8.3750	-1.2034
11	0.0000	0.0000	0.0000
12	0.4981	8.3125	1.1945
13	0.9954	16.6875	2.3969
14	1.4956	25.1875	3.6150
15	1.9936	33.5625	4.8121
16	2.4917	42.0625	6.0228
17	2.9895	50.5625	7.2281
18	3.4875	59.1875	8.4445
19	3.9851	67.8750	9.6621
20	4.4827	76.5625	10.8709
21	4.9801	85.3125	12.0786

Note: 1 inch =25.4 mm

Figure 7.2 shows the relationship between the input voltages and the scanning angles for the X mirror. Three different models between the input voltages and the scanning angles

have been fitted by the least squares technique for the data in Table 7.1. Table 7.2 shows the results. For simplicity, the subscript X is not shown in the first column of Table 7.2e. The estimated standard deviations of the residuals shown in the last column of Table 7.2 are calculated by

$$s = \sqrt{\frac{1}{21 - M} \sum_{i=1}^{21} \varepsilon_i^2} \tag{7.7}$$

where M is the number of the parameters.

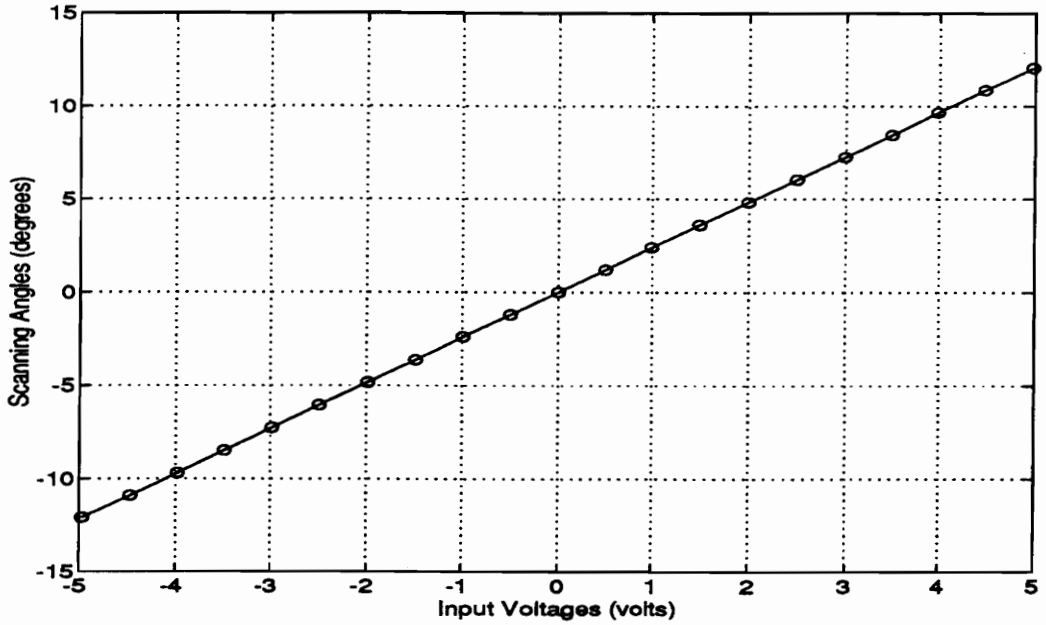

Figure 7.2 The scanning angles versus input voltages for X mirror (data in Table 7.1)

From above table, it can be seen that after including the offset a_x in the model, the estimated standard deviation is reduced from 0.0188 degrees to 0.0132 degrees, which is about 30 percent reduction. However, after including the quadratic term in the model, the standard deviation is reduced by only 4.5 percent. This shows that the relationship between the input voltages and the scanning angles can be linearly approximated.

Statistically, one can verify if the coefficient of the quadratic term is equal to zero or not. The two alternatives for this hypothesis test are

$$\left.\begin{array}{l} H_0\text{: } c_X = 0 \\ H_a\text{: } c_X \neq 0 \end{array}\right\} \tag{7.8}$$

From Eq. (5.45)

$$|t^*| = \left|\frac{\hat{c}_X - 0}{s(\hat{c}_X)}\right| = \left|\frac{-5.8302\times10^{-4}}{3.3936\times10^{-4}}\right| = 1.7180 < t(18;\ 0.025) = 2.1009 \tag{7.9}$$

The null assumption is accepted for a significant level α=0.05. Thus, the linear voltage-angle relation is acceptable for the X mirror.

Table 7.2 The results of three fitted models for X mirror

Different Model	Estimated parameters			s (degrees)
	$\hat{a}_X$	$\hat{b}_X$	$\hat{c}_X$	
$\varphi_i = bV_i + \varepsilon_i$		2.4272		0.0188
$\varphi_i = a + bV_i + \varepsilon_i$	-0.0133	2.4272		0.0132
$\varphi_i = a + bV_i + cV_i^2 + \varepsilon_i$	-0.0080	2.4273	-0.0006	0.0126

Table 7.3 shows a set of data obtained for calibrating the Y mirror. The measurement accuracy was the same as that for the X mirror. Due to the spatial limitation in the Y direction, the input voltages covered only from –3 volts to 3 volts.

Table 7.3 A set of calibration data for Y mirror (H=396.8622 inches)

Points	$V_{i,Y}$ (volts)	l_i (inches)	$\varphi_{i,Y}$ (degrees)
1	2.9893	52.8750	7.5890
2	2.4910	44.0000	6.3265
3	1.9931	35.1250	5.0579
4	1.4951	26.3125	3.7932
5	0.9950	17.3125	2.4979
6	0.4978	8.6875	1.2540
7	0.0000	0.0000	0.0000
8	-0.4971	-8.6875	-1.2540
9	-0.9945	-17.4375	-2.5159
10	-1.4917	-26.1875	-3.7753
11	-1.9896	-35.0000	-5.0400
12	-2.4873	-43.8125	-6.2998
13	-2.9851	-52.7500	-7.5712

Note: 1 inch =25.4 mm

Figure 7.3 shows the relationship between the input voltages and the scanning angles for the Y mirror. Again, three different models between the input voltages and the scanning angles have been fitted by the least squares technique for the data in Table 7.3. Table 7.4 shows the results. For simplicity, the subscript Y is not shown in the first column of the table. The estimated standard deviations of the residuals shown in the last column of the table are calculated by Eq. (7.7) with 13 data points.

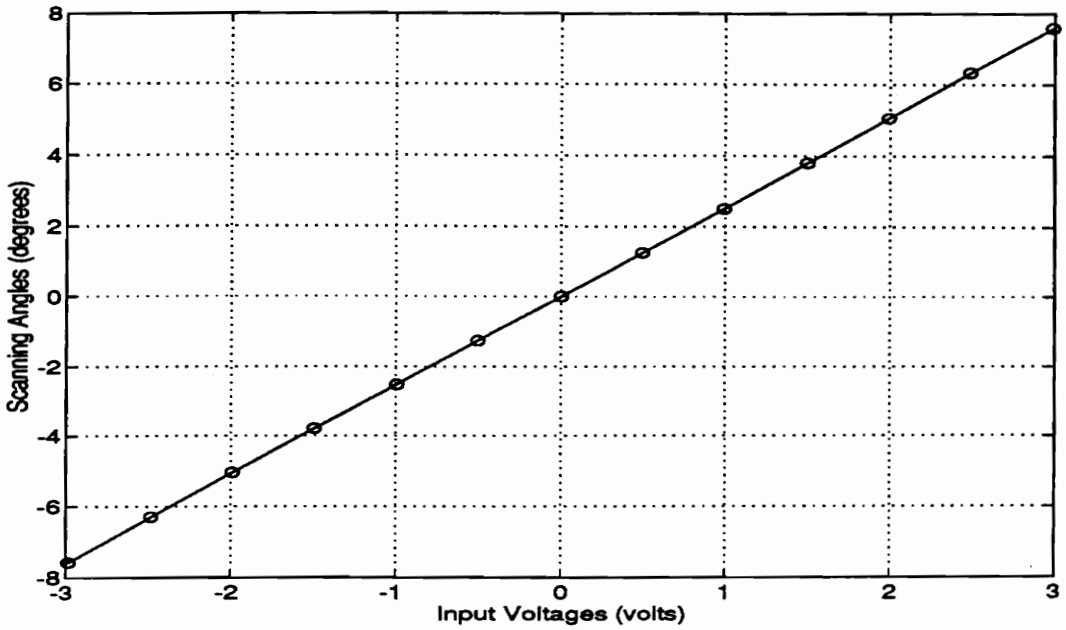

Figure 7.3 The scanning angles versus input voltages for Y mirror (data in Table 7.3)

Table 7.4 The results of three fitted models for Y mirror

Different Model	Estimated parameters			s (degrees)
	$\hat{a}_Y$	$\hat{b}_Y$	$\hat{c}_Y$	
$\varphi_i = bV_i + \varepsilon_i$		2.5355		0.0096
$\varphi_i = a + bV_i + \varepsilon_i$	0.0017	2.5355		0.0099
$\varphi_i = a + bV_i + cV_i^2 + \varepsilon_i$	-0.0021	2.5355	0.0011	0.0097

From above table, it can be seen that the relationship between the input voltages and the scanning angles can be linearly approximated. Statistically, one can verify if the coefficient of the quadratic term is equal to zero or not. Similar to the test for the X mirror, one has

$$|t^*| = \left|\frac{\hat{c}_Y - 0}{s(\hat{c}_Y)}\right| = \left|\frac{10.7731\times10^{-4}}{8.7163\times10^{-4}}\right| = 1.2360 < t(10;\ 0.025) = 2.2281 \quad (7.10)$$

The null assumption is accepted for a significant level α=0.05. Thus, the linear voltage-angle relation is acceptable for the *Y* mirror.

Using the results of the calibrations for the *X* and *Y* mirrors, the equal variance assumption about the errors in the scanning angles can be tested. The two alternatives for this test were shown in Eq. (6.18). The estimated variances of the residuals in the scanning angles from the results of fitting the data by linear relation (including the offset term a_X and a_Y) are the following.

$$\left.\begin{aligned} s^2_{\varphi_X} &= 1.7478\times10^{-4} \\ s^2_{\varphi_Y} &= 9.7947\times10^{-5} \end{aligned}\right\} \text{(degrees}^2\text{)} \tag{7.11}$$

From above equation, the statistic *F** can be calculated as

$$F^* = \frac{s^2_{\varphi_X}}{s^2_{\varphi_Y}} = 1.7844. \tag{7.12}$$

From the *F* distribution table, one can find that

$$\left.\begin{aligned} F(19,11;\ 0.025) &= 0.3617 \\ F(19,11;\ 0.975) &= 3.2428 \end{aligned}\right\} \tag{7.13}$$

From Eqs. (7.12-7.13), it is clear that

$$F(19,11;\ 0.025) < F^* < F(19,11;\ 0.975) \tag{7.14}$$

Thus, the variance of the errors in the *X* scanning angle is statistically equal to the variance of the errors in the *Y* scanning angles.

In this section, it has been shown that the linear voltage-angle relation is correct for the scanner. It has also shown that the equal variance assumption for the errors in the scanning angles is acceptable. The currently-used scanner parameters for transforming

between scanning angle and voltages were shown in Eq. (6.10). They are from the latest calibration by using the one-dimensional calibration method.

The verification of the linear voltage-angle relation is completed separately, i.e., one mirror at a time. To verify it simultaneously, one needs to analyze the residuals in the inverse model. This will be done later in this chapter in section **7.5**.

7.4 The repeatability tests of the D/A converter and scanner

Since the input voltages to the scanner controller is the output of a D/A converter, the repeatability tests need to check two things: (i) if the output voltages from the D/A converter are repeatable, and (ii) if the spatial locations of the laser beam are repeatable. The second thing is to test the repeatability of the scanner. The hysteresis error and thermal drifting errors are example of repeatability errors. To have less error, it is required that both of the D/A converter and the scanner have high repeatability.

Two repeatability tests have been completed and are described below.

7.4.1 The first repeatability test and its results

Figure 7.4 shows the experimental setup for the first repeatability test. The Macintosh IIfx is the host computer. The desired D/A voltages are sent to the D/A board whose outputs are connected to the analog beam deflection inputs (X and Y terminals) of the VPI sensor (scanner controller). Channel 0 of the D/A board is connected to the Y terminal which controls the Y mirror. Channel 1 is connected to the X terminal which controls the X

mirror. The voltages are measured between the D/A board and the VPI sensor. These voltages are the input voltages to the scanner controller. The VPI sensor is the power supply to the SLDV laser head. When referring to control of the scanner, the VPI sensor will be called the scanner controller. This is the unit through which one can control the rotation of the mirrors to deflect the laser beam to a desired spatial location. The spatial points are on the graph paper which are smoothly attached to a plywood board. The dimension of the graph paper is 30" by 30" (762 by 762 mm²) with 20 scales per inch. The graph paper is labeled from left to right and top to bottom, which give a structural coordinate system as shown in Figure 7.4.

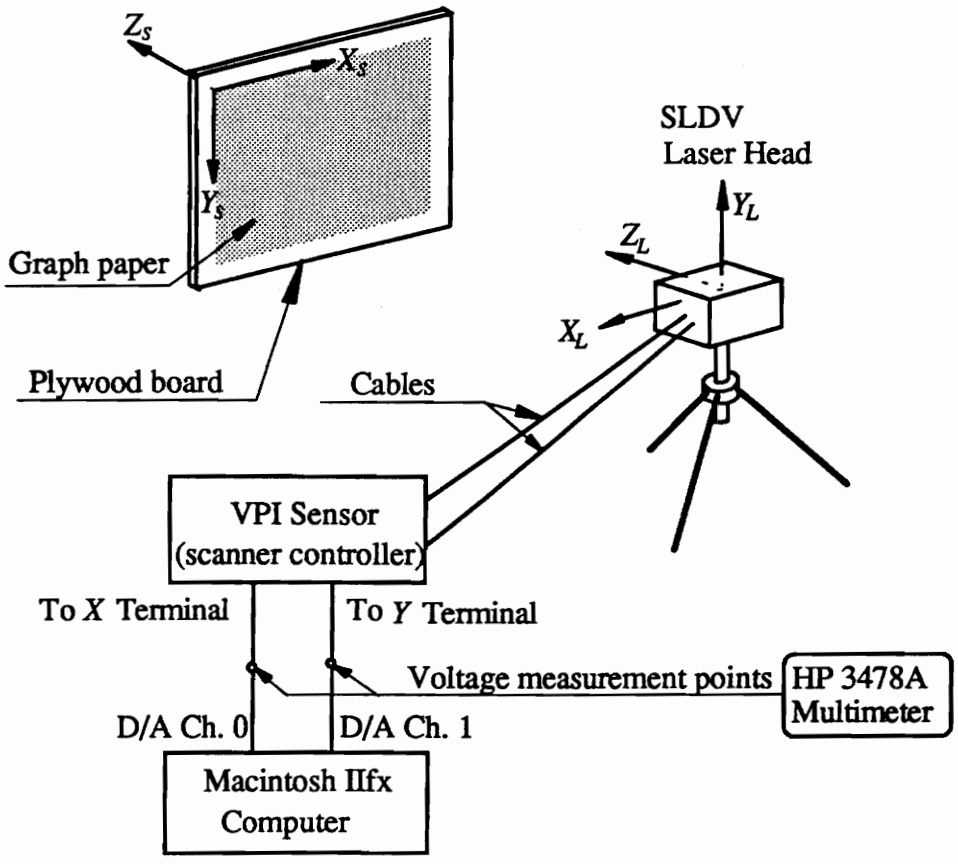

Figure 7.4 The experimental setup for the first repeatability test

Before starting the experiments, the accuracy of the HP multimeter was verified with a standard reference. The orientation of the laser head was adjusted to align with the graph paper roughly, i.e., the *HH* line shown in Fig. 2.2 overlapped a horizontal grid line of the graph paper and the *VV* line a vertical grid line. The distance between the laser head and the plywood board was adjusted such that at the full voltage range (negative 5 volts to positive 5 volts), the laser beam would cover the desired area on the graph paper. Five voltages (-4.9902, -2.5, 0 2.5, 4.9902 (volts)) were selected as the desired D/A voltages for each of the two channels. They formed 25 combinations. The order to send them to the D/A board is shown in the first three columns of Table 7.5. To reduce the thermal drifting error, the system was turned on for about 4 hours in advance.

Following is the experimental procedure.

I). The laser beam is moved to the upper left corner by sending positive 5 voltage to channel 0 and negative 5 voltages to change 1 and is held to stay there for 100 milliseconds before it is moved to any other points. The purpose of doing this is to eliminate the error of the hysterises.

II). The first pair of the selected desired D/A voltages are sent to the D/A board. The voltages between the D/A board and the VPI sensor are measured and recorded. The position of the laser beam spot on the graph paper is measured with the grid of the graph paper. The position is rounded to the scale (grid line), which means that the measurement resolution is a scale (1/20 inches (1.27 mm)). The measurements are done for x_s and y_s only. Zero is assumed for the z_s coordinate. As shown in Fig. 7.4, the origin of the structural coordinate system is put right on the graph paper.

III). Repeat (I) and (II) for all the 25 registration points.

Above three steps complete one test. Since this experiment was designed to check the system's repeatability, above three steps were repeated for 15 times. In the experiment, the system was turned on at about 12:00 PM. The experiment began at about 4:00PM lasted about a period of 8 hours.

After finishing the experiment, the estimated mean and the estimated standard deviation were obtained for each measured datum from the 15 measurements. Table 7.5 shows the estimated standard deviation. The first column is the order in which the selected desired D/A voltages pairs (shown in column two and three) are sent to the D/A board. Columns four and five are the standard deviation for the voltages measured between the D/A board and the scanner controller. Columns 6 and 7 are the standard deviation for the structural coordinates (X_S and Y_S.) From the results, one can see that the voltages are very stable and repeatable. The standard deviations for them are just about 0.1 millivolts. Thus, the repeatability of the D/A converter is excellent. The standard deviations for the measured structural coordinates of the laser beam spot on the graph paper vary from point to point. Some points are zero while others are not zeros. As observed in the experiment, for those points with zero standard deviations, the laser beam spot was right on the grid of the graph paper. For those points with nonzero deviations, the laser beam spot was on a place between the grid lines. When measuring the location, it was rounded to one of the two grid lines adjacent to it. One can see from the table that the maximum deviation in the structural coordinates is just about half of the resolution in measuring the structural

coordinates. Therefore, the repeatability of the scanner is very good, i.e., the spatial location of the laser beam are quite repeatable.

Table 7.5 The first repeatability test and its results

Order	Desired D/A voltages (volts)		Estimated standard deviation (volts)		Estimated standard deviation (inches)	
(point ID)	V_Y	V_X	s_{V_Y}	s_{V_X}	s_{X_s}	s_{Y_s}
1	4.9902	-4.9902	0.0001	0.0002	0.0207	0.0207
2	4.9902	-2.5000	0.0001	0.0001	0.0244	0.0244
3	4.9902	0.0000	0.0001	0.0001	0.0254	0.0254
4	4.9902	2.5000	0.0001	0.0001	0.0000	0.0000
5	4.9902	4.9902	0.0001	0.0001	0.0000	0.0000
6	2.5000	-4.9902	0.0001	0.0001	0.0000	0.0000
7	2.5000	-2.5000	0.0001	0.0001	0.0244	0.0244
8	2.5000	0.0000	0.0001	0.0001	0.0000	0.0000
9	2.5000	2.5000	0.0001	0.0001	0.0000	0.0000
10	2.5000	4.9902	0.0001	0.0001	0.0000	0.0000
11	0.0000	-4.9902	0.0001	0.0001	0.0129	0.0129
12	0.0000	-2.5000	0.0001	0.0001	0.0258	0.0258
13	0.0000	0.0000	0.0001	0.0001	0.0000	0.0000
14	0.0000	2.5000	0.0001	0.0001	0.0129	0.0129
15	0.0000	4.9902	0.0001	0.0001	0.0176	0.0176
16	-2.5000	-4.9902	0.0001	0.0001	0.0129	0.0129
17	-2.5000	-2.5000	0.0001	0.0001	0.0207	0.0207
18	-2.5000	0.0000	0.0001	0.0001	0.0000	0.0000
19	-2.5000	2.5000	0.0001	0.0001	0.0254	0.0254
20	-2.5000	4.9902	0.0001	0.0001	0.0000	0.0000
21	-4.9902	-4.9902	0.0001	0.0001	0.0244	0.0244
22	-4.9902	-2.5000	0.0001	0.0001	0.0176	0.0176
23	-4.9902	0.0000	0.0001	0.0001	0.0000	0.0000
24	-4.9902	2.5000	0.0001	0.0001	0.0000	0.0000
25	-4.9902	4.9902	0.0001	0.0001	0.0129	0.0129

Note: 1 inch =25.4 mm

It is noticed that the voltages measured between the D/A converter and the scanner controller are not exactly the same as the desired D/A voltages sent to the D/A board. The averaged difference is about 6 millivolts for the repeatability test. However, if the D/A converter is disconnected from the scanner controller, the output voltages from the D/A board is the same as the desired D/A voltages sent to the D/A converter. It is believed that the voltage difference is caused by the input impedance of the scanner controller. Based on the experiences with the system, this small voltage difference does not cause any problems in the accuracy of the determined pose of the SLDV. Therefore, the desired D/A voltages can be taken as the input voltages to the scanner controller.

In the above repeatability test, the distance between the graph paper and the laser head is about 54 inches (1372.87 mm). If a scanning angle error is less than 0.0265 degrees, the spatial location error of the laser beam on graph paper will be less than half of the resolution (1/40 inches (0.635 mm)). Thus, the above repeatability test can not detect a repeatability error less than 0.0265 degrees in the scanning angles. To detect a smaller repeatability error in the scanning angles, the test can be conducted at a greater range.

7.4.2 The second repeatability test and its results

In this test, the laser head was placed 1343" (34112.2 mm) from the graph paper. Figure 7.5 shows the set up and the relative dimensions. Four 7.5" by 5" (190.5 by 152.4 mm^2) graph papers are attached to a flat wall. The graph paper has 20 grids per inch. One point on each paper was selected as a reference point. The grid lines were aligned with the laser by overlapping the laser beam locus on a horizontal grid line. The distances shown in the Fig. 7.5 are the distance between the reference points. Point O is the home position of the

laser beam on the wall. The perpendicular distance between point *O* and the floor is about 56 inches (1422.4 mm). The distance between the wall and the mounting points of the laser head is about 1343 inches (34112.2 mm). Four pairs of desired D/A voltages were sent to the D/A board which would direct the laser beam roughly to the four reference points. The size of the laser beam spot on the graph paper is about two scales (0.1 inches (2.54 mm)) in diameter.

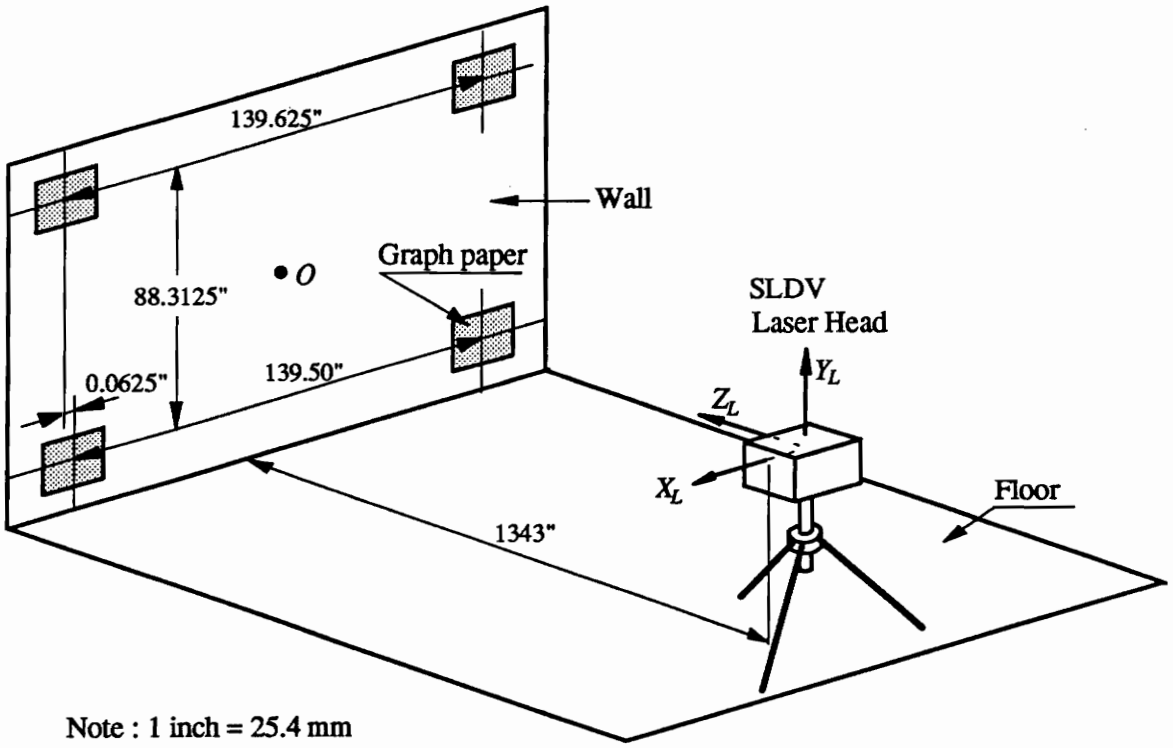

Figure 7.5 Experimental setup for the second repeatability test

The experimental procedure is the same as the first repeatability tests. However, half a scale resolution (1/40" (0.635 mm)) was used in measuring the location of the laser beam spot on the graph paper for this experiment. When the center of the laser beam spot was between two grid lines, its position was measured by putting it in either the center or the

two adjacent grid lines, depending on where it was more close to. The experiment began after the system was turned on for about two hours. The experiment lasted about two hours. Table 7.6 shows the results including the desired D/A voltages and the estimated standard deviation of the measured structural coordinates of the laser beam spot on the graph paper. From the table, one can see that the repeatability of the scanner is excellent. At this range, the maximum standard deviation is only about 0.0281 inches (0.7137 mm). Converting this to angle, one will get

$$s_{angle} = \frac{0.0281}{1343}(\text{radians}) = 0.0012 \text{ (degrees)}. \tag{7.15}$$

Table 7.6 The second repeatability test and its results

Order	Desired D/A voltages		Estimated standard deviation	
(point ID)	V_X	V_Y	s_{X_s} (inches)	s_{Y_s} (inches)
1	-1.0791	0.9814	0.0140	0.0281
2	1.4404	0.9814	0.0000	0.0154
3	-1.0791	-0.5518	0.0186	0.0065
4	1.4404	-0.5518	0.0000	0.0122

Note: 1 inch =25.4 mm

The results of the two repeatability tests show that the repeatability of the D/A converter and the scanner are excellent. Thus, the results of an experiment lasting a long time can be trusted and used in further analysis.

7.5 The evaluation of the inverse model

This section will concentrate on the assessment of the inverse model. The assessment will be conducted in four aspects: (i) the analysis of the residuals, (ii) the validation of the model by checking the predictive ability, (iii) the study of the effects of the number of registration points, and (iv) the study of the effects of the separation angles.

7.5.1 Analysis of the residuals

As stated before, the residuals are assumed to be identically and independently distributed normal random variables with zero mean and finite variance. Those assumptions are going to be checked by the residual analysis. The residuals in scanning angles are calculated by Eq. (6.13).

$$\left.\begin{aligned} \varepsilon_{\varphi_{P_i X}} &= -\varepsilon_{\theta_{P_i Y_L}} = -\left(\theta_{P_i Y_L} - \hat{\mu}_{P_i Y_L}\right) \\ \varepsilon_{\varphi_{P_i Y}} &= \varepsilon_{\theta_{P_i X_L}} = \theta_{P_i X_L} - \hat{\mu}_{P_i X_L} \end{aligned}\right\} \tag{7.16}$$

The normal probability plot of residuals is used to check if the residuals are normally distributed [5.5-5.6, 7.1]. If the inverse model is correct and the assumption of normality is appropriate, the plot should appear fairly straight.

For the residuals in different registration points, the assumptions that they are independent and have equal variance are acceptable. This is because that each registration point is independently measured by the same measurement tool and have the same measurement accuracy. For the same registration point, one needs to check if $\varepsilon_{\varphi_{P_i X}}$ and $\varepsilon_{\varphi_{P_i Y}}$ are uncorrelated and have equal variance. To check if they are uncorrelated, a linear correlation coefficient is calculated by [7.2]

$$\hat{\rho}_{\varepsilon_{\varphi_{ri}X}\varepsilon_{\varphi_{ri}Y}} = \frac{S_{\varepsilon_{\varphi_{ri}X}\varepsilon_{\varphi_{ri}Y}}}{S_{\varepsilon_{\varphi_{ri}X}} S_{\varepsilon_{\varphi_{ri}Y}}}. \tag{7.17}$$

To check if the variance of $\varepsilon_{\varphi_{ri}X}$ is equal to the variance of $\varepsilon_{\varphi_{ri}Y}$, two quantities are defined

$$MS\varepsilon_{\varphi_X} = \sqrt{\frac{1}{N}\sum_{i=1}^{N}\varepsilon_{\varphi_{ri}X}^2}\,, \text{ and } MS\varepsilon_{\varphi_Y} = \sqrt{\frac{1}{N}\sum_{i=1}^{N}\varepsilon_{\varphi_{ri}Y}^2}\,. \tag{7.18}$$

If the above two quantities are significantly different, one may suspect the equal variance assumption. In fact, the equal variance assumption have been verified twice in section **6.2.2** and section **7.3.2**, respectively.

The estimated mean and standard deviation of the residuals are calculated by Eqs. (7.19-7.20). Note Eq. (7.20) is the same as Eq. (5.58).

$$\hat{\mu}_{\varphi} = \frac{1}{2N}\sum_{i=1}^{N}\left(\varepsilon_{\varphi_{ri}X} + \varepsilon_{\varphi_{ri}Y}\right) \tag{7.19}$$

$$s_{\varphi} = \sqrt{\frac{1}{2N-6}\sum_{i=1}^{N}\left(\varepsilon_{\varphi_{ri}X}^2 + \varepsilon_{\varphi_{ri}Y}^2\right)} \tag{7.20}$$

Four sets of data have been collected for the analysis of the residuals. For the first three data sets, preselected 25 pair voltages are used. For the fourth data set, randomly generated (uniform distribution between -5 volts and 5 volts) 25 pairs of voltages are used. Figure 7.6 shows those points in scanning angles. Figure 7.6 (a) is for the first three data sets and Fig. 7.6 (b) is for the fourth data set. Note that they are not the locations of the 25 laser beam spots (registration points) on the graph paper.

The experimental setup and procedure for collecting those data are basically the same as those for the first repeatability test. One difference is that half a scale was used in measuring the position of the laser beam on the graph paper, which gives a resolution of 1/40 inches (0.635 mm). The distance between the board and the laser head was about 64 inches (1625.6 mm). The 1/40 inches (0.635 mm) resolution roughly gives a resolution of 0.0224 degrees in the scanning angles. The first three data sets were collected in one experiment but at different relative positions and orientations between the laser head and the graph paper. The fourth data set was collected during another experiment. As usual, the experiment began after the system was turned on for about two hours.

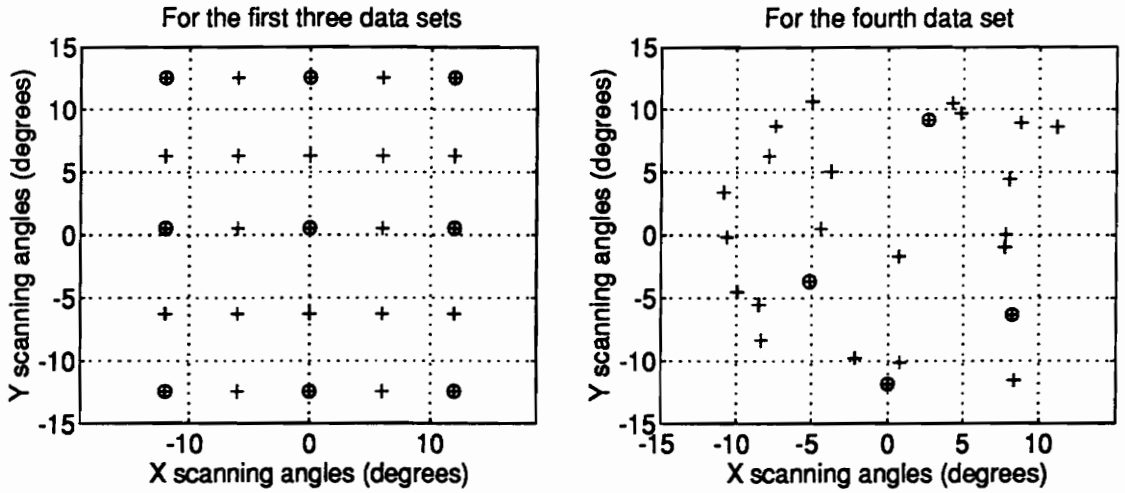

(a) (b)

Figure 7.6 The scanning angles for the 25 registration point

Table C.1 to C.4 in appendix C shows the four sets of data. In each table, the structural coordinates and the corresponding scanning angles shown were used to determine the pose of the SLDV. The residuals shown in the last two columns in each table were

calculated by Eq. (7.16) after the inverse model is fitted. The fitted scanning angles are obtained by using the estimated pose and the measured structural coordinates.

Table 7.7 shows the linear correlation coefficients (Eq. (7.17)), $MS\varepsilon_{\varphi_X}$, $MS\varepsilon_{\varphi_Y}$ (Eq. (7.18)), estimated mean and standard deviation of the residuals (Eqs. (7.19-7.20)) for all the four data sets.

Table 7.7 The correlation coefficients and other terms for the four data sets

Data set	$\hat{\rho}$	$MS\varepsilon_{\varphi_X}$ (degrees)	$MS\varepsilon_{\varphi_Y}$ (degrees)	$\hat{\mu}_{\varphi}$ (degrees)	s_{φ} (degrees)
1	0.1344	0.0110	0.0108	4.6667e-5	0.0116
2	-0.3650	0.0140	0.0118	8.2256e-5	0.0138
3	0.2764	0.0157	0.0144	8.5080e-5	0.0162
4	0.2067	0.0096	0.0085	1.5260e-5	0.0097

Figure 7.7 shows the normal probability plots for all the four data sets. From Fig. 7.7, one can see that the normal probability plots of the residuals for all the four data sets appear straight line. Thus, the residuals are from a normal distribution. The correlation coefficients shown in Table 7.7 are small, ε_{φ_X} and ε_{φ_Y} should not be considered to be correlated. The estimated means of the residuals for the four cases are very close to zero which is the assumption. The $MS\varepsilon_{\varphi_X}$ and $MS\varepsilon_{\varphi_Y}$ shown in Table 7.7 are not exactly the same. The difference is small. The equal variance assumption appears be acceptable again.

The results of the residual analysis have verified the assumption about the residuals in the inverse model. This also implies that the inverse model is a correct model. Therefore, the linear voltage-angle relation and the scanner model are correct models.

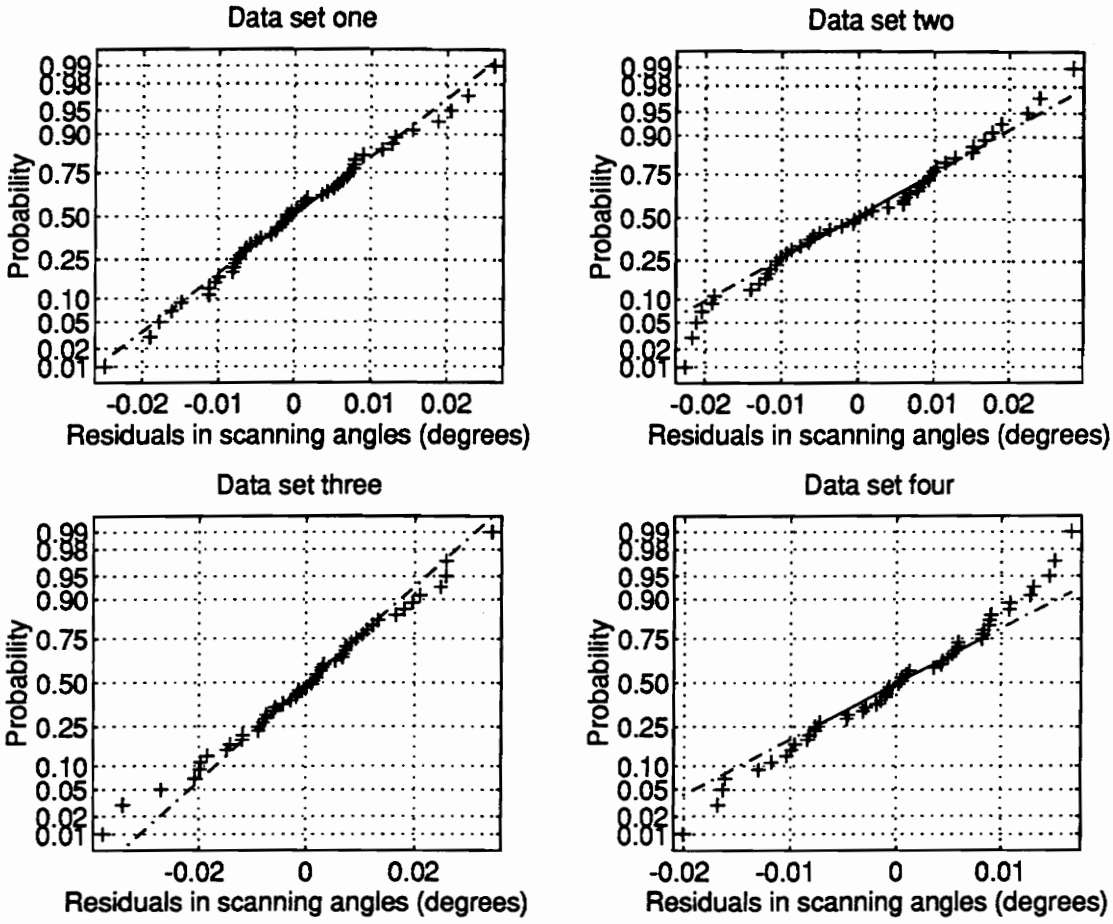

Figure 7.7 Normal probability plots of the residuals for all the four data sets

7.5.2 The validation of the inverse model

7.5.2.1 The procedure of model validation

In the last section, the inverse model was shown to be a correct model through residual analysis. This section will focus on the validation of the inverse model. There are several methods to validate a regression model [5.6]. The procedure used in this dissertation is the following.

I). Determination of the pose (fitting the inverse model)

The pose of the SLDV can be determined by using the information from current registration points.

II). Collection of new data

By collecting new data, one obtains the scanning angles and structural coordinates for a set of new registration points. For the experimental setup in the residual analysis, the new data may be collected in this way. A new set of voltage pairs is selected and sent to the D/A converter. The location of laser beam spot on the graph paper is measured for each voltage pair. The scanning angles are obtained by converting the selected voltage pairs through the use of Eq. (6.10). Thus, the structural coordinates and the corresponding scanning angles are obtained for the set of new registration points.

III). Verification of the predictive ability of the inverse model

The fitted scanning angles can be found for the new registration points by using the estimated pose and the structural coordinates which are from the newly collected data. This fitted scanning angles for the new registration points are called the predicted scanning angles. The prediction error is defined as the difference between the predicted scanning angles and the measuring scanning angle obtained in step (II).

$$\left.\begin{aligned} e_{\varphi_{P_j,X}} &= \varphi_{P_j,X} - \hat{\varphi}_{P_j,X} \\ e_{\varphi_{P_j,Y}} &= \varphi_{P_j,Y} - \hat{\varphi}_{P_j,Y} \end{aligned}\right\} \quad (\text{for } j=1, 2, ..., N1) \tag{7.21}$$

where $N1$ is the number of new registration points, $\varphi_{P_j,X}$ and $\varphi_{P_j,Y}$ are the measured scanning angles, and $\hat{\varphi}_{P_j,X}$ and $\hat{\varphi}_{P_j,Y}$ are the predicted scanning angles. By processing the

prediction error, the inverse model can be validated. There are two ways to process the prediction error. One way is to define a prediction standard deviation [5.6]

$$s_{Pre} = \sqrt{\frac{1}{2N1}\sum_{j=1}^{N1}\left(e^2_{\varphi_{r_j x}} + e^2_{\varphi_{r_j y}}\right)} \tag{7.22}$$

If s_{Pre} is fairly close to the estimated standard deviation, s_{φ}, of the residuals for the fitted inverse model, then the estimated standard deviation will give an appropriate indication of the predictive ability of the model.

The second way to process the prediction error is to use the confidence intervals. Using the fitted inverse model (estimated pose) and the structural coordinates of the new registration points, a confidence interval can be constructed for the expected scanning angles or for the prediction of the scanning angles. The calculation formulas for finding the intervals were derived in chapter 5 by linear approximation. If the prediction errors are within the interval, then the predictive ability of the model is good.

In practice, it is not necessary to collect new data. The data splitting technique can be used. A relatively large data set can be collected at one time. Part of the data set can be used to fit the model. The rest of the date set can be taken as newly collected data and used to check the inverse model and its predictive ability.

7.5.2.2 Model validation by data set one

Data set one, collected for the residual analysis, is used here to validate the inverse model. For that data set, 25 registration points are available. Using the data splitting technique, the 25 registration points are separated into two groups. The first group have nine

registration points. They are used to fit the inverse model. The scanning angles for the 9 points are shown in Fig. 7.6 (a) with the "o" enclosing the "+". They are almost uniformly located. The reason for this is that extrapolation should be avoided in predicting a scanning angle. That is also the way for selecting registration points in experimental data acquisition. The point ID for the 9 points are 1, 3, 5, 11, 13, 15, 21, 23, and 25 as shown in Table C.1. The other 16 points in Table C.1 are taken as the newly collected data and used to check the inverse model and its predictive ability.

The selected 9 registration points are used to determine the pose. The estimated standard deviation of the residuals for this fitting is calculated by Eq. (7.20).

$$s_{\varphi}=0.0144 \text{ (degrees)} \tag{7.23}$$

The maximum relative curvatures are

$$\eta_{max}^{PE}=0.0561, \text{ and } \eta_{max}^{IN}=0.0185. \tag{7.24}$$

Both of them are less than the CC.

$$CC=1/\left(2\sqrt{F(6,12;\ 0.05)}\right)=0.2889 \tag{7.25}$$

Thus, the statistical inferences by linear approximation are acceptable.

The residuals for the 9 registration points, the prediction errors for the 16 "new" registration points were calculated by using the obtained pose and the structural coordinates. The confidence intervals and prediction intervals for the 9 registration points and for the 16 "new" registration points were calculated by using Eq. (5.66) and (5.69). All those results are shown in Table C.5 and Table C.6. Table C.5 is for the 9 registration points. Column 1 is the point ID. Column 2 to column 4 are for the X scanning angles. Column 2 is the residual ε_{φ_x}. Column 3 is half of the length of confidence interval for the expected X scanning angles. Column 4 is half of the length of the prediction interval of the

prediction of the X scanning angles. Column 5 to column 7 are for the Y scanning angles. They have the same explanation as those for column 2 to column 4. Table C.6 is for the 16 "new" registration points. They have the same explanations as those for Table C.5 except that column 2 and 5 are the prediction error e_{φ_X} and e_{φ_Y}, respectively.

Using Eq. (7.22) and the data in Table C.6, the prediction standard deviation is found as

$$s_{Pre}=0.0114 \text{ (degrees)}. \tag{7.26}$$

Figure 7.8 shows the residuals, the confidence intervals, and the prediction intervals for the 9 registration points. The fitted scanning angles are not shown. The order in horizontal direction is the order in Table C.5. This order does not have any special meaning. The two broken lines close to the center are the confidence intervals for the expected scanning angles. The two solid lines in the top and the bottom are the prediction intervals for the prediction of the scanning angles. The purpose of connecting those intervals with a line is purely for visualization since the order in horizontal direction does not show any meaning. The 'o's in the plots are the residuals.

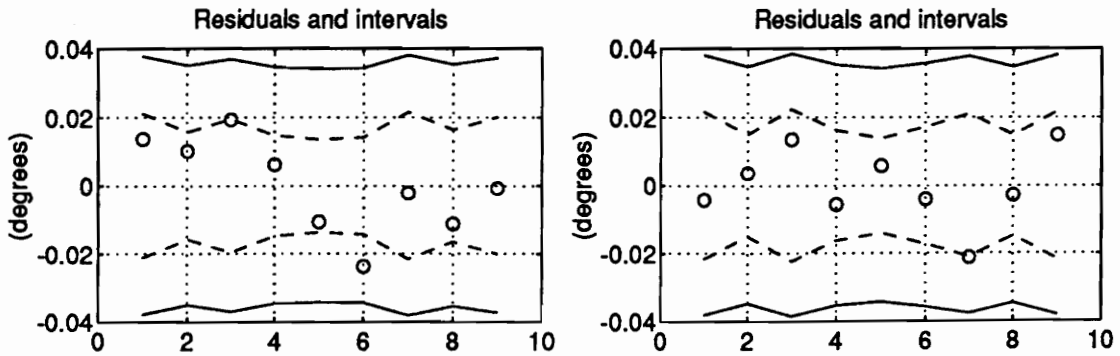

(a) For X scanning angle (b) For Y scanning angle

"--": 95% confidence intervals, "-": 95% prediction intervals

Figure 7.8 The residuals and confidence intervals for the 9 registration points

Figure 7.9 shows the prediction errors, the confidence intervals, and the prediction intervals for all the sixteen "new" registration points. The 'o's in the plots are the prediction errors. The others in the plots have the same meanings as those for Fig. 7.8.

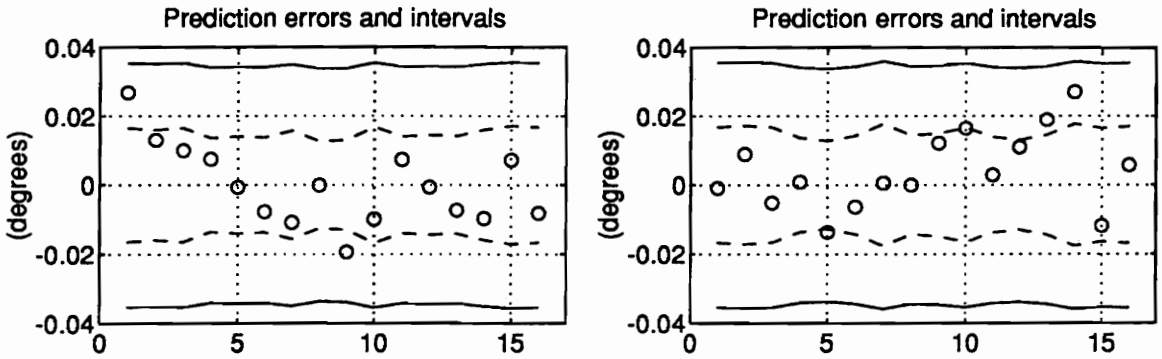

(a) For X scanning angle (b) For Y scanning angle

"--": 95% confidence intervals, "-": 95% prediction intervals

Figure 7.9 The residuals and confidence intervals for the 16 "new" registration points

Comparing Eq. (7.23) with Eq. (7.26), one finds that the s_{Pre} is close to the estimated standard deviation s_{φ}. From Fig. 7.8 and Fig. 7.9, one can see that although some residuals and prediction errors are out of the confidence intervals of the expected scanning angles, they are within the prediction intervals. Those results show that the fitted inverse model is a valid model. The predictive ability of the fitted model is good and can be trusted. Therefore, the inverse model is an acceptable model

7.5.3 Effects of number of registration points

In chapter 2, it was pointed out that at least four noncollinear registration points are required for a unique solution of the pose of the SLDV. The asymptotic normality in

chapter 5 shows that the more the number of registration points, the better. However, only limited number of registration points can be taken in the real data case. Therefore, one would like to know the minimum acceptable number of registration points in a statistical sense.

To answer this question, two things needs considering. One is the standard deviation. It is known that as the number of registration points increases, the estimated standard deviation of the residuals will be reduced. In the limit, it will be the true standard deviation of the residuals. In practice, after a certain number of registration points, using more points will not significantly reduce the estimated standard deviation any more. The other is the nonlinearity of inverse model. As the number of registration points increases, the maximum relative parameter-effects curvature and the intrinsic curvature will be reduced and the curvature criterion (*CC*) will increase. Even if the nonlinearity is high for a few registration points, it may be reduced to an acceptable level with more registration points. On the basis of these discussions, the minimum acceptable number of the registration points would be a number *Na* at which the maximum relative curvature is less than the *CC* and the estimated standard deviation is close to the true standard deviation (no significant reduction can be seen in the estimated standard deviation by using more registration points than *Na*).

The data collected for residual analyses has been used to study the effects of the number of registration points. For each data set, the estimated standard deviation, the $MS\varepsilon_{\varphi_x}$, the $MS\varepsilon_{\varphi_y}$, the maximum relative parameter-effects curvature, the maximum relative intrinsic curvature, and the *CC* are calculated as a function of the number of registration points. For the first three data sets, the order of the registration points was rearranged such that

the first four points are the four registration points in the four corners as shown in Fig. 7.6 (a), and the order of the other points was random. For the fourth data set, its order was already random since the registration points were randomly generated. The first four registration points are shown in Fig. 7.6 (b) with the "o" enclosing the "+". For each data set, 22 test cases (for N=4, ..., 25) were available. When k (k=4, ..., 25) registration points were used for a test case, the first k registration points were picked up.

Figures 7.10 and 7.11 show the results of all test cases. In figure 7.10, the estimated standard deviation, $MS\varepsilon_{\varphi_X}$, and $MS\varepsilon_{\varphi_Y}$ are shown to change with the number of registration points. As the number of registration point increases, the estimated standard deviation decreases. From the plots, the estimated standard deviations stabilize roughly at 9 or 10 registration points for the four cases. One can see from the picture that the $MS\varepsilon_{\varphi_X}$ and $MS\varepsilon_{\varphi_Y}$ are not the same. For some cases, the $MS\varepsilon_{\varphi_X}$ is larger than the $MS\varepsilon_{\varphi_Y}$. For other cases, the $MS\varepsilon_{\varphi_X}$ is smaller than the $MS\varepsilon_{\varphi_Y}$. The difference between them is small. One can also see that the estimated standard deviations with all 25 points being used are not the same. This will be further studied by more experiments in chapter 8.

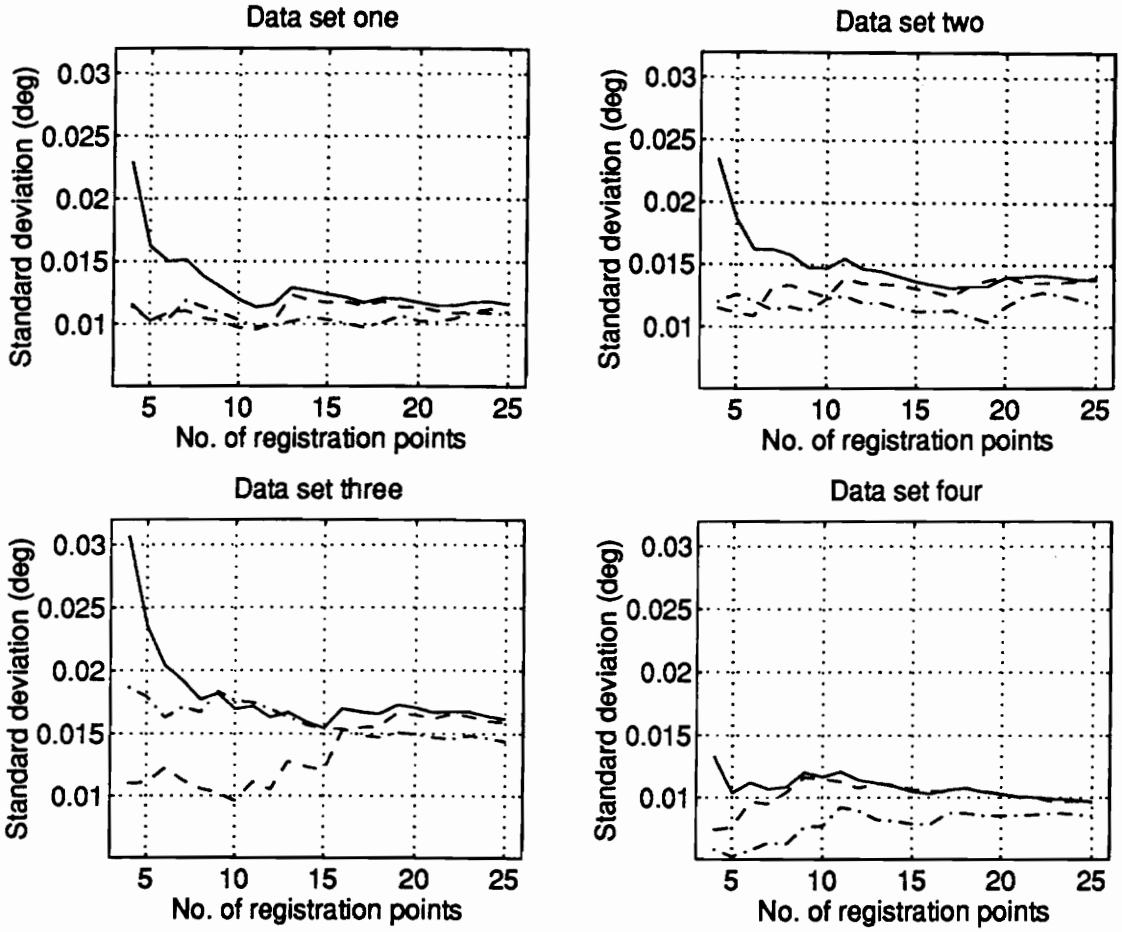

"-": Estimated standard deviation, "--": $MS\varepsilon_{\varphi_X}$, "---": $MS\varepsilon_{\varphi_Y}$

Figure 7.10 Standard deviations versus the number of registration points

Figure 7.11 shows that as the number of registration points increases, (i) the maximum relative curvatures decreases and (ii) the *CC* increases. For the first three data sets, the maximum relative parameter-effects curvatures are less the *CC* even for four registration points. For the fourth data set, when N=7, the maximum relative parameter-effects curvature becomes less than the *CC*. One can also see that the maximum intrinsic curvature is always less than the maximum relative parameter-effects curvature. This is true for almost every nonlinear regression problem [5.4-5.5, 5.10]

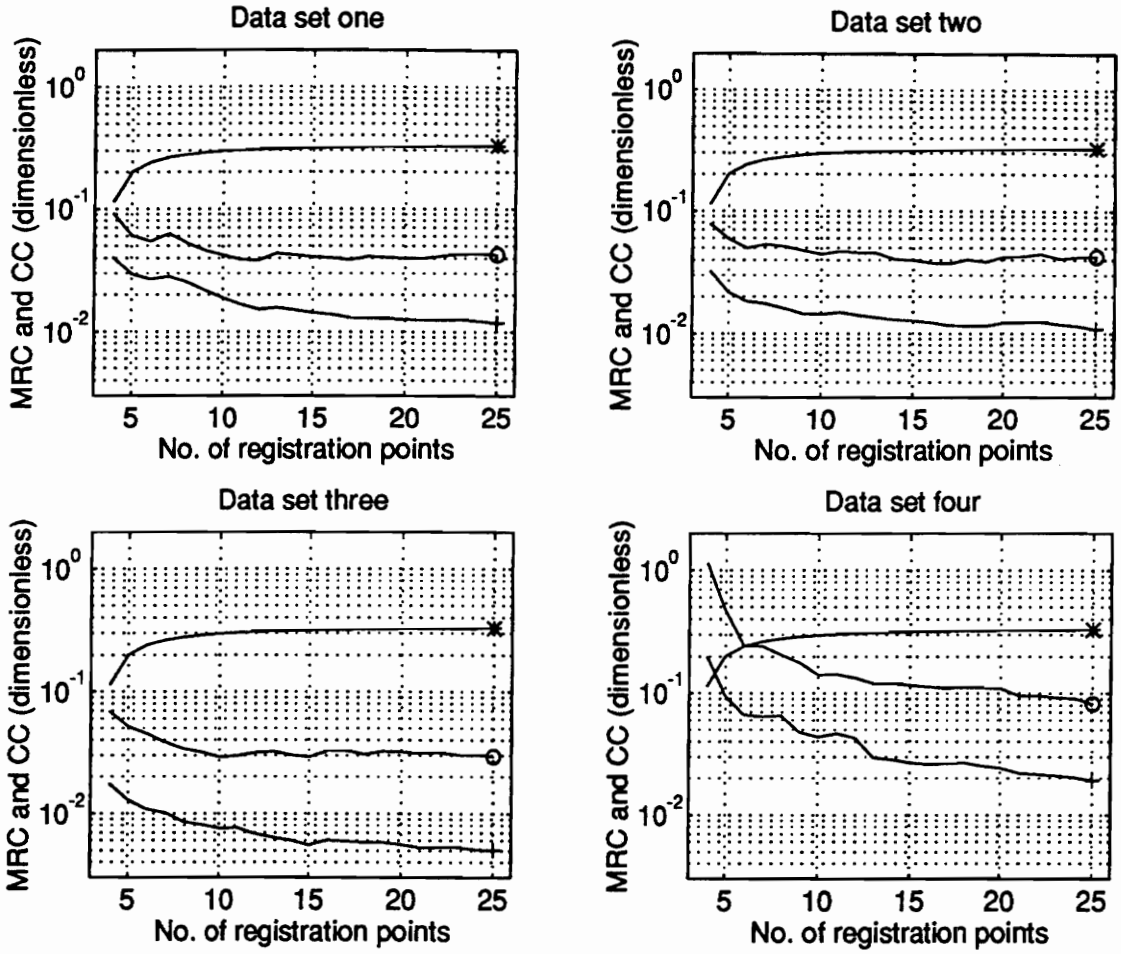

MRC: Maximum Relative Curvature, CC: Curvature Criterion

"*": Curvature criterion, "o": ρ_{max}^{PE}, "+": ρ_{max}^{IN}

Figure 7.11 Maximum relative curvatures versus the number of registration points

From the results of the four data sets, one can see that nine can be a minimum acceptable number of registration points. Since the curvatures are less than the *CC* at that number and the estimated standard deviation will not be significantly reduced after that number.

7.5.4 Effects of the separation angles

It can be seen from the Figs. 7.10 and 7.11 that when N=4, the relative maximum parameter-effects curvature for the first three data sets is much smaller than that for the fourth data set. Figures 7.10 and 7.11 also show that when N=4, the estimated standard deviation for the first three data sets is larger than that for the fourth data set. From Fig. 7.6, one can see that for the first three data sets, the points on the corner were the first four registration points. Their separation angles are larger than those of the four registration points in the fourth data set. The separation angle is defined as the view angle between two registration points as viewed from the laser head. What has been observed from the plots indicates that larger separation angles have smaller curvatures but larger estimated standard deviations. Large separation angles refers to that the separation angle between any two registration points out of the four is relatively large. If more than four registration points are used, the four registration points forming the largest quadrilateral will be considered.

To verify the observations and study the effects of the separation angles, two simulation tests were completed. The first one was designed to check if the estimated standard deviation depends on the separation angles. The second one was designed to check if the maximum relative curvature depends on the separation angles.

7.5.4.1 Estimated standard deviation and separation angles

For this test, two cases were considered. Each case had four registration points. One case had small separation angles (10 degrees along horizontal and vertical directions) while the

other large (25 degrees along horizontal and vertical directions). By assuming a range for all the registration points and the pose of the structural coordinate system, the simulated structural coordinates can be obtained for all registration points. The following is the assumed values.

$L_{P_i} = 60$ inches (1549.4 mm) (for all eight registration points in two cases)

$\gamma_1 = 10$ inches (254 mm), $\gamma_2 = 10$ inches (254 mm), $\gamma_3 = 100$ inches (2540 mm)(7.27)

$\gamma_4 = \pi$, $\gamma_5 = \pi / 3$, $\gamma_6 = \pi / 10$

Table 7.8 shows the scanning angles for the two cases.

Table 7.8 The scanning angles for the two test cases

Point ID	Case one (degrees)		Case two (degrees)	
	φ_X	φ_Y	φ_X	φ_Y
1	-5	5	-12.5	12.5
2	5	5	12.5	12.5
3	-5	-5	-12.5	-12.5
4	5	-5	12.5	-12.5

Random normal errors $N(0, 0.010(\text{degrees}))$ were added to the scanning angles for both cases. Thus, the two cases have the same measurement errors. Using these error-contaminated scanning angles and the simulated structural coordinates, the pose of the structural coordinates system and standard deviation of the residuals in scanning angles were estimated for each case. After repeating 100 times, 100 estimated standard deviations were obtained. The estimated standard deviations for the two cases are statistically the same. The average of the estimated standard deviation is about 0.0081 (degrees) for case one (the small separation angle case) while the average of the estimated standard deviations is about 0.0082 (degrees) for case two (the large separation angle

case). From this result, one can say that the accuracy of the developed algorithm is not dependent on the separation angles.

7.5.4.2 Relative curvatures and separation angles

For this test, four registration points were used. Two situations were considered. One is for small scanning angles. The other is for larger scanning angles. The following is the details of this test.

The assumed range (same for the four registration points and for all test cases) is

$$L_{P_i} = 60 \text{ inches (1524 mm).} \tag{7.28}$$

Three different poses are used in this simulation test. Equations (7.29), (7.30), and (7.31) are for poses one, two and three, respectively.

$$\left.\begin{array}{l}\gamma_1 = 10 \text{ inches} (254 \text{ mm}),\ \gamma_2 = 10 \text{ inches} (254 \text{ mm}),\ \gamma_3 = 100 \text{ inches} (2540 \text{ mm}) \\ \gamma_4 = \pi/4,\ \gamma_4 = \pi/10,\ \gamma_4 = \pi/3\end{array}\right\} \tag{7.29}$$

$$\left.\begin{array}{l}\gamma_1 = 10 \text{ inches} (254 \text{ mm}),\ \gamma_2 = 10 \text{ inches} (254 \text{ mm}),\ \gamma_3 = 100 \text{ inches} (2540 \text{ mm}) \\ \gamma_4 = \pi/4,\ \gamma_4 = 0,\ \gamma_4 = \pi/3\end{array}\right\} \tag{7.30}$$

$$\left.\begin{array}{l}\gamma_1 = 10 \text{ inches} (254 \text{ mm}),\ \gamma_2 = 10 \text{ inches} (254 \text{ mm}),\ \gamma_3 = 80 \text{ inches} (2032 \text{ mm}) \\ \gamma_4 = \pi/4,\ \gamma_4 = \pi/10,\ \gamma_4 = \pi/3\end{array}\right\} \tag{7.31}$$

The estimated standard deviation of the residuals is assumed to be

$$s_{\varepsilon_\varphi} = 1 \times 10^{-4} \text{ (radians).} \tag{7.32}$$

Those assumed values (Eq. 7.28-32) are used in the two situations.

Table 7.9 shows the pattern of the scanning angles for four registration points, i.e., the four points are symmetrical in the sense of the scanning angles. The φ_0 in Table 7.9 is defined as the scanning angle for the symmetrical point. The φ_0 was equal to zero degrees for the small scanning angle situation and 60 degrees for the large scanning angle situation. The φ_{os} in Table 7.9 is defined as the scanning angle offset. There were five test cases for each of the three poses and each of the two situations. The scanning angle offsets for the five cases were 2.5, 5, 7,5, 10 and 12.5 degrees. Note that the larger the scanning angle offset, the larger the separation angles.

Table 7.9 Scanning angle pattern for four points in simulation test

Point ID	1	2	3	4
X scanning angles	$\varphi_0 - \varphi_{os}$	$\varphi_0 + \varphi_{os}$	$\varphi_0 - \varphi_{os}$	$\varphi_0 + \varphi_{os}$
Y scanning angles	$\varphi_0 + \varphi_{os}$	$\varphi_0 + \varphi_{os}$	$\varphi_0 - \varphi_{os}$	$\varphi_0 - \varphi_{os}$

The simulated structural coordinates were calculated for each test case by using the assumed ranges, scanning angles, and poses. The maximum relative parameter-effects curvature and the intrinsic curvature were calculated for the thirty test cases by using assumed pose and the simulated structural coordinates. Table 7.10 shows the results for small scanning angle situation. Table 7.11 shows the results for the lager scanning angle situations.

Table 7.10 The maximum relative curvatures for the small scanning angle situation

Case number	φ_X, φ_Y (degrees)	Pose one		Pose two		Pose three	
		ρ_{max}^{PE}	ρ_{max}^{IN}	ρ_{max}^{PE}	ρ_{max}^{IN}	ρ_{max}^{PE}	ρ_{max}^{IN}
1	2.5	8.9020	1.0964	8.4912	1.0964	8.3258	1.0964
2	5.0	0.6409	0.1390	0.5976	0.1390	0.5570	0.1390
3	7.5	0.1517	0.0421	0.1376	0.0421	0.1213	0.0421
4	10.0	0.0576	0.0183	0.0514	0.0183	0.0433	0.0183
5	12.5	0.0280	0.0098	0.0250	0.0098	0.0205	0.0098

Table 7.11 The maximum relative curvatures for the large scanning angle situation

Case number	φ_{os} (degrees)	Pose one		Pose two		Pose three	
		ρ_{max}^{PE}	ρ_{max}^{IN}	ρ_{max}^{PE}	ρ_{max}^{IN}	ρ_{max}^{PE}	ρ_{max}^{IN}
1	2.5	619.62	4.5321	539.96	4.5321	490.28	4.5321
2	5.0	39.742	0.5509	34.566	0.5509	31.505	0.5509
3	7.5	8.2032	0.1556	7.1134	0.1556	6.5217	0.1556
4	10.0	2.7663	0.0611	2.3893	0.0611	2.2071	0.0611
5	12.5	1.2355	0.0284	1.0622	0.0284	0.9896	0.0284

It can be seen from Tables 7.10 and 7.11 that the maximum relative curvatures decrease with the increase of the separation angles for all the three poses. This agrees with the results shown in Fig. 7.11 The results also shows that the maximum relative intrinsic curvatures do not vary with different poses, which is expected. The curvatures for the large scanning angle situation is much larger than those for the small scanning angle situation. Note that the four registration points for the large scanning angle situation were in the same quadrant (quadrant I as specified in Fig. 2.2).

Compared to the smaller separation angles, the larger separation angles have smaller curvatures and same accuracy (same estimated standard deviation) as the small separation

angles. Therefore, larger separation angles should be used if it is possible in the data acquisition. Also, the registration points should be distributed in the four quadrants, which can be achieved by approximately putting the laser beam home position at the center of the area to be scanned.

7.6 Summary

This chapter has focused on the assessment of the inverse model. In section **7.1**, the inverse model and its assumptions are reviewed. In section **7.2**, the error sources involved in determination of the SLDV pose have been discussed. There are two kinds of errors: measurement errors and modeling errors. In the **7.3**, the linear voltage-angle relation for the scanner has been shown acceptable. In section **7.4**, it has been found by two experiments that the repeatability of the currently-used D/A converter and the scanner is excellent. The standard deviation for the D/A converter is about 0.1 millivolts. The repeatability error (standard deviation) of the scanner is about 0.0012 degrees in the scanning angles. In section **7.5**, the inverse model has been assessed in four aspects. Through analyzing the residuals in the scanning angles, it is found that the residuals agree with their assumptions. Thus, the inverse model is a correct model, which implies that the linear voltage-angle relation and the scanner model are valid. By using a data split technique, the fitted model is confirmed to have good predictive ability. By studying the effects of the number of registration points, it is found that nine would be a minimum acceptable number of registration points after the estimated standard deviations and the curvatures have taken into account. By studying the effects of separation angles through the use of simulated data, it is found that the accuracy for larger separation angle is the same as that for small separation angle if the measurement errors are the same. It is also

found that if the separation angles are larger, the maximum relative parameter-effects and the maximum relative intrinsic curvatures will be smaller. The simulation results also show that the curvatures for the situation that four points are in four quadrants (small scanning angle situation) are smaller than those for the situation that the four points are in the same quadrant (large scanning angle situation) even though the separation angles are the same for both situations.

CHAPTER EIGHT

CALIBRATION OF THE SCANNER AND THE ACCURACY EVALUATION OF THE DEVELOPED ALGORITHM

In this chapter, a new algorithm based on the inverse model will be developed for calibrating the scanner. The algorithm's implementation and application in calibration will be presented. Several experiments will be conducted to evaluate the accuracy of the developed (chapter 4 and 5) and implemented (chapter 6) algorithm in determining the SLDV pose. The results of the experiments will be given. The results obtained by using the newly calibrated scanner parameters will be compared with the results obtained by using the current scanner parameters.

8.1 Calibration of the scanner by a nonlinear regression

In the last chapter, the linear voltage-angle relations for the two mirrors have been verified. The currently used parameters a_X, a_Y, b_X, b_Y are obtained by the one-dimensional calibration method. As shown in Fig. 7.1, the distance between the laser head and the *OP* line needs to be measured. The orientation of the laser head relative to the *OP* line also needs adjusting. Both operations introduce measurement errors. It is desirable to calibrate the scanner without involving those operations, i.e., to calibrate the scanner by just using the input voltages and the structural coordinates. These variables can be directly measured.

This section will develop a new algorithm based on the inverse model for calibrating the scanner by just using the input voltages and the structural coordinates. The developed algorithm is able to calibrate the five scanner parameters simultaneously.

8.1.1 Development of the new algorithm for calibration

The nonlinear regressive model expresses the input voltages as functions of the structural coordinates. Figure 2.6 has shown this procedure. Equation (2.7) can also be written as

$$\left.\begin{aligned} V_X &= A_X + B_X \varphi_X \\ V_Y &= A_Y + B_Y \varphi_Y \end{aligned}\right\}. \tag{8.1}$$

Comparing Eq. (8.1) with Eq. (2.7), one has

$$\left.\begin{aligned} A_X &= -a_X / b_X, \; B_X = 1/b_X \\ A_Y &= -a_Y / b_Y, \; B_Y = 1/b_Y \end{aligned}\right\}. \tag{8.2}$$

From Eq. (5.4), Eq. (2.9), and Eq. (8.1), the following equation is obtained.

$$\left.\begin{aligned} V_{P,X} &= A_X + B_X \left(-tan^{-1}\left(\frac{x_{P,L}}{\sqrt{y_{P,L}^2 + z_{P,L}^2} + dl} \right) \right) \\ V_{P,Y} &= A_Y + B_Y \, tan^{-1}\left(\frac{y_{P,L}}{z_{P,L}} \right) \end{aligned}\right\} \tag{8.3}$$

where the laser coordinates ($x_{P,L}$, $y_{P,L}$, $z_{P,L}$) are calculated by Eq. (5.3), i.e.,

$$\begin{Bmatrix} x_P \\ y_P \\ z_P \end{Bmatrix}_L = {}^L_S\{T\} + {}^L_S[R] \begin{Bmatrix} x_P \\ y_P \\ z_P \end{Bmatrix}_S \tag{8.4}$$

Equations (8.3-8.4) show that the input voltages ($V_{P,X}$, $V_{P,Y}$) are expressed as functions of the structural coordinates ($x_{P,S}$, $y_{P,S}$, $z_{P,S}$). Considering the measurement errors, the following equation can be obtained for registration point P_i

$$\left.\begin{aligned} V_{P_i,X} &= A_X + B_X\left(-tan^{-1}\left(\frac{x_{P_i,L}}{\sqrt{y_{P_i,L}^2 + z_{P_i,L}^2} + dl}\right)\right) + \varepsilon_{V_{P_i,X}} \\ V_{P_i,Y} &= A_Y + B_Y\, tan^{-1}\left(\frac{y_{P_i,L}}{z_{P_i,L}}\right) + \varepsilon_{V_{P_i,Y}} \end{aligned}\right\} \qquad (8.5)$$

Equations (8.4-8.5) form a regressive model. The structural coordinates in Eq. (8.4) are the regressor variables. The input voltages in Eq. (8.5) are the response variables. The last two terms in Eq. (8.5) are the residuals which account for the measurements errors. They are assumed to be identically and independently distributed normal random variable with zero mean and finite variance. The parameters in this model include the six pose parameters and the five scanner parameters. The input voltages are linear functions of A_X and A_Y, but they are nonlinear functions of the six pose parameters and other scanner parameters. Therefore, the developed regressive model is a nonlinear model.

The eleven parameters in this nonlinear model can be obtained by using the least squares technique. Expressing the rotation matrix by the three Euler angles, the following optimization model can be formed after applying the least squares method to Eq. (8.5).

$$\left.\begin{aligned} &\text{Find } {}^{L}_{S}\{T\},\ \alpha,\ \beta,\ \gamma,\ A_X,\ B_X,\ A_Y,\ B_Y,\ dl \text{ that} \\ &\text{minimize } Q = \sum_{i=1}^{N}\left(\varepsilon_{V_{P_i,X}}^2 + \varepsilon_{V_{P_i,Y}}^2\right) \end{aligned}\right\} \qquad (8.6)$$

When the minimum of the function Q in the above equation is achieved, the parameters are obtained.

8.1.2 Implementation of the new algorithm and sensitivity analysis

The developed algorithm for calibrating the scanner parameters has been implemented in Matlab. Using the current scanning parameters, the pose of the structural coordinate system can be found by using the techniques developed in chapter 4 and chapter 5. The obtained pose parameters and the current scanner parameters are excellent initial values for the optimization algorithm to find the minimum of the function Q defined in Eq. (8.6).

After the implementation, a set of simulated data is generated for testing the implementation and for sensitivity analysis. The simulated data are formed in following steps. (i) The values for the eleven parameters are assumed. (ii) A set of voltages and a set of ranges for 25 registration points are formed. (iii) The related equations developed in chapter 2 are used to obtain the structural coordinates for the 25 points.

The function Q defined in Eq. (8.6) is a function of the eleven parameters. For the simulated data, Q is equal to zero at the assumed values of the eleven parameters. By varying one parameter (holding the rest at the assumed value) around its assumed value at a time, one can study the sensitivity of the function Q with respect to the eleven parameters. It is found that the Q is sensitive to the six pose parameters and two scanner parameters B_X and B_Y. The function Q is less sensitive to the other two scanner parameters A_X and A_Y. The function Q is very insensitive to the separation distance *dl*. Figure 8.1 shows how Q changes with *dl*. According to this result, the separation distance

dl is dropped from the calibration parameters. The current value (*dl*=46 mm) from the manufacture will be used in the pose determination algorithm and the calibration algorithm.

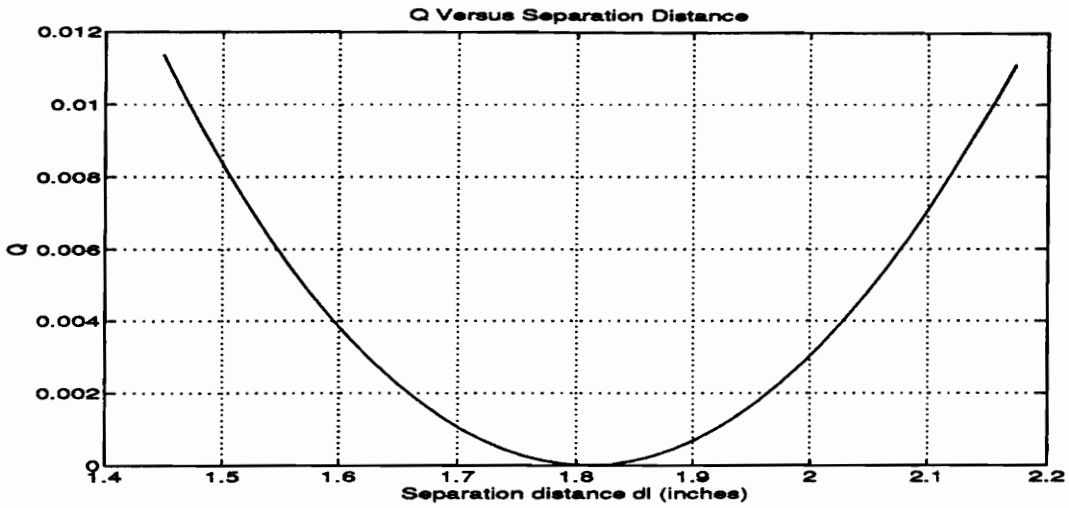

Figure 8.1 The sensitivity of the function Q to the separation distance *dl*

After dropping the *dl* from the parameters, the following optimization model is implemented.

$$\left.\begin{aligned} &\text{Find } {}^{L}_{S}\{T\},\ \alpha,\ \beta,\ \gamma,\ A_X,\ B_X,\ A_Y,\ B_Y \text{ that} \\ &\text{minimize } Q = \sum_{i=1}^{N}\left(\varepsilon^2_{V_{n_X}} + \varepsilon^2_{V_{n_Y}}\right) \end{aligned}\right\} \tag{8.7}$$

Using the simulated data, the implemented algorithm is tested. The results show that the implemented algorithm is able to recalculate the assumed values from an initial solution different from the assumed value.

8.1.3 Calibration experiment and results

The experimental setup for calibration was basically the same as that shown in Fig. 7.3. For convenience, it is repeated here. Figure 8.2 shows the board and the laser head only. However, a 48" by 96" (1912.2 by 2438.4 mm^2) board and a 36" by 96" (914.4 by 2438.4 mm^2) graph paper were used. Only a 36" by 36" (914.4 by 914.4 mm^2) area was used in the calibration. The graph paper has 10 scales per inch. The grid lines were marked form left to right and from top to bottom, resulting in a structural coordinate system shown in Fig. 8.2. The laser head was roughly aligned with the board, i.e., the *HH* line shown in Fig. 2.2 overlapped a horizontal grid line and the *VV* line a vertical grid line. The home position of the laser beam was on the center of the 36" by 36" (914.4 by 914.4 mm^2) area. The distance between the laser head and the graph paper was adjusted such that the laser beam would just cover the desired area (about 34" by 34" (863.6 by 863.6 mm^2)) at the maximum input voltages. Measured from the center of the laser head box, this distance was about 80 inches (2032 mm).

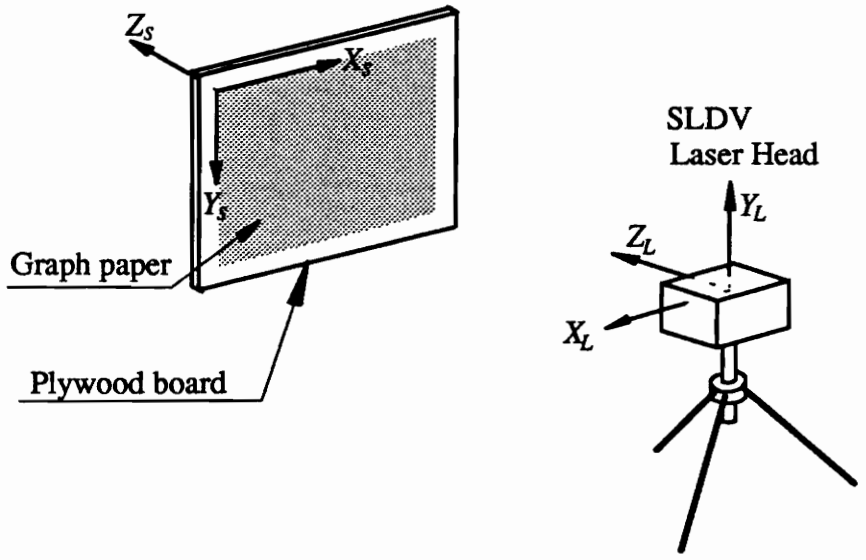

Figure 8.2 The experimental setup for the calibration experiment

For the calibration, 48 registration preselected points were used. Figure 8.3 shows the locations of the 48 points on the graph paper.

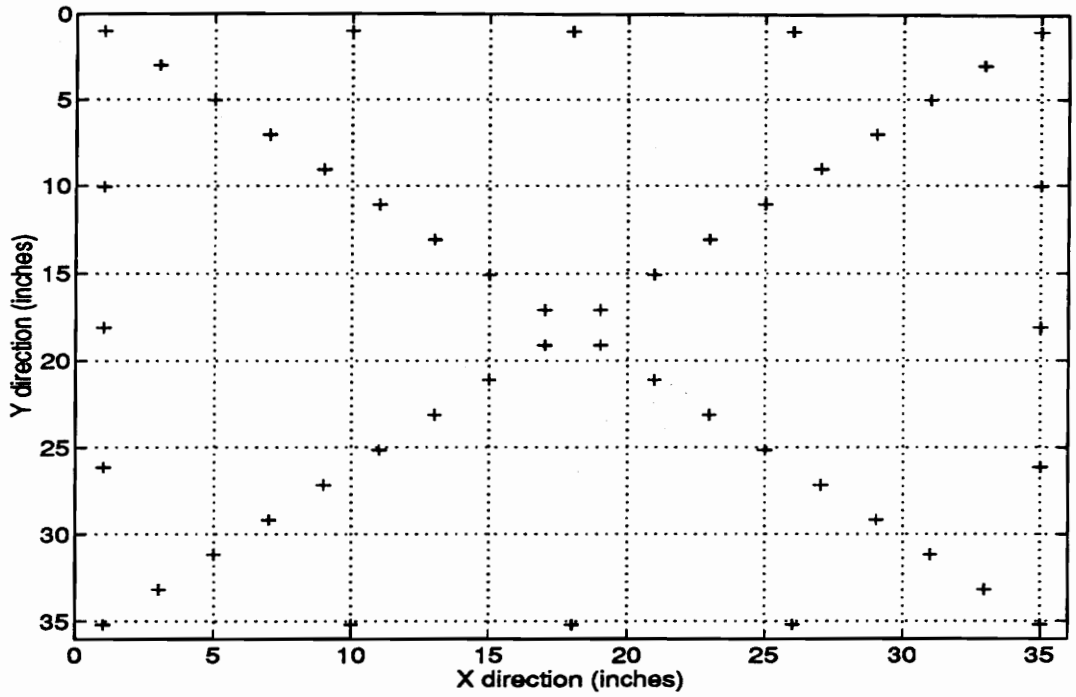

Figure 8.3 The selected 48 points for the calibration

As always, the measurements begin after the system is turned on for about two hours. The following is the experimental procedure.

I). The laser beam is manually aimed to the upper left corner by applying a positive 5 volts to the scanner controller for *Y* mirror and negative 5 volts for the *X* mirror.

II). The laser beam is manual aimed at the first preselected registration points on the graph paper from the upper left corner. The registration points are the crossing points of the grid

lines. If the laser beam is moved beyond the registration point, the laser beam is returned to the upper left corner. The purpose of doing this is to eliminate the hysteresis error.

III). Once the laser beam hits the registration point, the input voltages are recorded.

VI). Repeat steps (I) to (III) for all the 48 registration points.

Table C.7 in appendix C shows the measured data and the obtained residuals of the input voltages after completing the nonlinear fit. The following is the estimated scanner parameters from the nonlinear regression by using the data in Table C.7.

$$\left.\begin{aligned} a_X &= -0.3890,\ b_X = 2.3732 \\ a_Y &= 0.6624,\ b_Y = 2.4727 \end{aligned}\right\} \tag{8.8}$$

The estimated mean and standard deviation of residuals are

$$\hat{\mu}_V = \frac{1}{96}\sum_{i=1}^{48}\left(\varepsilon_{V_{R_i X}} + \varepsilon_{V_{R_i Y}}\right) = -1.29\times10^{-11}\,(\text{volts}) \tag{8.9}$$

$$s_V = \sqrt{\frac{Q}{2\times48-10}} = 0.0052\ (\text{volts}) \tag{8.10}$$

The estimated linear correlation coefficient is

$$\hat{\rho}_{\varepsilon_{V_{R_i X}},\varepsilon_{V_{R_i Y}}} = \frac{S_{\varepsilon_{V_{R_i X}},\varepsilon_{V_{R_i Y}}}}{S_{\varepsilon_{V_{R_i X}}} S_{\varepsilon_{V_{R_i Y}}}} = 0.0131 \tag{8.11}$$

Figure 8.4 is the normal probability plot for the residuals. Figure 8.5 plots the residuals versus the input voltages. The upper plot is for residuals ε_{V_X} and input voltages V_X. The

lower plot is for residuals ε_{V_Y} and input voltages V_Y. In both figures, dVx, Vx, dVy, and Vy present ε_{V_X}, V_X, ε_{V_Y}, and V_Y, respectively.

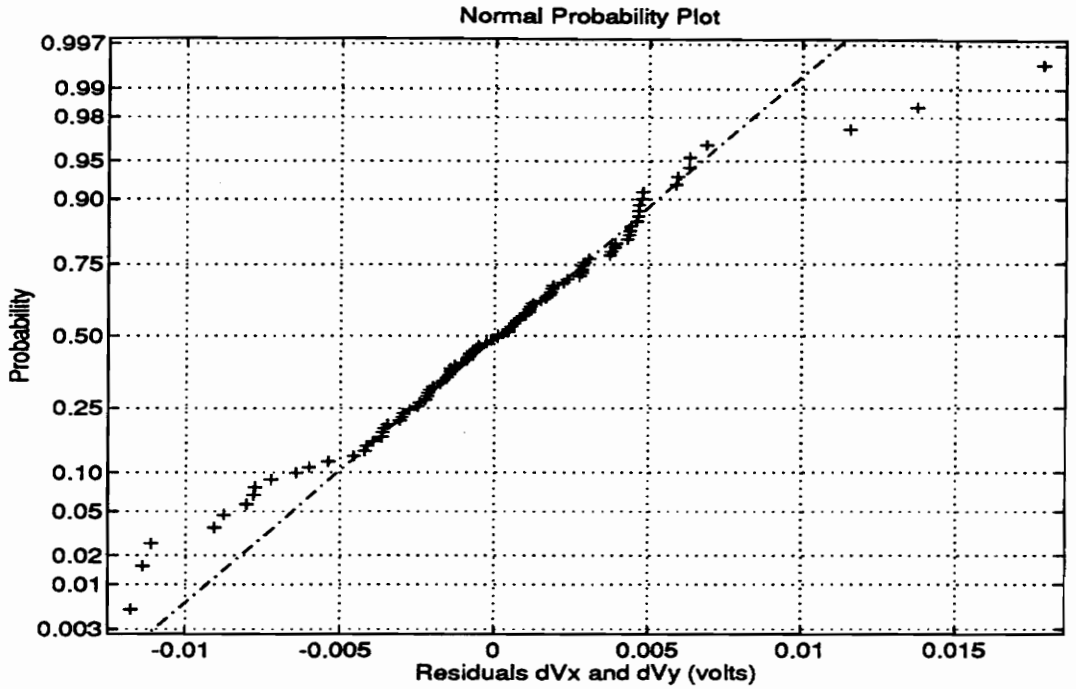

Figure 8.4 The normal probability plot of residuals for the calibration experiment

From Fig. 8.4, one can see that although a few points are away from the straight line, the data points appear fairly linear. In Fig. 8.5, no clear function relationships are shown between the residuals and the input voltages. The mean of the residuals is almost zero as shown in Eq. (8.9). The correlation coefficient is about 0.0131. According to these results, the residuals $\varepsilon_{V_{nX}}$ and $\varepsilon_{V_{nY}}$ agree with the assumption made about them. Thus, the nonlinear model for calibrating the scanner and the estimated parameters is acceptable. Once again, the inverse model is also verified since the nonlinear model for calibration is based on the inverse model. The calibrated four scanner parameters in Eq. (8.8) can be used in the future work.

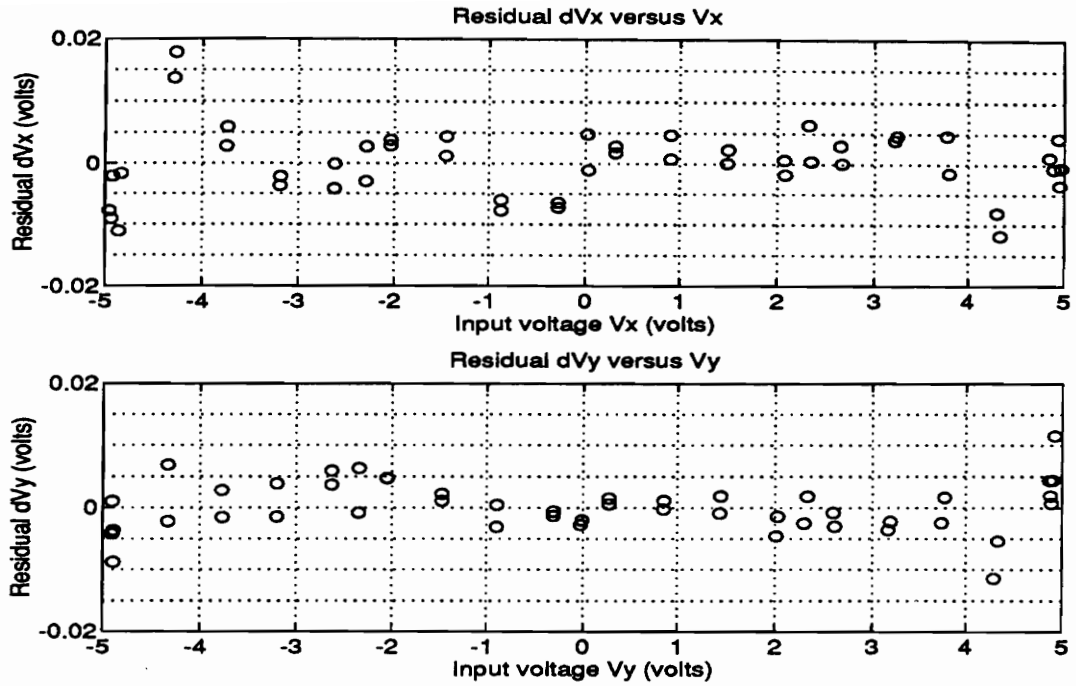

Figure 8.5 The residuals and the input voltages

8.2 Accuracy evaluation of the algorithm

In the experimental situation, there are always measurement errors. The accuracy of the developed algorithm should be evaluated in this environment. This section will present several experiments and their results for evaluating the accuracy.

8.2.1 Criteria for accuracy evaluation

Since the true solution of the pose is not known, one can not compare the experimental results with a "known" solution. However, if an estimated solution is close to the true solution, the estimated standard deviation of the residuals will be small. Thus, the

estimated standard deviation of the residuals can be used to evaluate the accuracy of the developed algorithm. As shown in chapter 5, all the confidence intervals are proportional to the estimated standard deviation of the residuals. In the inverse model, the estimated standard deviation of the errors or residuals in the scanning coordinates is

$$s_\theta = \sqrt{\frac{1}{2N-6}\sum_{i=1}^{N}\left\|\left\{\varepsilon_{P_i}\right\}_\theta\right\|^2} \tag{8.12}$$

where $\left\{\varepsilon_{P_i}\right\}_\theta$ is defined in Eq. (5.14). This is the same as that of Eq. (7.15). The smaller the standard deviation, the more precise the determined pose.

Another consideration is the maximum relative parameter-effects curvature. To make the statistical inferences by linear approximation valid, the curvature should be less than the *CC* although the smaller, the better. The maximum relative intrinsic curvatures will not be considered here since it is always less than the maximum parameter-effects curvatures.

Sometimes, the maximum absolute residual is of interest. If it is too large, the corresponding data may be considered as an outlier. If the algorithm used to find out the model parameter is not robust, the estimated parameters may not be accurate due to the effects of the outliers.

For all the tested cases, the estimated standard deviation, the $MS\varepsilon_{\varphi_X}$ and $MS\varepsilon_{\varphi_Y}$ (defined in Eq. (7.18)), the maximum relative parameter-effects curvature, and the maximum absolute residual are found.

8.2.2 Two sets of the scanner parameters

After the recalibration of the scanner in section 8.1, new values for the scanner parameters are obtained. The equation relating the input voltages to the scanning angles for the new scanner parameter values are (Eq. (8.8))

$$\left.\begin{aligned}\varphi_X &= -0.3890 + 2.3732V_X \\ \varphi_Y &= 0.6624 + 2.4727V_Y\end{aligned}\right\} \tag{8.13}$$

The currently used values for the scanner parameters are (Eq. (6.10))

$$\left.\begin{aligned}\varphi_X &= 0.0115 + 2.3988V_X \\ \varphi_Y &= 0.0212 + 2.4998V_Y\end{aligned}\right\} \tag{8.14}$$

Comparing the two equations, it can be seen that the variations of the slope parameter are small. Thus, one would like to know if the changes are real or if they are caused by uncertainty in the measurements. To evaluate this, both equations were used for all the experiments to convert the input voltages to the scanning angles. Thus for each case, two standard deviations were obtained. One was based on the scanning angles obtained by Equation (8.13) and the other was based on the scanning angles obtained by Eq. (8.14). Similarly, two $MS\varepsilon_{\varphi_X}$'s, two $MS\varepsilon_{\varphi_Y}$'s, two maximum parameter-effects curvatures, and two maximum absolute residuals were also obtained for each test case.

8.2.3 Experiments and their results

The objective of the accuracy evaluation is to determine the accuracy of the developed algorithm for various conditions. Four experiments were conducted. For each experiment, there were either eight or nine test cases. The following is the details of these experiments..

8.2.3.1 The general experimental setup and procedure

The experimental setup and procedure for the accuracy evaluation were the same as the calibration tests described in section **8.1.3**.

For the first three experiments, the relative position of the laser head to the graph paper was held constant as in the calibration experiment (Fig. 8.2). For the fourth experiment, the relative position of the laser head to the board was changed from case to case. Section **8.2.3.5** has the details.

For all the experiments, nine registration points were used. They were preselected for the purposes of the different experiments. For the first three experiments, the position of the nine points on the graph paper varied from case to case. For the fourth experiment, the nine points remained unchanged for all nine test cases.

8.2.3.2 First experiment: nine points on a square

This experiment was designed to check if the accuracy varies with the separation angles in both *X* and *Y* direction. There were eight test cases for this experiment. For all test cases, nine registration points are uniformly located on a square. Figure 8.6 shows the two squares. The outside square was for case 1, which was corresponding to the maximum separation angles. The *i*th square was for the *i*th test case. It was obtained by moving the four sides of the (*i*-1)th squares 2 inches (50.8 mm) toward the center. Nine registration points are shown on the *i*th square in Fig. 8.6. The 8th square was 6" by 6" (152.4 by

152.4 mm²) in dimension, which was corresponding to the smallest separation angles. Registration point 5 was used by all the test cases. The second column of Table 8.1a shows the ratios of the side length of all the squares to the side length of the largest square.

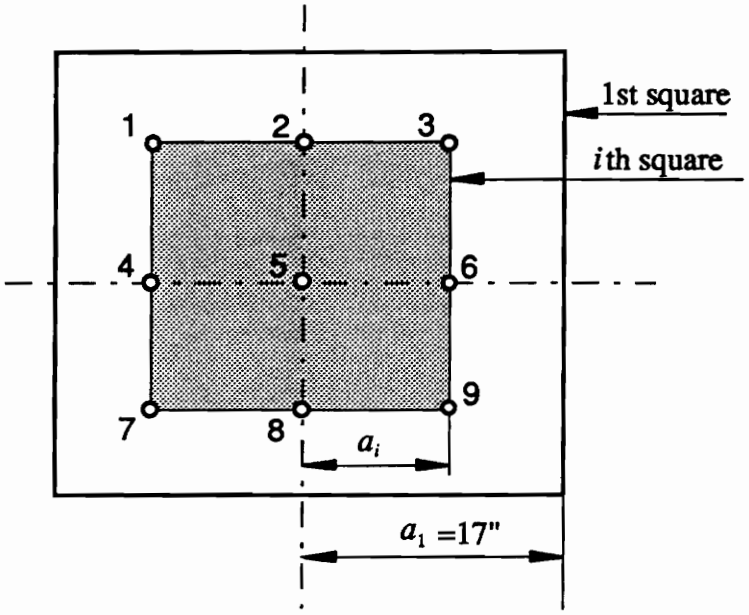

Note: 1 inch =25.4 mm

Figure 8.6 The squares for the first experiment

For each case, the experiment was performed with the procedure described in section **8.2.3.1**. For each test case, two estimated standard deviations, two $MS\varepsilon_{\varphi_x}$'s, two $MS\varepsilon_{\varphi_y}$'s, two maximum parameter-effects curvatures, and two maximum absolute residuals were obtained. The standard deviation is computed by use of Eq. (8.12). Figure 8.7 shows the estimated standard deviation of the residuals of the scanning angles for the eight cases. The legend "Old results" refers to the results obtained by using the old values of the scanner parameters (Eq. 8.14). The legend "New results" refers to the results obtained by

using the new values of the scanning parameters (Eq. (8.13)). These legends will be used in all the figures for presenting the standard deviations. Columns 3 to 6 in Table 8.1a shows the maximum relative parameter-effects curvatures and the maximum absolute residuals of the scanning angles. Table 8.1b shows the estimated standard deviation, the $MS\varepsilon_{\varphi_x}$, and $MS\varepsilon_{\varphi_y}$. The term "old results" and "new results" have the same meanings as those used in the figures.

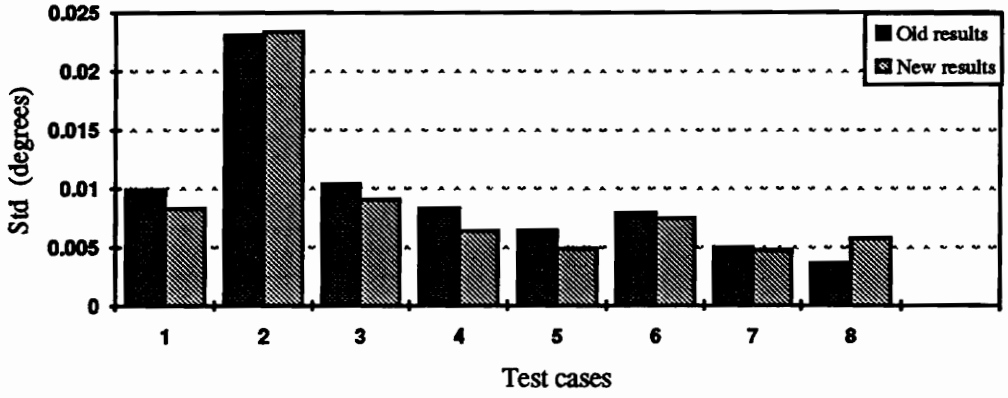

Figure 8.7 The estimated standard deviations for the first experiment

Table 8.1a The ratios, the maximum relative parameter-effects curvatures, the maximum absolute residuals for the first experiment

Case number	ratios	Maximum relative parameter-effects curvature		Maximum absolute residual (degrees)	
	a_i / a_1	Old results	New results	Old results	New results
1	1.000	0.0412	0.0370	0.0181	0.0133
2	0.882	0.1601	0.1678	0.0385	0.0355
3	0.765	0.1247	0.1119	0.0160	0.0136
4	0.647	0.1886	0.1489	0.0116	0.0112
5	0.529	0.3167	0.2488	0.0104	0.0079
6	0.412	1.0547	1.0299	0.0142	0.0136
7	0.297	2.4840	2.3955	0.0080	0.0076
8	0.176	11.6047	7.3358	0.0066	0.0079

Table 8.1b Estimated standard deviation, $MS\varepsilon_{\varphi_X}$, and $MS\varepsilon_{\varphi_Y}$ for the first experiment

Case Number	Estimated Standard deviation (degrees)		$MS\varepsilon_{\varphi_X}$ (degrees)		$MS\varepsilon_{\varphi_Y}$ (degrees)	
	Old results	New results	Old results	New results	Old results	New results
1	0.0099	0.0083	0.0099	0.0077	0.0058	0.0057
2	0.0231	0.0233	0.0200	0.0197	0.0177	0.0184
3	0.0105	0.0091	0.0093	0.0075	0.0076	0.0073
4	0.0083	0.0064	0.0078	0.0059	0.0057	0.0043
5	0.0064	0.0049	0.0057	0.0042	0.0048	0.0037
6	0.0079	0.0074	0.0070	0.0063	0.0060	0.0059
7	0.0050	0.0047	0.0040	0.0036	0.0042	0.0041
8	0.0036	0.0057	0.0032	0.0043	0.0028	0.0051

8.2.3.3 The second experiment: nine points on a rectangle with the base larger than height

This experiment was designed to check if the accuracy varies with the separation angles in *Y* direction. There were nine test cases. Figure 8.8 shows a square and a rectangle. The square (outside) was for the first test case. It was exactly the same square as the first test case in the first experiment. The *i*th rectangle shown in Fig. 8.8 was for the *i*th test cases. It was obtained by moving the top and bottom side of the (*i*-1)th rectangle 2 inches (25.4 mm) toward the horizontal center line. The rectangle for the 9th test cases was 34" by 2" (863.6 by 50.8 mm^2) in dimension. Nine registration points are shown on the *i*th rectangle in Fig. 8.8. Registration points 4, 5, and 6 were used by the nine test cases. The ratios of the height of all the rectangles to the side length of the largest square are shown in column two of Table 8.2a.

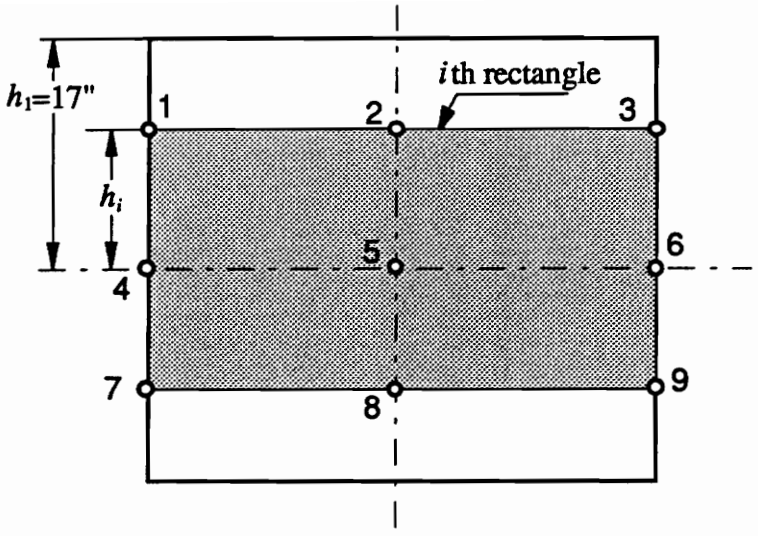

Note: 1 inch =25.4 mm

Figure 8.8 The rectangles with the base larger than height for the second experiment

The experimental procedure and the data processing were the same as that for the previous experiments. Figure 8.9 shows the estimated standard deviations for the nine test cases. Columns 3 to 6 in Table 8.2a show the maximum relative parameter-effects curvatures and the maximum absolute residuals of the scanning angles for the nine test cases. Table 8.2b shows the estimated standard deviation, the $MS\varepsilon_{\varphi_X}$, and $MS\varepsilon_{\varphi_Y}$.

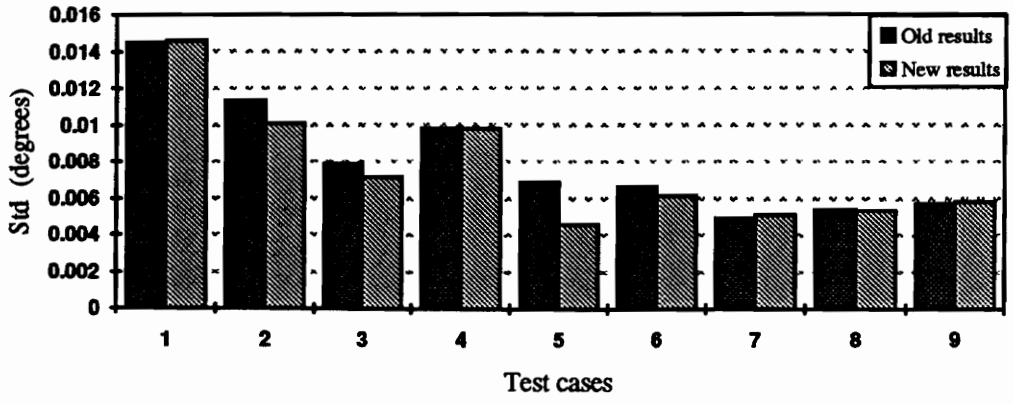

Figure 8.9 The estimated standard deviations for the second experiment

Table 8.2a The ratios, the maximum relative parameter-effects curvatures, the maximum absolute residuals for the second experiment

Case number	ratios	Maximum relative parameter-effects curvature		Maximum absolute residual (degrees)	
	h_i / h_1	Old results	New results	Old results	New results
1	1.000	0.0622	0.0648	0.0246	0.0210
2	0.882	0.0598	0.0550	0.0228	0.0203
3	0.765	0.0519	0.0488	0.0121	0.0111
4	0.647	0.0841	0.0870	0.0187	0.0166
5	0.529	0.0838	0.0579	0.0090	0.0079
6	0.412	0.1432	0.1370	0.0102	0.00989
7	0.297	0.2186	0.2325	0.0086	0.0077
8	0.176	0.6876	0.6993	0.0102	0.0091
9	0.059	6.5726	6.8640	0.0116	0.0117

Table 8.2b Estimated standard deviation, $MS\varepsilon_{\varphi_x}$, and $MS\varepsilon_{\varphi_y}$ for the second experiment

Case Number	Estimated Standard deviation (degrees)		$MS\varepsilon_{\varphi_x}$ (degrees)		$MS\varepsilon_{\varphi_y}$ (degrees)	
	Old results	New results	Old results	New results	Old results	New results
1	0.0145	0.0146	0.0131	0.0123	0.0104	0.0116
2	0.0114	0.0101	0.0110	0.0092	0.0071	0.0072
3	0.0078	0.0072	0.0072	0.0066	0.0055	0.0050
4	0.0098	0.0098	0.0083	0.0082	0.0077	0.0079
5	0.0069	0.0046	0.0065	0.0048	0.0046	0.0023
6	0.0066	0.0062	0.0059	0.0055	0.0050	0.0046
7	0.0049	0.0051	0.0047	0.0044	0.0033	0.0039
8	0.0054	0.0054	0.0036	0.0035	0.0052	0.0051
9	0.0057	0.0058	0.0033	0.0033	0.0058	0.0059

8.2.3.4 The third experiment: nine points on a rectangle with the height larger than base

This experiment was similar to the second experiment. The difference is that the *i*th rectangle was obtained by moving the left and the right side of the (*i*-1)th rectangle 2 inches (50.8 mm) toward the vertical center line. The *i*th rectangle shown in Fig. 8.10 was for the *i*th test case. Thus, the rectangle for the 9th test case was 2" by 34" (50.8 by 863.6 mm^2) in dimension. Registration points 2, 5 and 8 were used by all the test cases. The ratios of the base of the rectangles to the side length of the largest square are the same as those in Table 8.2a. For convenience, it is shown in column 2 of Table 8.3a again.

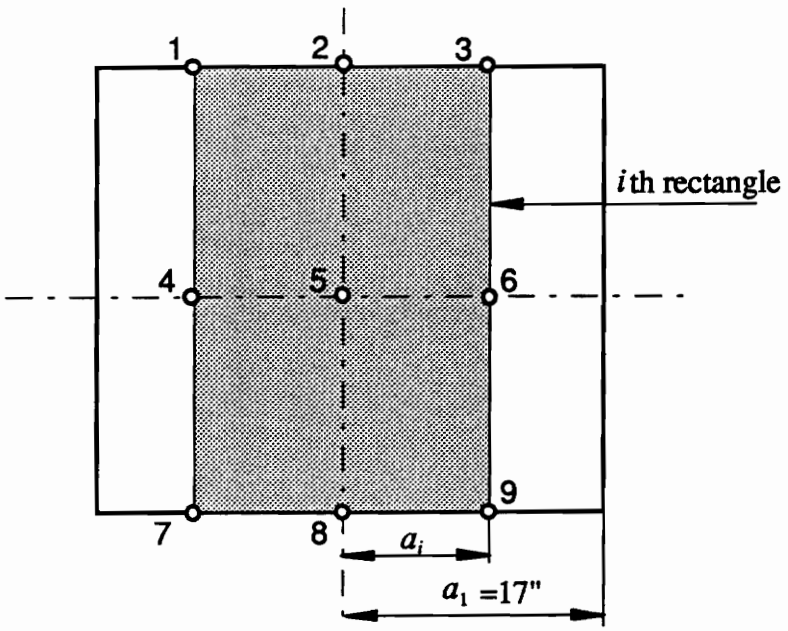

Note: 1 inch =25.4 mm

Figure 8.10 The rectangles with the base shorter than height for the third experiment

Figure 8.11 shows the estimated standard deviations for all nine test cases. Columns 3 to 6 in Table 8.3a show the maximum relative parameter-effects curvatures and the maximum absolute residuals in the scanning angles for all the nine cases. Table 8.3b shows the estimated standard deviation, the $MS\varepsilon_{\varphi_x}$, and $MS\varepsilon_{\varphi_y}$.

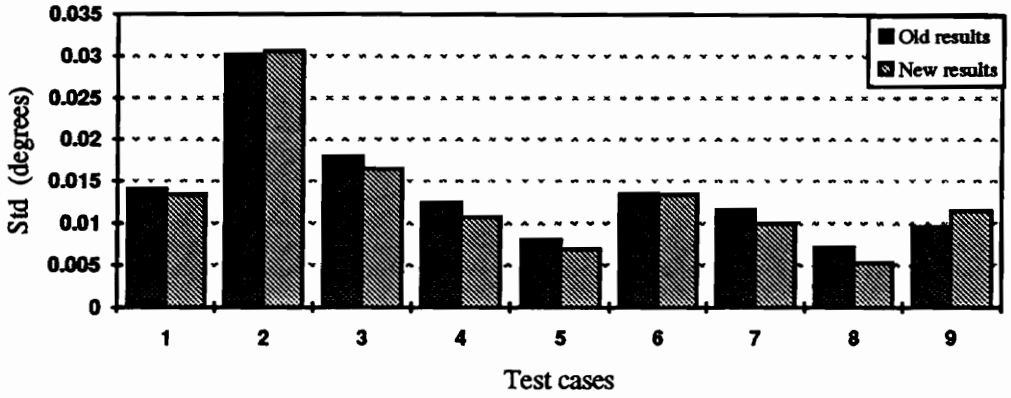

Figure 8.11 The estimated standard deviations for the third experiment

Table 8.3a The ratios, the maximum relative parameter-effects curvatures, the maximum absolute residuals for the third experiment

Case number	ratios	Maximum relative parameter-effects curvature		Maximum absolute residual (degrees)	
	a_i / a_1	Old results	New results	Old results	New results
1	1.000	0.0603	0.0596	0.0259	0.0222
2	0.882	0.1687	0.1769	0.0431	0.0408
3	0.765	0.1336	0.1274	0.0281	0.0233
4	0.647	0.1275	0.1142	0.0206	0.0176
5	0.529	0.1215	0.1075	0.0136	0.0109
6	0.412	0.3196	0.3312	0.0228	0.0230
7	0.297	0.5116	0.4585	0.0204	0.0172
8	0.176	0.8331	0.6483	0.0146	0.0092
9	0.059	9.3132	9.8470	0.0175	0.0157

Table 8.3b Estimated standard deviation, $MS\varepsilon_{\varphi_X}$, and $MS\varepsilon_{\varphi_Y}$ for the third experiment

Case Number	Estimated Standard deviation (degrees)		$MS\varepsilon_{\varphi_X}$ (degrees)		$MS\varepsilon_{\varphi_Y}$ (degrees)	
	Old results	New results	Old results	New results	Old results	New results
1	0.0141	0.0134	0.0125	0.0111	0.0104	0.0108
2	0.0302	0.0306	0.0276	0.0274	0.0213	0.0222
3	0.0179	0.0165	0.0178	0.0155	0.0105	0.0111
4	0.0124	0.0107	0.0121	0.0099	0.0076	0.0074
5	0.0081	0.0069	0.0072	0.0055	0.0060	0.0058
6	0.0134	0.0134	0.0141	0.0141	0.0064	0.0064
7	0.0116	0.0099	0.0127	0.0108	0.0040	0.0040
8	0.0071	0.0054	0.0073	0.0049	0.0038	0.0038
9	0.0096	0.0115	0.0101	0.0103	0.0051	0.0084

8.2.3.5 The fourth experiment: nine points on a square and different poses

This experiment was designed to check if the accuracy varies with the different relative positions of the laser head to the graph paper (the structural coordinate system). Nine registration points were uniformly located on a 22" by 22" (558.8 by 558.8 mm²) square and were used by all the nine test cases. Nine different relative positions were selected for this experiment. One position was for one case. Figure 8.12 shows the nine positions. For simplicity, the laser head is represented by a rectangle. The nine positions are roughly located in a plane parallel to the $X_S Y_S$ plane as shown in Fig. 8.12. At each position, the orientation of the laser head was adjusted such that the laser beam home position was at the center of the square on the graph paper. The locations of the laser head were roughly measured and are shown in Fig. 8.12. Position 5 was the position for the first three experiments, previously discussed.

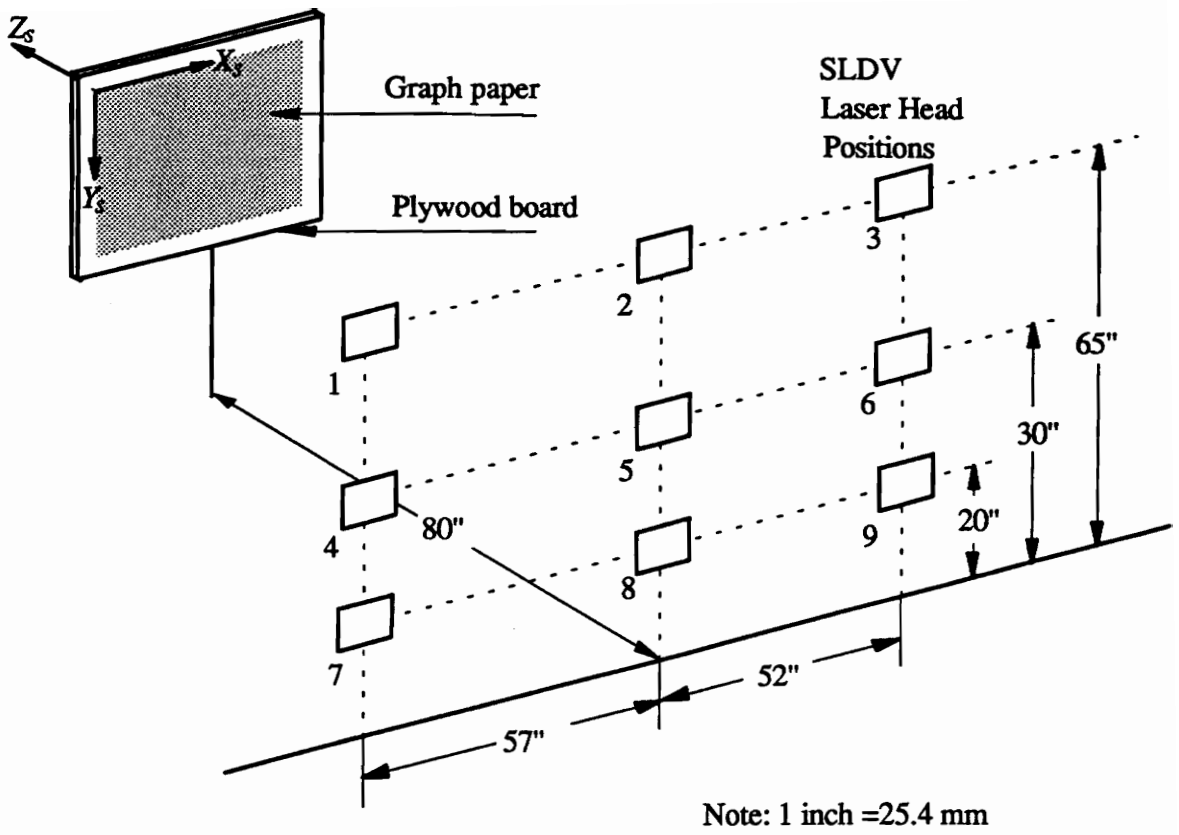

Figure 8.12 Nine laser head positions in fourth experiment

The experimental procedure and the data processing were the same as that for the first experiment. Figure 8.13 shows the estimated standard deviations of the residuals for the nine positions. Columns 2 to 5 in Table 8.4a show the maximum relative parameter-effects curvatures and the maximum absolute residuals of the scanning angles for the nine test cases. Table 8.2b shows the estimated standard deviation, the $MS\varepsilon_{\varphi_x}$, and $MS\varepsilon_{\varphi_y}$.

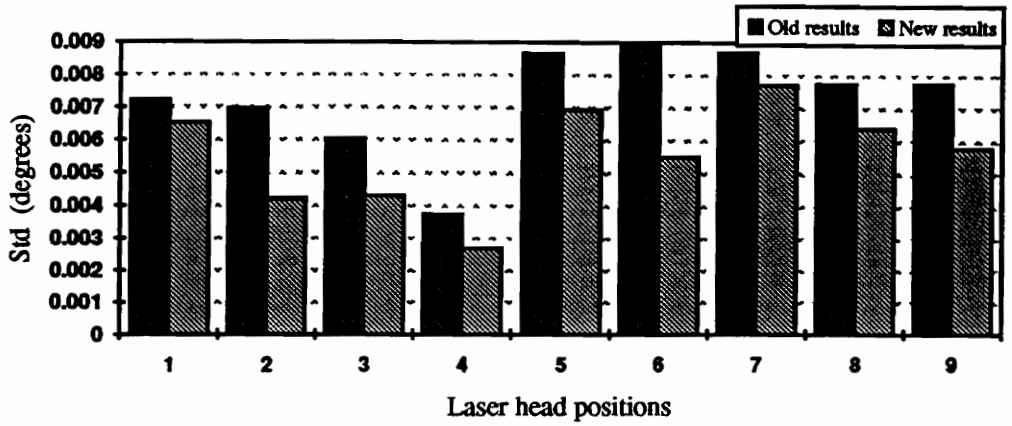

Figure 8.13 The estimated standard deviations for the fourth experiment

Table 8.4a The maximum relative parameter-effects curvatures, the maximum absolute residuals for the fourth experiment

Position number	Maximum relative parameter-effects curvature		Maximum absolute residual (degrees)	
	Old results	New results	Old results	New results
1	0.0176	0.0157	0.0117	0.0111
2	0.0382	0.0234	0.0145	0.0079
3	0.0148	0.0106	0.0132	0.0076
4	0.0108	0.0079	0.0073	0.0040
5	0.1960	0.1625	0.0162	0.0143
6	0.0231	0.0143	0.0155	0.0076
7	0.0243	0.0219	0.0135	0.0131
8	0.1647	0.1391	0.0142	0.0094
9	0.0227	0.0171	0.0130	0.0136

Table 8.4b Estimated standard deviation, $MS\varepsilon_{\varphi_X}$, and $MS\varepsilon_{\varphi_Y}$ for the fourth experiment

Case Number	Estimated Standard deviation (degrees)		$MS\varepsilon_{\varphi_X}$ (degrees)		$MS\varepsilon_{\varphi_Y}$ (degrees)	
	Old results	New results	Old results	New results	Old results	New results
1	0.0072	0.0065	0.0032	0.0020	0.0077	0.0070
2	0.0069	0.0042	0.0064	0.0042	0.0049	0.0025
3	0.0060	0.0043	0.0026	0.0021	0.0065	0.0045
4	0.0037	0.0027	0.0036	0.0020	0.0023	0.0024
5	0.0087	0.0069	0.0080	0.0061	0.0061	0.0052
6	0.0089	0.0055	0.0032	0.0041	0.0098	0.0049
7	0.0087	0.0077	0.0076	0.0062	0.0066	0.0065
8	0.0078	0.0064	0.0076	0.0059	0.0048	0.0045
9	0.0078	0.0058	0.0050	0.0060	0.0075	0.0030

8.2.4 Summary and analysis of the experimental results

In section **8.2.3**, four experiments and their results for accuracy evaluation were presented From those results, the following is obtained.

I). For all the test cases in the four experiments, the maximum absolute residuals are 1.5 to 2 times the estimated standard deviations. Statistically, those data points are not considered to be outliers. Thus, the estimated parameters are not affected by outliers.

II). For the first experiment, the estimated standard deviations tend to decrease with the reduction of the separation angles for the first four cases except for case 2. The reduction is not significant. The estimated standard deviations are basically the same for case 4 to case 8. The large estimated standard deviation in case 2 resulted from the measurement errors. See Fig. 8.5, the largest residuals occur at about ±4.3 volts in V_X and +4.3 volts in

V_Y. The input voltages for the outside registration points of case two are very close to those values. Thus, when the calibrated parameters are used to convert the input voltages into angles, relatively larger measurement errors are produced in the scanning angles. The maximum parameter-effects curvature increases with the reduction of separation angles, which agrees with the simulation results of the last chapter.

III). For the second experiment, the maximum separation angles were in the *X* direction. It remained the same for the nine cases. The separation angles in the *Y* direction gradually reduced from case 1 to case 9. The estimated standard deviations tend to decrease with reduction of the separation angle in the *Y* direction for the first five cases except for case four. The estimated standard deviations are basically the same for case 5 to case 9. The maximum parameter-effects curvature increases with the reduction of separation angles in *Y* direction.

IV). For the third experiment, the maximum separation angle was in the *Y* direction. It remained the same for all test cases. The separation angles in *X* direction gradually reduced from case 1 to case 9. The estimated standard deviations were about 0.01 degrees except for case 2. The larger error in case two is caused by the same reason as that for case two in the first experiment. The maximum parameter-effects curvature increases with the reduction of separation angles in *X* direction.

V). For the fourth experiment, the estimated standard deviations are all less than 0.01 degrees. They are independent of the relative poses. The maximum parameter-effects curvatures vary with different relative poses. It seems that position 5 and 8 have relatively larger curvatures compared with the other seven positions.

VI). The maximum relative parameter-effects curvatures for most of the cases in the first three experiments and all the cases in the fourth experiments are smaller than the *CC* value (=0.2889 for nine points and significant lever α=0.05). A few cases with smaller separation angles in the first three experiments have their ρ_{max}^{PE}'s larger than the *CC* value. It can be seen that the curvatures in experiment 2 and 3 are smaller than those in the first experiment The reason is that the separation angles for one direction are still larger in these two experiments. All the nine cases in experiment four have relatively large separation angles. Their ρ_{max}^{PE}"s are smaller than the *CC* value. The above results show that: (i) although nine registration points is recommended in chapter 7, they are not enough for very small separation angle cases from the point of view of the relative curvatures, (ii) it would be better to check the curvatures for each pose during data acquisition.

VII). Among the 35 test cases, there are two cases whose estimated standard deviations are above 0.02 degrees, one case about 0.018 degrees, and seven cases between 0.01 and 0.015 degrees. The estimated standard deviations for all the other cases are below 0.01 degrees. According to experiment four, the accuracy is not shown dependent on the relative poses.

VIII). For most of the test cases in the first three experiments, the estimated standard deviations obtained by using the new values of the scanner parameters are a little bit smaller than those obtained by using the old value. However, for the test cases in the fourth experiment, the estimated standard deviation from the new values is obviously smaller than those from the old values. This pattern is also observed for the maximum

parameter-effects curvatures. According to these results, it may be concluded that the new values of the scanner parameter should be used because it gives slightly better results for most of the test cases.

IX). For all the test cases, the $MS\varepsilon_{\varphi_X}$ is not equal to the $MS\varepsilon_{\varphi_Y}$. For some cases, the $MS\varepsilon_{\varphi_X}$ is larger than the $MS\varepsilon_{\varphi_Y}$. For other cases, the $MS\varepsilon_{\varphi_X}$ is smaller than the $MS\varepsilon_{\varphi_Y}$. The differences between them are small for most of the test cases.

The overall accuracy of the developed algorithm is satisfactory since for most of the test cases, the estimated standard deviations are less than 0.01 degrees which is less than 1 DAC step for currently used D/A board. The accuracy of grid lines of the graph paper was verified with a standard steel rule with resolution of 1/16 inches. For the best results, the input voltages for the outside registration points should be in the middle to large range of 0 to ±5 volts and should not be around ±4.3 for both V_X and V_Y.

8.3 Summary

This chapter has developed a new algorithm based on the inverse model for calibrating the scanner parameter simultaneously. The advantage of the developed algorithm over the one-dimensional calibration method is that it uses only the input voltages and structural coordinates. Experiment has been conducted to collect the required data for calibration of the scanner. The calibrated scanner parameters are acceptable since the residuals in the input voltages agree with their assumptions. It is recommended to use the newly calibrated scanner parameters since it gives better results for most of the tested cases in the sense of the estimated standard deviation and the maximum parameter-effects curvatures.

Four experiments have been completed to evaluate the accuracy of the developed algorithm for different situations. The criteria for the evaluation are the estimated standard deviations and the maximum parameter-effects curvatures. The two sets of scanner parameters are used and compared in the evaluation. For most of the test cases, the estimated standard deviation is less than 0.01 degrees. The estimated standard deviations do not show a dependency on different relative poses. The maximum relative parameter-effects curvatures increase with the reduction of the separation angles. For the some cases with smaller separation angles, the relative curvatures are larger than the *CC* value. Thus, for those cases, more than nine registration points are required.

CHAPTER NINE

CONCLUSIONS AND RECOMMENDATIONS

The objective of this dissertation is to develop a method that can give the best estimation of the SLDV pose and its statistics. By developing the nonlinear regressive model, the objective is achieved.

9.1 Conclusions

Overall, the developed inverse model is shown to be a correct model for determining the SLDV pose. The statistical inferences about the pose parameters, about the expected scanning angles, and about the prediction of the scanning angles can be obtained after the model is fitted.

Followings are a brief summary of other significant conclusions for this dissertation.

I). The developed scanner model (transformations between the scanning coordinates and the structural coordinates for any registration point) is correct. It is based on the geometry of the scanner.

II). The developed geometrical method can always give a good solution for the SLDV pose. With this pose as an initial solution, the best estimation of the SLDV pose can be obtained by an optimization algorithm for the inverse model. The techniques developed in chapter 4 for the geometrical method are effective and correct. Those techniques include: (i) finding the initial ranges by neglecting the separation distance *dl* and using four

registration points, (ii) eliminating the origin coordinates by translating the two coordinate systems to the center (average points) of all registration points, (iii) finding the equivalent axis and equivalent angle by using the concept of equivalence of the vector rotation and frame rotation.

III). The statistical inferences about the inverse model made by the linear approximation are acceptable if the maximum parameter-effects curvature is less than the *CC* value. Therefore, the maximum parameter-effects curvature is a valuable measurement of the nonlinearity. It can effectively validate the statistical inferences obtained by the linear approximation.

IV). The new algorithm based on the inverse model for calibrating the scanner parameters is shown to be correct. The results of accuracy evaluation show that accuracy obtained by using the new values of the scanner parameter is slightly better than that by using the current values of the scanner parameters for most of the testing cases. Thus, it is recommended to use it in future work.

V). The results of tests with the simulated data show that the accuracy of the developed inverse model is not dependent on the separation angles. The maximum relative parameter-effects curvature is dependent on the separation angles. The smaller the separation angles, the bigger the curvatures. The results also show that if the four registration points are in the same scanning quadrant, the maximum parameter-effects curvature will be larger compared to the case that the four registration points are distributed in the four scanning quadrants (see Fig. 2.2). The big curvature will make the inferences (made by the linear approximation) invalid. Therefore, large separation angles

should be used and all the registration points should be distributed in all the scanning quadrants.

VI). As the increase of the number of registration points, the estimated standard deviation and the maximum relative parameter-effects curvature will decrease. Although the minimum number of registration points required to determine the pose uniquely is four, more points are needed to reduce the estimated standard deviation and to satisfy the curvature criterion.

VII) The results of the accuracy evaluation show that the accuracy of the developed algorithm (geometrical method and inverse model) is satisfactory since for most of the testing cases, the estimated standard deviation of the errors in the scanning angles is less than 0.01 degree which is about the DAC step of the D/A converter for generating the input voltage to control the scanning mirrors.

9.2 Recommendations

To get more accurate estimation of the pose parameters, efforts should be made to reduce the modeling errors and measurement errors. Accordingly, following recommendations are made for future work.

I). A more accurate relation needs developing between the input voltages and the scanning angles. Although current linear voltage-angle relation is acceptable, there is room for improvement. Figure 8.5 shows that the residuals, ε_{V_x}, are larger at input voltage, V_x, being about 4.3 volts. A more accurate relation is able to reduce these large residuals. The

best thing is to measure the scanning angles and the corresponding input voltages directly. Using those data, a more accurate relation between them can be established.

II). To further reduce the estimated standard deviation of the errors in the scanning angles, a high resolution should be used in the measurement of the structural coordinates of the registration points. A coordinate measurement machine can be used for this purpose. Also, a D/A converter with more than 12 bits are needed.

III). Weighted least squares method can be used in finding the least squares solution of the SLDV pose in the case that the measured data does have outliers.

REFERENCES

CHAPTER ONE

[1.1] Drain, L. E., *The Laser Doppler Technique*, John Wiley and Sons Ltd, Chichester, 1980.

[1.2] Ometron Limited, *VPI Sensor Operator's Manual*, London, England, 1987

[1.3] Halliwell, N. A., "Laser Doppler Measurement of Vibrating Surface: a Portable Instrument," *Journal of Sound and Vibration*, Vol. 62, No. 2, 1979, pp. 312-315.

[1.4] Barker, A. J., P. E. Jaeger, and D. E. Oliver, "Non-contacting Vibration Measurement: Role in Design and Industrial Applications," *Stress and Vibration: Recent Developments in Industrial Measurement and Analysis*, SPIE Vol. 1084, 1989, pp. 293-299.

[1.5] Kochersberger, K., L. D. Mitchell, and A. L. Wicks, "Structural Angular Velocity Extraction Using DFT/IDFT Techniques," *Proceedings of the 9th International Modal Analysis Conference*, Florence, Italy, April 14-18, 1991, pp. 657-663.

[1.6] Sun, F. P., and L. D. Mitchell, "Two-dimensional Velocity Data Smoothing and Structural Angular Velocity Extraction Using a DFT-IDFT Technique," *Modal analysis, Modeling, Diagnostics, and Control - Analytical and Experimental*, ASME DE-Vol. 38, 1991, pp. 303-309.

[1.7] Galaitsis, G. S., *Extraction of Drilling-angular Velocities Using a Nodal Array of In-plane Translational Velocities*, MS Thesis, Mechanical Engineering Department, Virginia Polytechnic Institute and State University, May, 1993.

[1.8] Arruda, J. R. F., "Surface Smoothing and Partial Spatial Derivatives Computation Using a Regressive Discrete Fourier Series," *Mechanical Systems and Signal Processing*, Vol. 6, No. 1, 1992, pp. 41-50.

[1.9] Bream, R. G., B. C. Gasper, B. E. Lloyd, and G. M. Everett, "Application of Vibration Pattern Imaging to Modal Analysis; a Comparison with Full-field and Point Measurement Technique, " *Stress and Vibration: Recent Developments in Industrial Measurement and Analysis*, SPIE Vol. 1084, 1989, pp. 279-292.

[1.10] Sriram, P., J. I. Craog, and S. Hanagud, "A Scanning Laser Doppler Vibrometer for Modal Testing," *International Journal of Analytical and Experimental Modal Analysis*, Vol. 5, No. 3, July 1990, pp. 155-167.

[1.11] Yienger, J. M., R. L. West, and L. D. Mitchell, "Laser Based Structural Imaging of an Open and Closed Automobile Door for Noise Control Purpose," *Proceedings of the 11th International Modal Analysis Conference*, Vol. 1, Kissimmee, Florida, February 1-4, 1993, pp. 144-151.

[1.12] Liu, Y., *The Development of a Systematic Experimental Method for Damage Identification*, MS Thesis, Mechanical Engineering Department, Virginia Polytechnic Institute and State University, January, 1994.

[1.13] Li, W. X., L. D. Mitchell, and M. Lu, "Non-modal Method of Structural Dynamic Response Identification for a Prototype Commercial Jet Aircraft Fuselage," *Proceedings of the 12th International Modal Analysis Conference*, Vol. 1, Honolulu, Hawaii, January 31-February 3, 1994, pp. 255-261.

[1.14] Paone, N., C. Santolini and E. P. Tomasini, "Application of a Laser Doppler Vibrometer to Evaluate Engine Poppet Valve Kinematics," *Proceedings of the 12th International Modal Analysis Conference*, Vol. 1, Honolulu, Hawaii, January 31-February 3, 1994, pp. 146-152.

[1.15] Pedrazzo, G., G. L. Rossi, C. Santolini and E. P. Tomasini, "Vibration Measurements of the Human Body by a Laser Scanning Vibromter," *Proceedings of the 12th International Modal Analysis Conference*, Vol. 2, Honolulu, Hawaii, January 31-February 3, 1994, pp. 1218-1223.

[1.16] Agee, B. L., X. Zeng, and L. D. Mitchell, "An Automated System for Acquiring Modal Analysis Data," *Sound and Vibration*, Vol. 26, No. 6, June 1992, pp. 14-21.

[1.17] Agee, B. L., *Development of a Laser-based Automated Mechanical Mobility Measurement System for One-dimensional Experimental Modal Analysis*, MS Thesis, Mechanical Engineering Department, Virginia Polytechnic Institute and State University, February, 1992.

[1.18] Dominguez, J. C. L., *Reconstruction of 3-D Structural Dynamic Response Fields: an Experimental, Laser-Based Approach with Statistical Emphasis*, Ph.D. Dissertation, Mechanical Engineering Department, Virginia Polytechnic Institute and State University, August, 1994.

[1.19] Montgomery, D. E., R. L. West and A. L. Wicks, "Estimation of In-plane Motion Using Multiple Laser Doppler Vibrometer Scans," *Proceedings of the 12th International Modal Analysis Conference*, Vol. 2, Honolulu, Hawaii, January 31-February 3, 1994, pp. 1182-1187.

CHAPTER TWO

[2.1] Li, X. W., *A Precision Laser Scanning System For Experimental Modal Analysis: its Test and Calibration*, MS Thesis, Mechanical Engineering Department, Virginia Polytechnic Institute and State University, October, 1992

CHAPTER THREE

[3.1] Lenz, R. K. and R. Y. Tsai, "Calibrating a Cartesian Robot with Eye-on-Hand Configuration Independent of Eye-to-Hand relationship," *Proceedings of Computer Vision and Pattern Recognition*, Ann Arbor, MI, June 5-9, 1988, pp. 67-75

[3.2] Fallon, J. B., "Determining the Pose of Robot End-Effectors Using Computer Vision", *Preliminary Research Proposal*, Mechanical Engineering Department, Virginia Polytechnic Institute and State University, July, 1993.

[3.3] Wahba, G., Section on Problems and Solutions: "A Least Squares Estimate of Satellite Attitude," *SIAM Review*, Vol. 8, No. 3, July, 1966, pp. 384-385.

[3.4] Stephens M. A., "Vector Correlation," *Biometrika*, Vol. 66, No. 1, 1979, pp. 41-48.

[3.5] Craig, J. J., *Introduction to Robotics: Mechanics and Control*, second edition, Addison-Wesley Publishing Company, Reading, Massachusetts, 1989.

[3.6] Chou, J. C. K., and M. Kamel, "Finding the Position and Orientaiton of a Sensor on a Robot Manipulator Using Quaternions," *The International Journal of Robotics Research*, Vol. 10, No. 3, June 1991, pp. 240-254.

[3.7] Sanso, F., "An Exact Solution of the Roto-Translation Problem," *Photogrammetria*, Vol. 29, 1973, pp. 203-216.

[3.8] Moran, P. A. P., "Quaternions, Haar Measure and the Estimation of a Palaeomagnetic Rotation," in *Perspectives in Probability and Statistics,* Edited by J. Gani, Applied Probability Trust, Academic Press, 1976, pp. 295-301.

[3.9] Tsai, R. Y., "An Efficient and Accurate Camera Calibration Technique for 3D Machine Vision," *Proceedings of the IEEE Computer Society Conference on Computer Vision and Pattern Reconginition*, Miami, Florida, June 22-26, 1986, pp. 364-374.

[3.10] Tsai, R. Y. "A Versatile Camera Calibration Technique for High-Accuracy 3D Machine Vision Metrology Using off-the-Shelf Cameras and Lenses," *IEEE Journal of Robotics and Automation*, Vol. RA-3, No. 4, August 1987, pp. 323-344.

[3.11] Tsai, R. Y. and R. K. Lenz, "A New Technique for Fully Autonomous and Efficient 3D Robotics Hand/Eye Calibration," *IEEE Transactions on Robotics and Automation*, Vol. 5, No. 3, June 1989, pp. 345-358.

[3.12] Shiu, Y. C. and S. Ahmad, "Finding the Mounting Position of a Sensor by Solving a Homogeneous Transform Equation of the Form *AX=XB*," *Proceedings of the 1987 IEEE Internaitonal Conference on Robotics and Automation*, Vol. 3, Raleigh, North Carolina, March 31-April 3, 1987, pp. 1666-1671.

[3.13] Shiu, Y. C. and S. Ahmad, "Calibration of Wrist-Mounted Robotic Sensors by Solving Homogeneous Transform Equations of the Form *AX=XB*," *IEEE Transactions on Robotics and Automation*, Vol. 5, No. 1, Feb. 1989, pp. 16-29.

[3.14] Chang, Y.-L., X. Lebegue, and J. K. Aggarwal, "Calibraitng a Mobil Camera's Parameters," *Pattern Recognition*, Vol. 26, No. 1, 1993, pp. 75-88.

[3.15] Chen, C. and Y. F. Zheng, "A New Robotic Hand/Eye Calibration Method by Active Viewing of a Checkboard Pattern," *Proceedings of the IEEE Internaitonal Conference on Robotics and Automation*, Vol. 2, Atlanta, George, May 2-6, 1993, pp. 770-775.

[3.16] Chang, Y.-L. and P. Liang, "On Recursive Calibration of Cameras for Robot Hand-eye System," *Proceedings of the 1989 IEEE Internaitonal Conferecne on Robotic and Automation*, Vol. 3, 1989, pp. 838-843.

[3.17] Shih, S.-W., Y.-P. Hung, and W.-S. Lin; "An Efficient and Accurate Camera Calibration Technique for 3D Computer Vision," *Optics, Illumination, and Image Sensing for Machine Vision VI*, SPIE Vol. 1614, 1991, pp. 133-145.

[3.18] Ito, M. and A. Ishii, "A Non-iterative Procedure for Rapid and Precise Camera Calibration", *Pattern Recognition*, Vol. 27, No. 2, 1994, pp. 301-310.

[3.19] Lai, J. Z. C., "On the Sensitivity of Camera Calibration," *Image and Vision Computing*, Vol. 11, No. 10, December, 1993, pp. 656-664.

[3.20] Wang, L.-L., and W.-H. Tsai, "Camera Calibration by Vaninshing Lines for 3-D Computer Vision," *IEEE Transactions on Pattern Analysis and Machine Intelligence*, Vol. 13, No. 4, April 1991, pp. 370-376.

[3.21] Wei, G.-Q. and S. D. Ma, "A Complete Two-plane Camera Calibration Method and Experiemtnal Comparisons, "*Proceedings of the Fourth International Conference on Computer Vision*, Berlin, Germany, May 11-14, 1993, pp. 439-446.

[3.22] Basu, Anup, "Active Calibration," *Proceedings of the IEEE International Conference on Robotics and Automation*, Atlanta, Georgia, May 2-6, 1993, pp. 764-769.

[3.23] Foster, N. J. and A. C. Sanderson, "Determining Object Orientation using ellipse Fitting," *Intelligence Robots and Computer Vision*, SPIE Vol. 521, 1984, pp. 34-43.

[3.24] Platin, B. E., Z. Gan, and N. Olgac, "3-D Object Configuration Sensor Utilizing Single-Camera Images," *ASME paper 90-WA/DSC-22*, 1990, 7 pages.

[3.25] Ferri, M. and F. Mangili, "Monocular Pose Determination of Quadrics of Revolution," *Intelligent Robots and Computer Vision X*, SPIE Vol. 1608, 1991, pp. 128-138.

[3.26] Rothwell, C. A., A. Zisserman, C. I. Marinos, D. A. Forsyth, and J. L. Mundy, "Relative Motion and Pose from Arbitrary Plane Curves," *Image and Vision Computing*, Vol. 10, No. 4, May, 1992, pp. 250-262.

[3.27] Safaee-Rad, R., I. Tchoukanov, K. C. Smith and B. Benhabib, "Constraints on Quadratic-Curved Features under Perspective Projection," *Image and Vision Computing*, Vol. 10, No. 8, October, 1992, pp. 532-548.

[3.28] Haralick, R. M. and H. Joo, "2D-3D Pose Estimation," *Proceedings of the 9th International Conference on Pattern Recongnition*, Vol. 1, Rome, Italy, November 14-17, 1988, pp. 385-391.

[3.29] Haralick, R. M., C. N. Lee, X. Zhuang, V. G. Vaidya, and M. B. Kim, "Pose Estimation from Corresponding Point Data," *IEEE Computer Society Workshop on Computer Vision*, Miami Beach, Florida, Nov. 30-Dec. 3, 1987, pp. 258-263.

[3.30] Haralick, R. M., H. Joo, C. N. Lee, X. Zhuang, V. G. Vaidya, and M. B. Kim, "Pose Estimation from Corresponding Point Data," *IEEE Transactions on Systems, Man, and Cybernetics*, Vol. 19, No. 6, November/December 1989, pp. 1426-1446.

[3.31] Ho, C.-C. J., and N. H. MaClamrock, "A Spacecraft Docking Problem: Position and Orientation Estimating Uisng a Computer Vision Approach," *Proceedings of the 1991 American Control Conference*, June 26-28, 1991, Boston, Massachusettes, pp.827-832.

[3.32] Haralick, R. M., "Monocular Vision Using Inverse Perspective Projection Geometry: Analytical Relations," *Proceedings of the IEEE Computer Society*

Conference on Computer Vision and Pattern Recognition, San Diego, California, June 4-8, 1989, pp. 370-378.

[3.33] Wolfe, W. J., C. Weber-Sklair, D. Mathis, and M. Magee, "Locating known Objects in 3-D from a single perspective View," *Intelligent Robots and Computer Vision: Seventh in a Series*, SPIE Vol. 1002, 1988, pp. 550-566.

[3.34] Wolfe, W. J., C. Weber-Sklair, D. Mathis, and M. Magee, "The Perspective View of Three Points," *IEEE Transactions on Pattern Analysis and Machine Intelligence*, Vol. 13, No.1, January, 1991, pp. 66-73.

[3.35] Linnainmaa, S, D. Harwood, and L. S. Davis, "Pose Determination of a Three-Dimensional Object Using Triangle Pairs", *IEEE Transactions on Pattern Analysis and Machine Intelligence*, Vol. 10, No. 5, September, 1988, pp. 634-647.

[3.36] Haralick, R. M., "Determining Camera Parameters from the Perspective Projection of a Rectangle," *Pattern Recognition*, Vol. 22, No. 3, 1989, pp. 225-230.

[3.37] Hung, Y., P.-S. Yeh, D. Harwood, "Passive Ranging to Known Planar Point Sets," *Proceedings of the 1985 IEEE International Conference on Robotics and Automation*, St. Louis, Missouri, March 25-28, 1985, pp. 80-85.

[3.38] Montgomery, D. E. and R. L. West, "Position Registration of Scanning Lasers For Experimental Spatial Dynamics Modeling," *Proceedings of the Twentieth ASME Design Automation Conference*, Minneapolis, Minnesota, September 11-14, 1994.

[3.39] Mikhail, E. M., and F. Ackermann, *Observations and Least Squares*, IEP--A Dun-Donnelley Publisher, New York, 1976.

[3.40] Mackenzie, J. K., "The Estimation of an Orientation Relationship," *Acta Cystallograhpica*, Vol. 10, 1957, pp. 61-62.

[3.41] Chang, T., "Spherical Regression," *The Annals of Statistics*, Vol. 14, No. 3, 1986, pp. 907-924.

[3.42] Chang, T., "On the Statistical Properties of Estimated Rotations," *Journal of Geophysical Research*, Vol. 92, No. B7, June, 1987, pp. 6319-6329.

[3.43] Chang, T., "Spherical Regression with Errors in Variables," *The Annals of Statistics*, Vol. 17, No. 1, 1989, pp. 293-306.

[3.44] Chang, T., "Spherical Regression and the Statistics of Tectonic Plate Reconstructions," *International Statistical Review,* Vol. 61, No. 2, 1993, pp. 299-316.

[3.45] Watson, G. S., "Statistics of Rotations," in *Probability Measures on Groups IX*, Springer-Verlag, 1989, pp. 389-413.

[3.46] Mardia, K. V. and P. E. Jupp, "A Unified View of the Theory of Directional Statistics, 1975-1988," *International Statistical Review,* Vol. 57, No. 3, 1989, pp. 261-294.

[3.47] Zeng, X., L. D. Mitchell, and B. L. Agee, "A Laser Position Determination Algorithm for an Automated Mechanical Mobility Measurement System, " *Proceedings of the 11th International Modal Analysis Conference*, Vol. 1, Kissimmee, Florida, February 1-4, 1993, pp. 122-129

[3.48] Zeng, X., L. D. Mitchell, and B. L. Agee, "The Determination of the Scanning List for a Laser-Based Mobility Measurement System," *Technical Report to Zonic Corporation*, Milford, Ohio, January, 1992.

[3.49] Press, W. H., S. A. Teukosky, W. T. Vetterling, and B. P. Flannery, *Numerical Receipes in C: The Art of Scientific Computing*, second eddition, Cambridge University Press, 1992.

CHAPTER FOUR

CHAPTER FIVE

[5.1] Helga, B. and O. Bunke, *Nonlinear Regression, Functional Relations and Robust Methods: Statistical Method of Model Building*, Volumn 2, John Wiley & Sons, Chichester, 1989.

[5.2] Pazman, A., *Nonlinear Statistical Models,* Kluwer Academin Publishers, Dordrecht, 1993.

[5.3] Seber, G. A. F. and C. J. Wild, *Nonlinear Regression*, John Wiley & Sons, New York, 1989.

[5.4] Ratkowsky, D. A., *Nonlinear Regression Modeling: A Unified Practical Approach*, Marcel Dekker, Inc., New York, 1983.

[5.5] Bates, D. M. and D. G. Watts, *Nonlinear Regression analysis and its Applicatio*n, John and Wiley & Sons, New York, 1988.

[5.6] Neter, J., W. Wasserman, and M. H. Kutner, *Applied Linear Statistical Models: Regression, Analysis of Variance and Experimental Design*, Third Edition, Richard D. Irwin, Inc., Boston, 1990.

[5.7] Hsia, T. C., *System Identification: Least-Squares Methods,* Lexington Books, D. C. Heath and Company, Lexington. Massachusetts, 1977.

[5.8] Ott, L., *An Introduction to Statistical Methods and Data Analysis*, third edition, PWS-KENT Publishing Company, Boston, 1988.

[5.9] Johnson, R. A. and D. W. Wichern, *Applied Multivariate Statistical Analysis,* Third edition, Prentice-Hall, Inc., Englewood Cliffs, New Jersey, 1992.

[5.10] Bates, D. M., and D. G. Watts, "Relative Curvature Measures of Nonlinearity (with Discussion)," *Journal of the Royal Statistical Society, Ser. B*, Vol. 42, No. 1, 1980, pp. 1-25.

[5.11] Beale, E. M. L., "Confidence Regions in Nonlinear Estimation (with Discussion)," *Journal of the Royal Statistical Society, Ser. B*, Vol. 22, No. ?1, 1960, pp. 41-88.

[5.12] Zeng, X. and A. L. Wicks, "A Comparison of Two Methods for Estimating the Magnitude and Phase Angle of a Harmonic Wave," *Proceedings of the 11th International Modal Analysis Conference*, Vol. 1, Kissimmee, Florida, February 1-4, 1993, pp. 906-912.

CHAPTER SIX

[6.1] The Math Works, Inc., *MATLAB reference guide*, 24 Prime Park Way, Natick, Mass. 01760, 1993.

[6.2] Stephen Wolfram, *Mathematica: a System for Doing Mathematics by Computer*, Second Edition, Addison-Wesley Publishing Company, Inc., New York, 1991.

CHAPTER SEVEN

[7.1] Jones, B., *Statistics Toolbox User's Guide*, The Math Works, Inc., 1993.

[7.2] Bendat, J. S. and A. G. Piersol, *Random Data: Analysis and Measurement Procedure*, Second Edition, John Wiley & Sons, New York, 1986.

CHAPTER EIGHT

CHAPTER NINE

APPENDIX A

DERIVATIVE COMPUTATION OF THE INVERSE MODEL

In this appendix, the first order and the second order derivatives of the expectation function of the inverse model with respect to the six pose parameters will be derived. Due to the complexity of the expressions, those derivatives are obtained by using Mathematica.

A.1 Analytical expressions for the derivatives of the inverse model

The inverse model developed in chapter 5 has following expectation functions for spatial point P_i (Eq. (5.18))

$$\mu_{P_i X_L} = tan^{-1}\left(\frac{y_{P_i L}}{z_{P_i L}}\right), \quad \mu_{P_i Y_L} = tan^{-1}\left(\frac{x_{P_i L}}{\sqrt{y_{P_i L}^2 + z_{P_i L}^2} + dl}\right) \tag{A.1}$$

where the laser coordinates are obtained through the coordinate transformation (Eq. (2.2))

$$\begin{Bmatrix} x_{P_i} \\ y_{P_i} \\ z_{P_i} \end{Bmatrix}_L = {}^L_S[T] + {}^L_S[R] \begin{Bmatrix} x_{P_i} \\ y_{P_i} \\ z_{P_i} \end{Bmatrix}_S \tag{A.2}$$

If the rotation matrix is expressed by three Euler angles, the rotation matrix is (Eq. (3.5))

$${}^L_S[R] = \begin{bmatrix} \cos\alpha\cos\beta & \cos\alpha\sin\beta\sin\gamma - \sin\alpha\cos\gamma & \cos\alpha\sin\beta\cos\gamma + \sin\alpha\sin\gamma \\ \sin\alpha\cos\beta & \sin\alpha\sin\beta\sin\gamma + \cos\alpha\cos\gamma & \sin\alpha\sin\beta\cos\gamma - \cos\alpha\sin\gamma \\ -\sin\beta & \cos\beta\sin\gamma & \cos\beta\cos\gamma \end{bmatrix} \tag{A.3}$$

Note that the three angles are the $Z_S - Y_S - X_S$ Euler angles. By defining a parameter vectors (Eq. (5.18)) for the six pose parameters

$$\left.\begin{array}{l} \gamma_1 = {}^L_S T_x, \quad \gamma_2 = {}^L_S T_y, \quad \gamma_3 = {}^L_S T_z \\ \gamma_4 = \alpha, \quad \gamma_5 = \beta, \quad \gamma_6 = \gamma \end{array}\right\} \tag{A.4}$$

The laser coordinates become functions of the six pose parameters. Putting the Eqs. (A.3) and Eq. (A.4) into Eq. (A.2), one has

$$\begin{aligned} x_{P_i,L} = {} & \gamma_1 + (\cos\gamma_4 \cos\gamma_5) x_{P_i,S} + (\cos\gamma_4 \sin\gamma_5 \sin\gamma_6 - \sin\gamma_4 \cos\gamma_6) y_{P_i,S} \\ & + (\cos\gamma_4 \sin\gamma_5 \cos\gamma_6 + \sin\gamma_4 \sin\gamma_6) z_{P_i,S} \end{aligned} \tag{A.5}$$

$$\begin{aligned} y_{P_i,L} = {} & \gamma_2 + (\sin\gamma_4 \cos\gamma_5) x_{P_i,S} + (\sin\gamma_4 \sin\gamma_5 \sin\gamma_6 + \cos\gamma_4 \cos\gamma_6) y_{P_i,S} \\ & + (\sin\gamma_4 \sin\gamma_5 \cos\gamma_6 - \cos\gamma_4 \sin\gamma_6) z_{P_i,S} \end{aligned} \tag{A.6}$$

$$z_{P_i,L} = \gamma_3 + (-\sin\gamma_5) x_{P_i,S} + (\cos\gamma_5 \sin\gamma_6) y_{P_i,S} + (\cos\gamma_5 \cos\gamma_6) z_{P_i,S} \tag{A.7}$$

If the laser coordinates (Eqs. (A.5-A.7)) are directly put into Eq. (A.1), one can obtain expressions in which the expectation functions are explicitly expressed as functions of the six pose parameters. However, for the purpose of obtaining derivatives, it is not necessary to do that since the chain rule can be applied to get the derivatives.

The first order derivatives are needed in three places: (i) the Gauss-Newton algorithm for the parameter estimation (section **5.2.2**), (ii) the statistical inferences by the linear approximation (section **5.3.2.2**), and (iii) the measures of the nonlinearity (section **5.4.3**). The second order derivatives are needed only in the measures of the nonlinearity.

Due to the complexity of the expressions of Eqs. (A.1) and (A.5-A.7), the first and second order derivatives of the inverse model with respect to the six pose parameters are obtained

by using Mathematica. Program listing A.1 is the Mathematica code to symbolically get the analytical expressions for those derivatives.

Program listing A.1 Mathematica code for obtaining the derivatives

```
(* ---------------------------- derive.math  ------------------------- *)
(*                                                                      *)
(*Mathematica program to find out the derivatives of the inverse model*)
(*                                                                      *)
(* ---------------------------------------------------------------------- *)

(* ->1. define the x, y, z as functions of the six pose parameters*)

x[r1_,r4_,r5_,r6_]=r1+ Cos[r4] Cos[r5] x0+
                    (Cos[r4] Sin[r5] Sin[r6] - Sin[r4] Cos[r6]) y0+
                    (Cos[r4] Sin[r5] Cos[r6] + Sin[r4] Sin[r6]) z0

y[r2_,r4_,r5_,r6_]=r2+ Sin[r4] Cos[r5] x0+
                    (Sin[r4] Sin[r5] Sin[r6] + Cos[r4] Cos[r6]) y0+
                    (Sin[r4] Sin[r5] Cos[r6] - Cos[r4] Sin[r6]) z0

z[r3_,r4_,r5_,r6_]=r3- Sin[r5] x0 + Cos[r5] Sin[r6] y0 +
                    Cos[r5] Cos[r6] z0

(* ->2. define the inverse model for theta_X and theta_y *)

thx=ArcTan[y[r2,r4,r5,r6]/z[r3,r4,r5,r6]]

thy=ArcTan[x[r1,r4,r5,r6]/(Sqrt[y[r2,r4,r5,r6]^2+z[r3,r4,r5,r6]^2]+dl)]

(* ->3. take the first-order derivatives *)
thxD1=D[thx,r1]
thxD2=D[thx,r2]
thxD3=D[thx,r3]
thxD4=D[thx,r4]
thxD5=D[thx,r5]
thxD6=D[thx,r6]

thyD1=D[thy,r1]
thyD2=D[thy,r2]
thyD3=D[thy,r3]
thyD4=D[thy,r4]
thyD5=D[thy,r5]
thyD6=D[thy,r6]

(* ->4 take the second-order derivatives of thx      *)
(* Note: thx is not a funciton of r1, thus its second order *)
(* derivatives are zero (skip)                                  *)
thxD22=D[thx,{r2,2}]
thxD23=D[thx,r2,r3]
thxD24=D[thx,r2,r4]
```

```
thxD25=D[thx,r2,r5]
thxD26=D[thx,r2,r6]

thxD33=D[thx,{r3,2}]
thxD34=D[thx,r3,r4]
thxD35=D[thx,r3,r5]
thxD36=D[thx,r3,r6]

thxD44=D[thx,{r4,2}]
thxD45=D[thx,r4,r5]
thxD46=D[thx,r4,r6]

thxD55=D[thx,{r5,2}]
thxD56=D[thx,r5,r6]

thxD66=D[thx,{r6,2}]

(* ->5. take the second-order derivatives of thy *)
thyD11=D[thy,{r1,2}]
thyD12=D[thy,r1,r2]
thyD13=D[thy,r1,r3]
thyD14=D[thy,r1,r4]
thyD15=D[thy,r1,r5]
thyD16=D[thy,r1,r6]

thyD22=D[thy,{r2,2}]
thyD23=D[thy,r2,r3]
thyD24=D[thy,r2,r4]
thyD25=D[thy,r2,r5]
thyD26=D[thy,r2,r6]

thyD33=D[thy,{r3,2}]
thyD34=D[thy,r3,r4]
thyD35=D[thy,r3,r5]
thyD36=D[thy,r3,r6]

thyD44=D[thy,{r4,2}]
thyD45=D[thy,r4,r5]
thyD46=D[thy,r4,r6]

thyD55=D[thy,{r5,2}]
thyD56=D[thy,r5,r6]

thyD66=D[thy,{r6,2}]

(* ->6. save all the derivatives *)
  Save["derive.txt",
        thxD1,thxD2,thxD3,thxD4,thxD5,thxD6,
        thyD1,thyD2,thyD3,thyD4,thyD5,thyD6,
        thxD22,thxD23,thxD24,thxD25,thxD26,
        thxD33,thxD34,thxD35,thxD36,
        thxD44,thxD45,thxD46,
        thxD55,thxD56,
        thxD66,
        thyD11,thyD12,thyD13,thyD14,thyD15,thyD16,
        thyD22,thyD23,thyD24,thyD25,thyD26,
```

```
        thyD33,thyD34,thyD35,thyD36,
        thyD44,thyD45,thyD46,
        thyD55,thyD56,
        thyD66]

(* ------------------------- the end ---------------------------- *)
```

In the above Mathematica code, *ri* (*i*=1, 2, ..., 6) are the six pose parameters. *x*0, *y*0, and *z*0 are the structural coordinates for point P_i. *x*, *y*, and *z* are the laser coordinates for point P_i. The first order derivatives are *thxDi* and *thyDi* (*i*=1, 2, ..., 6). The second order derivatives are *thxDjk* and *thyDjk* (*j*, *k*=1, 2, ..., 6). Due to the symmetry, only the uppertriangle part of the complete matrix is obtained. Once the analytical derivative expressions are obtained, one can get the numerical values of the derivatives for any given registration point and given pose parameters.

The first order derivative matrix of the inverse model is a 2*N* by 6 matrix for *N* registration points. Its *i*th submatrix is for point P_i

$$\left[V_{P_i}\right]=\begin{bmatrix} thxD1 & thxD2 & thxD3 & thxD4 & thxD5 & thxD6 \\ thyD1 & thyD2 & thyD3 & thyD4 & thyD5 & thyD6 \end{bmatrix} \tag{A.8}$$

The whole matrix is

$$[V]=\begin{bmatrix} \left[V_{P_1}\right] \\ \vdots \\ \left[V_{P_N}\right] \end{bmatrix} \tag{A.9}$$

When used in the Gauss-Newton algorithm, [*V*] is evaluated at the current solution of the six parameter $\{\gamma\}=\{\gamma^*\}$. This will result in matrix [*J*] as defined in Eq. (5.27). When used in the statistical inferences and in the measures of the nonlinearity, [*V*] is evaluated at

the least squares estimation of the six parameters $\{\gamma\}=\{\hat{\gamma}\}$. This will result in matrix $[\hat{J}]$.

The second order derivative array of the inverse model will be a $2N$ by 6 by 6 array. For point P_i, there will be two faces of the three-dimensional array. One is the $(2i\text{-}1)$th face

$$\left[\dot{V}\right]_{2i-1,jk} = thxDjk \qquad (\text{for } j, k=1, 2, ..., 6), \tag{A.10}$$

and the other is the $(2i)$th face

$$\left[\dot{V}\right]_{2i,jk} = thyDjk \qquad (\text{for } j, k=1, 2, ..., 6) \tag{A.11}$$

Since this array is used in the measures of the nonlinearity, it will be evaluated at the least squares estimation of the six parameter $\{\gamma\}=\{\hat{\gamma}\}$.

A.2 The numerical evaluation of the derivatives

The analytical expressions for those derivatives from Mathematica are imported to Matlab for numerical evaluation. The reason for this is that the other parts such as statistical inferences and the measures of nonlinearity are implemented in Matlab. To make sure there is no mistake during the importation process, a numerical derivative scheme is used to check the analytical derivatives. The numerical derivatives are obtained by using three point formulas, i.e.

$$\left.\frac{df}{dx}\right|_{x=x_0} = \frac{1}{2h}\left(f(x_0+h)-f(x_0-h)\right) \tag{A.11}$$

$$\left.\frac{d^2f}{dx^2}\right|_{x=x_0} = \frac{1}{h^2}\left(f(x_0+h)+f(x_0-h)-2f(x_0)\right) \tag{A.12}$$

By changing only one variable at a time and using Eqs. (A.11-A.12), the partial derivatives of the inverse model can be obtained. For the purpose of comparing the numerical derivative and analytical derivative, arbitrary pose parameters and structural coordinates may be used. The following are assumed values.

$\gamma_1 = 100$ inches (2540 mm); $\gamma_2 = 80$ inches (2032 mm); $\gamma_3 = 10$ inches (254 mm)(A.13)

$\gamma_4 = \pi/3$; $\gamma_5 = \pi/4$; $\gamma_6 = \pi/6$ (A.14)

$x_{P,S} = 30$ inches (762 mm); $y_{P,S} = 20$ inches (508 mm); $z_{P,S} = 20$ inches (508 mm)(A.15)

dl=1.8110 inches (46 mm) (A.16)

Step length h=0.01 is used for all the six parameters when finding the numerical derivatives.

Table A.1 shows the numerical derivatives and the analytical derivatives (numerical evaluation of the analytical expressions) for the inverse model. The left column is the name of the derivatives. The central column is the numerical derivatives obtained by using Eqs.(A.11) or (A.12) and using the assumed pose parameter and structural coordinates. The last column is the numerical evaluation of the analytical derivatives at the assumed pose parameters and structural coordinates. Since $\partial \mu_{P,X_L} / \partial \gamma_1$ and $\partial^2 \mu_{P,X_L} / \partial \gamma_1^2$ are always zero, they are not listed in Table A.1.

From the results shown in Table A.1, the numerical derivative and the analytical derivative are almost identical. Therefore, the imported analytical derivative expressions from Mathematica are correct and can be used for statistical inferences and measures of the nonlinearity of the inverse model.

Table A.1 Comparison of the numerical and analytical derivatives

Derivative Name	Numerical Derivatives	Analytical Derivatives
$\partial\mu_{P,X_L}/\partial\gamma_2$	0.000572	0.000572
$\partial\mu_{P,X_L}/\partial\gamma_3$	-0.008381	-0.008381
$\partial\mu_{P,X_L}/\partial\gamma_4$	0.007966	0.007966
$\partial\mu_{P,X_L}/\partial\gamma_5$	0.338763	0.338765
$\partial\mu_{P,X_L}/\partial\gamma_6$	-0.048632	0.048634
$\partial\mu_{P,Y_L}/\partial\gamma_1$	0.004381	0.004381
$\partial\mu_{P,Y_L}/\partial\gamma_2$	-0.004121	-0.004121
$\partial\mu_{P,Y_L}/\partial\gamma_3$	-0.000281	-0.000281
$\partial\mu_{P,Y_L}/\partial\gamma_4$	-0.227205	-0.227207
$\partial\mu_{P,Y_L}/\partial\gamma_5$	0.014009	0.014009
$\partial\mu_{P,Y_L}/\partial\gamma_6$	0.151358	0.151360
$\partial^2\mu_{P,X_L}/\partial\gamma_2^2$	-0.000010	-0.000010
$\partial^2\mu_{P,X_L}/\partial\gamma_3^2$	0.000010	0.000010
$\partial^2\mu_{P,X_L}/\partial\gamma_4^2$	-0.024032	-0.024031
$\partial^2\mu_{P,X_L}/\partial\gamma_5^2$	-0.010932	-0.010932
$\partial^2\mu_{P,X_L}/\partial\gamma_6^2$	0.143055	0.143055
$\partial^2\mu_{P,Y_L}/\partial\gamma_1^2$	-0.000036	-0.000036
$\partial^2\mu_{P,Y_L}/\partial\gamma_2^2$	0.000036	0.000036
$\partial^2\mu_{P,Y_L}/\partial\gamma_3^2$	-0.000034	-0.000034
$\partial^2\mu_{P,Y_L}/\partial\gamma_4^2$	0.053591	0.053590
$\partial^2\mu_{P,Y_L}/\partial\gamma_5^2$	-0.000454	-0.000455
$\partial^2\mu_{P,Y_L}/\partial\gamma_6^2$	0.052606	0.052606

APPENDIX B

AN ALGORITHM FOR CALCULATING THE RELATIVE CURVATURES AND ITS IMPLEMENTATION

As shown in section **5.4.2**, the relative parameter-effects and intrinsic curvatures vary with the direction vector $\{h\}$. To study the nonlinearity of the model function, the maximum of each of those two curvatures needs to be found. Directly using the formulas in that section to calculate the maximums is not efficient. Bates and Watts [5.10] developed an efficient algorithm to do that. The basic idea in their algorithm is to simplify the calculation by linear coordinate transformation in both the parameter space and the response space. In this appendix, their algorithm will be derived, implemented and verified.

B.1 Coordinate transformation in both the parameter and the response space

In the response space, the coordinates are rotated such that the first M coordinate vectors are parallel to the tangent plane and the last N-M are orthogonal to the tangent plane. This can be done by premultiplying all the vectors in the response space by an orthogonal matrix $[Q]^T$, where $[Q]$ is one part of the QR decomposition of the matrix $[V]$, i.e.

$$[V]=[Q][R]=[Q]\begin{bmatrix}[\tilde{R}]\\ [0]\end{bmatrix} \tag{B.1}$$

where $[\tilde{R}]$ is an M by M upper triangle matrix, $[0]$ is an $(N\text{-}M)$ by M zero matrix.

In the parameter space, the coordinate transformation is defined as

$$\{\phi\}=[\tilde{R}](\{\gamma\}-\{\hat{\gamma}\}) \tag{B.2}$$

After the transformation, the first order derivatives of the expectation function with respect to the parameter $\{\phi\}$ is

$$[U]=\frac{d\{\mu\}}{d\{\phi\}}\Big|_{\{\phi\}=\{0\}}=\frac{d\{\mu\}}{d\{\gamma\}}\Big|_{\{\gamma\}=\{\hat{\gamma}\}}\frac{d\{\gamma\}}{d\{\phi\}}\Big|_{\{\phi\}=\{0\}}$$
$$=[Q]\begin{bmatrix}[\tilde{R}]\\ [0]\end{bmatrix}[\tilde{R}]^{-1}=[Q]\begin{bmatrix}[I]\\ [0]\end{bmatrix} \tag{B.3}$$

Thus, $[U]$ is the first M columns of the $[Q]$ matrix. The second order derivatives of the expectation function with respect to the parameter $\{\phi\}$ is

$$\lfloor \dot{U} \rfloor=\frac{\partial \mu_i}{\partial\phi_j\partial\phi_k}=[L]^T\lfloor \dot{V} \rfloor[L] \tag{B.4}$$

where $[L]=[\tilde{R}]^{-1}$. The multiplication in Eq. (B.4)) is completed on each face, i.e., the ith face of matrix $\lfloor \dot{U} \rfloor_i$ is defined as

$$\lfloor \dot{U} \rfloor_i=[L]^T\lfloor \dot{V} \rfloor_i[L]. \tag{B.5}$$

Each face of the three-dimensional array is an M by M matrix.

In the rotated response space, the first order derivative matrix $[U]$ becomes

$$[U]_R=[Q]^T[U]=[Q]^T[Q]\begin{bmatrix}[I]\\ [0]\end{bmatrix}=\begin{bmatrix}[I]\\ [0]\end{bmatrix} \tag{B.6}$$

From the above equation, one can see that in the rotated response space, the derivatives of the expectation function with respect to the parameters $\{\phi\}$ are the standard basis vectors.

In the rotated response space, the second order derivative array $\lfloor \dot{U} \rfloor$ becomes

$$\lfloor \dot{U} \rfloor_R=[Q]^T\lfloor \dot{U} \rfloor \tag{B.7}$$

The right hand side is the multiplication of a matrix by a three-dimensional array. The result is still a three-dimensional array, this multiplying operation is defined as

$$\dot{U}_{ijk,R} = \sum_{l=1}^{N} Q_{il}^{T} \dot{U}_{ljk} \tag{B.8}$$

The array $\lfloor \dot{U} \rfloor_R$ can be written as

$$\lfloor \dot{U} \rfloor_R = \lfloor \dot{U} \rfloor_R^{PE} + \lfloor \dot{U} \rfloor_R^{IN} \tag{B.9}$$

where $\lfloor \dot{U} \rfloor_R^{PE}$ is the first M faces of $\lfloor \dot{U} \rfloor_R$ and is parallel to the tangent plane, $\lfloor \dot{U} \rfloor_R^{PE}$ is the last N-M faces of $\lfloor \dot{U} \rfloor_R$ and is perpendicular to the tangent plane.

From the above derivations, the velocity and acceleration vectors of the expectation function with respect to the parameters $\{\phi\}$ are expressed in the rotated response space. As shown in next section, this expression will simplify the relative curvature calculations.

B.2 Calculation of the relative curvatures

The curvatures for an arbitrary direction $\{h\}$ in the $\{\gamma\}$ parameter space is (Eq. (5.90))

$$c_{\{h\}} = \frac{\left\| \left\{ \ddot{\mu}_{\{h\}} \right\} \right\|}{\left\| \left\{ \dot{\mu}_{\{h\}} \right\} \right\|^2} \tag{B.10}$$

From Eq. (5.87), it can be seen this curvature is independent of the length of the direction vector $\{h\}$. The straight line $\{\gamma\} = \{\hat{\gamma}\} + \lambda\{h\}$ in the $\{\gamma\}$ parameter space become a straight line in the $\{\phi\}$ parameter space, i.e.

$$\{\phi\} = \left[\tilde{R}\right]\left(\{\hat{\gamma}\} + \lambda\{h\} - \{\hat{\gamma}\}\right) = \lambda\left[\tilde{R}\right]\{h\} = \lambda\{d\} \tag{B.11}$$

where $\{d\} = [\tilde{R}]\{h\}$. It can be shown [5.3] that the derivatives of the expectation function along the direction $\{d\}$ in $\{\phi\}$ parameter space is equal to the derivatives along the direction $\{h\}$ in $\{\gamma\}$ parameter space, i.e.,

$$\left.\begin{aligned} \{\dot{\mu}_{\{h\}}\} &= \{\dot{\mu}_{\{d\}}\} = [U]\{d\} \\ \{\ddot{\mu}_{\{h\}}\} &= \{\ddot{\mu}_{\{d\}}\} = \{d\}^T \lfloor \dot{U} \rfloor \{d\} \end{aligned}\right\} \tag{B.12}$$

Since the curvature is independent of the length of the direction $\{h\}$, the curvatures can be calculated by using a unit vector $\{d\}$. In the rotated response space, one has

$$\left.\begin{aligned} \{\dot{\mu}_{\{d\}}\}_R &= [U]_R\{d\} = \begin{Bmatrix}\{d\} \\ \{0\}\end{Bmatrix} \\ \{\ddot{\mu}_{\{h\}}\}_R &= \{\ddot{\mu}_{\{d\}}\} = \{d\}^T \lfloor \dot{U} \rfloor_R \{d\} \end{aligned}\right\} \tag{B.13}$$

Since the rotation does not change the length of a vector,

$$\left\|\{\dot{\mu}_{\{d\}}\}_R\right\| = \left\|\{\dot{\mu}_{\{d\}}\}\right\|, \quad \left\|\{\ddot{\mu}_{\{d\}}\}_R\right\| = \left\|\{\ddot{\mu}_{\{d\}}\}\right\| \tag{B.14}$$

Since $\{d\}$ is a unit vector, the length of the vector $\{\dot{\mu}_{\{d\}}\}$ is equal to one. The curvature along direction $\{d\}$ is

$$c_{\{d\}} = \left\|\{\ddot{\mu}_{\{d\}}\}\right\| = \left\|\{d\}^T \lfloor \dot{U} \rfloor_R \{d\}\right\| \tag{B.15}$$

The relative parameter-effects curvature is

$$\eta^{PE}_{\{d\}} = \rho \left\|\{d\}^T \lfloor \dot{U} \rfloor^{PE}_R \{d\}\right\| \tag{B.16}$$

where ρ is the standard radius defined in Eq. (5.93). The relative intrinsic curvature is

$$\eta^{IN}_{\{d\}} = \rho \left\|\{d\}^T \lfloor \dot{U} \rfloor^{IN}_R \{d\}\right\| \tag{B.17}$$

The maximum relative parameter-effect and the maximum intrinsic curvatures can be obtained by changing the direction vector $\{d\}$. Bates and Watts [5.10] developed a iterative method to find it. They found that if the gradient $\nabla\left(\eta_{\{d\}}^{PE}\right)$ has the same direction as vector $\{d\}$, then direction vector $\{d\}$ will locate a local maximum for $\eta_{\{d\}}^{PE}$. In their method, they used $\nabla\left(\eta_{\{d\}}^{PE}\right)^2$ instead of $\nabla\left(\eta_{\{d\}}^{PE}\right)$ since $\nabla\left(\eta_{\{d\}}^{PE}\right)^2$ is in the same direction as $\nabla\left(\eta_{\{d\}}^{PE}\right)$. The following is the procedure for finding the maxim parameter-effects curvature.

I). Select an initial direction vector $\{d\}_i$

II). Calculate $\{g\}_i = \nabla\left(\eta_{\{d\}_i}^{PE}\right)^2 = 4\left\{\{d\}_i^T \left\lfloor \dot{U} \right\rfloor_R^{PE} \{d\}_i\right\}^T \left(\left\lfloor \dot{U} \right\rfloor_R^{PE} \{d\}_i\right)$ and

$\{\tilde{g}\}_i = \{g\}_i / \left\|\{g\}_i\right\|$

III). If $\{\tilde{g}\}_i^T \{d\}_i < 1-e$, then set $\{d\}_{i+1} = \{\tilde{g}_i\}$ and repeat from step (II), otherwise set

$$\eta_{max}^{PE} = \rho\left\|\{d\}_i^T \left\lfloor \dot{U} \right\rfloor_R^{PE} \{d\}_i\right\|$$

The error e in step (III) is the convergence criterion which control how close to being in the same direction the $\{d\}_i$ and the gradient are required to be. It may be set that e=0.0001 or smaller.

The outlined procedure can be used to find the maximum relative intrinsic curvature η_{max}^{IN} with $\left\lfloor \dot{U} \right\rfloor_R^{PE}$ being replaced by $\left\lfloor \dot{U} \right\rfloor_R^{IN}$. The experience of Bates and Watts shows that their algorithm tends to oscillate about the optimum as it gets close to convergence. They modified step (III) to set

$$\{d\}_{i+1} = \frac{\left(3\{\tilde{g}\}_i + \{d\}_i\right)}{\left\|\left(3\{\tilde{g}\}_i + \{d\}_i\right)\right\|} \tag{B.18}$$

They also noticed that using a QR decomposition with pivoting to define $\lfloor \dot{U} \rfloor_R$, $\{d\}_i$ tended to lie close to $\{d\}_0 = (0,\ 0,\ ...,\ 1)^T$. Thus, they set the initial direction vector $\{d\}_i$ to be $\{d\}_0$

With the above starting value and convergence criterion, the modified algorithm usually converged in about four iterations and never required more than ten iterations in any of their examples. Bates and Watts also developed a method for calculating bounds for the relative curvatures. If the calculated maximum falls in the bounds, a global maximum is considered to be achieved

B.3 Implementation and verification of the algorithm

The discussed algorithm has been implemented in Matlab. In the implementation, Eq (B.18) is used to update $\{d\}_i$. The initial value for direction vector $\{d\}$ is from the calling program. The implementation looks straight forward. However, some efforts have been made to handle the three-dimensional second order derivative arrays and the related multiplication operations with them since Matlab only allows two-dimensional array (matrix). The three-dimensional N by M by M arrays are expressed as an NM by M matrices. Each M by M submatrix is one face of the original three-dimensional array. The related multiplication with those arrays is adjusted based on the matrix expressions.

To verify the effectiveness of the algorithm and correctness of the implementation, three cases have been tested. The following is the details.

I). One parameter case

This is the example used in section **5.4.1.2.** The regressive models is

$$y_i = 1 - e^{-t_i \gamma_1} + \varepsilon_i \tag{B.19}$$

Two assumed observations are (i) t_1=0.4, y_1=0.57; (ii) t_2=1.5, y_2=0.93. Using the least squares method, the parameters and the standard deviation of the residuals are obtained as

$$\hat{\gamma}_1 = 2.0555, \; s = 0.0260 \tag{B.20}$$

Using the implemented algorithm, the relative parameter-effects and intrinsic curvatures are found as

$$\eta^{PE} = 0.0751, \; \eta^{IN} = 0.0513 \tag{B.21}$$

This is the same as what has obtained in section **5.4.2.5** (Eq. (5.105)). In that section the second order derivative was directly projected onto the tangent line and a line perpendicular to the tangent line.

II). Two parameters case

Again this is the example used in section **5.4.1.2.** The regression model is

$$y_i = \gamma_1 \sin(\omega t_i + \gamma_2) + \varepsilon_i \tag{B.22}$$

Three assumed observations are: (i) t_1=0.00, y_1=0.70; (ii) t_2=0.40, y_2=–0.15; (iii) t_3=0.80, y_3=–0.45. The frequency ω is assumed to be 2π. Using the least squares method, the two parameters and the standard deviation of the residuals are estimated as

$$\hat{\gamma}_1 = 0.9901, \; \hat{\gamma}_2 = 0.7830, \; s = 0.0034 \tag{B.23}$$

Putting the estimated parameters into Eqs. (5.106) and (5.107), one can find the velocity and acceleration vectors. Using the implemented algorithm, the maximum relative parameter-effects curvature and the intrinsic curvature are obtained.

$$\eta_{max}^{PE} = 0.0073,\ \eta_{max}^{IN} = 0.0000 \tag{B.24}$$

In section **5.4.2.5,** it was shown that the acceleration vectors were in the tangent plane, the intrinsic curvature was zero. Here the same conclusion is obtained. It can be found that $F(2,\ 1;\ 0.05) = 199.5$, thus,

$$\eta_{max}^{PE} = 0.0073 < 1/\left(2\sqrt{F}\right) = 0.0354 \tag{B.24}$$

Therefore, the linear approximation for this model is acceptable. Looking at Fig. 5.4, one would not say that the expectation surface is not flat enough.

Since this model contains only two parameters, the parameter space is a two-dimensional space. Any unit direction vector in the parameters can be expressed as

$$\{h\} = \begin{Bmatrix} cos\,\alpha \\ sin\,\alpha \end{Bmatrix} \tag{B.25}$$

where α is the angle between the vector $\{h\}$ and the first parameter axis. This is shown in Fig. B.1.

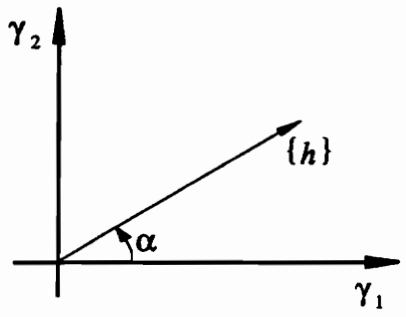

Figure B.1 Direction vector $\{h\}$ in two-dimensional parameter space

Multiplying Eq. (5.90) by the standard radius, one will get the relative curvature

$$\eta_{\{h\}} = \rho c_{\{h\}} = \rho \frac{\left\| \left\{ \ddot{\mu}_{\{h\}} \right\} \right\|}{\left\| \left\{ \dot{\mu}_{\{h\}} \right\} \right\|^2} \tag{B.26}$$

where $\left\{ \dot{\mu}_{\{h\}} \right\}$ and $\left\{ \ddot{\mu}_{\{h\}} \right\}$ are calculated by Eq. (5.87). The relative curvature $\eta_{\{h\}}$ can be obtained for different direction vectors. Figure B.2 shows the result.

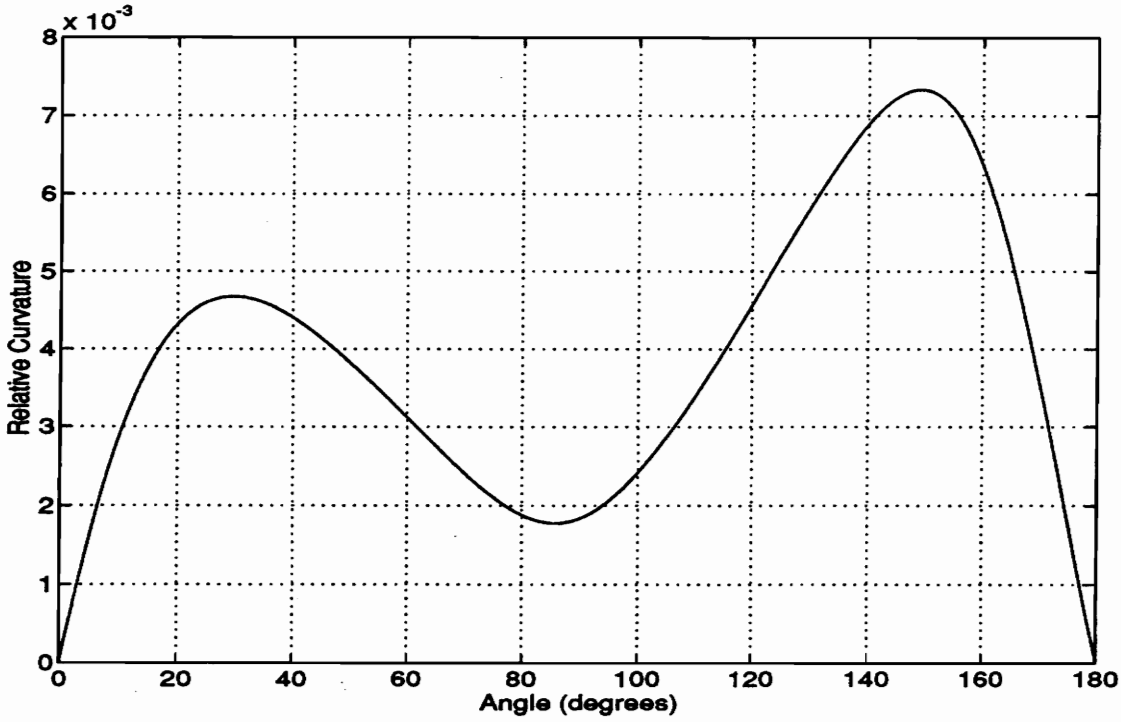

Figure B.2 The relative curative versus the angle of direction $\{h\}$ in the parameter space

Since the intrinsic curvature is zero, the relative curvature shown in Fig. B.2 is equal to the parameter-effects curvatures. The maximum in Fig. B.2 is

$$\eta_{max}=0.0073. \tag{B.27}$$

Which is the same as the one obtained by the implemented algorithm. This provides an example which shows the implemented algorithm in this appendix is correct

III). A case in Bates and Watts' paper

The regressive model in their paper [5.10] is

$$Y_i = \frac{\gamma_1 x_{i1}}{\gamma_2 + x_{i1}} + \varepsilon_i \qquad \text{(B.28)}$$

Using the observations and the estimated parameters from their paper, the first order and the second order derivatives are obtained. Then, by using the implemented algorithm the maximum relative parameter-effects curvature and the maximum relative intrinsic curvature are computed. The following is the results.

$$\eta_{max}^{PE} = 0.7669,\ \eta_{max}^{IN} = 0.0834 \qquad \text{(B.29)}$$

η_{max}^{IN} is the same as the one in the paper by Bates and Watts. However, they reported the maximum relative curvature (defined in the Eq. (B.26)) as η_{max}^{PE} in their paper. Since the intrinsic curvature is not zero for this model, the maximum relative curvature is not equal to the maximum relative parameter-effects curvature. The former is larger.

The above three examples have shown that the algorithm for calculating the relative curvatures is effective and the implementation are correct. Thus, the implemented algorithm can be used to find the maximum relative parameter-effects curvature and the maximum relative intrinsic curvature for the inverse model developed in chapter 5.

APPENDIX C

DATA COLLECTED FOR MODEL ASSESSMENT AND SCANNER CALIBRATION

The collected data and the obtained residuals for sections **7.5** and **8.1.** are presented here.

Table C.1 Data set one for residual analysis in section **7.5.1**

Point ID	Structural coordinates (z_S=0) (inches)		Scanning angles (degrees)		Residuals in scanning angles (degrees)	
	x_S	y_S	φ_X	φ_Y	ε_{φ_X}	ε_{φ_Y}
1	0.3500	0.4000	-11.9591	12.4958	0.0079	-0.0030
2	7.8000	0.4750	-5.9855	12.4958	0.0227	0.0014
3	15.1000	0.5500	0.0115	12.4958	0.0090	0.0069
4	22.3250	0.6250	6.0085	12.4958	0.0154	0.0132
5	29.6250	0.7000	11.9821	12.4958	0.0262	0.0188
6	0.6250	7.8000	-11.9591	6.2707	0.0057	-0.0076
7	7.9500	7.8500	-5.9855	6.2707	0.0043	-0.0010
8	15.1000	7.8750	0.0115	6.2707	-0.0016	-0.0150
9	22.2000	7.9250	6.0085	6.2707	-0.0057	-0.0072
10	29.3750	7.9750	11.9821	6.2707	-0.0050	0.0003
11	0.7250	14.4500	-11.9591	0.5217	0.0037	-0.0100
12	8.0000	14.4750	-5.9855	0.5217	-0.0022	-0.0044
13	15.1000	14.5000	0.0115	0.5217	-0.0113	0.0017
14	22.1500	14.5250	6.0085	0.5217	-0.0178	0.0079
15	29.2750	14.5250	11.9821	0.5217	-0.0190	-0.0080
16	0.6750	22.2500	-11.9591	-6.2283	-0.0105	0.0115
17	7.9500	22.2250	-5.9855	-6.2283	0.0063	-0.0024
18	15.0750	22.2250	0.0115	-6.2283	-0.0012	0.0052
19	22.1500	22.2250	6.0085	-6.2283	-0.0064	0.0128
20	29.3000	22.2250	11.9821	-6.2283	-0.0065	0.0205
21	0.4250	29.5250	-11.9591	-12.4534	-0.0009	-0.0247
22	7.8250	29.5000	-5.9855	-12.4534	0.0073	-0.0162
23	15.0750	29.4750	0.0115	-12.4534	-0.0113	-0.0082
24	22.2500	29.4500	6.0085	-12.4534	-0.0078	-0.0004
25	29.5000	29.4250	11.9821	-12.4534	0.0010	0.0078

Note: 1 inch = 25.4 mm

Table C.2 Data set two for residual analysis in section **7.5.1**

Point ID	Structural coordinates (z_S=0) (inches)		Scanning angles (degrees)		Residuals in scanning angles (degrees)	
	x_S	y_S	φ_X	φ_Y	ε_{φ_X}	ε_{φ_Y}
1	0.7750	1.5000	-11.9591	12.4958	0.0002	-0.0087
2	7.7500	1.2500	-5.9855	12.4958	0.0093	-0.0007
3	14.8000	0.9750	0.0115	12.4958	0.0078	-0.0117
4	22.0250	0.7250	6.0085	12.4958	0.0223	0.0039
5	29.6000	0.4250	11.9821	12.4958	0.0283	-0.0114
6	1.1000	8.4750	-11.9591	6.2707	-0.0140	-0.0051
7	7.9250	8.3000	-5.9855	6.2707	0.0177	-0.0204
8	14.8750	8.1500	0.0115	6.2707	-0.0075	-0.0107
9	21.9750	8.0000	6.0085	6.2707	-0.0005	0.0018
10	29.4000	7.8000	11.9821	6.2707	0.0103	-0.0225
11	1.2500	14.7500	-11.9591	0.5217	-0.0211	-0.0101
12	8.0500	14.7000	-5.9855	0.5217	-0.0058	0.0094
13	14.9250	14.6250	0.0115	0.5217	-0.0063	0.0067
14	22.0000	14.5500	6.0085	0.5217	-0.0191	0.0060
15	29.3750	14.4750	11.9821	0.5217	-0.0093	0.0080
16	1.2500	22.1250	-11.9591	-6.2283	-0.0216	0.0099
17	8.0750	22.1500	-5.9855	-6.2283	-0.0022	0.0060
18	15.0000	22.2000	0.0115	-6.2283	-0.0187	0.0239
19	22.0750	22.2250	6.0085	-6.2283	-0.0037	0.0189
20	29.5000	22.2500	11.9821	-6.2283	-0.0064	0.0128
21	1.0750	29.0250	-11.9591	-12.4534	-0.0106	-0.0121
22	8.0000	29.1500	-5.9855	-12.4534	0.0152	-0.0129
23	15.0250	29.3000	0.0115	-12.4534	0.0085	0.0063
24	22.2250	29.4250	6.0085	-12.4534	0.0166	0.0010
25	29.7750	29.5750	11.9821	-12.4534	0.0150	0.0115

Note: 1 inch = 25.4 mm

Table C.3 Data set three for residual analysis in section **7.5.1**

Point ID	Structural coordinates (z_S=0) (inches)		Scanning angles (degrees)		Residuals in scanning angles (degrees)	
	x_S	y_S	φ_X	φ_Y	ε_{φ_X}	ε_{φ_Y}
1	1.7000	0.6000	-11.9591	12.4958	0.0068	0.0258
2	9.5000	1.1000	-5.9855	12.4958	0.0010	0.0258
3	16.6250	1.5500	0.0115	12.4958	0.0033	0.0195
4	23.2750	1.9750	6.0085	12.4958	0.0122	0.0180
5	29.6500	2.3750	11.9821	12.4958	-0.0149	0.0092
6	2.1000	7.7250	-11.9591	6.2707	0.0083	-0.0017
7	9.7000	7.9500	-5.9855	6.2707	0.0209	-0.0080
8	16.7000	8.1750	0.0115	6.2707	0.0013	0.0028
9	23.2250	8.3500	6.0085	6.2707	0.0030	-0.0208
10	29.4750	8.5500	11.9821	6.2707	-0.0185	-0.0119
11	2.3250	14.1250	-11.9591	0.5217	-0.0075	0.0000
12	9.8250	14.1250	-5.9855	0.5217	0.0248	-0.0014
13	16.7750	14.1250	0.0115	0.5217	-0.0074	-0.0029
14	23.2500	14.1250	6.0085	0.5217	-0.0118	-0.0043
15	29.4500	14.1250	11.9821	0.5217	-0.0340	-0.0057
16	2.3500	21.5750	-11.9591	-6.2283	0.0067	-0.0061
17	9.8750	21.3250	-5.9855	-6.2283	0.0344	0.0072
18	16.8250	21.0750	0.0115	-6.2283	0.0165	0.0019
19	23.3250	20.8500	6.0085	-6.2283	0.0019	0.0054
20	29.5250	20.6250	11.9821	-6.2283	-0.0088	-0.0018
21	2.2500	28.5500	-11.9591	-12.4534	-0.0270	-0.0375
22	9.8750	28.0500	-5.9855	-12.4534	0.0104	-0.0198
23	16.9250	27.5750	0.0115	-12.4534	-0.0088	-0.0142
24	23.4750	27.1500	6.0085	-12.4534	0.0112	0.0073
25	29.7750	26.7250	11.9821	-12.4534	-0.0198	0.0132

Note: 1 inch = 25.4 mm

Table C.4 Data set four for residual analysis in section **7.5.1**

Point ID	Structural coordinates (z_S=0) (inches)		Scanning angles (degrees)		Residuals in scanning angles (degrees)	
	x_S	y_S	φ_X	φ_Y	ε_{φ_X}	ε_{φ_Y}
1	15.0250	29.0000	-0.0002	-11.8552	-0.0096	-0.0011
2	24.8250	22.4250	8.2457	-6.3381	0.0144	0.0149
3	8.8750	19.4250	-5.1305	-3.6894	-0.0082	0.0009
4	18.1250	4.5250	2.6469	9.1392	-0.0010	-0.0084
5	25.1500	28.5750	8.3862	-11.5745	0.0165	0.0090
6	2.1750	15.3250	-10.6121	-0.1496	0.0053	-0.0162
7	12.4250	26.5250	-2.1554	-9.7680	-0.0104	-0.0029
8	5.5750	7.8750	-7.8127	6.2707	-0.0168	0.0002
9	25.5000	4.8500	8.7962	8.8828	0.0130	-0.0077
10	1.8500	11.2250	-10.8463	3.4023	0.0081	0.0042
11	24.2500	15.0250	7.8123	0.0579	-0.0046	-0.0201
12	4.7750	21.5500	-8.4803	-5.4959	0.0005	-0.0007
13	28.3500	5.2250	11.1153	8.5655	-0.0130	-0.0118
14	15.9750	26.9250	0.7963	-10.1220	-0.0073	0.0056
15	4.9250	24.9250	-8.3164	-8.3643	-0.0009	0.0005
16	3.0000	20.4250	-9.9210	-4.5194	0.0088	0.0043
17	20.7000	3.9250	4.8021	9.6762	0.0107	0.0127
18	10.5000	9.3250	-3.7601	5.0379	-0.0164	0.0058
19	24.1750	16.2250	7.7537	-0.9675	0.0035	0.0012
20	15.8250	17.0750	0.7143	-1.6754	0.0049	0.0083
21	8.9250	2.7250	-4.9782	10.6283	-0.0015	-0.0077
22	9.7500	14.6000	-4.4043	0.4851	-0.0100	0.0081
23	20.0500	2.9500	4.2399	10.4940	-0.0019	0.0088
24	24.5250	10.0250	8.0465	4.4276	0.0108	-0.0047
25	6.0250	5.1000	-7.3793	8.6265	0.0058	-0.0032

Note: 1 inch = 25.4 mm

Table C.5 Residuals and intervals for the 9 registration points in section **7.5.2**

Point ID	For X scanning angles (degrees)			For Y scanning angle (degrees)		
	ε_{φ_X}	Confidence interval	Predication interval	ε_{φ_Y}	Confidence interval	Predication interval
1	0.0137	0.0211	0.0378	-0.0043	0.0216	0.0381
3	0.0102	0.0156	0.0350	0.0036	0.0149	0.0347
5	0.0193	0.0195	0.0369	0.0135	0.0223	0.0385
11	0.0063	0.0146	0.0346	-0.0056	0.0162	0.0352
13	-0.0106	0.0135	0.0341	0.0059	0.0138	0.0342
15	-0.0237	0.0141	0.0343	-0.0040	0.0172	0.0357
21	-0.0022	0.0216	0.0380	-0.0213	0.0211	0.0377
23	-0.0111	0.0164	0.0353	-0.0029	0.0148	0.0346
25	-0.0008	0.0201	0.0372	0.0148	0.0218	0.0382

Table C.6 Residuals and intervals for the 16 "new" registration points in section **7.5.2**

Point ID	For X scanning angles (degrees)			For Y scanning angle (degrees)		
	ε_{φ_X}	Confidence interval	Predication interval	ε_{φ_Y}	Confidence interval	Predication interval
2	0.0267	0.0164	0.0354	-0.0009	0.0167	0.0355
4	0.0129	0.0160	0.0351	0.0088	0.0171	0.0357
6	0.0099	0.0165	0.0354	-0.0052	0.0167	0.0355
7	0.0074	0.0135	0.0341	0.0009	0.0136	0.0341
8	-0.0007	0.0140	0.0343	-0.0136	0.0127	0.0338
9	-0.0078	0.0137	0.0342	-0.0064	0.0142	0.0344
10	-0.0109	0.0156	0.0350	0.0005	0.0177	0.0359
12	-0.0001	0.0125	0.0337	-0.0001	0.0143	0.0344
14	-0.0194	0.0129	0.0339	0.0120	0.0149	0.0347
16	-0.0099	0.0168	0.0355	0.0164	0.0166	0.0354
17	0.0073	0.0139	0.0343	0.0029	0.0138	0.0342
18	-0.0007	0.0144	0.0345	0.0109	0.0130	0.0339
19	-0.0073	0.0141	0.0343	0.0189	0.0144	0.0345
20	-0.0097	0.0160	0.0351	0.0270	0.0176	0.0359
22	0.0072	0.0171	0.0357	-0.0118	0.0164	0.0354
24	-0.0082	0.0167	0.0355	0.0058	0.0169	0.0356

Table C.7 The measured data and the residuals for the calibration experiment in section **8.1.3**

Point ID	Structural coordinates (z_S=0) (inches)		Input voltages (volts)		Residuals in input voltages (volts)	
	x_S	y_S	V_X	V_Y	ε_{V_X}	ε_{V_Y}
1	1.0000	1.0055	-4.8584	4.9219	-0.0111	0.0115
2	35.0000	1.0055	4.8877	4.8682	-0.0007	0.0044
3	1.0000	35.1930	-4.8340	-4.9023	-0.0017	0.0010
4	35.0000	35.1930	4.8438	-4.8926	0.0011	-0.0088
5	10.0000	1.0055	-2.2900	4.9024	-0.0030	0.0044
6	18.0000	1.0055	0.0293	4.8877	-0.0011	0.0007
7	26.0000	1.0055	2.3437	4.8779	0.0004	0.0019
8	3.0000	3.0165	-4.2920	4.3360	0.0137	-0.0054
9	33.0000	3.0165	4.3359	4.2920	-0.0118	-0.0114
10	5.0000	5.0276	-3.7500	3.7695	0.0028	0.0016
11	31.0000	5.0276	3.7939	3.7354	-0.0015	-0.0024
12	7.0000	7.0386	-3.1934	3.1885	-0.0037	-0.0022
13	29.0000	7.0386	3.2373	3.1641	0.0046	-0.0036
14	9.0000	9.0496	-2.6221	2.6074	-0.0041	-0.0030
15	27.0000	9.0496	2.6611	2.5928	0.0001	-0.0008
16	1.0000	10.0551	-4.9365	2.3291	-0.0091	0.0018
17	35.0000	10.0551	4.9512	2.2949	-0.0035	-0.0025
18	11.0000	11.0607	-2.0361	2.0264	0.0029	-0.0014
19	25.0000	11.0607	2.0801	2.0117	-0.0017	-0.0046
20	13.0000	13.0717	-1.4502	1.4453	0.0043	0.0018
21	23.0000	13.0717	1.4990	1.4356	0.0023	-0.0009
22	15.0000	15.0827	-0.8740	0.8594	-0.0078	0.0011
23	21.0000	15.0827	0.9082	0.8545	0.0008	-0.0003
24	17.0000	17.0938	-0.2832	0.2735	-0.0073	0.0005
25	19.0000	17.0938	0.3174	0.2735	0.0017	0.0015
26	1.0000	18.0993	-4.9561	-0.0146	-0.0078	-0.0020
27	35.0000	18.0993	4.9658	-0.0293	-0.0005	-0.0028
28	17.0000	19.1048	-0.2832	-0.3125	-0.0064	-0.0013
29	19.0000	19.1048	0.3174	-0.3125	0.0028	-0.0006
30	15.0000	21.1158	-0.8740	-0.8935	-0.0060	0.0004
31	21.0000	21.1158	0.9082	-0.8984	0.0047	-0.0031
32	13.0000	23.1268	-1.4551	-1.4746	0.0012	0.0011
33	23.0000	23.1268	1.4893	-1.4746	0.0001	0.0022
34	11.0000	25.1379	-2.0361	-2.0508	0.0037	0.0048

35	25.0000	25.1379	2.0703	-2.0508	0.0006	0.0047
36	1.0000	26.1434	-4.9219	-2.3389	-0.0021	0.0063
37	35.0000	26.1434	4.9365	-2.3437	0.0043	-0.0008
38	9.0000	27.1489	-2.6172	-2.6269	-0.0001	0.0059
39	27.0000	27.1489	2.6465	-2.6269	0.0030	0.0037
40	7.0000	29.1599	-3.1885	-3.2031	-0.0022	0.0039
41	29.0000	29.1599	3.2129	-3.2031	0.0039	-0.0014
42	5.0000	31.1710	-3.7402	-3.7744	0.0059	0.0028
43	31.0000	31.1710	3.7695	-3.7695	0.0046	-0.0016
44	3.0000	33.1820	-4.2773	-4.3359	0.0178	0.0069
45	33.0000	33.1820	4.3018	-4.3310	-0.0080	-0.0022
46	10.0000	35.1930	-2.2852	-4.9023	0.0027	-0.0042
47	18.0000	35.1930	0.0195	-4.8974	0.0048	-0.0039
48	26.0000	35.1930	2.3193	-4.8926	0.0063	-0.0036

Note: 1 inch = 25.4 mm

Vita

Xiandi Zeng was born in Taihe, Jiangxi Province, People's Republic of China on December 26, 1959. He grew up in his hometown. He attended the University of Electronics Science and Technology of China, Chengdu, China and graduated with a Bachelor of Science in Mechanical Engineering degree in January, 1982. In February, 1982, he began his graduate work at Southeast University, Nanjing, China and in July, 1984 he completed the requirements for the degree of Master of Science in General Mechanics. In August, 1984, he joined the Faculty of Southeast University as a lecturer. In March, 1986, he joined the Research Institute of Vibration Engineering, Nanjing University of Aeronautics and Astronautics, Nanjing, China. In August, 1989, he enrolled in the graduate school at Virginia Polytechnic Institute and State University, Blacksburg, Virginia. In November, 1994, he completed the requirements for the degree of Doctor of Philosophy in Mechanical Engineering.

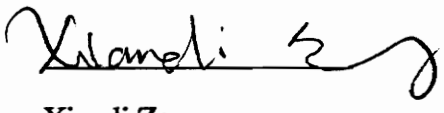

Xiandi Zeng